EARTHQUAKE-INDUCED COLLAPSE OF STEEL MOMENT RESISTING FRAMES WITH CONVENTIONAL AND HIGH PERFORMANCE STEEL COLUMNS

By

Yusuke Suzuki

Department of Civil Engineering and Applied Mechanics
McGill University, Montreal

November 2018

A thesis submitted to McGill University in partial fulfillment of the requirements of the degree of Doctor of Philosophy

CHAPTER 5: Experimental Studies on the Collapse Behaviour of Steel Columns in Moment Resisting Frames

5.1 Introduction

Shake table collapse experiments of steel frame structures (Suita et al. 2008, Lignos 2008, Lignos et al. 2011, Lignos et al. 2013) demonstrated that prior to earthquake-induced collapse, a structure deforms asymmetrically with large monotonic pushes and a few small inelastic cycles. This is also known as ratcheting behaviour as discussed by Ibarra and Krawinkler (2005). This necessitates the characterization of the collapse behaviour of structural components such as columns with protocols that mimic this behaviour. End columns in moment resisting frames (MRFs) may experience large variations in their axial load demands due to dynamic overturning effects. This aspect has been overlooked in prior testing programs (see Chapter 2). The testing program discussed in this chapter was developed with the goal to address both issues. In particular, the experimental program provides: (1) a unique data set of large-scale quasi-static cyclic column tests that experience complex deteriorating mechanisms associated with loss of the member's axial and flexural load carrying capacity; and (2) the validation of numerical models (see Chapters 6 and 7) for simulating the steel column behaviour through collapse. The

discussion of the experimental program mainly focuses on issues associated with column axial and flexural strength deterioration, low-cycle fatigue, as well as column axial shortening. A detailed summary of each test is provided in Appendix A of this thesis.

5.2 Testing Program

5.2.1 Test matrix

The testing matrix includes 21 cantilever ASTM A992 Grade 50 (i.e., nominal yield stress, f_y=345MPa) wide flange and ASTM A500 grade B (i.e., nominal yield stress, f_y=315MPa) steel HSS columns. The selected column sizes cover a representative range of local slenderness and shear span-to-depth ratios typically used in the North American and Japanese construction practice. All the columns are subjected to combined axial load coupled with lateral drift demands. The test matrix is summarized in Tables 5.1 and 5.2 for HSS and wide flange steel columns, respectively. These tables also include the nominal yield stress of the columns, their local slenderness ratios and the employed lateral and axial loading protocols. Referring to Figure 5.1 a 4- and 5-index specimen designation is used for HSS and wide flange specimens, respectively. For instance, "W-6-34-M-C" indicates that a W-shape steel column is tested with a $b_f/2t_f$ and h/t_w ratios equal to 6 and 34, respectively; the specimen is tested under monotonic lateral loading (i.e., "M") that is coupled with constant (i.e., "C") axial load (see Figure 5.1b).

Referring to Table 5.1, two HSS shapes (HSS 254×9.5 and HSS 305×16) are considered such that the effect of depth-to-thickness ratio, D/t, on local buckling and strength and stiffness deterioration is investigated. The D/t ratio for the HSS 254×9.5 is 26.7, which is close to the highly ductile compactness limit (D/t < 28.0) according to the Japanese seismic provisions (BCJ

2014). Specimen HSS 305×16 has a nominal D/t=19.1. Both specimens have the same shear span-to-depth ratio, L/D = 6.0. This is a common value for typical Japanese steel frame buildings (see Chapters 4 and 8). Note that HSS 300 columns are commonly used in low- to mid-rise steel MRFs. Therefore the specimen profile represents a full-scale column in a low- to mid-rise steel building or a 2/3 scale of a first story column in a mid- to high-rise steel frame buildings (Inoue et al. 1995).

Referring to Table 5.2, three types of wide flange shapes are selected. The main variation parameter of the wide flange sections is the web and flange width-to-thickness ratios (h/t_w and $b_f/2t_f$). A W14×82 is a seismically compact section in accordance with the U.S. and Canadian seismic steel provisions (AISC 2016, CSA 2010). The W14×61 has the same aspect ratio (D/b_f) as the W14×82 but has a more slender web and flange than that of the W14×82. Therefore, its $b_f/2t_f$ ratio slightly exceeds the current seismic compactness limit of 7.2 according to the AISC (2016) provisions. However, it is within the corresponding limit of 7.8 as per the CSA S16-09 seismic provisions. The W14×53 has a narrow flange width compared to the one of the W14×61 and W14×82 specimens. The $b_f/2t_f$ ratio of the W14×53 is the same with the one from the W14×82 section. Interestingly, the h/t_w ratio is the same with the one from W14×61. The latter is more prone to web local buckling than flange local buckling due to the high web slenderness ratio. Similarly with the HSS specimens, the span-to-depth ratio, L/D is representative of a full-scale low-rise MRF or a 2/3 scaled model of a first story column of a mid-rise MRF. Note that the W14×53 specimen has a different aspect ratio compared to the W14×61 and W14×82 specimens. The member slenderness ratio, L/r_y changes from 25 to 32.

This issue could potentially cause lateral torsional buckling to the W14×53 column coupled with local buckling.

The last varying parameter of the testing program is the lateral and axial loading protocol. Six different loading protocols are employed. The first one involves monotonic lateral loading with constant axial load (applied axial load ratio P/P_y=-0.3). The second one involves a symmetric lateral loading protocol (Clark et al. 1997) with constant axial load. The third and fourth protocols are collapse-consistent with constant and varying axial load, respectively (see Chapter 4). These protocols represent the loading that a first story interior and end column would "see" as part of a steel MRF when subjected to a near-fault ground motion. The fifth and sixth specimens are subjected to collapse-consistent loading protocols represent of long-duration ground motions. Details of the loading protocols are discussed in Chapter 4.

5.2.2 Test specimens

The wide flange and HSS specimens are fabricated in accordance with the North American and Japanese fabrication practice (AISC 2010b, BCJ 2011). Figures 5.2 and 5.3 show the specimen drawings including their weld details. The specimens are either 1,436 mm (HSS254×9.4) or 1,737 mm long and directly welded to a 76 mm and 51 mm thick base plates at the bottom and top ends, respectively. Specimens with HSS are connected to base and top plates through a complete joint penetration (CJP) single bevel groove weld with steel backing as shown in Figure 5.2. Specimens with wide-flange cross sections are connected to base and top plates through a CJP groove weld with back gouging as shown in Figure 5.3. The weld access holes are designed in accordance with AISC341-10 (AISC 2010b). Ultrasonic (UT) non-destructive testing confirmed that discontinuities due to welds are within the allowable limits per AWS

D1.1/D1.1M:2010 (AWS 2010). Figure 5.4 shows examples of fabricated welds and weld access holes of the H-27-C1-V and W-6-34-S-C specimens. Weld surfaces were grounded so that possible weld notches were removed. The W14×61 (W-8-34 series), W14×82 (W-6-25 series) and HSS305×16 (H-19 series) specimens were sand blasted prior to fabrication. Tables 5.3 and 5.4 summarize the corresponding measured dimensions for each specimen. Note that the HSS specimens are made of cold-formed hollow sections with a single side seam welding. The seam weld was oriented on the web of specimens H-27-M-C, H-27-C1-C, H-19-S-C, H-19-C1-C and H-19-C1-V; the seam weld was oriented at the flange of specimens H-27-S-C, H-27-C1-V, H-27-C2-C and H-27-C2-V.

5.2.3 Test setup

Figures 5.5 and 5.6 illustrate the elevation and plan views of the test setup, respectively. Figure 5.7 shows an image of the test setup overview after the installation of an HSS column in place. Figures 5.8 and 5.9 show a detailed view of the lateral reaction system and vertical loading system, respectively. For the W14×53 and HSS254×9.5 specimens a single-ended +450/-650 kN lateral actuator with +/-1000mm stroke is employed. For the W14×61, W14×82 and HSS305×16 specimens a +/-1,000kN dual-ended dynamic actuator with +/-500mm stroke is employed. Referring to Figure 5.8, these actuators react against a reaction frame that consists of a W14×159 reaction beam. This transfers the column base shear to two W14×257 vertical reaction posts. These reaction posts have bolt holes every 100 mm such that the loading height can be easily adjusted in order to accommodate specimens with different heights. The vertical reaction posts are anchored and braced to the laboratory strong floor through a set of 50 mm thick base plates and steel brackets, respectively. The base plates and steel brackets are pre-

tensioned to the strong floor through a total of 20 high strength ASTM A193 grade B7 steel rods with a 38 mm nominal diameter each (i.e., nominal yield stress, f_y = 830 MPa). Each one of the rods is pre-tensioned to about 400 kN such that the reaction frame can safely transfer 1000 kN base shear at the strong floor.

Referring to Figure 5.9, a vertical actuator of 11,000kN is utilized to apply the constant or varying axial load on the steel column specimens. This actuator has a 300 mm displacement stroke. The axial load is applied to a steel column specimen through an axially rigid link that is designed for -4,000kN in compression and 2,000kN in tension. The top end of the axially rigid link is connected to a structural pin attached to the vertical actuator. The other end of the rigid link is also connected to a nominally identical structural pin, which is connected to a steel column specimen at the other end. The location of this pin represents the inflection point of a first story column when it behaves elastically during cyclic loading. The structural pins are shown in Figure 5.10. They were designed for -4,000kN compressive and 2,000kN tensile axial load. The two pins allow for the lateral displacement of a test specimen up to about 20% lateral drift ratio without transferring any moments at the top of the vertical loading system. Figure 5.11 shows a column nearly at 20% lateral drift ratio. Because the vertical load is applied on a steel column with load control, in case that a steel column loses its axial load carrying capacity (i.e., column fully squashes) then the actuator control is automatically switched to displacement control.

A steel column is bolted to the strong floor through a 76 mm thick base plate, which is bolted through a set of twelve ASTM A490 structural bolts with 38 mm diameter to a 100 mm thick adapter plate. The steel column top end is connected through a 51 mm thick steel plate to a

loading plate adaptor, which is connected to the pin joint of the lateral and vertical actuators. Therefore a steel column specimen can be idealized with fixed-pin boundary conditions. The loading height of various column specimens summarized in Tables 5.1 and 5.2 are either 1,525 mm or 1,825 mm to match the target span-to-depth ratio per specimen shown in the same tables.

To minimize the base plate thickness of each test specimen a 100mm thick adapter plate is utilized as shown in Figure 5.12. This plate is connected to the strong floor through a set of twelve 38mm diameter ASTM A490 fully threaded bolts. In order to accommodate varying axial load up to about 1,300 kN in tension (i.e., P / P_y = +20%) shear keys are employed to prevent slip of both the adapter and the steel column base plates. These shear keys are shown in Figure 5.12. The A490 bolts of the base plate as well as the adapter plate are pre-tensioned to 200kN. This load corresponds to about 25% of the yield strength of the bolt (38 mm structural bolt, ASTM A490). In the case of variable axial load, the applied bolt pre-tension forces are 400kN.

A test specimen is laterally braced at its loading height to restrain any out-of-plane movement. A set of slider plates is used for this purpose as shown in Figure 5.13. This allows for a column specimen to slide against two longitudinal wide-flange beams (noted as lateral braces) located on each side of the loading plate adapter. To minimize friction between the two sliding surfaces a thick lubricant is used. After the first test (i.e., W-6-34-M-C) it was found that the out-of-plane deflection of the lateral bracing system was fairly large thus, the lateral support system was reinforced with a set of four additional braces (see Figures 5.6 and 5.14).

5.2.4 Instrumentation

In order to be able to deduce the moment-rotation of the steel column specimens including the effect of P-Delta and axial shortening on their hysteretic response a set of instruments is used.

Two different data acquisition (DAQ) systems are employed. The first one records the signals from strain gauges, linear string potentiometers, linear variable differential transformers (LVDTs), inclinometers and actuator displacement and load readings. The sampling rate that is used in this DAQ is 0.1Hz. In order to be able to record potential torsional mode deflections in the wide flange steel columns and the extent of cross-sectional distortion due to local buckling a Krypton K600 optical wireless measuring system is also used. The sampling rate in this unit is set to be 0.05Hz.

In order to trace the strain profiles within a column cross-section to trace the position of neutral axis during cyclic loading, 27 strain gauges are installed. These are standard 120 Ω resistance gauges with measurement strains range from 0 to 150,000με. The location of strain gauges was decided based on a detailed finite element study prior to the testing program. Figure 5.15 shows the location and designation of strain gauges for the HSS and wide flange specimens. Table 5.5 shows the strain gauge length as well as the gauge factors for all the strain gauges that are installed per specimen. These locations depend on the column depth and width as shown in the same figures. Note that the first layer of strain gauges from the bottom is positioned at a 0.15*D* distance from the base plate such that the strain readings are not measured within the heat affected zone near the base CJP welds.

Figures 5.16 and 5.17 illustrate the position and notation of the LVDTs, inclinometers and string potentiometers for a typical steel column. Figure 5.18 shows a snapshot of the setup of those instrumentations. Table 5.6 summarizes the setup dimensions to be used in calculation of a specimen's deformation. Specimen deformation is calculated based on the considered configuration of the specimen as shown in Figure 5.19. In summary, four LVDTs are positioned

vertically at the base plate (named v_{BW1}, v_{BW2}, v_{BE1}, v_{BE2}). These are used to monitor potential base plate uplift. This is done based on Equation 5.1, as follows,

$$v_b = (v_{BE1} + v_{BW1} + v_{BE2} + v_{BW2})/4 \tag{5.1}$$

Base plate rotation is also measured with two inclinometers (θ_{BW} and θ_{BE}) as shown in Figures 5.16 to 5.18 that are placed in line with the vertical LVDTs. These measurements are used as a backup in case that the primary measurements from the LVDTs won't work during a test. The base plate rotation, θ_{b1}, can be deduced based on the LDVT measurements from Equation 5.2. If the inclinometers are employed for the same purpose, the base plate rotation (noted as, θ_{b2}) can be deduced from Equation 5.3,

$$\theta_{b1} = \{(v_{BE1} + v_{BW1})/2 - (v_{BE2} + v_{BW2})/2\}/L_b \tag{5.2}$$

$$\theta_{b2} = (\theta_{BW} + \theta_{BE})/2 \tag{5.3}$$

From Figures 5.16 to 5.18, two additional LVDTs (noted as u_{B1} and u_{B2}) are positioned on the side of the base plate in plane with the lateral displacement loading in order to monitor potential base plate slip during a test. The base plate slip can be deduced from Equation 5.4,

$$u_b = (u_{B1} + u_{B2})/2 \tag{5.4}$$

Two string potentiometers are used to measure the lateral displacement of a column (u_{TE} and u_{TW}) as well as its axial shortening (v_{TE} and v_{TW}). These are shown in Figure 5.16. An additional string potentiometer (noted as u_{Pin}) is also used to measure the lateral displacement of the top-end pin of the rigid link with respect to the strong floor because the vertical loading system is not braced.

The relative displacement, u_t, of a steel column with respect to the strong floor can then be deduced based on Equation 5.5,

$$u_t = (u_{TE} + u_{TW})/2 \tag{5.5}$$

The average axial shortening of the same column can be deduced based on Equation 5.6,

$$v_t = (v_{TE} + v_{TW})/2 \tag{5.6}$$

A set of two inclinometers is also positioned at the top plate welded to a steel column to measure the inclination of this plate (θ_{TE} and θ_{TW}) during a test (see Figure 5.16). The average inclination can be deduced based on Equation 5.7,

$$\theta_t = \frac{\theta_{TE} + \theta_{TW}}{2} \tag{5.7}$$

In order to be able to compute the top plate lateral and vertical displacements (noted as u_0 and v_0) at the centerline of the adaptor plate as shown in Figure 5.19 with respect to the global coordinate system, the following set of equations should be used,

$$u_0 = \sqrt{(L_h + u_t)^2 - (v_0 + L_{t2} sin\theta_t)^2} - L_h - L_{t2}(1 - cos\theta_t) \tag{5.8}$$

$$v_0 = L_v - \sqrt{(L_v - v_t)^2 - (u_t - L_{t2}(1 - cos\theta_t) - L_{t1} sin\theta_t)^2} + L_{t1}(1 - cos\theta_t) \tag{5.9}$$

In these equations, L_v and L_h correspond to the initial length of the string potentiometers for vertical and lateral displacement of the specimen; L_{t1} and L_{t2} correspond to distances from string potentiometer target to specimen centerline as shown in Figure 5.16. The axial displacement, δ, of a steel column can then be computed by using Equation 5.10,

$$\delta = H - \sqrt{(u_o - u_b)^2 + (H - v_o - v_b)^2} \tag{5.10}$$

In this equation, H corresponds to the specimen height (distance from top surface of base plate to loading plate).

In order to compute the deduced chord rotation, θ of a steel column specimen as shown in Figure 5.19, the top pin rotation, θ_{pin} should first be deduced with respect to the strong floor due to the lateral movement of the high force MTS test frame. This rotation is defined in Figure 5.19 and can be computed based on Equation 5.11,

$$\theta_{pin} = \tan^{-1}\left(\frac{u_{pin} - u_b}{H + L_{t3} + H_{act} - v_b}\right) \tag{5.11}$$

In this equation, H_{act} corresponds to the distance of two pins connected to the rigid link for vertical load. The deduced chord rotation of a steel column can then be computed based on Equation 5.12,

$$\theta = \tan^{-1}\left(\frac{u_o - u_b}{H - v_o - v_b}\right) - \theta_{b1} \tag{5.12}$$

In order to deduce the position of the center of the bottom pin in terms of vertical and lateral displacements with respect to the global coordinate system (noted as u_2 and v_2, respectively), Equations 5.13 and 5.14 should be used, respectively. This point infers to the position of the column inflection point,

$$v_1 = v_o + L_{t3}(1 - \cos\theta_t) \tag{5.13}$$

$$u_1 = u_o + L_{t3}\sin\theta_t \tag{5.14}$$

In these equations, L_{t3} corresponds to the distance from the loading plate to the center of the pin for vertical load. Another point that is necessary to deduce its relative coordinates with respect to the global coordinate system of the test setup is the center of the pin of the lateral load actuator, which is attached to the adapter plate that loads the specimen laterally. The horizontal and

vertical displacements of this point are noted as u_2 and v_2, respectively as shown in Figure 5.19. In order to compute these two displacements Equations 5.15 and 5.16 should be used,

$$u_2 = u_o - L_{t5}(1 - \cos\theta_t) \tag{5.15}$$

$$v_2 = v_o + L_{t5}\sin\theta_t \tag{5.16}$$

In these equations, L_{t5} corresponds to the distance from the specimen centerline to the center of pin for lateral load.

In order to deduce the moment at a steel column base plate, we first need to compute the inclinations of the two actuators with respect to the undeformed configuration of the steel column. Equations 5.17 and 5.18 can be used to compute the inclination, θ_{actL} of the lateral actuator with respect to the strong floor and the inclination of the vertical actuator, θ_{actV} with respect to the vertical undeformed configuration as shown in Figure 5.19.

$$\theta_{actL} = \tan^{-1}\left(\frac{v_2}{L_{act} - u_2}\right) \tag{5.17}$$

$$\theta_{actV} = \tan^{-1}\left(\frac{u_1 - u_{pin}}{H_{act}}\right) \tag{5.18}$$

In these equations, L_{act} and H_{act} are defined as the distances of the two pins connected to the lateral actuator and the rigid link for vertical load. Therefore, the vertical load, P', applied to the column specimen can be computed based on Equation 5.19,

$$P' = P\cos\theta_{actV} + W - Q\sin\theta_{actL} \tag{5.19}$$

In this equation, P is the axial load that is measured at the vertical actuator as shown in Figure 5.19 at the inclined position; W and Q are defined as the self-weight of the pin assemblies (pins, rigid link, W_v, and half of lateral actuator, W_h) and applied load of lateral actuator, respectively.

The deduced moment of the column at the base plate location can be defined based on Equation 5.20,

$$M = Q\cos\theta_{actL}\frac{(H+v_2)}{1000} - (W_h - Q\sin\theta_{actL})\frac{(L_{t5}+u_2)}{1000} + P\sin\theta_{actV}\frac{(H+L_{t3}-v_1)}{1000} + (P\cos\theta_{actV} + W_v)\frac{u_1}{1000} \quad (5.20)$$

A Krypton optical wireless measuring system (System K600) is also used in order to accurately measure a potential lateral torsional deflection movement of the steel column specimens as well as to monitor any potential deflection of the lateral support system. The same unit is used as a backup system to monitor the specimen's base plate slip. The Krypton camera unit is placed 5 m away from the north side of a specimen. It is able to monitor the movement of a light-emitting diode (LED) target attached on the column specimen and setup. Figure 5.20 shows the positions and designation of the LED targets that are used. Figure 5.21 shows the instrumentation setup of the Krypton wireless measurement system. The LED targets that are placed on the base plate are used to measure any potential base plate slip. The LED targets that are placed on the lateral bracing system are used to monitor the elastic out-of-plane deflection of the lateral support system. For the HSS254×9.5 specimens, the LED targets are attached both on the flange and web of the specimens. Plastic brackets are epoxied on the web so that the LED targets are visible from the camera. For the HSS305×16 and all the wide flange columns, the LED targets are attached only on the north flange of each specimen. A detailed summary of all the sensors can be found in Tables 5.7 to 5.9.

5.3 Loading Protocols

The collapse-consistent loading protocols are based on a 12-story MRF (frame height = 45 m) reference frame discussed in detail in Chapter 8 as well as concepts discussed in Chapter 4 of

this thesis. Figure 5.22 illustrates the employed collapse-consistent lateral loading protocols for HSS columns representing the effects of a near-fault ground motion (see Figure 5.22a and Figure 5.22c) and a long-duration (see Figure 5.22b). Note that the number of loading steps observed in a long-duration collapse consistent protocol is about three times more than the ones in the near-fault collapse loading protocol for reasons discussed in Chapter 4. Figure 5.22c shows the employed loading history for the more compact HSS cross-section. A more compact section is likely to experience less number of small inelastic cycles prior to collapse than a slender one. In case that a full loading protocol is completed but the steel column does not reach zero flexural capacity and/or complete loss of its axial load carrying capacity then, the same protocol is repeated from the deformed configuration. Each time that a protocol is repeated a steel column specimen experiences a new loading phase.

In Figure 5.22, the axial load synchronization coupled with the lateral drift loading protocol is also shown. For a 12-story MRF (i.e., 45 m height) the axial load ratio (P / P_y) due to dead and live load is estimated to be -0.15 and -0.3 for end and interior columns, respectively. This difference is due to the tributary floor area of the end column compared to the interior column for the assumed building configuration (see Chapters 4 and 8). In the case of constant axial load (representative of interior columns), a compressive axial load P = -0.3P_y is applied to the steel column. This load remains constant throughout the test. In the case of varying axial load (representative of end columns), the steel column is loaded axially in compression (-0.15P_y). During the lateral deformation of the column the applied axial load ratio varies from -0.5 in compression to +0.2 in tension. The collapse-consistent loading protocols for wide-flange cross-sections are developed in a similar manner and are shown in Figure 5.23.

In order to assess the differences of the employed near collapse loading protocols compared to traditionally used loading protocols, the AISC symmetric loading protocol (Clark 1997, AISC 2010a) is utilized. In order to uniquely define the backbone curve of the tested steel columns, a monotonic lateral loading is also considered. The monotonic and symmetric lateral loading protocols are coupled with a constant axial load P/P_y = -0.3. Figures 5.24 and 5.25 show both protocols in terms of column lateral drift ratio versus number of cycles. Because the emphasis of the testing program is at collapse, the number of cycles of the first three displacement amplitudes (i.e., 0.00375rad, 0.005rad and 0.0075rad) of the AISC symmetric loading protocol are slightly modified. During these cycles, test specimens' behaviour is essentially elastic.

5.4 Tensile Coupon Tests

The HSS sections are fabricated by ASTM A500 grade B steel (i.e., nominal yield stress, f_y = 315 MPa). The wide flange sections are fabricated by ASTM A992 Grade 50 steel (i.e., nominal yield stress, f_y = 345MPa). The material properties of these sections are obtained from tensile coupon tests and compared with certified mill test reports. ASTM E8/E8M (ASTM 2009) rectangular tension test specimens (plate-type standard) are considered for the HSS flat part of the cross section as well as the wide flange sections, as shown in Figure 5.26a. In addition, tensile coupon tests are conducted to extract the mechanical properties of the large-diameter tubular products (specimen 1) in the HSS corner sections, as shown in Figure 5.26b. Figure 5.27 illustrates a set of drawings indicating the location from which the tensile coupons are extracted. Three tensile coupons per location are fabricated per steel heat.

The steel coupons are tested under uniaxial tension. Figure 5.28 shows the general setup including the instrumentation. The gauge length of the flat plate and corner section coupons are

200 mm and 50 mm, respectively. The maximum elongation of the extensometer is 25 mm. Typically, the tensile coupons elongate more than 25 mm prior to fracture. Therefore, the extensometer is reset once the gauge length closes. This operation changes the gauge length during the test. The estimated gauge length after the first lock of the extensometer is around 170 mm. This typically leads to an estimated ultimate elongation, which is 2-3% larger than the case of a 200 mm gauge length. Strain gauges are also installed to detect the initiation of yielding and also verify the Young's modulus of the respective steel materials.

Table 5.10 summarizes the chemical composition of the steel material used per steel column shape as reported from the mill certificates. Tables 5.11 and 5.12 summarize the measured coupon dimensions and mechanical properties obtained from the engineering stress strain curves based on the tensile tests for the HSS and wide flange steel columns, respectively. In summary, from these tables, the average yield stress (noted as YS) and ultimate stress (noted as TS) are above the specified nominal yield and ultimate stress regardless of the steel material and steel plate considered in this study. Figures 5.29 and 5.30 illustrate the engineering stress-strain curves per steel material. Note that all three coupons per location are superimposed in the same graph for comparison purposes. The stress strain curves from the tensile coupons from the HSS steel columns do not have a typical yield plateau. This is mainly due to the material pre-straining during the manufacturing process. The reported values of the measured yield stress per tensile coupon are determined based on the 0.2% offset elastic module line. From Figures 5.29 and 5.30 and Tables 5.11 and 5.12, the measured mechanical properties for all cases are within a 5% range compared to the mill certificates obtained from the steel fabricator. The only exception is the H-19-F series (HSS 305×16). In this case, the measured yield and tensile stress is about 40MPa off compared to values from the mill certificate because the measured plate thicknesses of these

coupons were 1 mm thinner than their nominal thickness (see Table 5.11). From Table 5.11 and Figure 5.29, the steel coupons extracted from the HSS columns have a small strain hardening value; in particular, the yield-to-tensile stress ratios of these materials taken from flat parts (noted as YR) are 0.85 (H-27-F series) and 0.78 (H-19-F series). The uniform elongations are 10% to 15%. In the case of tensile coupons obtained from the wide flange columns (see Table 5.12 and Figure 5.30), all the engineering stress-strain curves show a typical yield plateau. The measured mechanical properties from these coupons are fairly consistent. The YR of the flange is around 0.75 and the corresponding uniform elongation is around 15% or more regardless of the steel wide flange section.

5.5 Test Results and Discussion

A detailed description of each test is presented in Appendix A together with a comprehensive set of figures that show the deformed shape of the member. This section only discusses selective findings from the experimental program grouped per cross-section type (HSS, wide flange) for brevity. Note that the reported results in terms of moment-rotation relations have been post-processed such that friction has been subtracted from the measurements based on a systematic approach that is illustrated schematically in Figures 5.31. Figure 5.31a shows an example of the deduced moment versus chord rotation of specimen H-27-S-C that was tested with a symmetric lateral loading protocol under constant axial load ratio. From this figure, it can be seen that the succeeding loading excursion initiates with a very high lateral stiffness. Once the moment drops, the unloading stiffness becomes equal to the elastic stiffness of the specimen. This difference in the lateral stiffness is attributed due to friction of the structural pins. To subtract the friction from the measured moment data, post-test data processing is employed, as schematically shown in Figure 5.31b. The post-test data processing includes the following steps:

- The elastic stiffness of the steel column is extrapolated to the point that the current excursion starts in terms of deformation.
- Friction is deduced as the gap between the moment at the measured peak of the previous excursion (i.e., 22nd excursion in the figure) and the moment that is linearly extrapolated from the elastic stiffness in the current excursion (23rd excursion in this case).
- In the last step, let the moment shift such that the last point of the previous excursion and the initial point of the current excursion extrapolated from the elastic stiffness joint together at the middle point of the deduced friction.

Figure 5.31c shows the measured moment-rotation relation including friction in comparison with the post-processed one after subtracting friction from the measurements.

5.5.1 Observed failure modes

5.5.1.1 HSS specimens

Figure 5.32 shows the deformed shapes of the tested HSS specimens. The primary failure mode in all cases is local buckling. Table 5.13 summarizes the observed failure modes and locations of local buckling of the tested HSS specimens. In HSS columns, the buckling half wavelength ranged from $0.8D$ to $1.0D$ unless if the elephant foot buckling mode occurred. In this case, the buckling half wavelength was equal to $0.6D$. Notably, the elephant foot mode was only observed in highly compact HSS cross-sections (D/t = 19) under constant compressive axial load ratios. This agrees with earlier findings from experiments on HSS steel columns (Mukaide et al. 2016). The center of the local buckling wave was at a height range equal to $0.4D$ to $0.7D$ from the top surface of the column base plate. In the H-19-C1-V specimen, local buckling occurred at a higher location. During the varying axial load, the high compressive axial load demand increases

the P-delta moment thereby, shifting the location of the maximum moment away from the column base. The observed buckling mode in this case is not the same as that in HSS specimens under constant compressive axial load. This issue is further explored in Chapter 6 by means of continuum finite element analysis.

Fracture did not occur in any of the tested HSS columns. Ductile tearing was only observed at the corner portion of the H-19-C1-V specimen near the end of the test. No observed cracks were evident at the welding toe of all the HSS columns even for very compact cross-sections.

5.5.1.2 Wide flange specimens

Figure 5.33 shows the observed deformed shapes of the tested wide flange specimens. Table 5.14 summarizes the observed failure modes and locations of local buckling of the wide flange specimens. Local bucking near the base of the wide flange steel columns typically included two types. The first one initially formed at a location close to the column base plate; the second one typically developed above the first buckling wave. Although the corresponding L/r_y ratios were well below 50 in all cases, the second buckling mode triggered lateral torsional buckling in most cases. This sequential buckling mode formation was observed in most of the wide flange specimens as summarized in Table 5.14. From the same table, the observed buckling lengths of the first and second buckling wave were equal to $0.6D$ to $1.0D$, respectively. The locations of the buckling center ranged from $0.4D$ to $0.7D$ for the first buckling wave and from $0.9D$ to $1.2D$ for the second one from the base plate's top surface, respectively. The location and the corresponding buckling length did not change regardless of the employed lateral loading protocol and the specimen section profile. Interestingly, in the case of W-6-34-C2-V and W-8-34-C1-V columns where a varied axial load was coupled with the lateral loading protocol, the second

buckling mode did not develop. This is because the first buckling wave did not grow much. In the case of W-6-25-S-C, the first buckling wave occurred at a higher location compared to the rest of the columns with the same cross section. The test observations suggest that once the buckling center location is at a higher position with respect to the column base, this triggers the torsional deflection of a wide flange column while it displaces laterally. Referring to Figures 5.33c and 5.33d, local buckling deformation of W-6-34-C1-C under constant compressive axial load after phase 2 loading (i.e. achieved rotation was 0.084 rads) is much more substantial compared to the W-6-34-C1-V specimen under varying axial load. Referring to Figures 5.33c and 5.33e, W-6-34-C2-C (long-duration collapse protocol) developed more local buckling damage than that of W-6-34-C1-C (near-fault collapse protocol).

Figure 5.34 shows photos of typical fracture modes observed in the wide flange specimens. Referring to Figure 5.34a, wide flange columns subjected to a constant compressive axial load (typically interior columns in moment resisting frames) is likely to experience fracture in the k-area. This is attributed to the substantial growth of local buckling around the steel column web due to severe axial shortening. Referring to Figure 5.34b, stockier wide flange columns subjected to varying axial load may experience fracture in the flange welding toe and the web access hole if the AISC design provisions are not strictly followed. This is attributed to the high strain demand at the column base due to the delay of the local buckling formation.

5.5.2 Deformation performance

Table 5.15 summarizes the achieved loading phase and associated maximum rotation of the specimens. From this table, except for specimens H-27-C1-V, H-27-C2-V, W-6-34-C1-V, W-6-25-C1-C and W-6-25-C1-V, the rest completely lost flexural strength and/or fractured as shown

in Figure 5.34. All specimens were tested to the stage where the bending moment degraded by at least 50% with respect to the peak moment. The general consensus is that end columns behaved better than interior columns that experienced a constant compressive axial load and were subjected to the same lateral loading history.

5.5.2.1 H-27 series

Specimen H-27-C1-C collapsed during the Phase 2 loading and was able to achieve 8.5% in rotation. Specimen H-27-C2-C failed at the very beginning of Phase 2 loading. In this case, the achieved rotation was 5.8% rads. This indicates the influence of long-duration on the column performance. In particular, the effect of cyclic deterioration on the column flexural strength is more pronounced than the case of a near-fault collapse protocol. Note that these specimens satisfy the seismic compactness limits according to the Japanese and Canadian seismic provisions (BCJ 2014, CSA 2014). The current compactness limits as per the AISC seismic provisions (AISC 2016) for HSS are more stringent than the Japanese provisions; therefore the H-27 specimens do not satisfy the AISC limitations. Because both specimens failed during Phase 2 loading (i.e., second repetition of the collapse-consistent loading protocol that is a representative of a seismic event with low probability of occurrence), it is implied that a seismically compact HSS column does not fully lose its axial load carrying capacity during a low-probability of occurrence earthquake. However, if a similar magnitude event would occur for a second time then such column would lose its axial load carrying capacity. This could be potentially important in case of aftershocks following major earthquake events.

End columns in steel MRFs (H-27-C1-V and H-27-C2-V) were tested under varying axial load conditions. These specimens showed better performance in terms of the achieved rotation (8.6%

and 9.6% rads) and number of increasingly repeated loading phases. The test observations suggest that the buckling wave near the end column base did not grow as much compared to specimens subjected to the same lateral loading protocol coupled with a constant compressive axial load as discussed in Section 5.5.1. This implies that interior steel MRF columns experience much more inelastic damage compared to end columns within the same story during an earthquake.

The achieved drift ratios of the H-27-M-C and H-27-S-C specimens were 15.5% and 4.4%, respectively. The performance of the same columns subjected to the collapse protocols discussed earlier in terms of maximum deformation ranged between the ones observed from monotonic and symmetric cyclic loading protocol. Note that the achieved drift of the H-27-C1-C was twice the corresponding drift that the H-27-S-C specimen achieved. This illustrates that a symmetric lateral loading protocol may not be realistic to assess the collapse performance of a steel MRF column subjected to a near-fault ground motion. The reason is that this protocol includes far more inelastic cycles than the ones typically observed in near-fault earthquakes that cause cyclic deterioration in strength and stiffness of the column. On the other hand, long duration collapse-consistent loading protocols pronounce the effect of cyclic deterioration on the column flexural strength due to the large number of small inelastic cycles that one would typically observe in such earthquakes.

5.5.2.2 H-19 series

Specimens H-19-C1-C and H-19-C1-V (D/t = 19), achieved rotations of 14.9% and 12.7% rads, respectively. These specimens were able to resist four phases of the collapse-consistent lateral loading protocol. Similarly, the difference of the achieved drift amplitudes prior to collapse

between a near collapse and a symmetric loading protocol becomes larger than the observed one in H-27 specimens. In particular, the achieved lateral drift under collapse-consistent loading protocol was three times larger than the one from a symmetric loading protocol. Looking at the maximum rotation of the H-19-S-C specimen versus the H-27-S-C specimen, a symmetric lateral loading protocol would not properly quantify the collapse resistance of a more compact steel column. This is particularly important when non-simulated collapse criteria are employed within the nonlinear response history analysis of frame structures.

5.5.2.3 W-6-34 series

Specimens W-6-34-C1-C and W-6-34-C1-V achieved a 12% rads rotation and were able to sustain three phases of the imposed collapse-consistent loading protocol. Similarly with the HSS columns, this performance is twice larger than the corresponding one of the same column subjected to a symmetric lateral loading protocol. Due to the varying axial load, an end column in a steel MRF would be able to accommodate far more inelastic cycles than an interior column within the same story of the same frame. In this case, the achieved drift was 6.4% (W-6-34-C2-C) and 10% (W-6-34-C2-V). A long-duration collapse protocol typically leads the steel column to collapse at smaller displacement amplitudes than a near-fault collapse protocol. Same observations hold true with HSS columns regarding the influence of the loading history.

5.5.2.4 W-8-34 series

The achieved rotations of this set of wide-flange columns were around 12% (W-8-34-C1-C) and 14% (W-8-34-C1-V) under the near-fault collapse protocol. The deformation capacities were similar to the ones from W-6-34-C1-C and W-6-34-C1-V specimens. The effect of flange slenderness on the maximum deformation capacity of a column is fairly small in this case.

However, the flange slenderness has an effect on the observed failure mode. The W-8-34 specimens have a more slender flange compared to that of the W-6-34 specimens. This implies that a W-8-34 column would deteriorate in strength more rapidly than a W-6-34 column. However, the torsional resistance of the W-8-34 column is enhanced compared to the W-6-34 one. Those effects balanced the deformation performance of the W-8-34 specimens.

5.5.2.5 W-6-25 series

The achieved rotations of the W-6-25-C1-C and W-6-25-C1-V were 14.6% and 13.3%, respectively. However, the specimens did not reach zero strength due to the lateral actuator load capacity limitations. Therefore the actual deformation capacities of these specimens are more than the documented values prior to collapse. Note that the plastic deformation of this specimen is fairly high compared to the other wide flange specimens. On the contrary, the achieved lateral drift prior to collapse of this column when it was subjected to a symmetric protocol did not change by much compared to the corresponding values from specimens W-6-34-S-C and W-8-34-S-C that have much higher local slenderness ratios.

5.5.3 Effect of loading history on moment-rotation relation

5.5.3.1 Columns under constant compressive axial load

Figure 5.35 shows a comparison of the deduced moment- and axial shortening-rotation relations for the HSS and wide flange steel columns subjected to different lateral loading protocols (monotonic, symmetric and collapse-consistent protocols) coupled with a constant compressive axial load. From these figures, strength and stiffness deterioration occurred due to monotonic and cyclic loading. The moment degraded both in the positive and negative loading direction. This is attributed to the fact that both the north and south flange of the steel columns buckled in all cases

(see Figures 5.32 and 5.33). Cyclic deterioration in strength and stiffness depends on the number of inelastic cycles that each column is subjected to. The general consensus is that the effect of cyclic deterioration on column strength and stiffness is larger when a symmetric cyclic loading protocol is employed compared to a collapse-consistent long-duration or a near-fault loading protocol. The observed trends are general and they do not depend on the employed cross-section. Very compact cross-sections (e.g., H-19 and W-6-25 specimens) have considerable plastic deformation capacities as seen in Figures 5.35b and 5.35e. However, this issue is not depicted when these columns are tested under symmetric cyclic loading histories. This is an important observation in the context of seismic assessment methodologies consistent with ASCE 41-17 (ASCE 2017b). This has been recognized in prior related work (Elkady and Lignos 2018b).

5.5.3.2 Columns under varying axial load

Figure 5.36 shows a comparison of the deduced moment- and axial shortening-rotation relations of columns subjected to different collapse-consistent loading protocols (near-fault and long-duration collapse protocols) coupled with varying axial load. Strength deterioration occurred once the large monotonic drift amplitude was imposed in the positive loading direction. Interestingly, cyclic strength deterioration did not occur in this case because each time that the column displaced in the negative loading direction the already developed buckling wave in the previous loading excursion was stretched due to the application of axial tension. Instead, the moment demand in the negative loading direction increased due to material cyclic hardening. However, this depends on the drift amplitude reversal. The H-27-C2-V specimen experienced flexural strength deterioration in the same loading direction once its south flange buckled.

5.5.4 Effect of loading history on column axial shortening

5.5.4.1 Columns under compressive axial load

Referring to Figure 5.35, axial shortening accumulates in the positive and negative loading direction in all specimens subjected to a constant compressive axial load. Therefore the amount of axial shortening depends on the number of cycles and the corresponding displacement amplitude of the imposed lateral loading protocol. Squashing occurred when the axial shortening achieved a certain level (around 5% for H-27 specimens and 10% for W-6-34 specimens). Columns subjected to constant compressive axial load lose their axial load carrying capacity at about the same amount of axial shortening regardless of the employed lateral loading protocol once they reach similar amounts of cumulative plastic rotation, $\sum \theta_p$. This indicates the dependence of column axial shortening with $\sum \theta_p$. The column loses its axial load carrying capacity when the flexural resistance reaches to zero in both loading directions. Figure 5.35 suggests that columns with lower local slenderness ratios tend to shorten less under a given lateral loading history. This indicates the dependence of column axial shortening on the cross-section slenderness. Although the applied axial load ratio is not a parameter that is varied during the testing program, a similar dependence between the column axial shortening and the applied axial load ratio has been identified (Elkady and Lignos 2018a, b).

5.5.4.2 Columns under varying axial load

Referring to Figure 5.36, a striking issue is that axial shortening in end columns varies linearly with respect to the column chord rotation. When a column displaces in the negative loading direction and the axial load reverses from compression to tension, the column axial shortening becomes nearly zero. Physically the local buckling wave straightens (see Figures 5.32 and 5.33);

thereby the resultant residual axial shortening is much smaller than that observed in interior steel columns of the same story that experience the same lateral loading history (see Figure 5.35). This implies that within the first story of a steel MRF there could be slab tilting and catenary action prior to structural collapse. This issue is examined carefully in the following section and in Chapter 8 through system level collapse simulations.

5.5.5 Interior versus end column hysteretic behaviour

Figure 5.37 compares the moment- and column axial shortening-rotation relations for nominally identical steel columns subjected to the same lateral loading coupled with varying and constant compressive axial load. The former represents the loading conditions that an end column of a steel MRF experiences during an earthquake. The applied axial load demand varies due to the dynamic overturning effect. The latter represents the loading conditions of interior steel MRF columns during an earthquake. Referring to Figure 5.37, the flexural strength of a steel column typically deteriorates faster under varying axial load at the beginning of the lateral loading protocol because of the high axial compressive load demand prior to the onset of column local buckling. The column flexural strength under constant compressive axial load deteriorates cyclically regardless of the applied lateral loading protocol; however, this is not the case for an end column. Cyclic deterioration in strength in this case depends on the direction of the lateral loading. As a result the end column achieves larger lateral deformation than that of the interior column. For the case of H-19-C1-V specimen, moment deterioration is faster compared to the same column subjected to constant axial load (H-19-C1-C). This is attributed to the fact that the deterioration of axial load variation amplitude is relatively less compared to the other slender sections (see Figure 5.22).

Another notable observation is that the column flexural strength in the negative loading direction (i.e., column displaces south) in most cases does not deteriorate when the axial load varies. This occurs because the column is subjected to a tensile axial load when it displaces to the negative loading direction. As a result the buckling wave near the base of the steel column is stretched. As a consequence, the south flange of the steel column does not buckle due to the neutral axis position within the cross-section (see Figures 5.32 and 5.33). As such, the flexural strength of a steel column under constant axial load deteriorates cyclically in both lateral loading directions; though, its peak strength moment is typically not reached. The prior observations become more evident in slender steel columns subjected to a long-duration lateral loading protocol. This protocol includes a large number of inelastic cycles that cause cyclic deterioration in the column flexural strength. This can be seen clearly in Figures 5.37b and 5.37e for the slender HSS and wide flange columns tested herein, respectively. Similar observations hold true for the unloading stiffness deterioration of wide flange steel columns.

5.5.6 Interior versus end column axial shortening

Referring to Figure 5.37, the column axial shortening under constant axial load (i.e., interior steel columns) accumulates through the lateral loading history. On the other hand, the column axial shortening under varying axial load varies linearly with respect to the column chord rotation. Notably, its magnitude is at least 6 to 7 times smaller than the corresponding one of an interior column subjected to the same lateral loading history regardless of the cross-section type and respective local slenderness. This implies that at large deformations a differential gap between end and interior columns can be created.

Figure 5.38 compares the achieved axial shortening after every collapse-consistent loading phase for the HSS and wide flange columns that were examined as part of the testing program. The more slender a cross section is, the larger the differential gap between an interior and end column within the same steel MRF story. The reason is that a more slender column would develop larger axial shortening during the same inelastic deformation compared to a more compact column. From Figure 5.38, after Phase 1 loading, the difference between the axial shortening for a compact column under constant compressive and varying axial load is around 1% of the column length. As the lateral loading protocol progresses, the same difference becomes 5% of the column's initial length. In stockier cross sections, the axial shortening grows slower than that in more slender ones. Therefore the differential gap of adjacent columns is expected to be small in this case.

Figure 5.39 shows the column axial shortening versus the cumulative plastic rotation grouped per cross-section that was examined. The column axial shortening under constant axial load can be correlated with the cumulative plastic rotation that a steel column experiences. This agrees with earlier findings by MacRae et al. (1990, 2009) and more recent findings by Elkady and Lignos (2018a, 2018b). This observation holds true regardless of the applied lateral loading protocol. The reason is that in the case of constant compressive axial loading application, both the north and south flange of the column buckles (see Figures 5.32 and 5.33); the growth of both buckling waves with the number of applied inelastic cycles causes column axial shortening (see Figure 5.35). On the other hand, the axial shortening of a column under varying axial load varies linearly with respect to the column chord rotation (see Figure 5.36). Therefore, in this case the relationship between the column axial shortening and the cumulative plastic rotation is not obvious.

Figure 5.40 shows the strain distribution of H-19-C1-C, H-19-C1-V, W-6-25-C1-C and W-6-25-C1-V specimens along the latitudinal direction at the end of the first four loading excursions. The strain gauge locations were located at a distance of 0.5D above the top surface of the column base plate. Strain gauges N2M and S2M were in the center location of the north and south flange of the steel column, respectively. Strain gauges E1M to E3M are on the web of the steel column (see Figure 5.15 for various strain gauge locations). In the first four excursions, the specimens displaced 1.9% drift amplitude. For both H-19 and W-6-25 specimens the occurrence of local buckling at the cross section was delayed given their small local slenderness ratio. Referring to Figures 5.40a and 5.40c, it is obvious that the neutral axis shifts to the north and south side of the column when it is subjected to a constant compressive axial load. On the other hand, referring to Figures 5.40b and 5.40d, the position of the neutral axis within the cross-section always stays on the south side when a steel column is subjected to a varying axial load. From the same figures all the engineering strains under a constant compressive axial load stay compressive and they progressively increase. On the other hand, strain demands in columns subjected to varying axial load vary from compression to tension.

5.5.7 Strain demands

Figure 5.41 shows plots of strain versus column rotation relation. The strain locations are on the north flange at a height equal to 0.15D from the top surface of the column base plate (strain gauge notations are N1B, N2B and N3B shown in Figure 5.15). These are the recorded strain histories closer to the base plate welds. From these figures, the strain demand at the selected location increases prior to the occurrence of local buckling near the column base. After local buckling initiation, the strain demands near the welds stabilize. This is attributed to the

redistribution of stresses once local buckling is formed. Comparing the strain histories of W-6-25-C1-C and W-6-25-C1-V (see Figure 5.41c and 5.41d), the maximum strain demand of W-6-25-C1-C was recorded at the peak drift amplitude of the 5th excursion in Phase 1 loading (i.e., lateral drift of 4% rads). On the other hand, the peak strain demand of W-6-25-C1-V specimen was recorded at the peak drift amplitude of the 5th excursion in Phase 2 loading. This is attributed to the fact that the local buckling progression for W-6-25-C1-C is much more evident compared to W-6-25-C1-V specimen. Due to the varying axial load demands the strain demand near the base plate welds became large; however, the maximum strain demand in this case was still less than 1% in tension to -4% in compression, which is far less than the level of fracture strain of the base metal. The same trend is observed in H-19-C1-C and H-19-C1-V specimens (see Figure 5.41a and 5.41b).

5.5.8 Out-of-plane deformation in wide flange specimens

Figure 5.42 shows the orbit of NL4 and NR4 LED targets measured from the Krypton system (locations are defined in Figure 5.20) of the wide flange specimens subjected to near-fault collapse-consistent loading protocols. The selected LED locations are located on north flange and $H/3$ away from the surface of the base plate. These locations are away from the region that local buckling occurred. In this figure, the out-of-plane deflection of the steel column under constant compressive axial load substantially increased during the 5th loading excursion (large monotonic push) of Phase 2 (W-8-25-C1-C) and Phase 3 loading (W-6-34-C1-C and W-6-25-C1-C). These displacements agree with the occurrence of the second wave buckling that triggers plastic lateral torsional buckling. Therefore the measured data from the Krypton system supports that the formation of the second wave buckling is coupled with lateral torsional buckling. This

suggests that for small L_b/r_y ratios this issue is not related to the theory of elastic lateral torsional buckling. The out-of-plane displacement of the north flange of the same steel column under constant axial load increased while the column was moving in the positive loading direction. From the same figure, the out-of-plane deformation of the north flange remains constant when the column displaces in the negative loading direction. In the negative loading direction, local buckling near of the south flange of the column was growing. Therefore the out-of-plane deformation of the steel column accumulates with the progression of the lateral loading protocol. On the other hand, the out-of-plane deformation of the specimens under varying axial load became nearly zero when the column moved from the positive to the negative loading direction because of the local buckling wave stretching. Therefore, steel columns subjected to varying axial load are not expected to develop the same magnitude of out-of-plane deformations with interior columns experiencing constant compressive axial load.

5.6 Summary and Conclusions

An experimental study that characterized the hysteretic behaviour of steel HSS and wide flange columns at large deformations associated with collapse was conducted. The steel columns reflect the current seismic design of steel moment resisting frames (MRFs) in Japan and North America. The landmark data can serve for the validation and refinement of comprehensive deterioration models for simulating the collapse behaviour of steel columns. This is discussed in detail in Chapter 7 of this thesis. The same data set can facilitate the validation of rigorous finite element models presented in Chapter 6. A number of important findings were also highlighted through the same experimental program. In particular,

- Steel columns under constant compressive axial load, deteriorate cyclically faster than nominally identical steel columns subjected to the same lateral loading history but varying axial load demands. In the former, local buckling occurs on both flanges, while in the latter the axial load reversals stretch the local buckle region, thereby resulting into less cyclic strength deterioration when the lateral drift angle reverses under varying axial load.
- Column axial shortening is a predominant failure mode associated with column instability. Interior columns within a steel MRF bay accumulate 6 to 7 times larger axial shortening than adjacent end columns. In this case the axial shortening varies linearly with the column rotation in end columns. The axial shortening in interior columns correlates to cumulative plastic rotations. This issue becomes more pronounced for slender but seismically compact columns.
- The column buckling half wave length is within a range of $0.8D$ to $1.0D$, and is typically located $0.4D$ to $1.1D$ away from the top surface of the column base plate when the compressive axial load remains constant. On the other hand, the varying axial load demand tends to push the buckling location higher due to the member P-delta effects.
- Very compact HSS columns (D/t = 19) tend to develop an elephant foot buckling mode. On the other hand, the buckling mode of wide flange specimens typically consists of two buckling waves. The first one occurred at the bottom end of the column. The second wave buckling occurs above the first one. This buckling wave typically triggers plastic lateral torsional buckling. From the measured data obtained from the Krypton wireless measurement system, it was confirmed that the development of torsional deflection initiates when the second wave local buckling forms.

- Fracture is typically not an issue for the range of HSS cross sections that were examined. On the other hand, in some instances, steel wide flange columns under constant axial load fractured in the k-area near the column base due to excessive local buckling distortion. Columns under varying axial load demands could be prone to fracture initiation in the flange welds and the web access hole if the current AISC recommendations are not respected.
- The strain demands near the column base weld toes ($0.15D$ away from the column base top surface) increase up to the formation of local buckling. After this point, due to the force redistribution occurring within the member the strain demands either decrease or stabilize and fracture is not an issue for steel beam-columns. This agrees with prior studies (Elkady and Lignos 2018b).
- From the recorded strain distribution along the latitudinal direction of a column, a neutral axis shifting is observed. In particular, the neutral axis shifted both on north and south flange sides under constant axial load demands. On the other hand, the neutral axis of a cross section under varying axial load stayed only near the south flange of the steel column. This is the primary reason for the fundamental differences between the moment- and axial shortening-rotation relations of interior and end columns within the same steel MRF story.

Table 5.1 Test matrix of HSS columns

No.	Section	Steel	Depth-to-thickness ratio D/t	Span-to-depth ratio L/D	Loading protocol	
					Lateral	Axial
H-27-M-C	HSS 254×9.5	ASTM A500 grade B (f_y=315MPa)	26.7	6.0	Mono.	Constant
H-27-S-C					Sym.	Constant
H-27-C1-C					Collapse (near-fault)	Constant
H-27-C1-V						Varying
H-27- C2-C					Collapse (long-duration)	Constant
H-27-C2-V						Varying
H-19-S-C	HSS 305×16		19.1	6.0	Sym.	Constant
H-19-C1-C					Collapse (near-fault)	Constant
H-19-C1-V						Varying

Table 5.2 Test matrix of wide flange columns

No.	Section	Steel	Width-to-thickness ratio		Span-to-depth ratio L/D	Loading protocol	
			flange h/t_w	web $b/2t_f$		Lateral	Axial
W-6-34-M-C	W14×53	ASTM A992 (f_y=345 MPa)	34.1	6.1	5.2	Mono.	Constant
W-6-34-S-C						Sym.	Constant
W-6-34-C1-C						Collapse (near-fault)	Constant
W-6-34-C1-V							Varying
W-6-34-C2-C						Collapse (long-duration)	Constant
W-6-34-C2-V							Varying
W-8-34-S-C	W14×61		33.7	7.7	5.2	Sym.	Constant
W-8-34-C1-C						Collapse (near-fault)	Constant
W-8-34-C1-V							Constant
W-6-25-S-C	W14×82		24.6	5.9	5.0	Sym.	Constant
W-6-25-C1-C						Collapse (near-fault)	Constant
W-6-25-C1-V							Varying

Table 5.3 Measured dimensions of HSS columns (unit: mm)

Specimen		Column length		Outside dimension			
		L_S	L_N	D_N	D_S	B_W	B_E
HSS 254×9.5	H-27-M-C	1562	1558	254.5	254	254	254
	H-27-S-C	1557	-	254	-	-	-
	H-27-C1-C	1558	-	254	-	-	-
	H-27-C1-V	1556	-	254	-	-	-
	H-27- C2-C	1559	1561	256	256	254	254
	H-27-C2-V	1559	1557	255	255	254	254
	Nominal size	1558		254			
HSS 305×16	H-19-S-C	1863	1864	305	305	305	305
	H-19-C1-C	1865	1864	306	306	306	306
	H-19-C1-V	1864	1864	306	305	306	306
	Nominal size	1864		305			

Table 5.4 Measured dimensions of wide flange columns (unit: mm)

Specimen		Column length		Outside dimension			
		L_S	L_N	D_N	D_S	D_W	D_E
W14×53	W-6-34-M-C	1862	-	353	353.5	205	203
	W-6-34-S-C	1865	-	353	353	204	203
	W-6-34-C1-C	1865	-	353	353.5	205	204
	W-6-34-C1-V	1860	-	354	353	204	205
	W-6-34-C2-C	-	-	353	352	204	204
	W-6-34-C2-V	1862	-	353	353	203.5	205
	Nominal size	1864		354		205	
W14×61	W-8-34-S-C	1862	1864	355	355	252	253
	W-8-34-C1-C	1862	1861	355	355	252	252
	W-8-34-C1-V	1865	1861	355	355	252	253
	Nominal size	1864		353		254	
W14×82	W-6-25-S-C	1860	1863	361	362	257	255
	W-6-25-C1-C	1860	1859	360	362	257	255
	W-6-25-C1-V	1862	1860	362	362	257	255
	Nominal size	1864		363		257	

Specimen		Flange thickness				Web thickness	
		$t_{f,NW}$	$t_{f,NE}$	$t_{f,SW}$	$t_{f,SE}$	$t_{w,W}$	$t_{w,E}$
W14×53	W-6-34-M-C	15.96	16.49	16.51	16.05	10.04	9.97
	W-6-34-S-C	15.79	16.37	16.62	16.19	9.95	10.32
	W-6-34-C1-C	16.47	16.42	16.60	16.29	9.86	10.15
	W-6-34-C1-V	16.31	16.21	16.80	16.01	9.89	9.91
	W-6-34-C2-C	16.20	16.64	15.96	16.12	9.72	9.62
	W-6-34-C2-V	16.94	16.47	16.12	15.90	9.98	9.69
	Nominal size	16.8				9.4	
W14×61	W-8-34-S-C	15.15	16.56	15.10	15.50	9.54	9.22
	W-8-34-C1-C	14.91	16.64	15.01	15.34	9.68	9.19
	W-8-34-C1-V	16.00	15.24	15.66	16.09	9.79	9.60
	Nominal size	16.4				9.5	
W14×82	W-6-25-S-C	21.69	21.47	21.68	20.74	13.03	13.43
	W-6-25-C1-C	21.89	21.11	21.68	21.02	13.56	14.62
	W-6-25-C1-V	21.18	21.55	21.68	21.88	13.48	13.55
	Nominal size	21.7				13.0	

Table 5.5 Strain gauge length and gauge factors

Specimen	Location	Gauge length [mm]	Gauge factor
H-27-M-C	all	10	2.09
H-27-S-C	N1-B	10	2.09
	Other than above	5	2.11
H-27-C1-C	N1-B, N3-B	5	2.11
	Other than above	5	2.13
H-27-C1-V	all	10	2.11
H-27-C2-C	all	10	2.11
H-27-C2-V	all	10	2.11
H-19-S-M	all	5	2.13
H-19-C1-C	all	5	2.13
H-19-C1-V	all	5	2.13
W-6-34-M-C	all	10	2.11
W-6-34-S-C	all	10	2.11
W-6-34-C1-C	all	10	2.11
W-6-34-C1-V	all	10	2.11
W-6-34-C2-C	all	10	2.11
W-6-34-C2-V	all	10	2.11
W-8-34-S-C	all	5	2.13
W-8-34-C1-V	all	5	2.13
W-8-34-C1-V	all	5	2.13
W-6-25-S-C	all	5	2.13
W-6-25-C1-C	all	5	2.13
W-6-25-C1-V	all	5	2.13

Table 5.6 Dimensions of the test setup for deflection calculations

Specimen	H [mm]	H_{act} [mm]	L_{act} [mm]	L_h [mm]	L_v [mm]	W_h [kN]	W_v [kN]
HSS254×9.5	1525	1720	2900	1372	1372	30	25.44
HSS305×16	1825	1720	2875	1372	1625	30	25.44
W14×53	1825	1720	2900	1372	1670	30	25.44
W14×61 W14×82	1825	1720	2875	1372	1625	30	25.44

Specimen	L_b [mm]	L_{t1} [mm]	L_{t2} [mm]	L_{t3} [mm]	L_{t4} [mm]	L_{t5} [mm]
HSS254×9.5	254	105	395	307	592	785
HSS305×16	305	150	395	307	592	836
W14×53	355	105	395	307	592	785
W14×61 W14×82	350	150	395	307	592	836

Table 5.7 Channel list of instrumentations

Channel	Location	Load/ Displacement/ Rotation/ Strain	Unit	Direction	Designation	Instrumentation
1	Actuator	Load	kN	Vertical	P	Load cell
2		Displacement	mm		u_{stroke}	Piston stroke
3		Load	kN	Horizontal	Q	Load cell
4		Displacement	mm		v_{stroke}	Actuator stroke
5	Top plate	Displacement	mm	Horizontal	u_{TN}	String potentiometer
6					u_{TS}	
7				Vertical	v_{TN}	
8					v_{TS}	
9		Rotation	rad	In-plane	$\theta_{TW,in}$	Inclinometer
10					$\theta_{TE,in}$	
11				Out-of-plane	$\theta_{TW,out}$	
12					$\theta_{TE,out}$	
13	Base plate	Displacement	mm	Horizontal	u_{B1}	LVDT
14					u_{B2}	
15				Vertical	v_{BN1}	
16					v_{BN2}	
17					v_{BS1}	
18					v_{BS2}	
19		Rotation	rad	In-plane	$\theta_{BW,in}$	Inclinometer
20					$\theta_{BE,in}$	
21				Out-of-plane	$\theta_{BW,out}$	
22					$\theta_{BE,out}$	
23	Top pin	Displacement	mm	Horizontal	u_{pin}	String potentiometer

Table 5.8 Channel list of strain gauges

Channel	Location	Load/ Displacement/ Rotation/ Strain	Unit	Direction	Designation	Instrumentation
24	Specimen	Stain	με	Longitudinal	N1-B	Strain gauge
25					N2-B	
26					N3-B	
27					S1-B	
28					S2-B	
29					S3-B	
30					E1-B	
31					E2-B	
32					E3-B	
33					N1-M	
34					N2-M	
35					N3-M	
36					S1-M	
37					S2-M	
38					S3-M	
39					E1-M	
40					E2-M	
41					E3-M	
42					N1-T	
43					N2-T	
44					N3-T	
45					S1-T	
46					S2-T	
47					S3-T	
48					E1-T	
49					E2-T	
50					E3-T	

Table 5.9 Channel list of LED target

Channel	Location	Load/ Displacement/ Rotation/ Strain	Unit	Direction	Designation	Instrumentation
51	Specimen	Displacement	mm	3D	NR1	LED target
52					NR 2	
53					NR 3	
54					NR 4	
55					NR 5	
56	Base plate				BR	
57					BR2	
58					BR3	
59					BR4	
60	Lateral brace				LR	
61	Pin assembly				TRT	
62					TRB	
67	Specimen				NL1	
68					NL2	
69					NL3	
70					NL4	
71					NL5	
72	Base plate				BL	
73					BL2	
74					BL3	
75					BL4	
76	Lateral brace				LL	
77	Pin assembly				TLT	
78					TLB	

Table 5.10 Chemical composition (mass%)

Specimen	Steel	*C*	*Si*	*Mn*	*P*	*S*	*CE**
HSS254×9.5	ASTM	0.20	0.026	0.79	0.007	0.010	0.34
HSS305×16	A500	0.19	0.010	0.76	0.008	0.008	0.33
Specification	grade B	0.26	1.35	-	0.035	0.035	-
W14×53		0.11	0.17	0.47	0.033	0.023	
W14×61	ASTM	0.08	0.29	1.11	0.012	0.023	0.33
W14×82	A992	0.07	0.31	1.10	0.012	0.023	0.30
Specification		0.23	0.10-0.40	0.50-1.60	0.055	0.045	0.45

$* CE = C + \frac{Mn+Si}{6} + \frac{Cr+Mo+V}{5} + \frac{Cu+Ni}{15}$

Table 5.11 Mechanical properties of the HSS specimens

Specimen	Location	Notation	Specimen dimension		Result			
			Thickness [mm]	Width [mm]	YS [MPa]	TS [MPa]	YR (YS/TS)	EL
HSS 254×9.5 (H-27 series)	Flat	H-27-F-1	9.20	40.22	417.5	493.0	0.85	0.20
		H-27-F-2	9.31	40.38	435.6	497.2	0.88	0.17
		H-27-F-3	9.17	40.38	401.7	480.5	0.84	0.20
		Average	9.23	40.33	418.3	490.2	0.85	0.19
		Mill certificate	-	-	405.5	476.7	0.85	0.36
		Spec.	9.53	40.0	315<	400<	-	0.23<
	Corner	H-27-C-1	9.62	12.59	545	594	0.92	0.15
		H-27-C-2	9.67	12.48	544	590	0.92	0.16
		H-27-C-3	9.71	12.61	548	596	0.92	0.15
		Average	9.67	12.56	545	593	0.92	0.15
		Spec.	9.53	12.5	-	-	-	-
HSS 305×16 (H-19 series)	Flat	H-19-F-1	14.56	40.08	333.5	424.0	0.79	0.28
		H-19-F-2	14.74	40.09	339.8	428.4	0.79	0.26
		H-19-F-3	14.53	40.07	321.9	424.4	0.76	0.29
		Average	14.61	40.08	331.7	425.6	0.78	0.28
		Mill certificate	-	-	373.4	463.4	0.81	0.42
		Spec.	15.88	40.0	315<	400<	-	0.23<
	Corner	H-19-C-1	15.11	12.55	434	490	0.89	0.23
		H-19-C-2	15.06	12.54	460	492	0.93	0.20
		H-19-C-3	15.04	12.55	455	490	0.93	0.22
		Average	15.07	12.55	460	491	0.92	0.22
		Spec.	15.88	12.5	-	-	-	-

Table 5.12 Mechanical properties of the wide flange specimens

Specimen	Location	Notation	Specimen dimension		Result			
			Thickness [mm]	Width [mm]	YS [MPa]	TS [MPa]	YR (YS/TS)	EL
W14×53 (W-8-34 series)	Flange	W-8-34-F-1	15.54	40.04	377.7	519.7	0.73	0.25
		W-8-34-F-2	15.46	40.05	380.0	521.2	0.73	0.25
		W-8-34-F-3	15.70	40.04	371.7	512.9	0.72	0.23
		Average	15.57	40.04	376.4	517.9	0.73	0.24
		Mill certificate	-	-	381.9	520.5	0.74	0.24
		Spec.	16.4	40.0	345<	450<	<0.85	0.18<
	Web	W-8-34-W-1	9.35	40.07	399.6	505.5	0.79	0.22
		W-8-34-W-2	9.29	40.01	404.9	507.3	0.80	0.23
		W-8-34-W-3	9.26	40.08	402.6	510.2	0.79	0.23
		Average	9.30	40.05	402.4	507.7	0.79	0.23
		Spec.	9.5	40.0	345<	450<	<0.85	0.18<
W14×61 (W-6-34 series)	Flange	W-6-34-F-1	16.12	40.16	383.6	510.4	0.75	0.26
		W-6-34-F-2	15.97	39.82	373.8	503.6	0.74	0.23
		W-6-34-F-3	16.41	40.13	380.2	496.0	0.77	0.27
		Average	16.17	40.04	379.2	503.3	0.75	0.25
		Mill certificate	-	-	386.0	520.5	0.74	0.26
		Spec.	16.8	40.0	345<	450<	<0.85	0.18<
	Web	W-6-34-W-1	10.16	40.36	385.0	490.3	0.79	0.25
		W-6-34-W-2	9.80	40.32	401.6	507.8	0.79	0.26
		W-6-34-W-3	9.79	40.12	397.9	507.4	0.78	0.26
		Average	9.92	40.27	394.8	501.8	0.79	0.26
		Spec.	9.4	40.0	345<	450<	<0.85	0.18<
W14×82 (W-8-25 series)	Flange	W-6-25-F-1	21.31	40.10	365.9	490.8	0.75	0.29
		W-6-25-F-2	21.08	40.12	368.3	490.5	0.75	0.30
		W-6-25-F-3	20.96	40.08	368.1	491.5	0.75	0.28
		Average	21.12	40.10	367.4	490.9	0.75	0.29
		Mill certificate	-	-	379.0	510.0	0.74	0.27
		Spec.	21.7	40.0	345<	450<	<0.85	0.18<
	Web	W-6-25-W-1	13.47	40.07	384.9	502.8	0.77	0.25
		W-6-25-W-2	13.45	40.07	378.6	498.0	0.76	0.26
		W-6-25-W-3	13.43	40.02	372.8	495.9	0.75	0.25
		Average	13.45	40.05	378.8	498.9	0.76	0.25
		Spec.	13.0	40.0	345<	450<	<0.85	0.18<

Table 5.13 Observed failure modes of HSS specimens

Section	Specimen	Local buckling mode		Fracture location	Coupling of lateral-torsional buckling	Squashing
		Halfwave length**	Location			
HSS 254×9.5	H-27-M-C	1.0D (in)	0.6D	-	-	-
	H-27-S-C	0.8D (out)	0.7D	-	-	squashed
	H-27-C1-C	0.8D (in)	0.4D	corner (due to squashing)	-	squashed
	H-27-C1-V	0.8D (out)	0.7D	-	-	-
	H-27-C2-C	0.8D (out)	0.7D	-	-	squashed
	H-27-C2-V	0.8D (out)	0.7D	-	-	-
HSS 305×16	H-19-S-M	0.6D*	0.5D*	-	-	(local buckling fully closed)
	H-19-C1-C	0.6D*	0.5D*	-	-	-
	H-19-C1-V	0.8D (in)	1.1D	corner (ductile tearing but not critical)	-	-

* Elephant foot local buckling mode

** in/out in bracket means the flange buckled inward or outside

Table 5.14 Observed failure modes of wide flange specimens

Section	Specimen	Local buckling mode (first/second wave)		Fracture location	Coupling of lateral-torsional buckling	Squashing
		Halfwave length	Location			
W14×53	W-6-34-M-C	1.0*D*/1.0*D*	0.6*D* /1.2*D*	-	coupled	-
	W-6-34-S-C	0.8*D* /0.8*D*	0.4*D* /0.9*D*	-	coupled	squashed
	W-6-34-C1-C	0.8*D*/1.0*D*	0.4*D* /1.0*D*	-	coupled	-
	W-6-34-C1-V	0.8*D*/0.8*D*	0.4*D* /1.0*D*	-	coupled	-
	W-6-34-V2-C	0.7*D* /1.0*D*	0.4*D* /1.0*D*	k-area (ductile tearing)	coupled	squashed
	W-6-34-C2-V	0.6*D*	0.5*D*	flange weld toe and web access hole (ductile tearing)	coupled	-
W14×61	W-8-34-S-C	0.6*D* /0.9*D*	0.4*D* /0.9*D*	k-area (brittle fracture)	coupled	-
	W-8-34-C1-C	0.8*D* /1.0*D*	0.5*D* /1.0*D*	k-area (brittle fracture)	coupled	-
	W-8-34-C1-V	0.8*D*	0.5*D*	web access hole (ductile tearing)	coupled	
W14×82	W-6-25-S-C	0.9*D*	0.7*D*	k-area (ductile tearing)	coupled	-
	W-6-25-C1-C	0.9*D* /0.9*D*	0.5*D* /1.1*D*	-	coupled	-
	W-6-25-C1-V	0.8*D* /0.8*D*	0.5*D* /0.9*D*	web access hole (ductile tearing)	coupled	

Table 5.15 Achieved rotation and protocol phase

Section	Specimen	Achieved load phase and step	Achieved rotation [rad]	Critical failure mode that test ended
HSS 254×9.5	H-27-M-C	-	15.5%	Achieved zero moment.
	H-27-S-C	-	4.4%	Achieved zero moment.
	H-27-C1-C	Phase 2, 11/20step	8.5%	Achieved zero moment.
	H-27-C1-V	Phase 2, 11/20step	8.6%	Moment degraded to 30% of capping moment.
	H-27-C2-C	Phase 2, 2/48step	5.8%	Achieved zero moment.
	H-27-C2-V	Phase 2, 31/48step	9.6%	Moment degraded to 19% of capping moment.
HSS 305×16	H-19-S-C	-	5.8%	Local buckling fully closed.
	H-19-C1-C	Phase 4, 12/12step	14.9%	Achieved zero moment. (0.25*Py* axial load in phase 4)
	H-19-C1-V	Phase 4, 5/12step	12.7%	Achieved zero moment.
W14×53	W-6-34-M-C	-	20.1%	Achieved zero moment.
	W-6-34-S-C	-	5.9%	Achieved zero moment.
	W-6-34-C1-C	Phase 4, 5/12step	12.9%	Achieved zero moment.
	W-6-34-C1-V	Phase 4, 5/12step	12.1%	Moment degraded to 29% of capping moment.
	W-6-34-V2-C	Phase 2, 32/32step	6.4%	Fractured and achieved zero moment.
	W-6-34-C2-V	Phase 3, 32/32step	10%	Fractured.
W14×61	W-8-34-S-C	-	4.4%	Fractured.
	W-8-34-C1-C	Phase 3, 5/12step	11.9%	Fractured.
	W-8-34-C1-V	Phase 4, 7/12step	13.8%	Fractured.
W14×82	W-6-25-S-C	-	5.8%	Fractured.
	W-6-25-C1-C	Phase 4, 12/12step	14.6%	Moment degraded to 40% capping moment then reached actuator limit.
	W-6-25-C1-V	Phase 4, 12/12step	13.3%	Moment degraded to 50% capping moment then reached actuator limit.

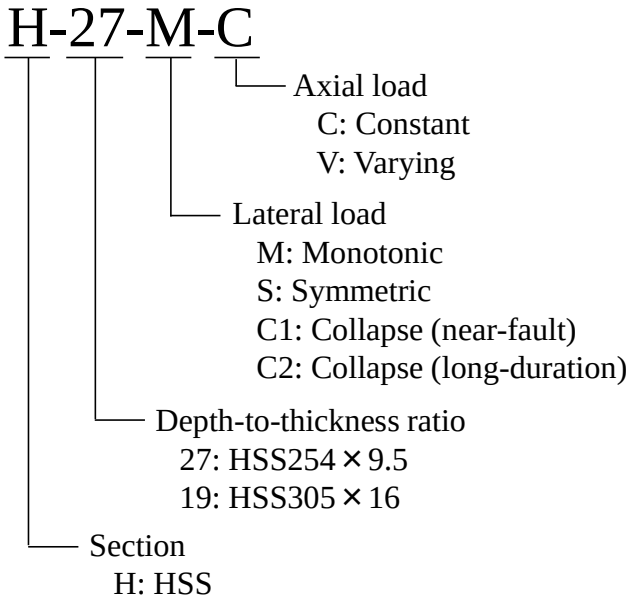

(a) HSS columns

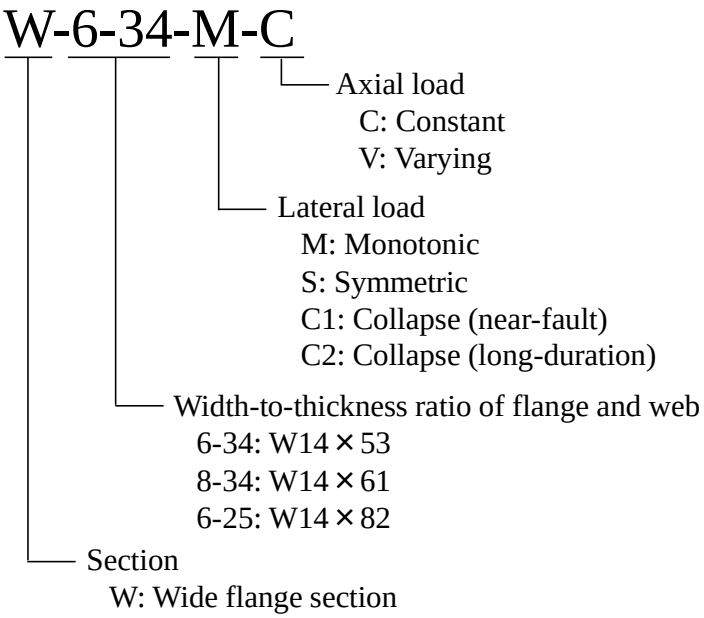

(b) wide flange columns

Figure 5.1 Specimen designation

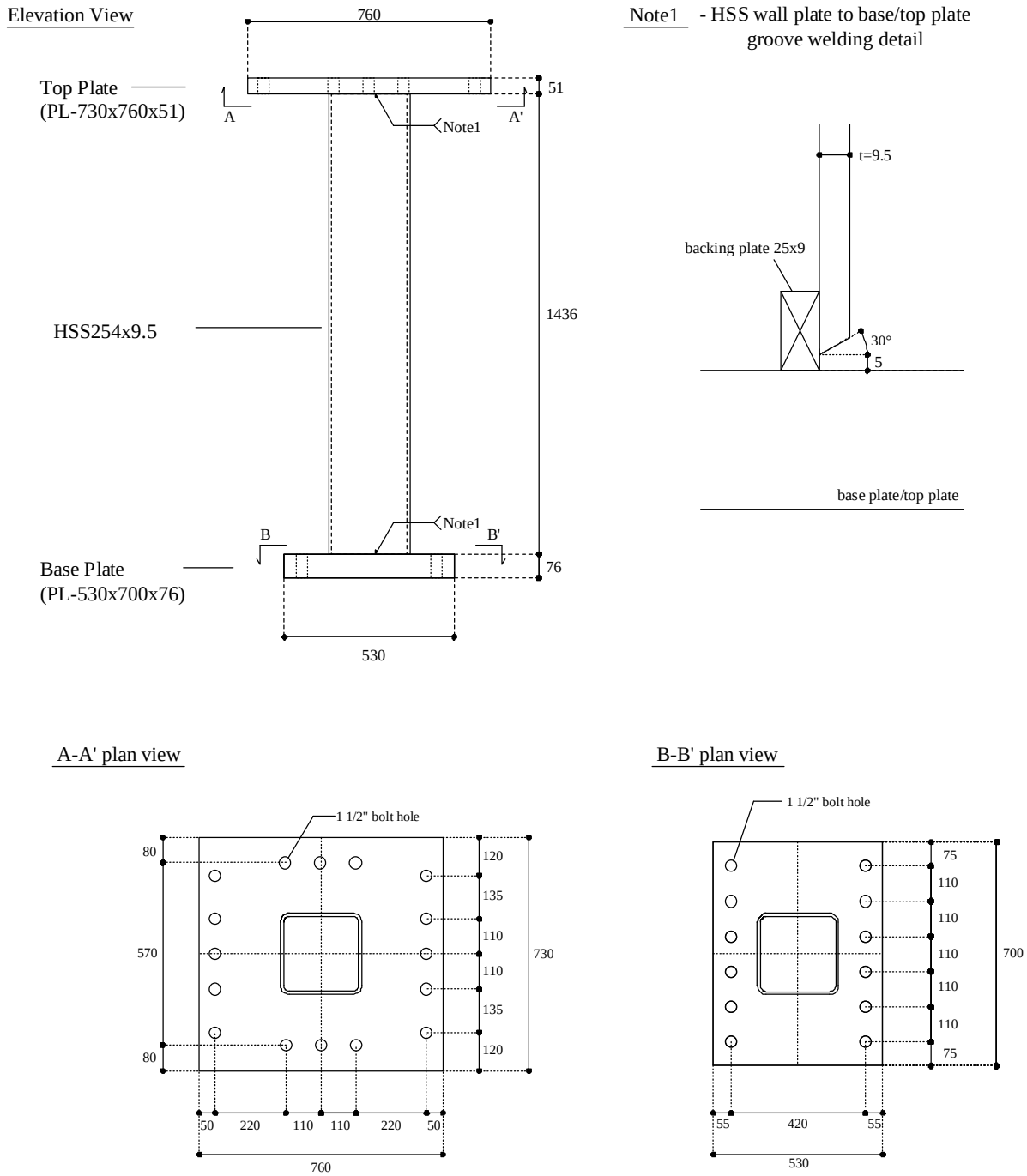

(a) HSS254×9.4

Figure 5.2 Specimen drawings of HSS columns

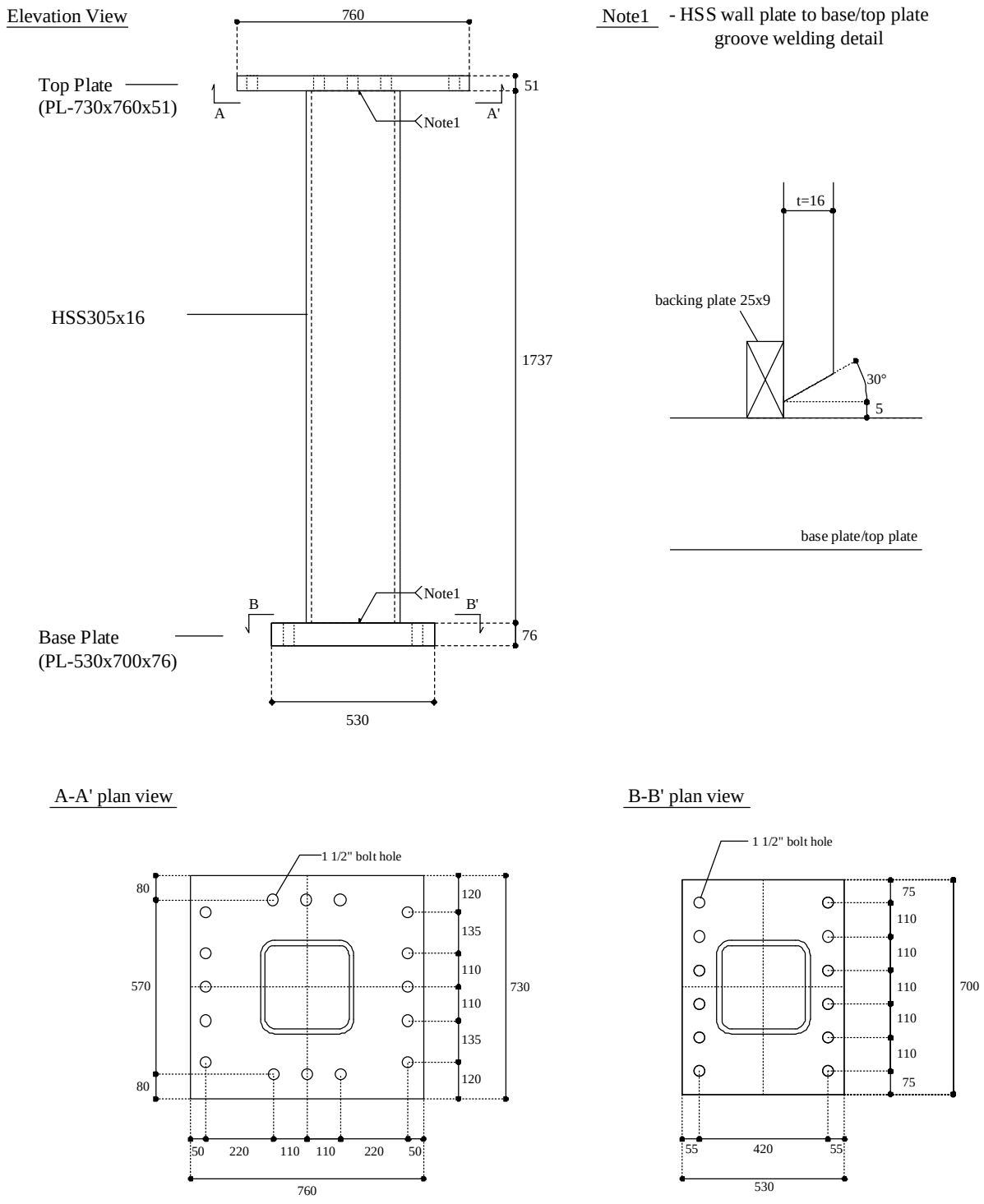

(b) HSS305×16

Figure 5.2 Specimen drawings of HSS columns (continued)

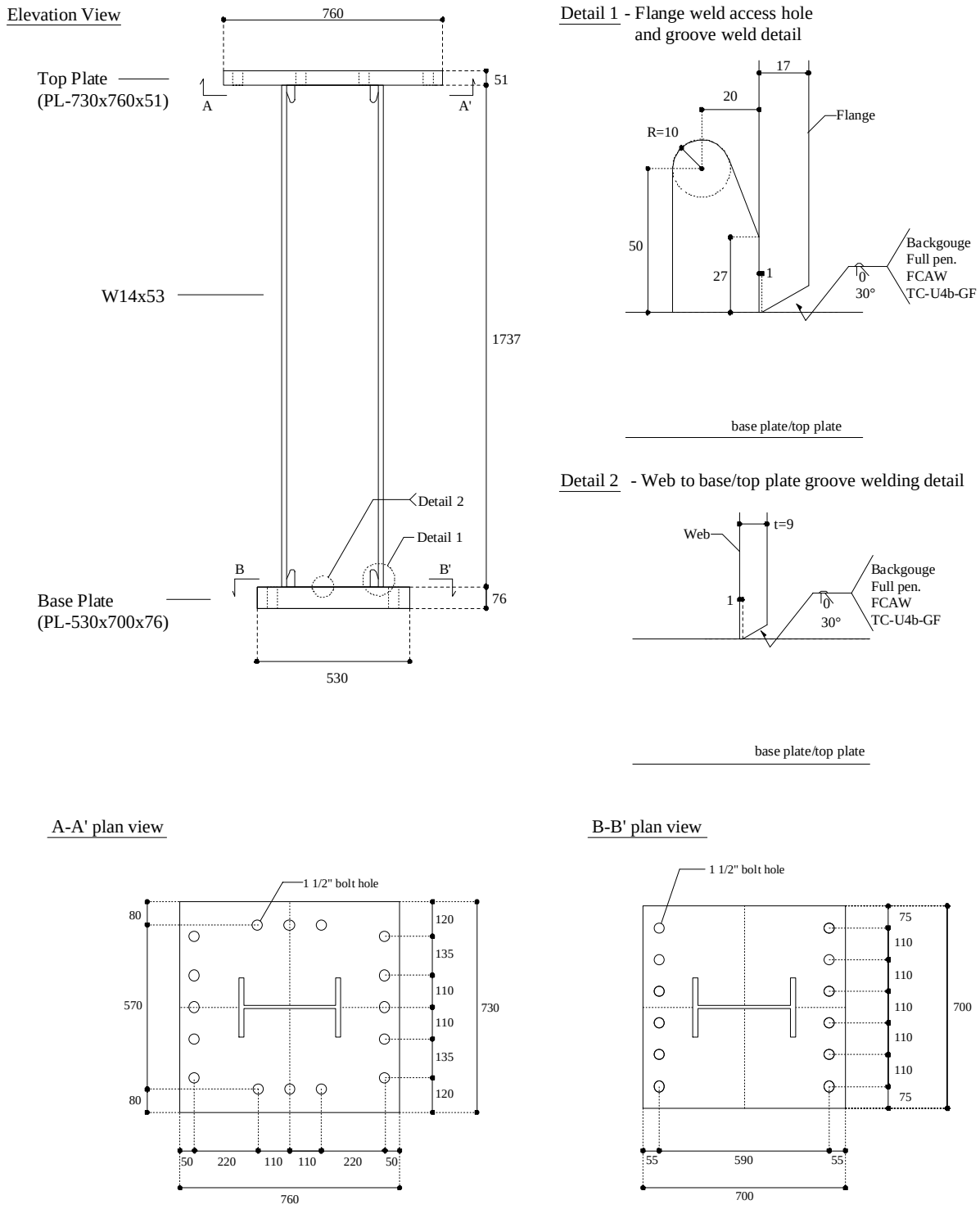

(a) W14×53

Figure 5.3 Specimen drawings of wide flange columns

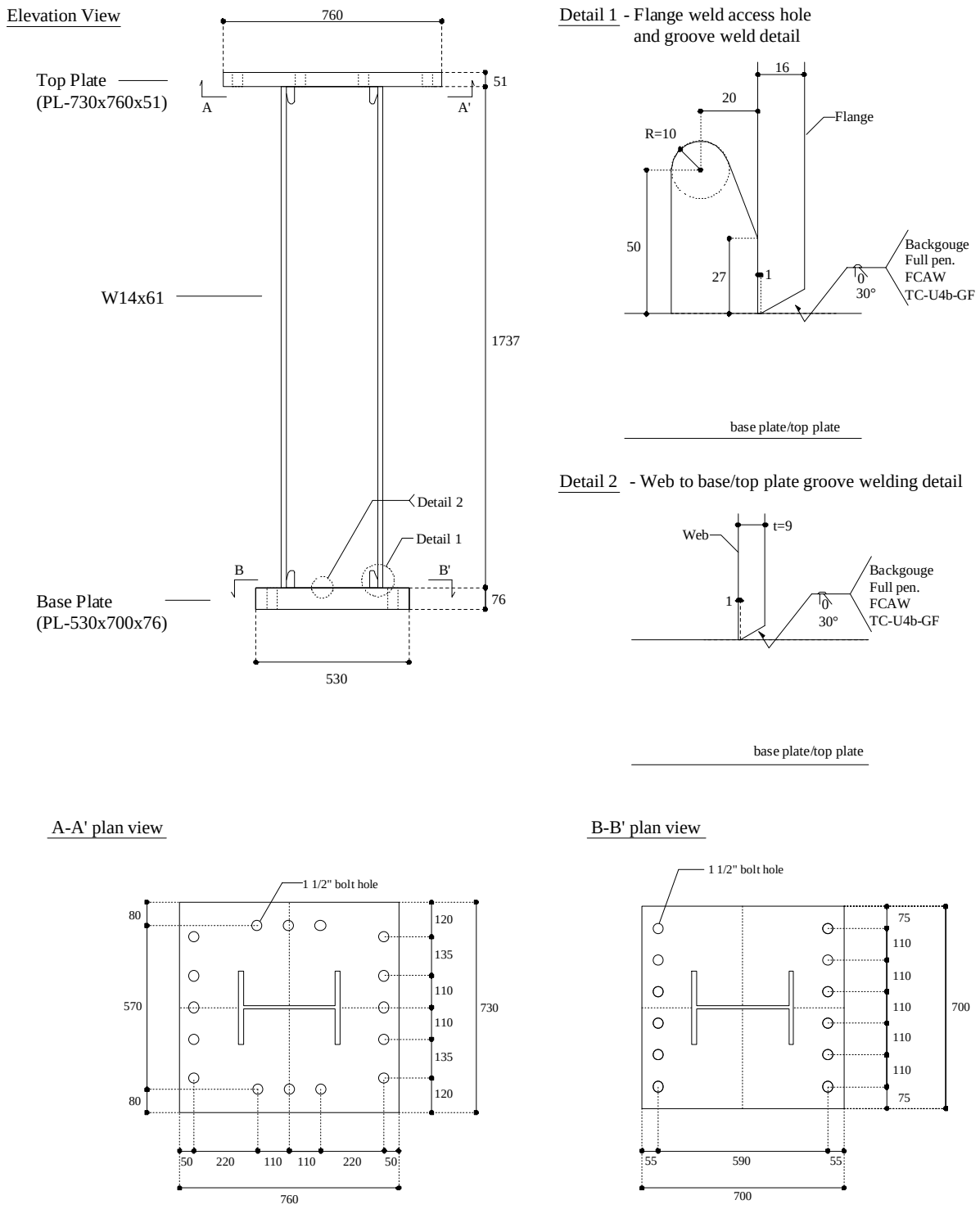

(b) W14×61

Figure 5.3 Specimen drawings of wide flange columns (continued)

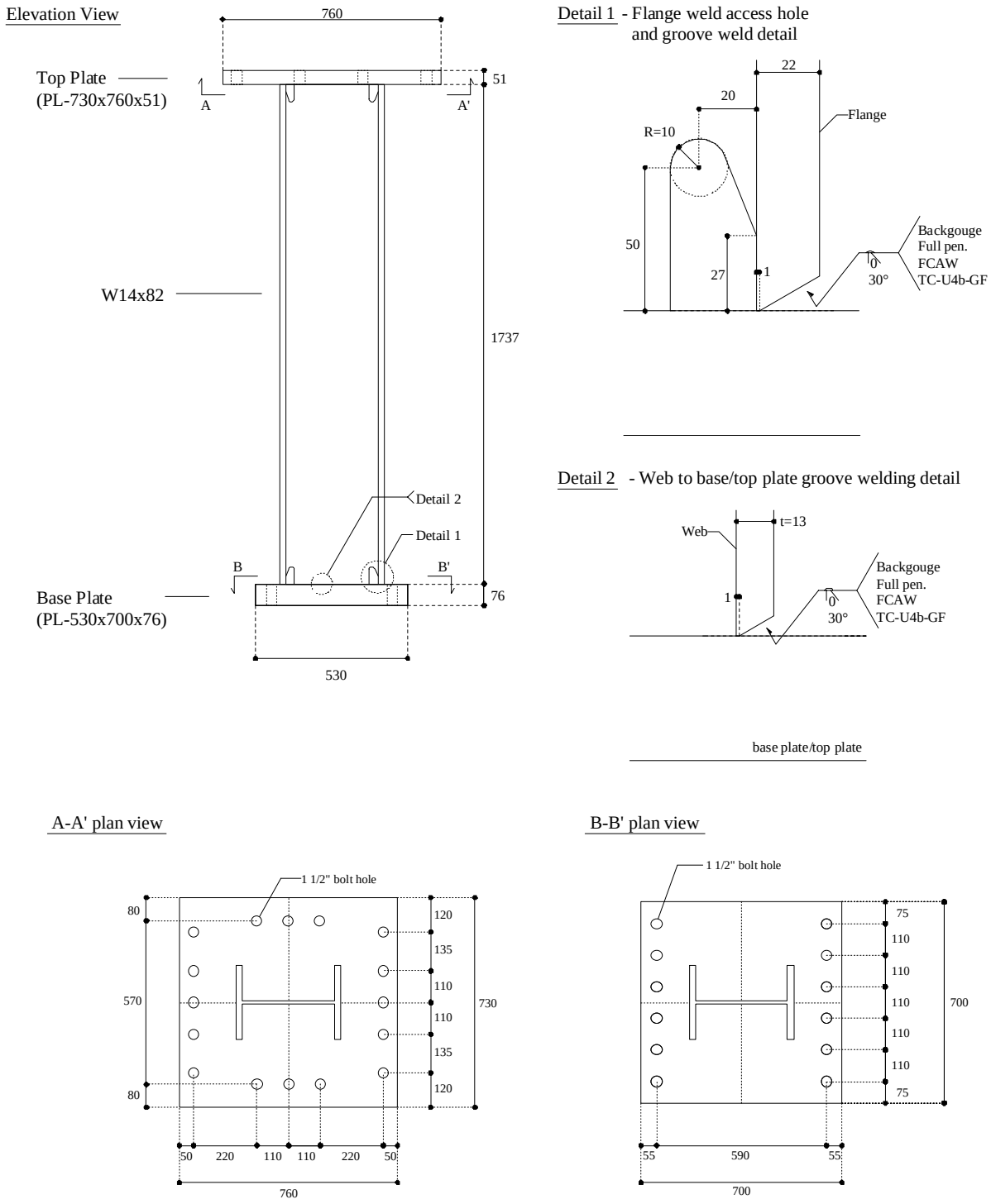

(c) W14×82

Figure 5.3 Specimen drawings of wide flange columns (continued)

(a) HSS-to-base plate welding (H-27-C1-V)

(b) Flange-to-base plate welding (W-8-34-S-C)

(c) Web-to-base plate welding and weld access holes (W-8-34-S-C)

Figure 5.4 Examples of welds and web access holes

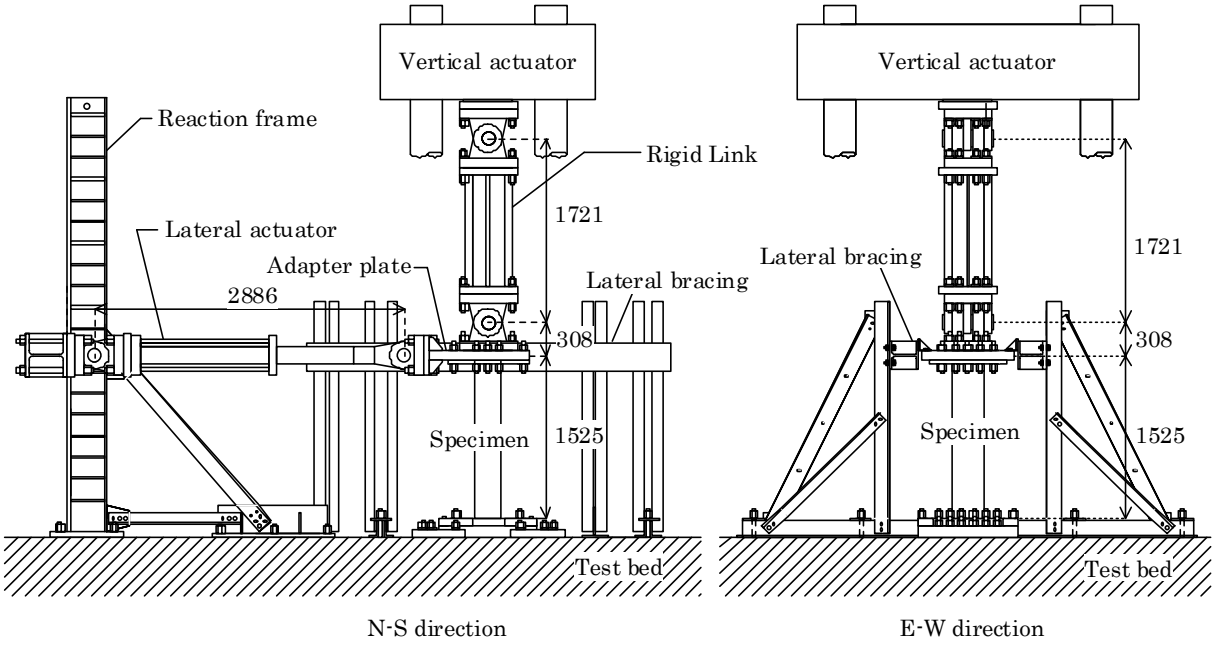

(a) H-27 series specimens

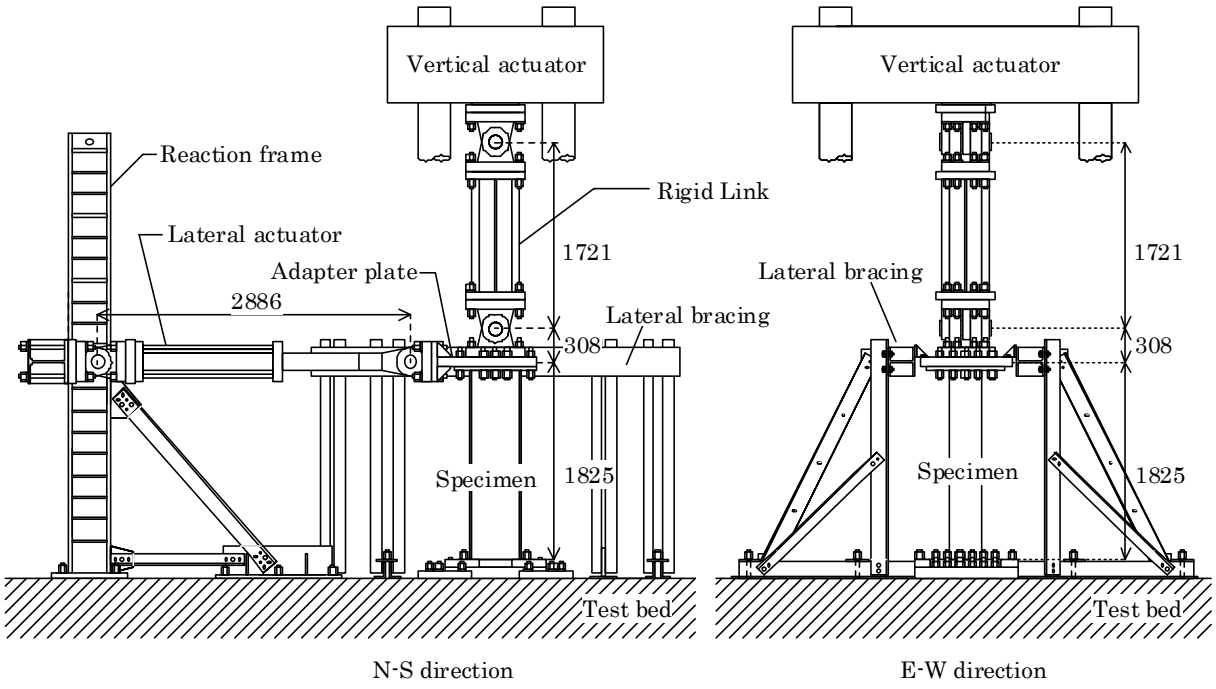

(b) other than H-27 series specimens

Figure 5.5 Elevation view of test setup

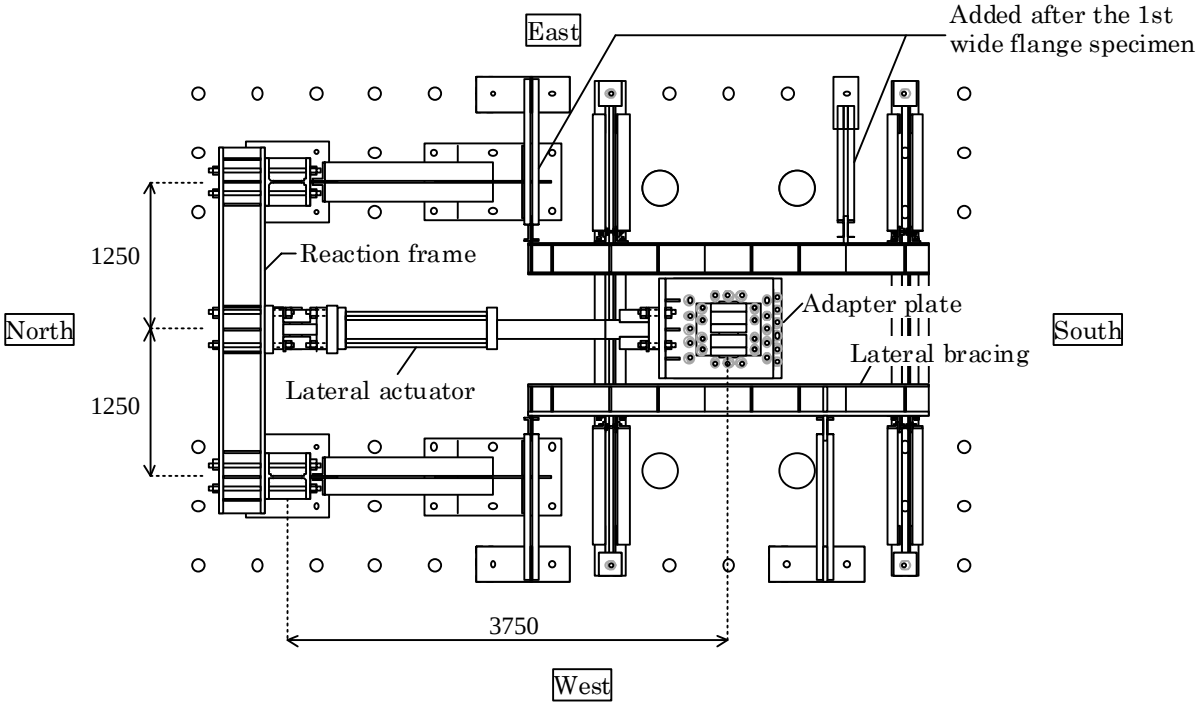

Figure 5.6 Plan view of test setup

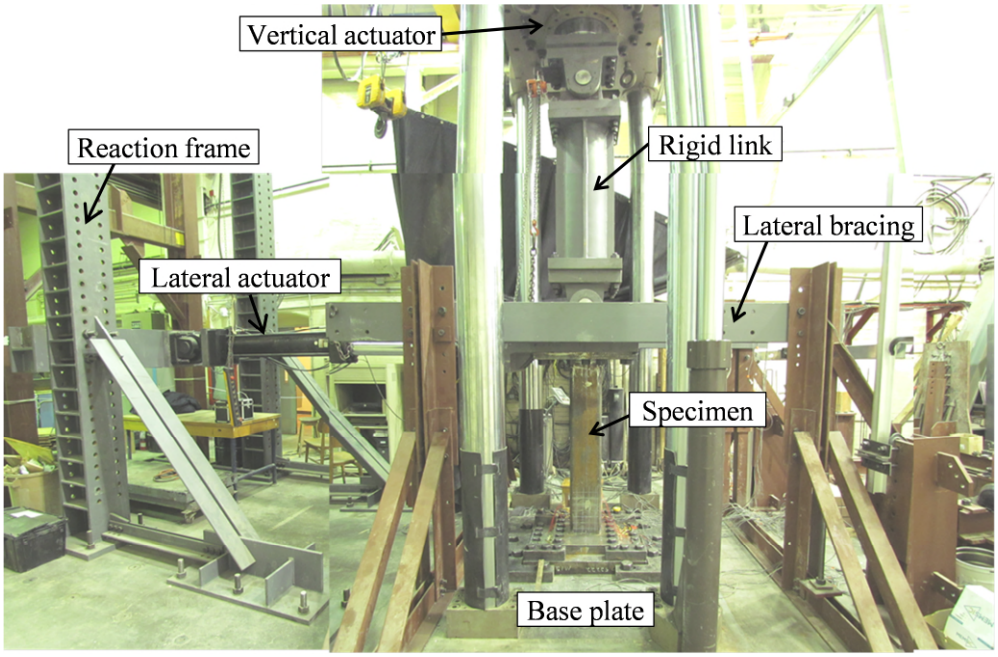

Figure 5.7 Elevation view of test setup

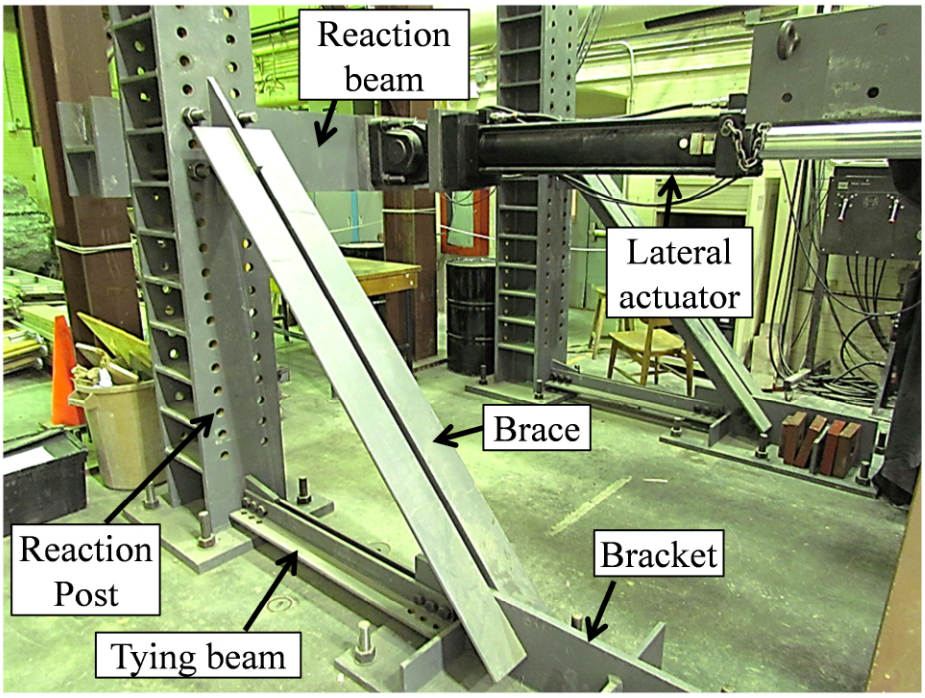

Figure 5.8 Detailed view of reaction frame

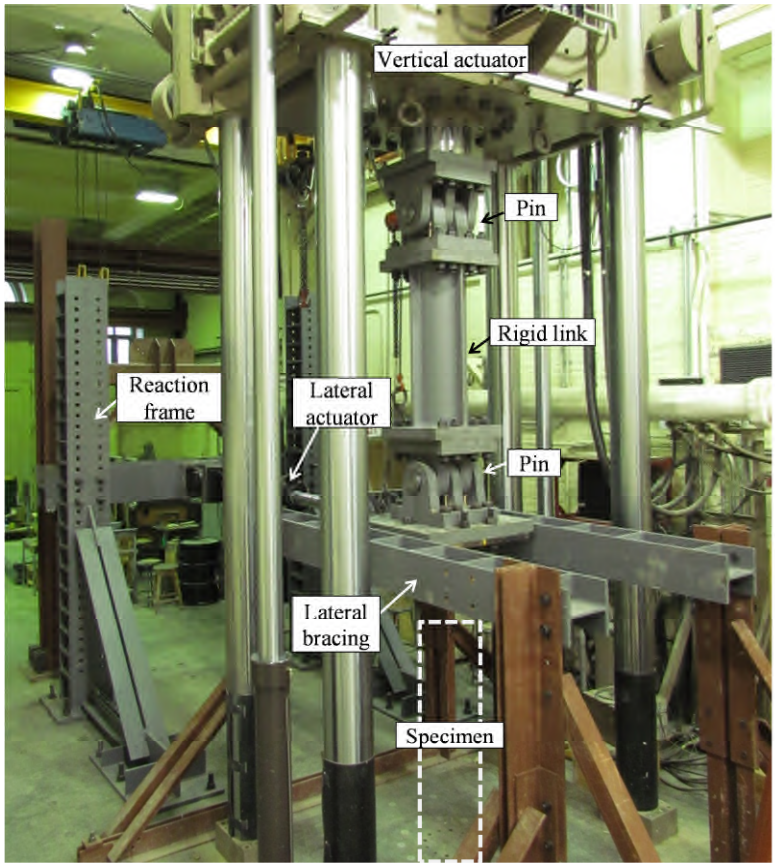

Figure 5.9 Detailed view of vertical loading system

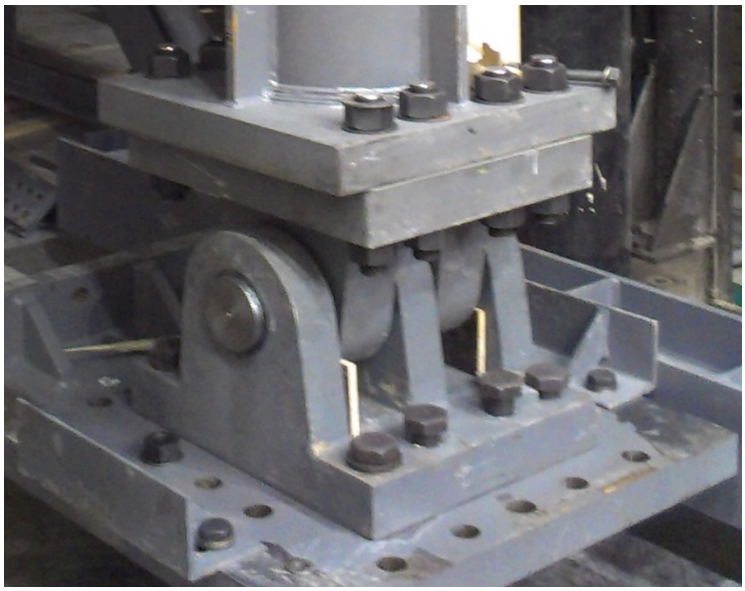
Figure 5.10 Detailed view of structural pin

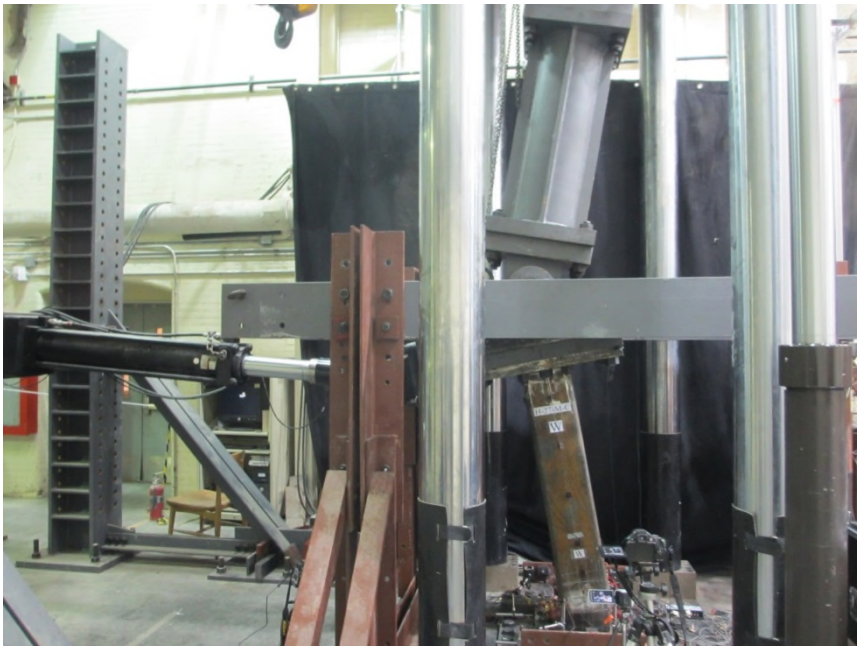

Figure 5.11 Deformed configuration of test setup

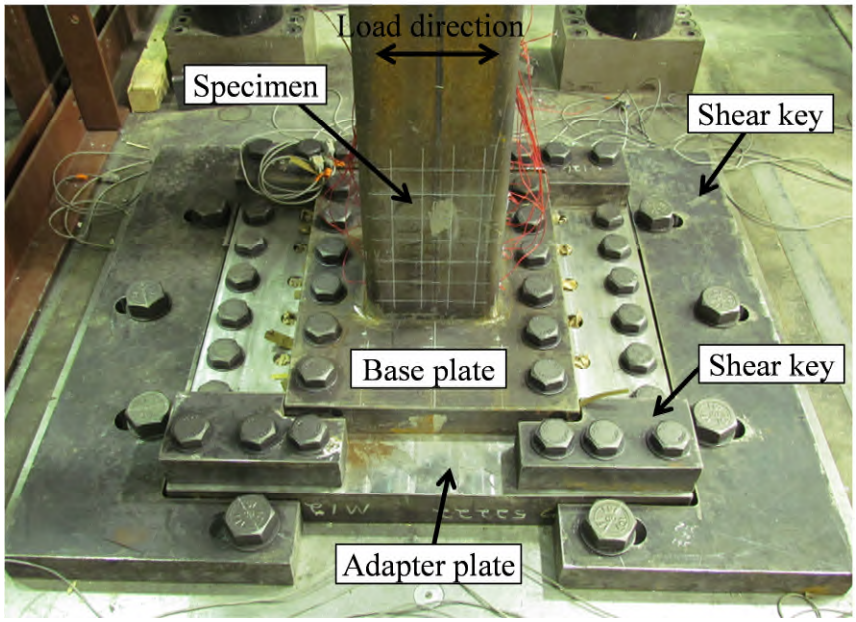

Figure 5.12 Detailed view of base plate

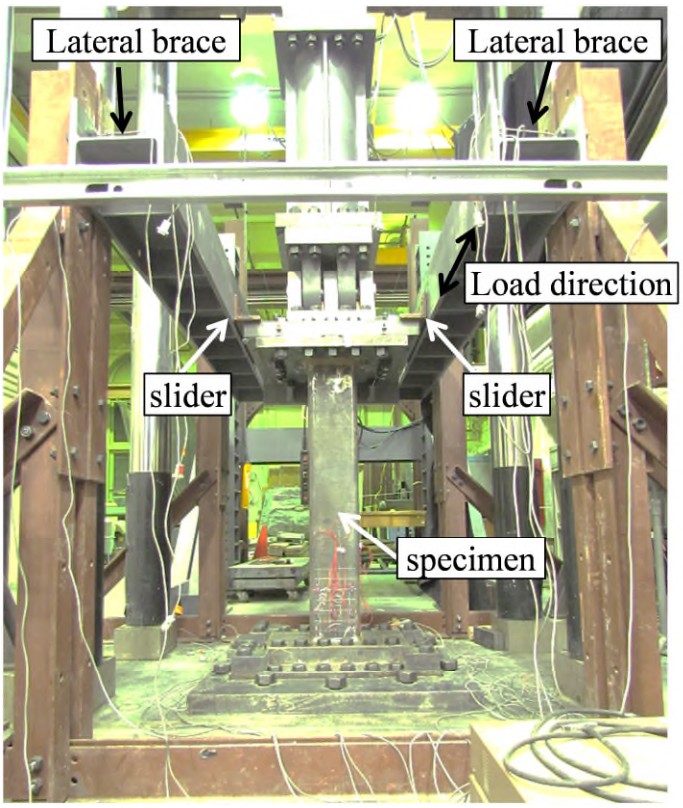

Figure 5.13 Detailed view of lateral bracing system

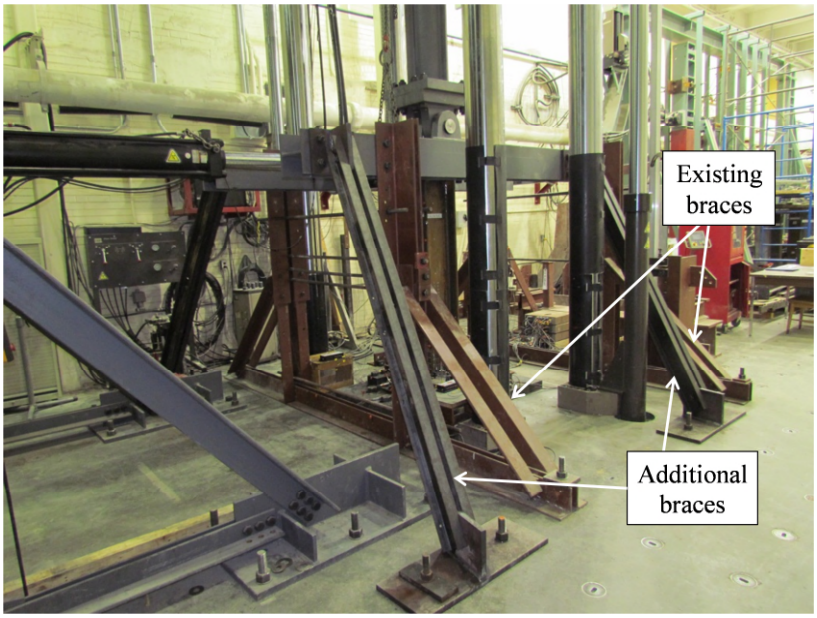

Figure 5.14 Reinforcement of existing lateral bracing system

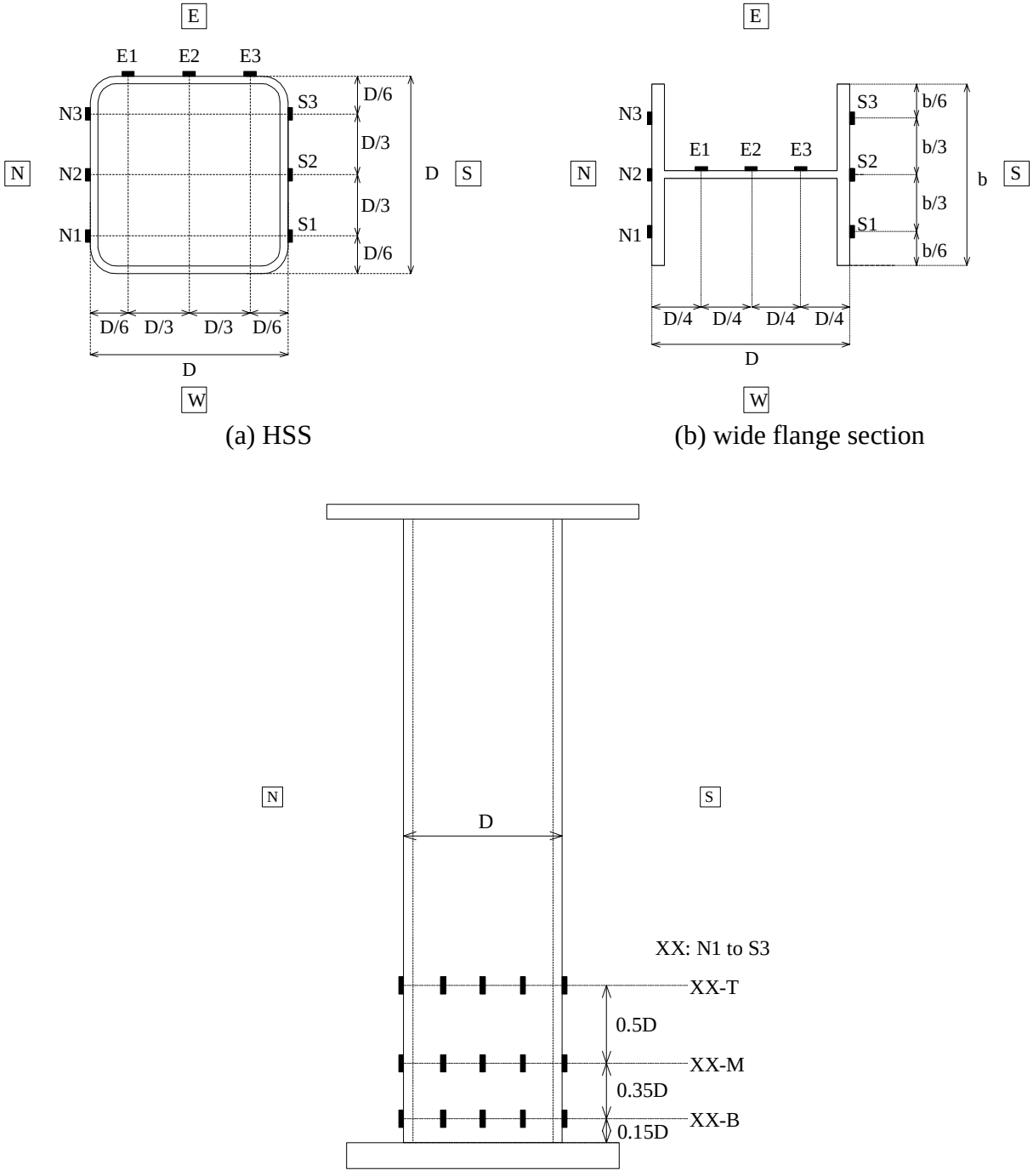

(a) HSS

(b) wide flange section

(c) Elevation view (N-S direction)

Figure 5.15 Strain gauge location and designation

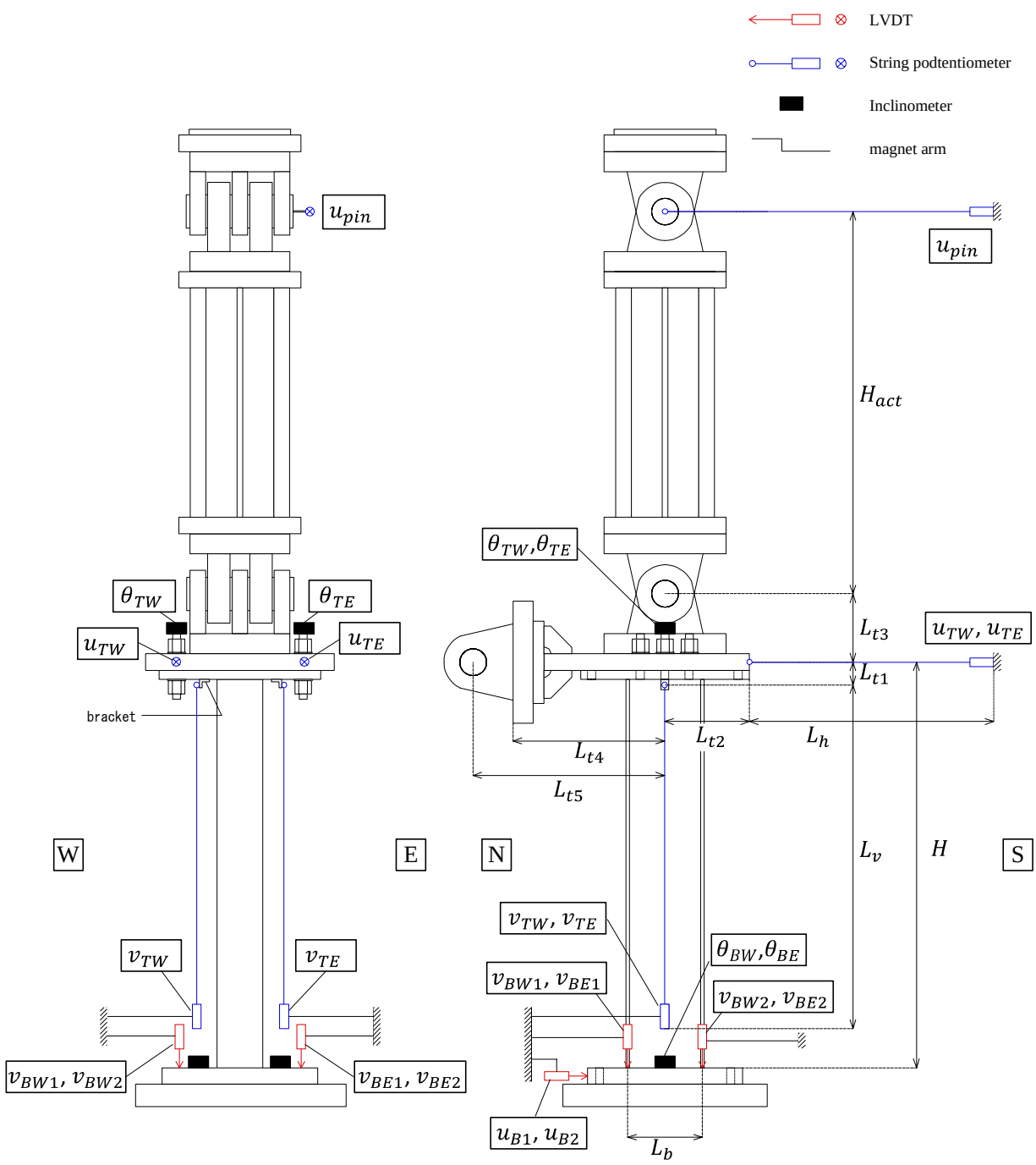

(a) N-S direction (b) E-W direction

Figure 5.16 Positions and designations of LVDTs, string potentiometers and inclinometers (elevation view)

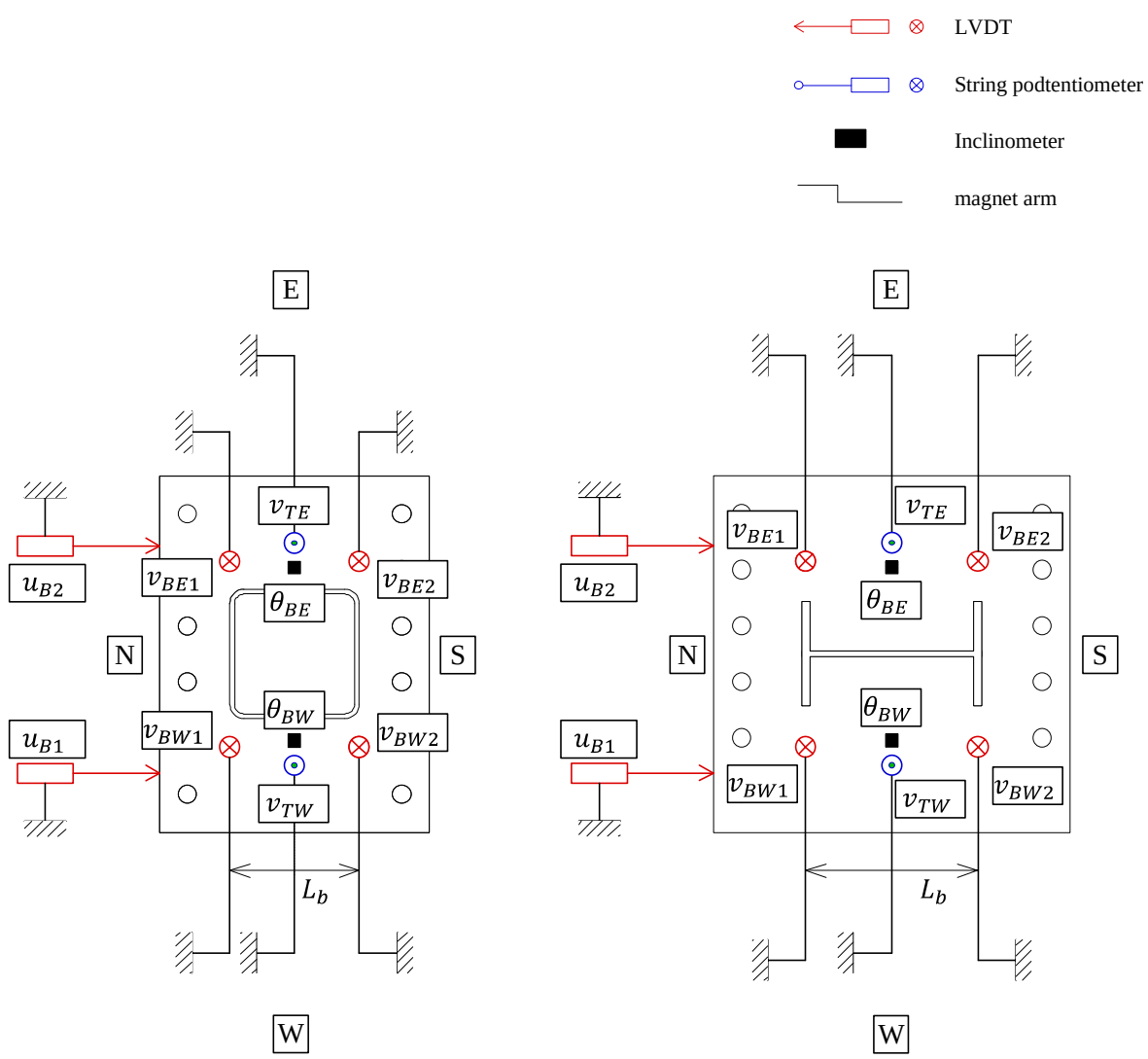

(a) HSS column (b) Wide flange column

Figure 5.17 Positions and designations of LVDTs, string potentiometers and inclinometers (plan view of base plate)

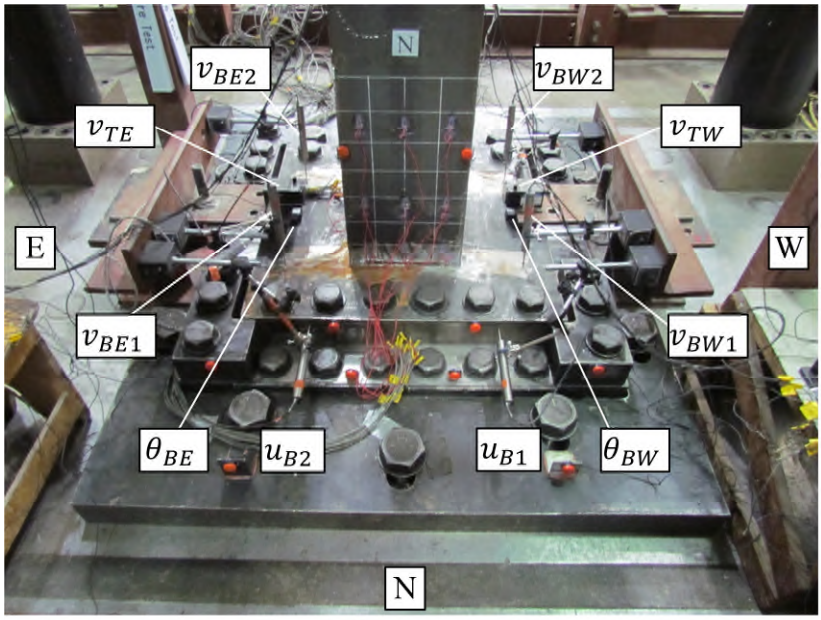

(a) LVDTs, inclinometers, string potentiometers on the base plate

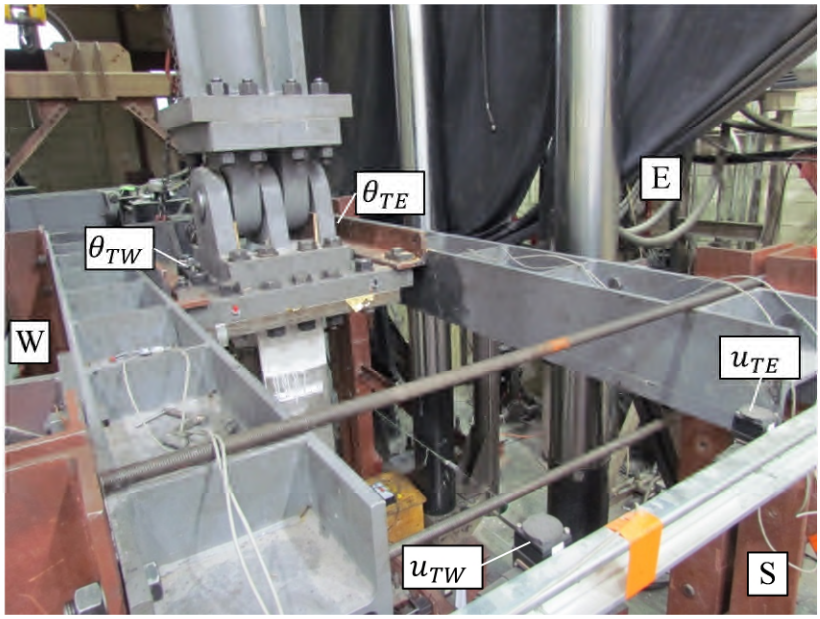

(b) LVDTs, inclinometers, string potentiometers on the top plate

Figure 5.18 Photos of instrumentation setup

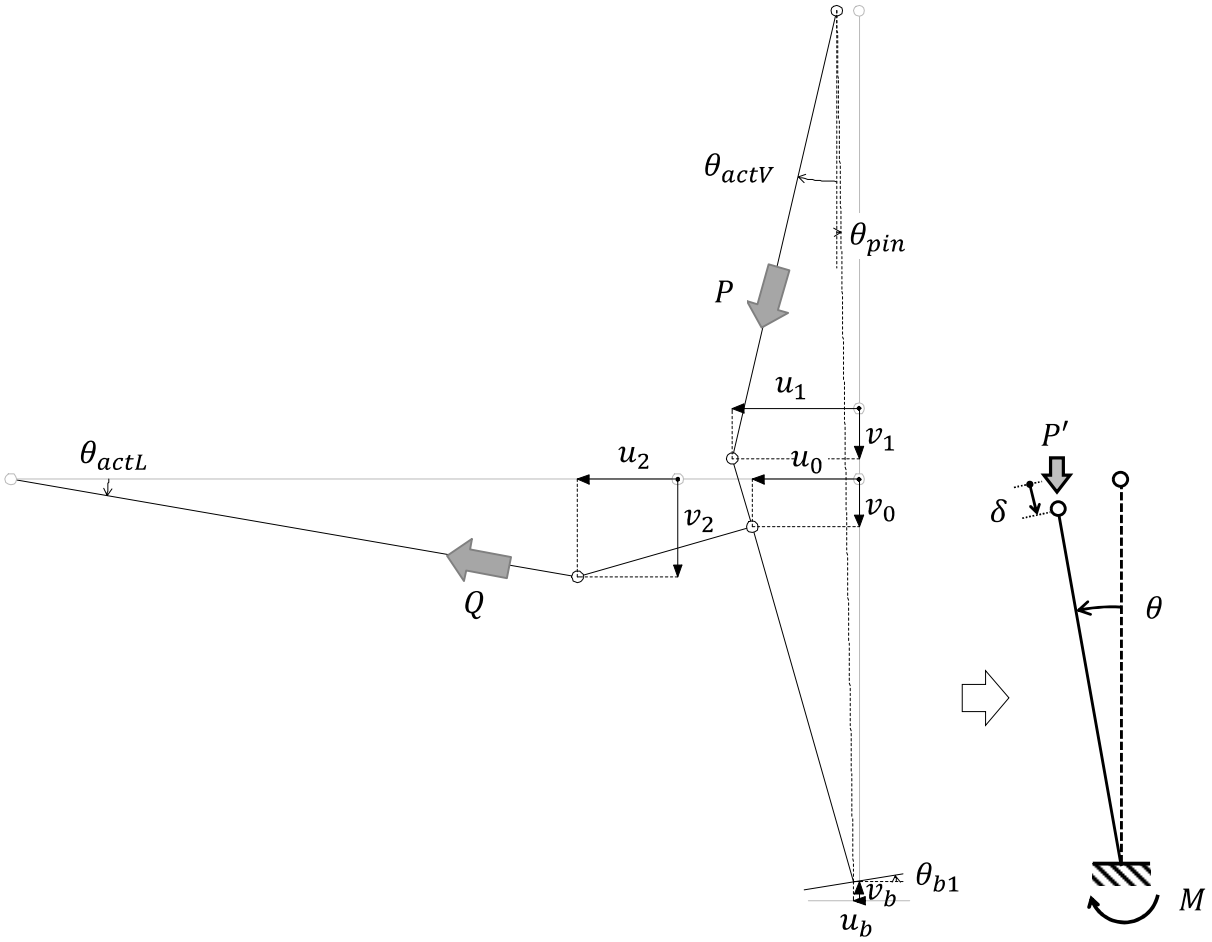

Figure 5.19 Considered deformation mode of the specimen including definitions of the positive rotation

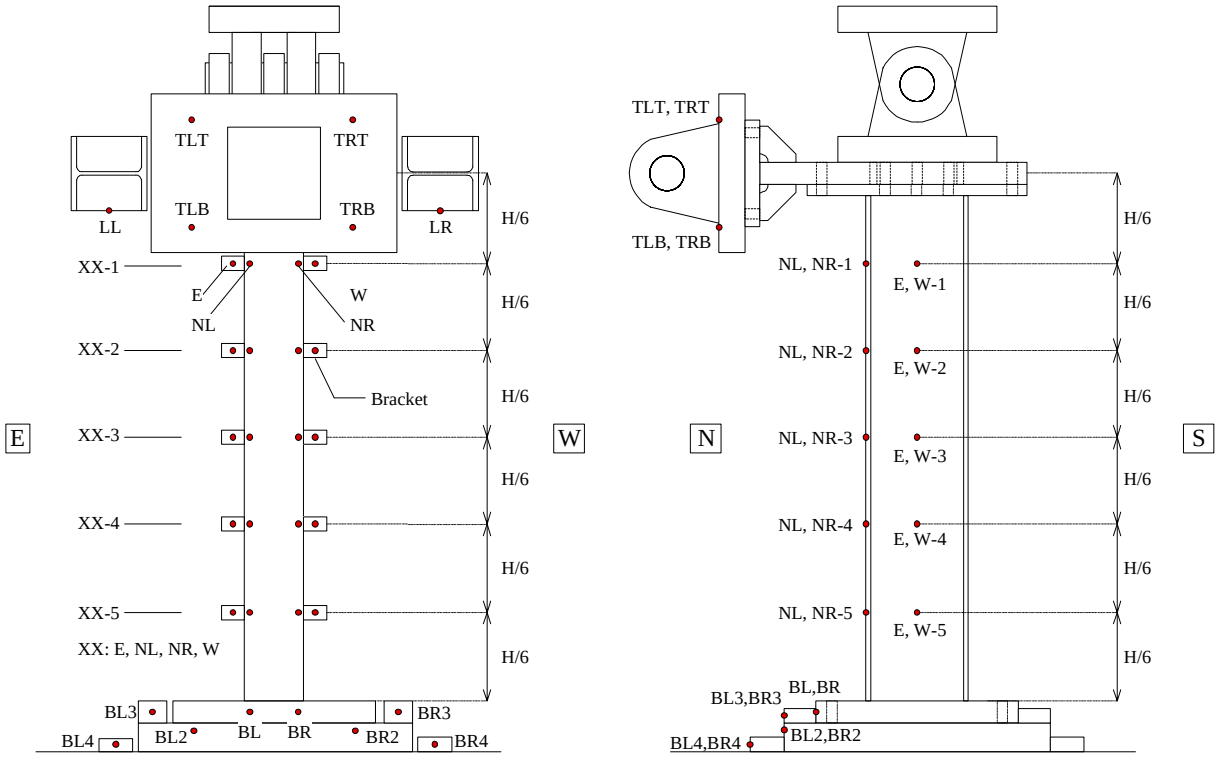

Figure 5.20 Positions and designations of Krypton LED targets

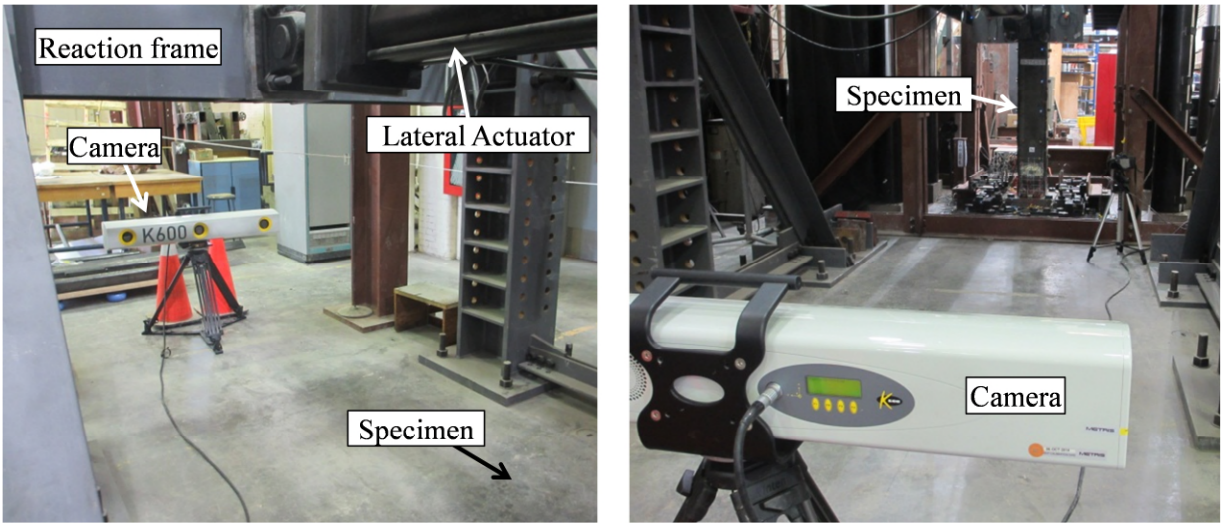

Figure 5.21 Photo of Krypton wireless system setup

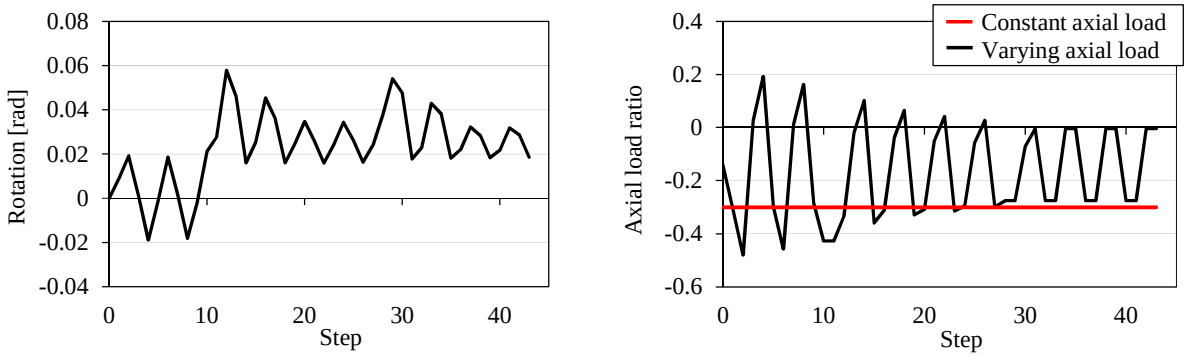

(a) Case 1 - near-fault collapse protocol for H-27 series

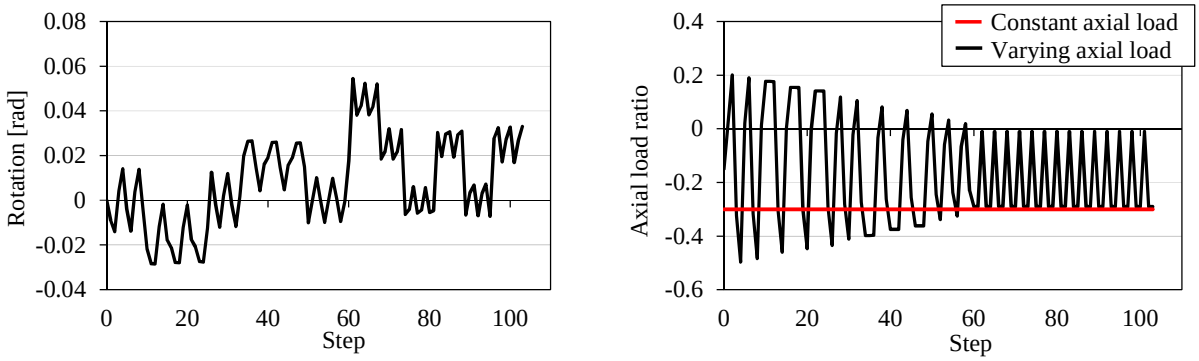

(b) Case 2 - long-duration collapse protocol for H-27 series

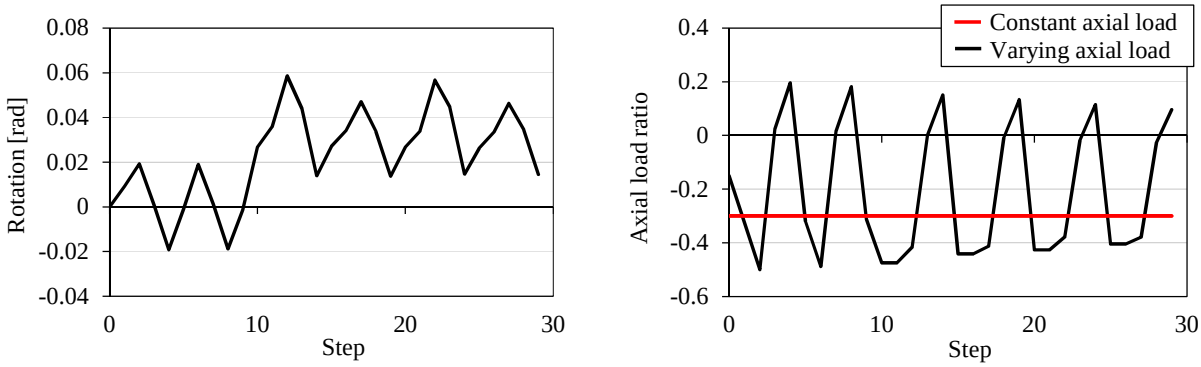

(c) Case 3 - near-fault collapse protocol for H-19 series

Figure 5.22 Collapse-consistent lateral loading protocols for HSS specimens
(left: lateral drift, right: axial load ratio)

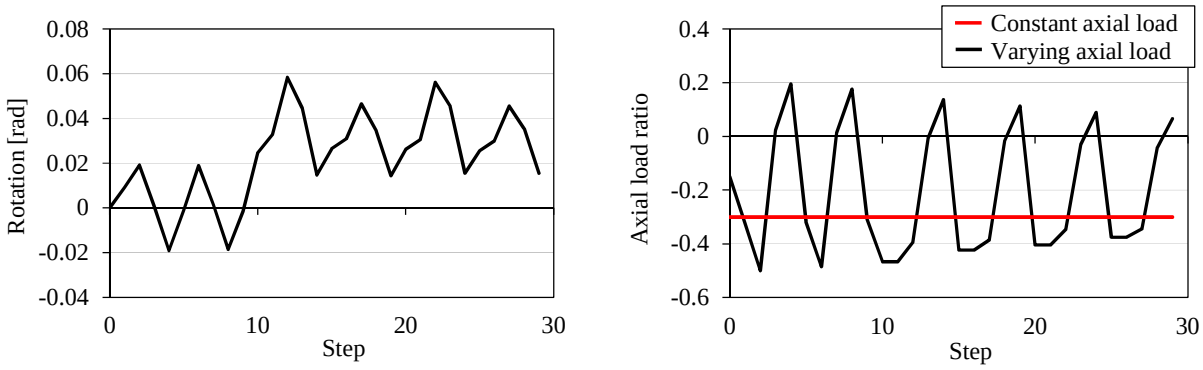

(a) Case 4 – near-fault collapse protocol

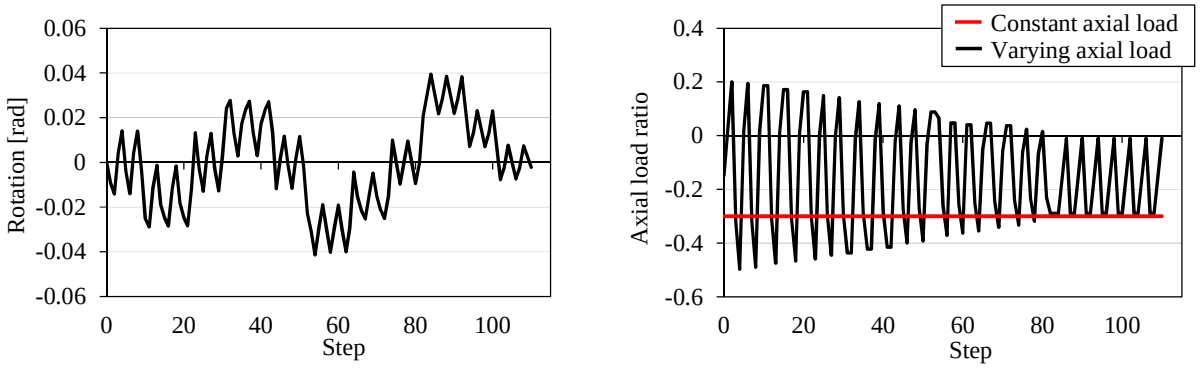

(b) Case 5 – long-duration collapse protocol

Figure 5.23 Collapse-consistent lateral loading protocols for wide flange specimens (left: lateral drift, right: axial load ratio)

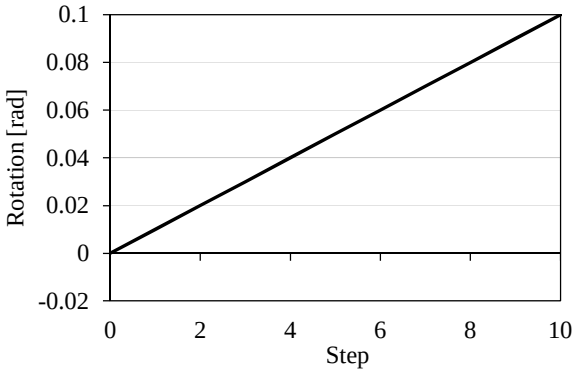

Figure 5.24 Monotonic loading protocol

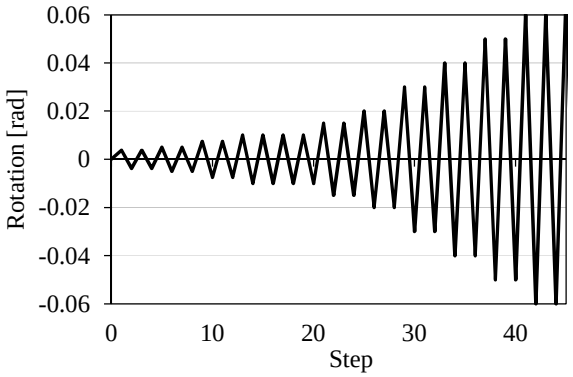

Figure 5.25 Symmetric cyclic loading protocol

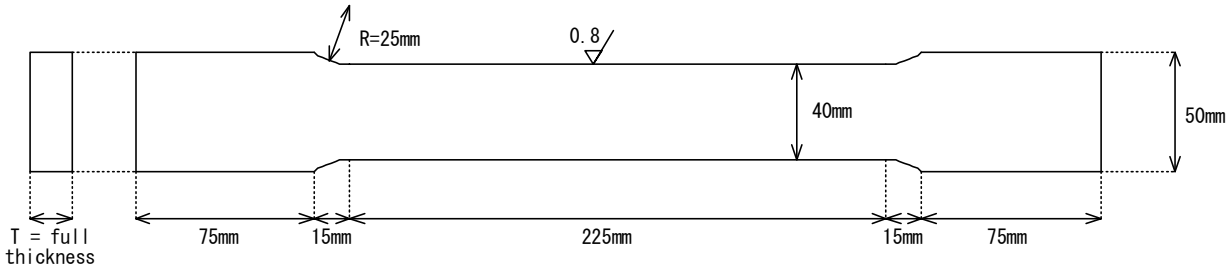

(a) Rectangular tension test specimen (plate-type standard) (ASTM E8/E8M)

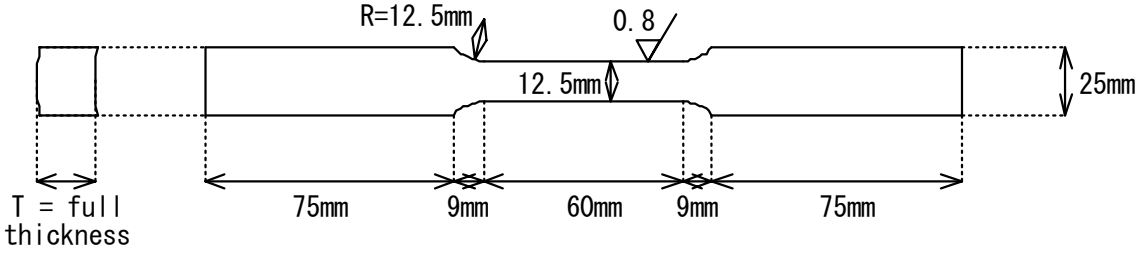

(b) Tension test specimen for large-diameter tubular products (specimen 1) (ASTM E8/E8M)

Figure 5.26 Typical coupon specimens

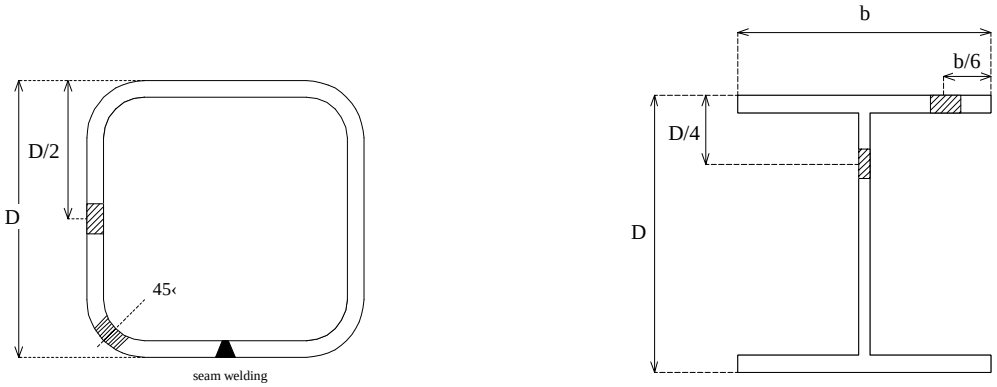

(a) HSS (b) wide flange section

Figure 5.27 Coupon specimen locations

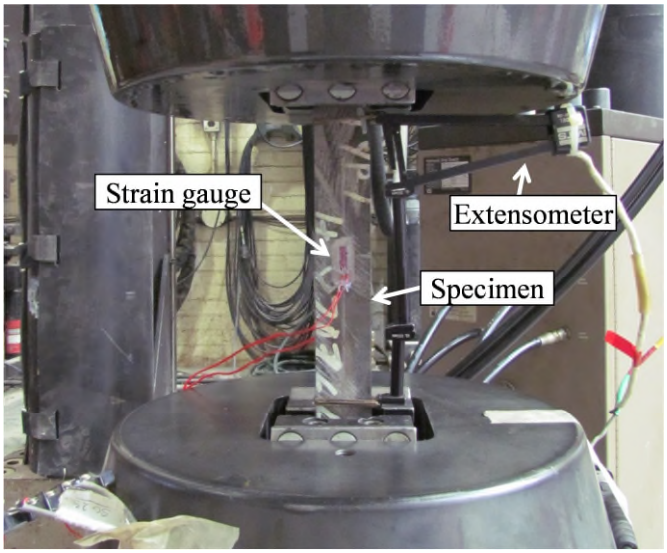

Figure 5.28 General setup of tensile coupon tests

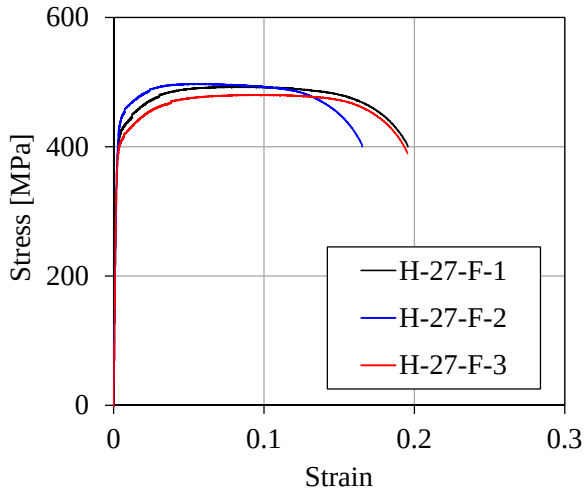

(a) HSS254×9.5, flat part

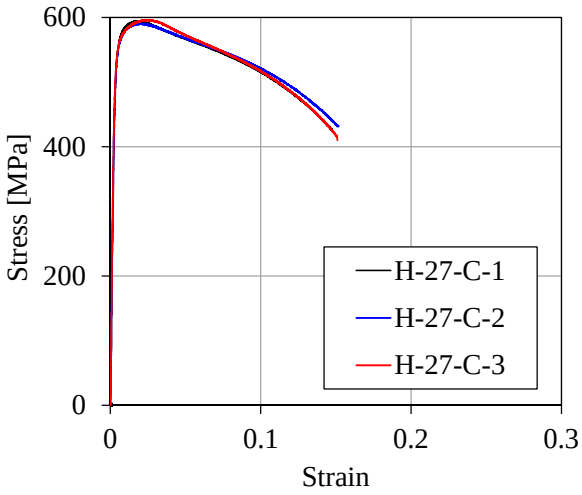

(b) HSS254×9.5, corner part

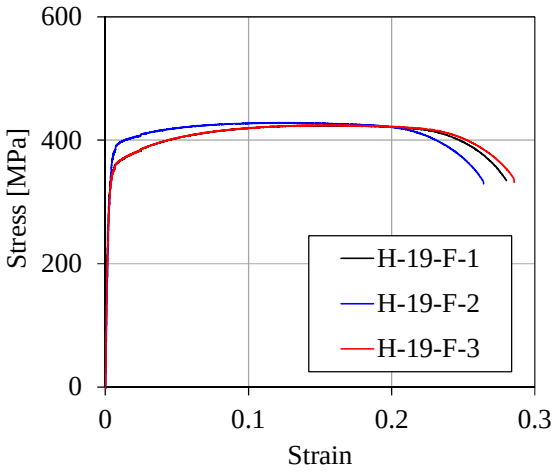

(c) HSS305×16, flat part

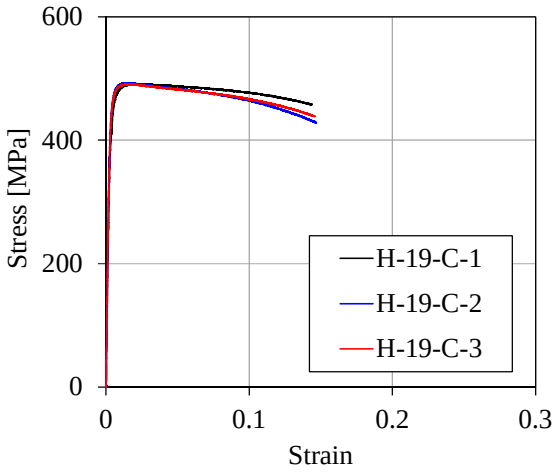

(d) HSS305×16, corner part

Figure 5.29 Engineering stress-strain relation of HSS specimens

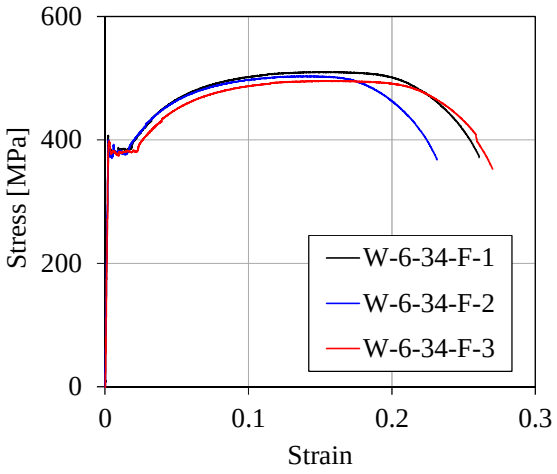

(a) W14×53, flange

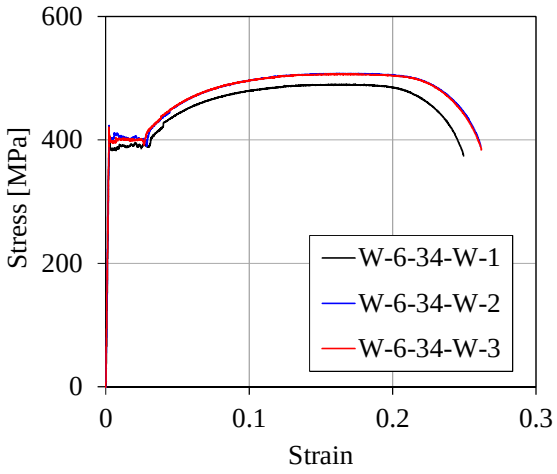

(b) W14×53, web

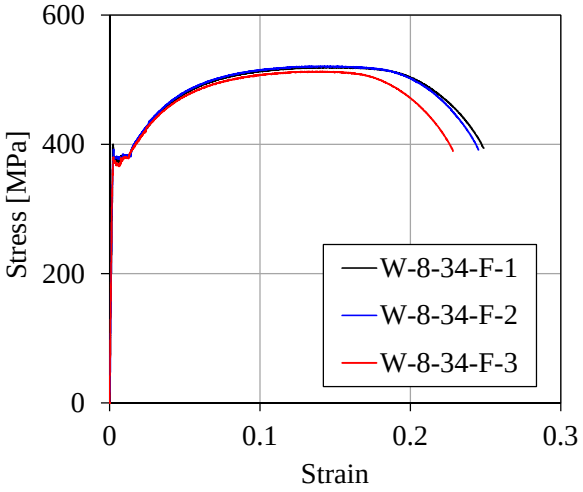

(c) W14×61, flange

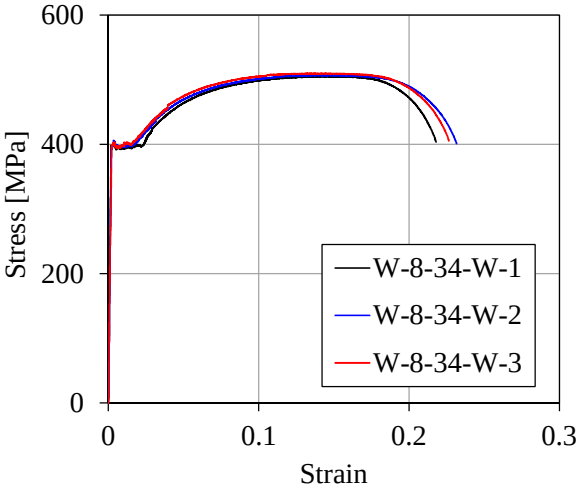

(d) W14×61, web

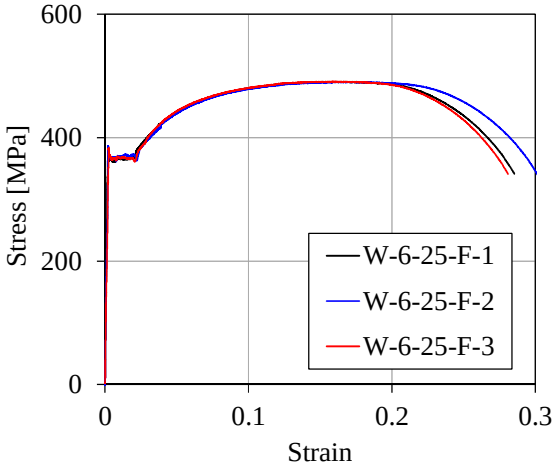

(e) W14×82, flange

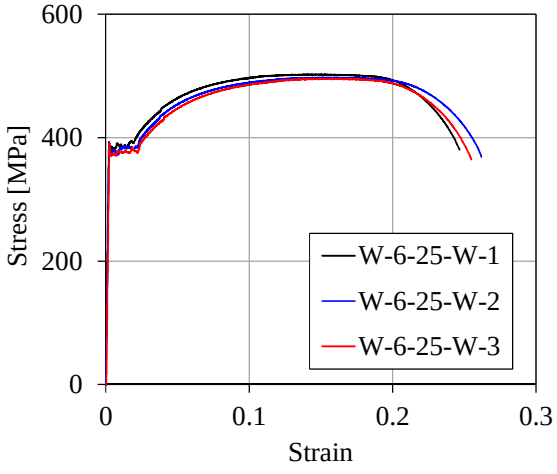

(f) W14×82, web

Figure 5.30 Engineering stress-strain relation of wide flange specimens

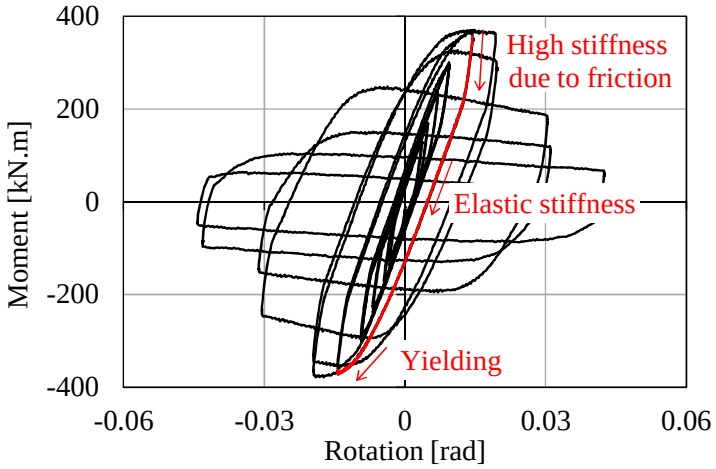

(a) Measured moment-rotation relation (H-27-S-C)

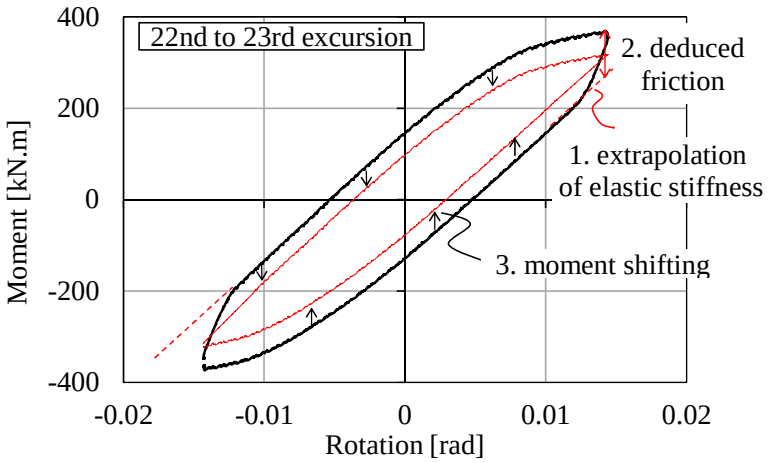

(b) Schematic process of friction subtraction

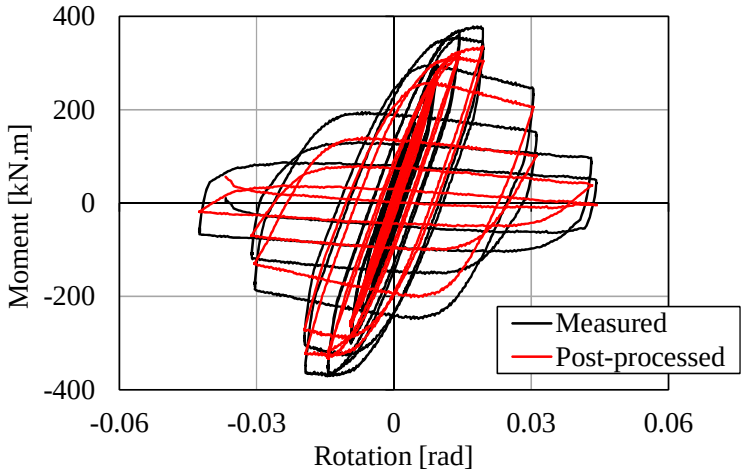

(c) Measured and post-processed moment-rotation

Figure 5.31 Post-processing on moment-rotation relation for friction subtraction

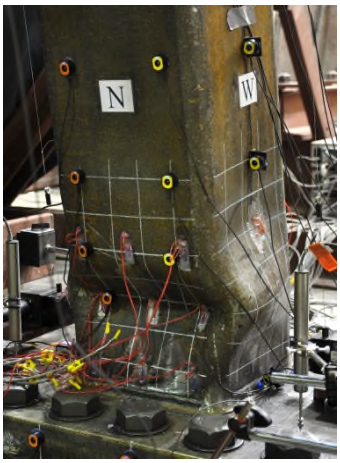

(a) H-27-M-C
(θ_{max}=0.14 rads)

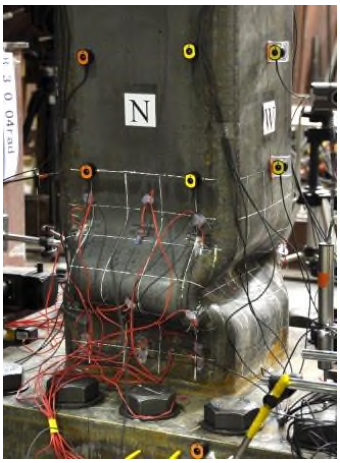

(b) H-27-S-C
(θ_{max}=4%)

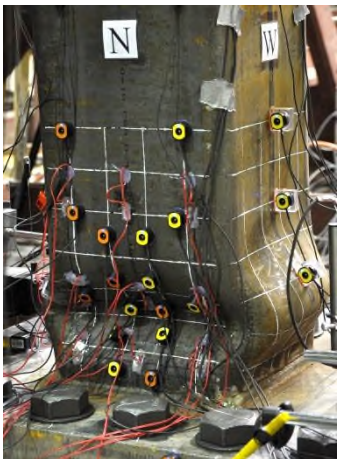

(c) H-27-C1-C
(after phase 1 loading)

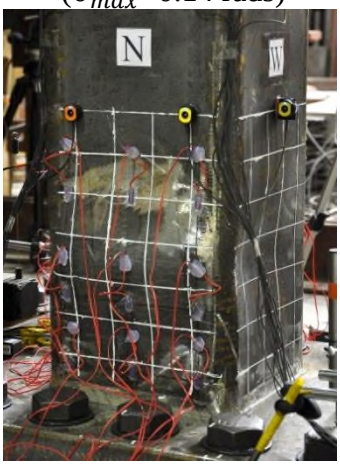

(d) H-27-C1-V
(after phase 1 loading)

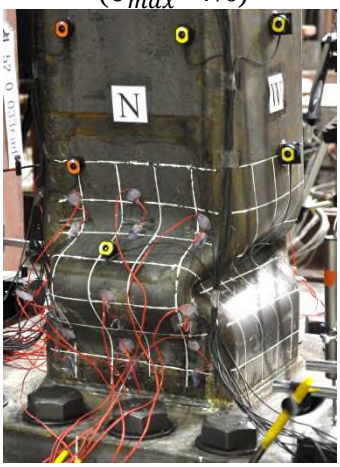

(e) H-27-C2-C
(after phase 1 loading)

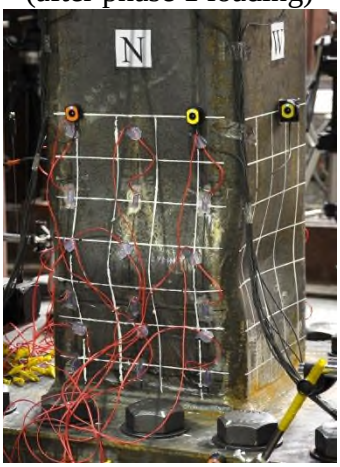

(f) H-27-C2-V
(after phase 1 loading)

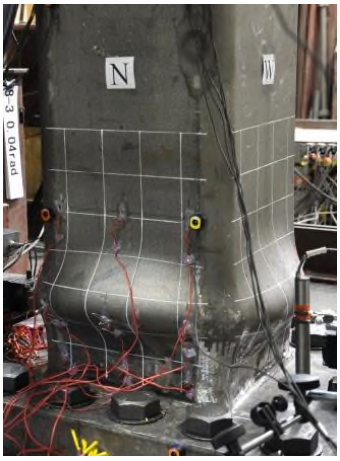

(g) H-19-S-C
(θ_{max}=0.04 rads)

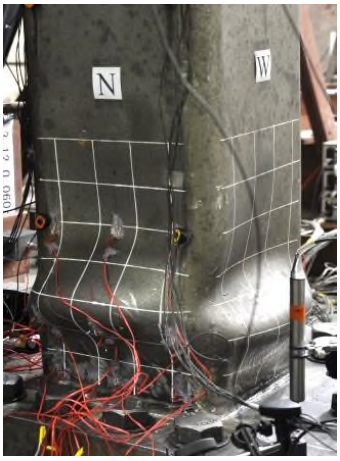

(h) H-19-C1-C
(after phase 3 loading)

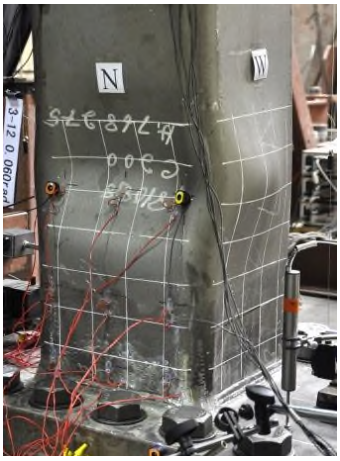

(i) H-19-C1-V
(after phase 3 loading)

Figure 5.32 Deformed shape of HSS specimens

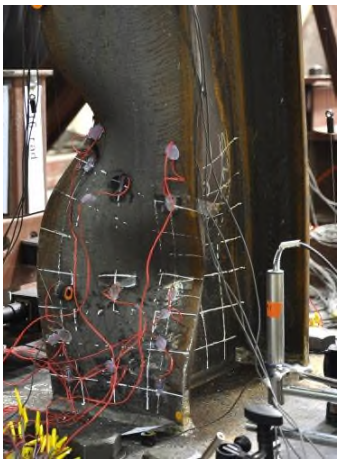

(a) W-6-34-M-C
(θ_{max}=0.16 rads)

(b) W-6-34-S-C
(θ_{max}=5 rads)

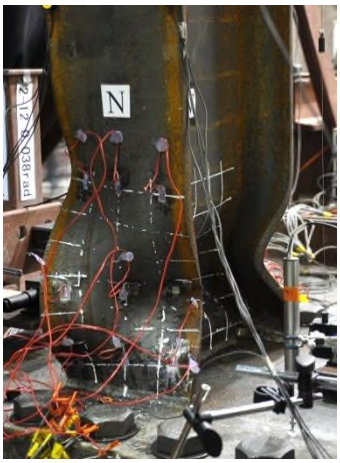

(c) W-6-34-C1-C
(after phase 2 loading)

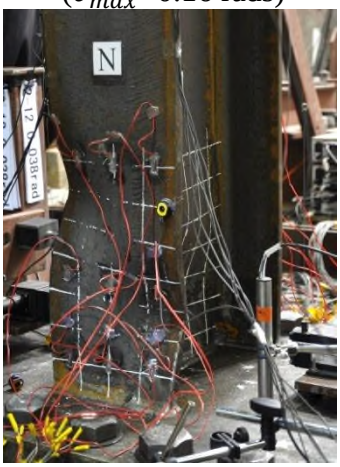

(d) W-6-34-C1-V
(after phase 2 loading)

(e) W-6-34-C2-C
(after squashing in phase 2)

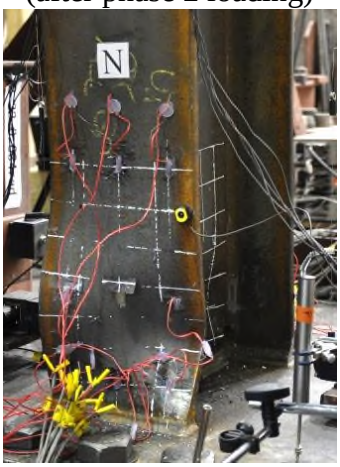

(f) W-6-34-C2-V
(after phase 2 loading)

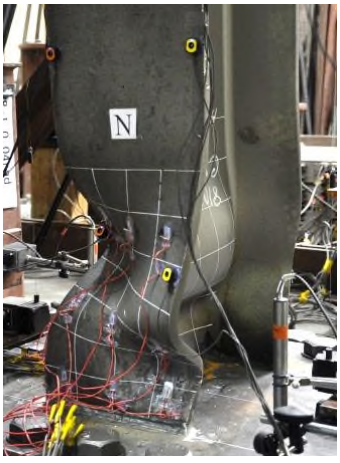

(g) W-8-34-S-C
(θ_{max}=0.04 rads)

(h) W-8-34-C1-C
(after phase 2 loading)

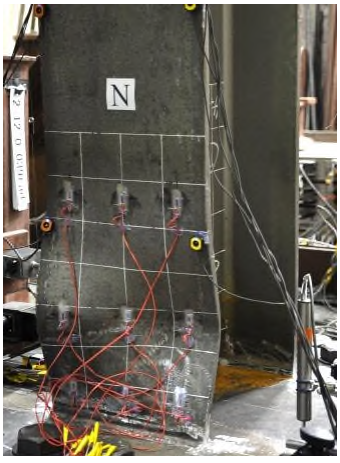

(i) W-8-34-C1-V
(after phase 2 loading)

Figure 5.33 Deformed shape of wide flange specimens

(g) W-6-25-S-C
(θ_{max}=0.05 rads)

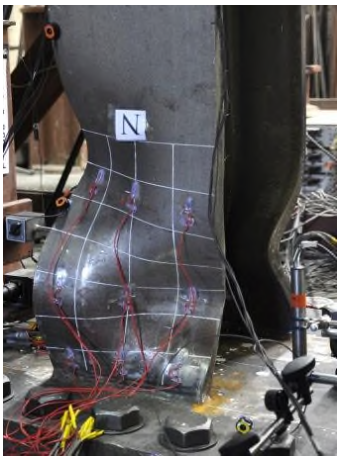

(h) W-6-25-C1-C
(after phase 3 loading)

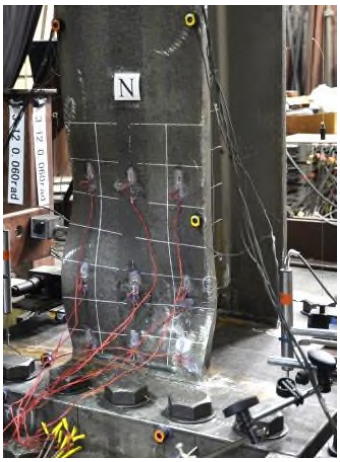

(i) W-6-25-C1-V
(after phase 3 loading)

Figure 5.33 Deformed shape of the tested wide flange specimens (continued)

(a) k-area
(W-8-34-S-C)

(b) flange weld toe and weld access hole
(W-6-34-C2-V)

Figure 5.34 Typical fracture modes of wide flange specimens

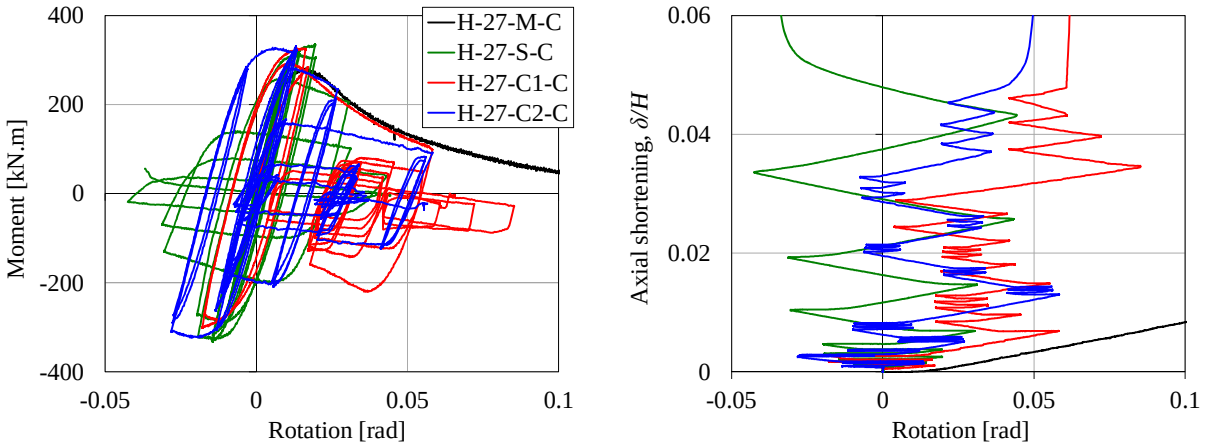

(a) H-27 series

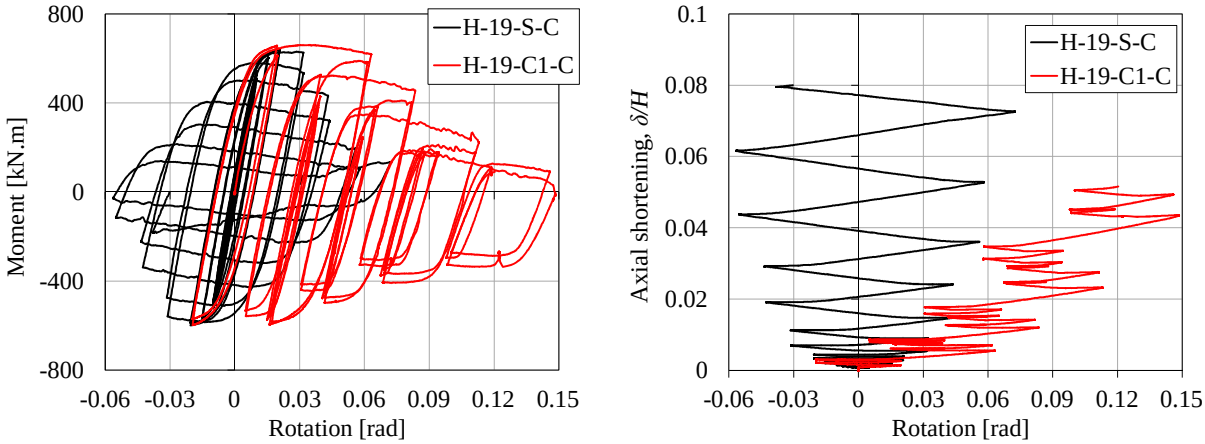

(b) H-19 series

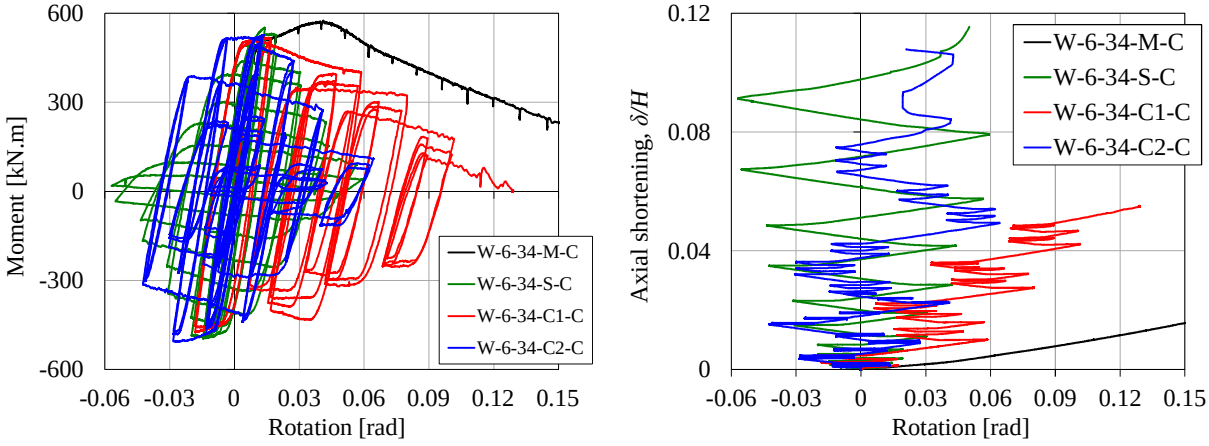

(c) W-6-34 series

Figure 5.35 Effect of loading protocol under constant axial load

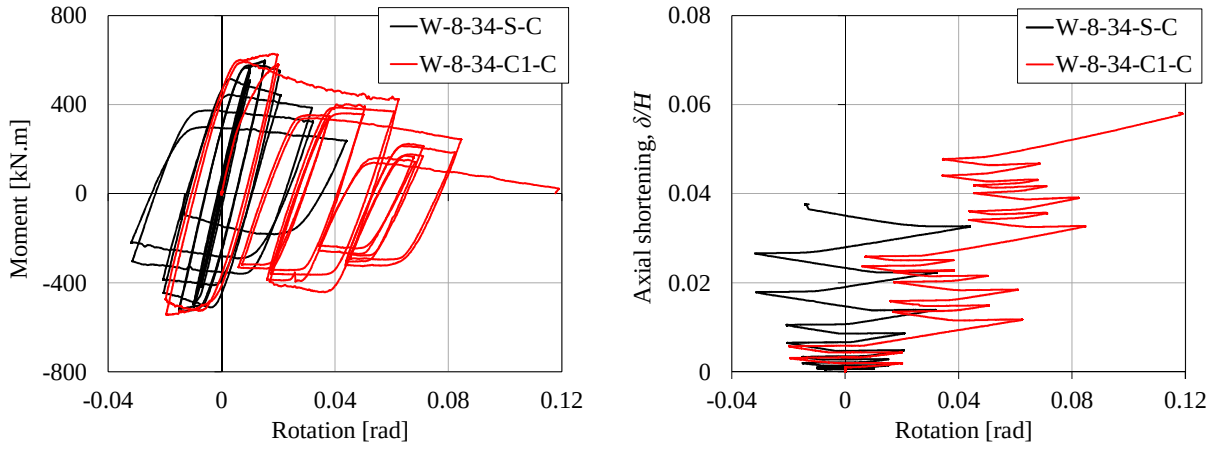

(d) W-8-34 series

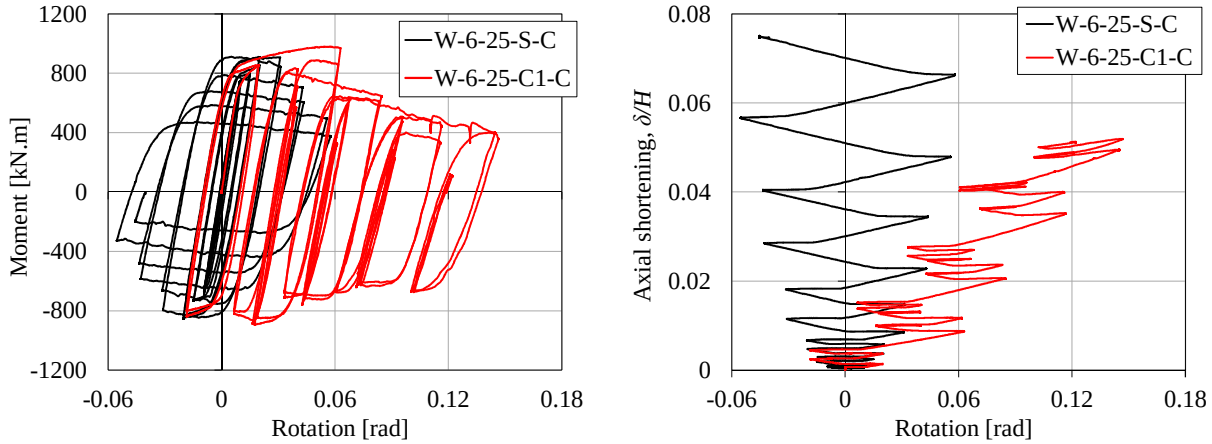

(e) W-6-25 series

Figure 5.35 Effect of loading protocol under constant axial load (continued)

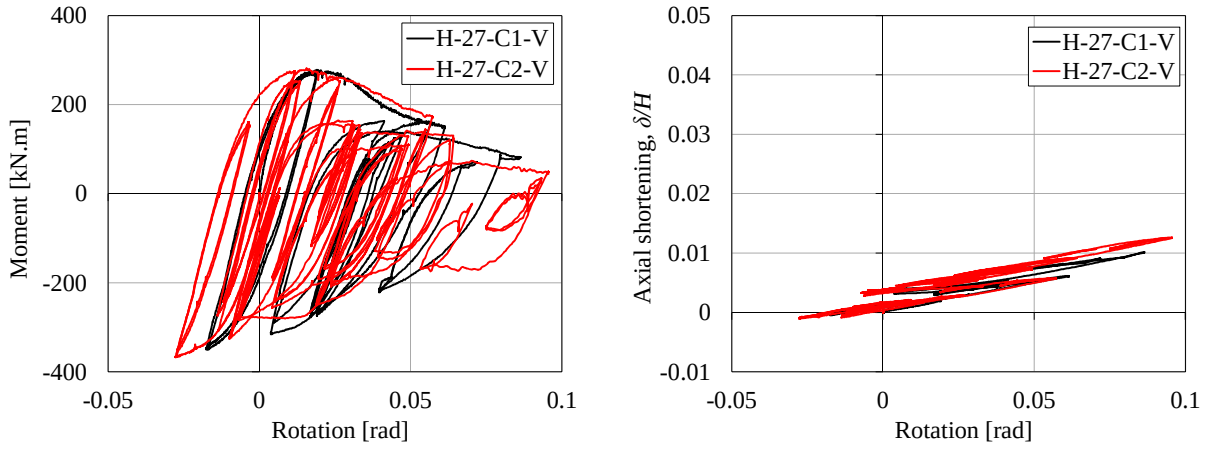

(a) H-27 series

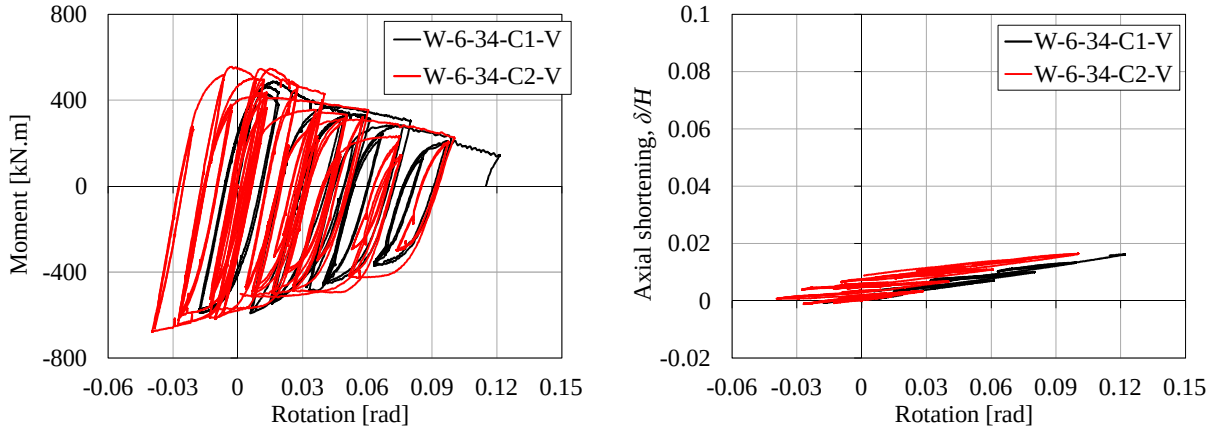

(b) W-6-34 series

Figure 5.36 Effect of loading protocol under varying axial load

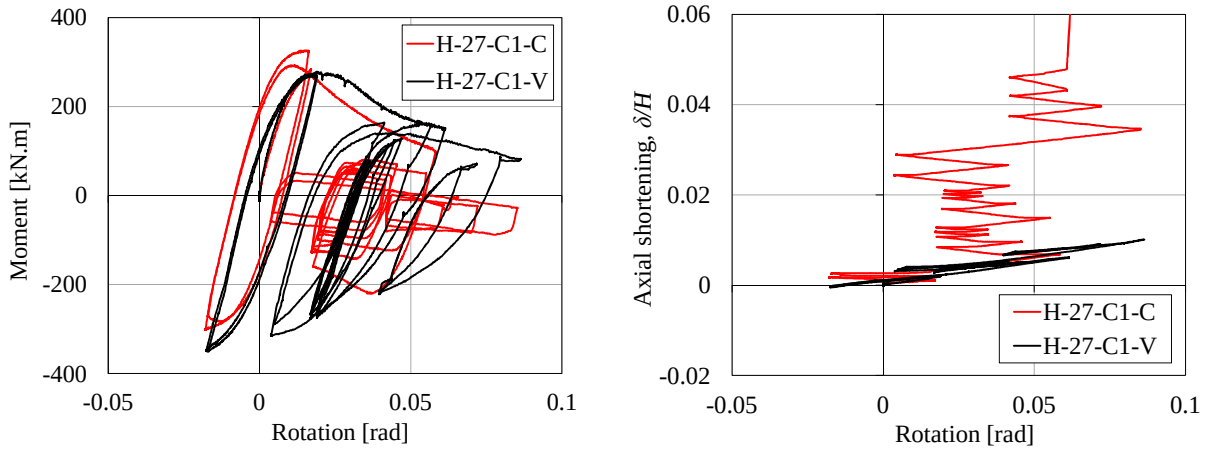

(a) H-27-C1-C versus H-27-C1-V

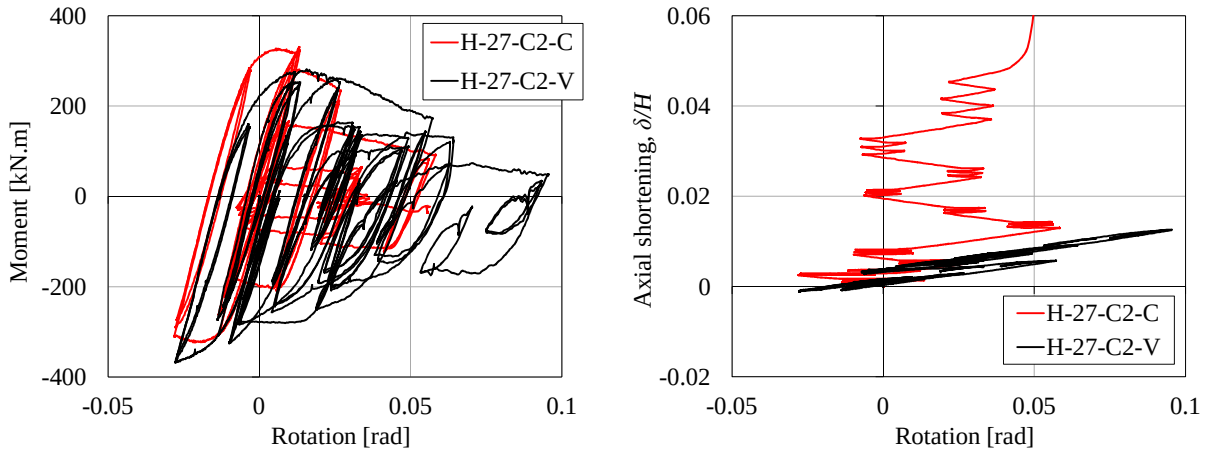

(b) H-27-C2-C versus H-27-C2-V

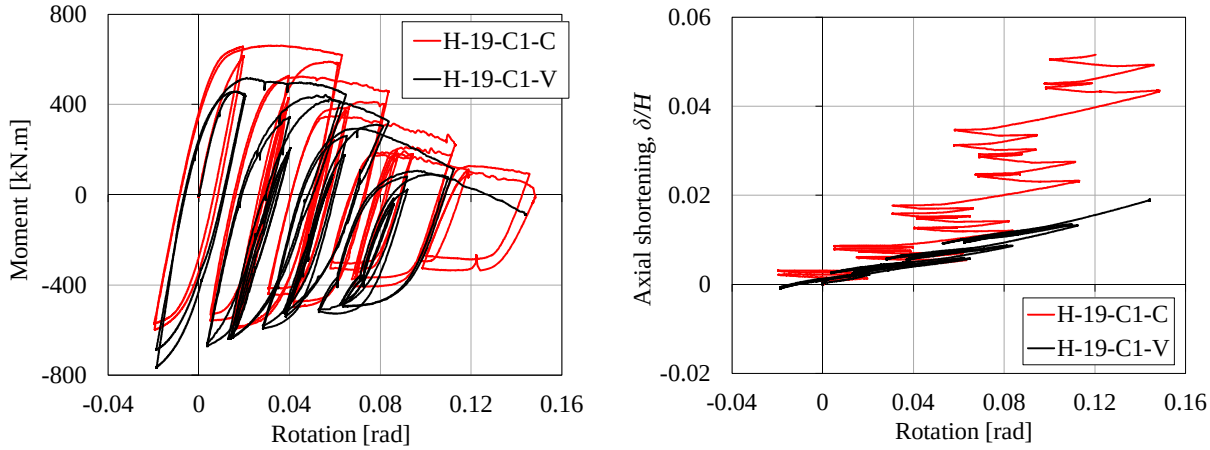

(c) H-19-C1-C versus H-19-C1-V

Figure 5.37 Effect of axial load variation

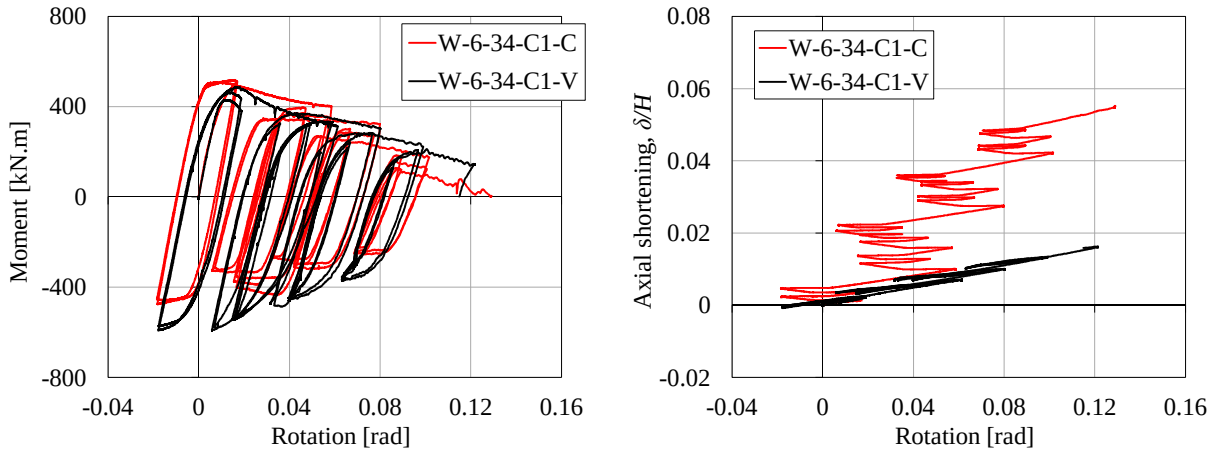

(d) W-6-34-C1-C versus W-6-34-C1-V

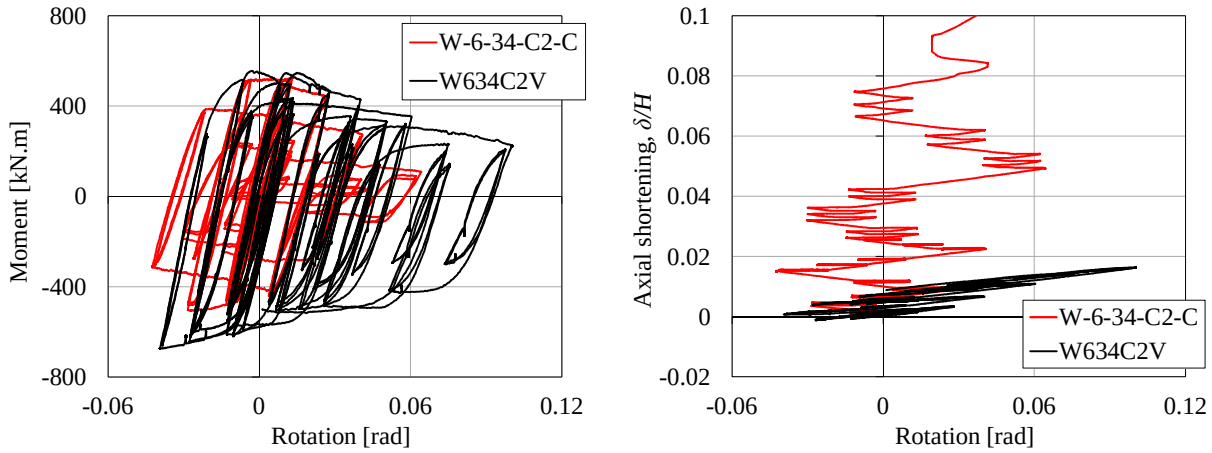

(e) W-6-34-C2-C versus W-6-34-C2-V

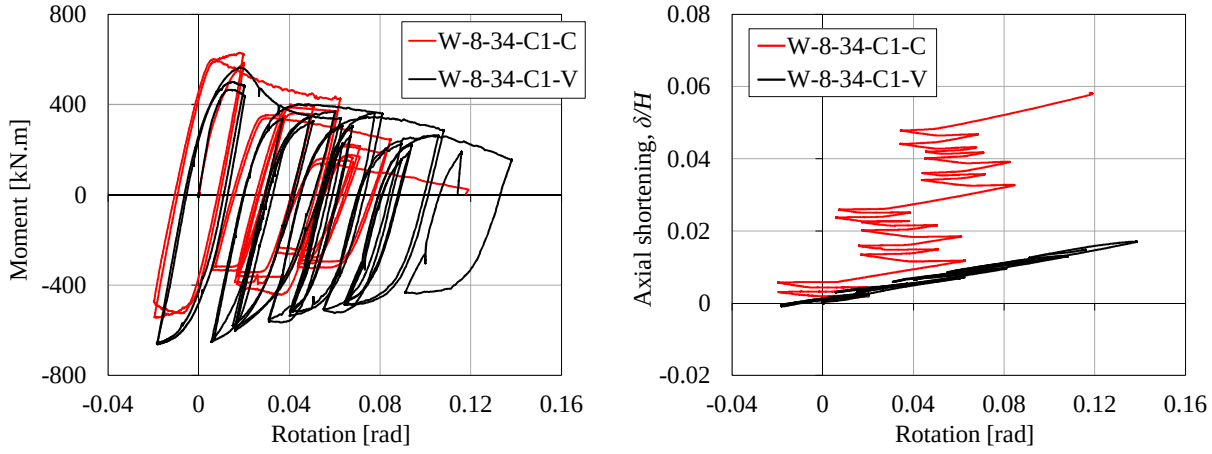

(f) W-8-34-C1-C versus W-8-34-C1-V

Figure 5.37 Effect of axial load variation (continued)

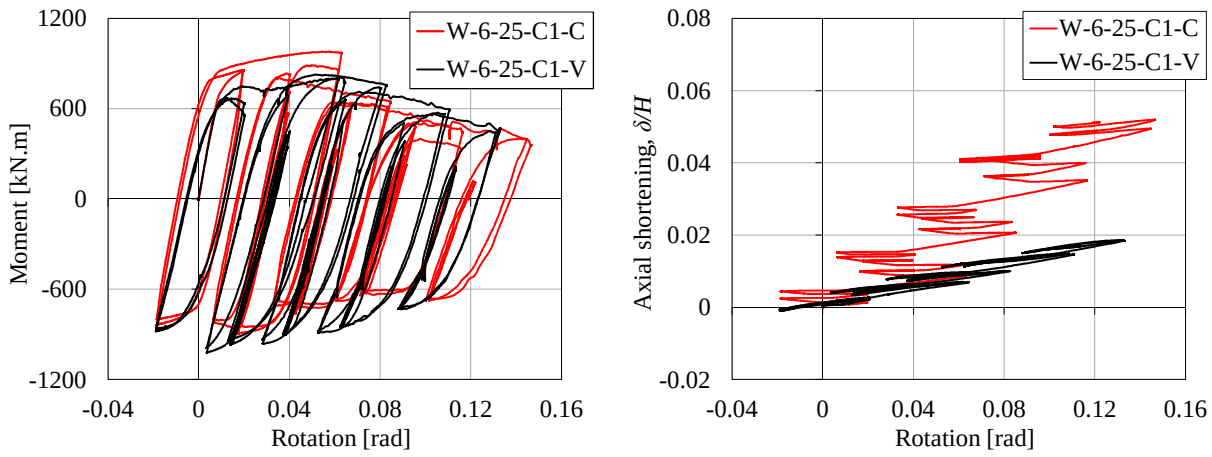

(g) W-6-25-C1-C versus W-6-25-C1-V

Figure 5.37 Effect of axial load variation (continued)

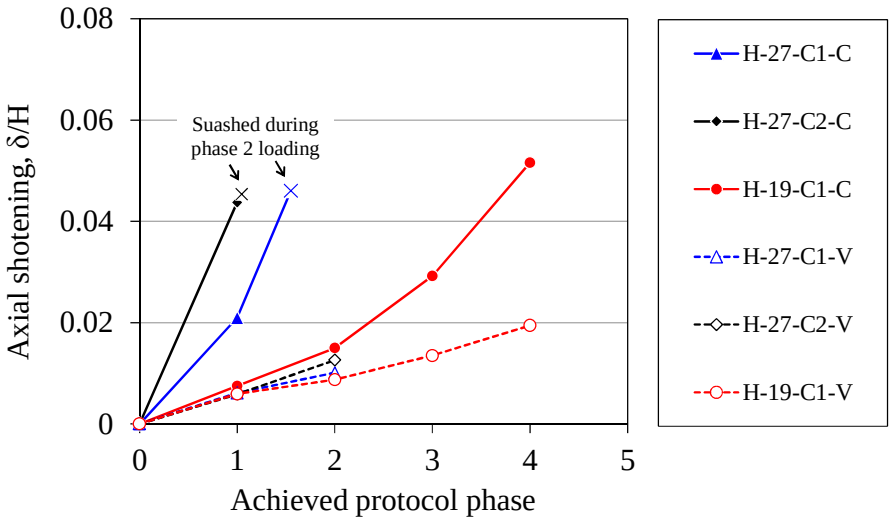

(a) HSS specimens

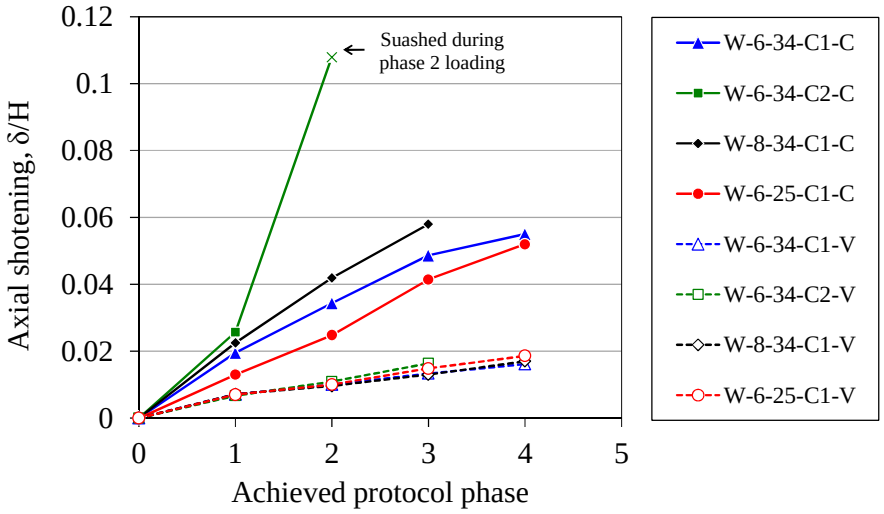

(b) wide flange specimens

Figure 5.38 Achieved axial shortening after every collapse-consistent loading protocol phase

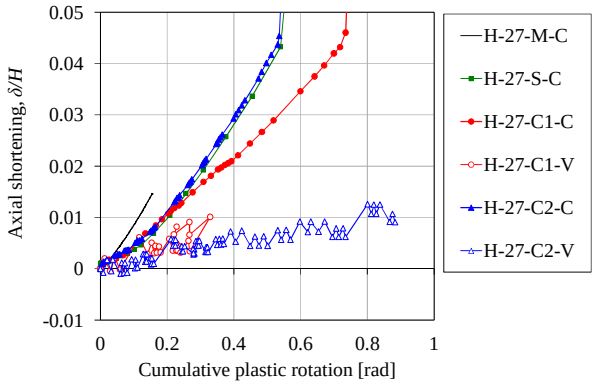

(a) H-27 specimens

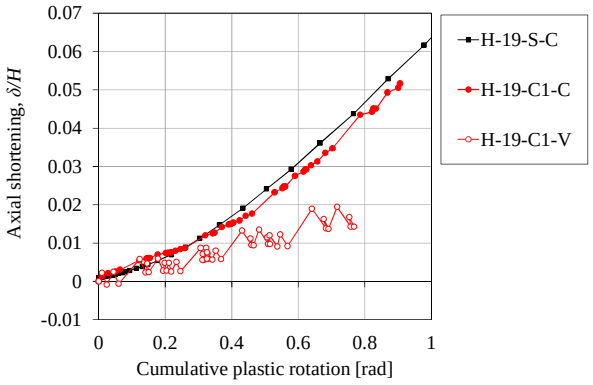

(b) H-19 specimens

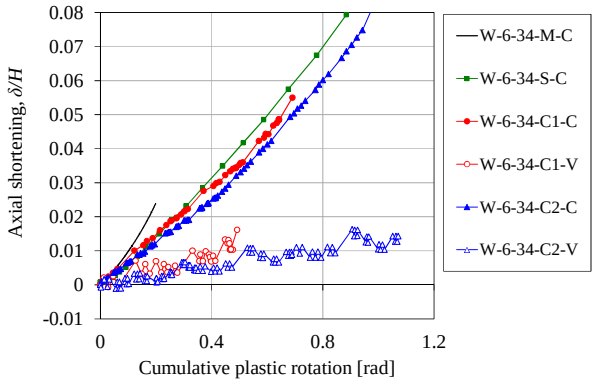

(c) W-6-34 specimens

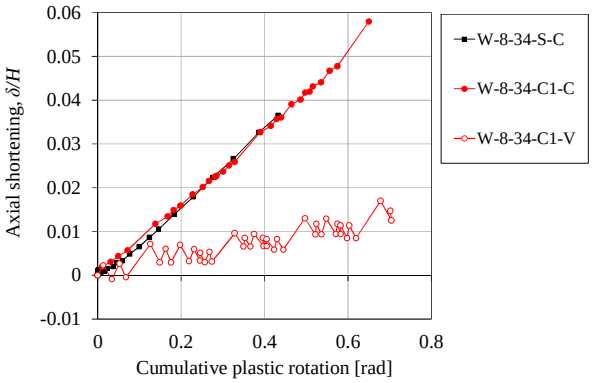

(d) W-8-34 specimens

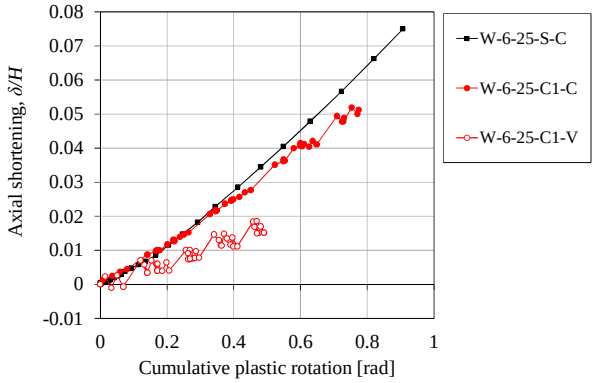

(e) W-6-25 specimens

Figure 5.39 Column axial shortening versus cumulative plastic rotation

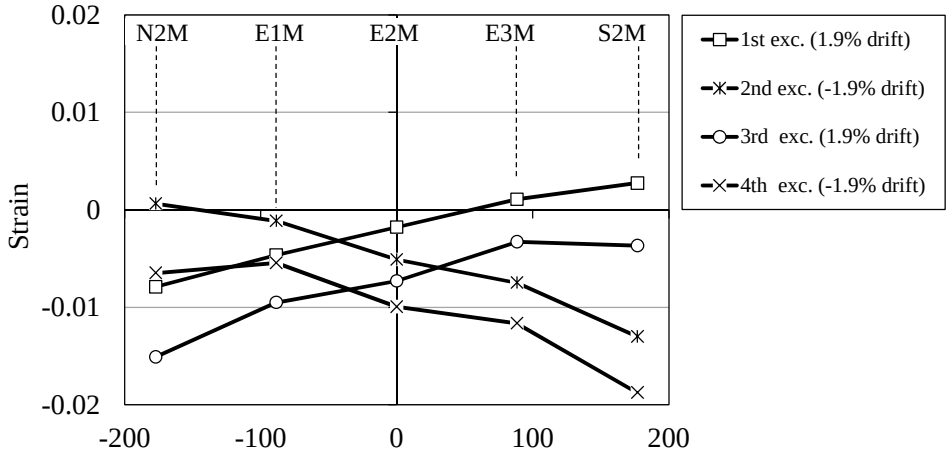

(a) H-19-C1-C

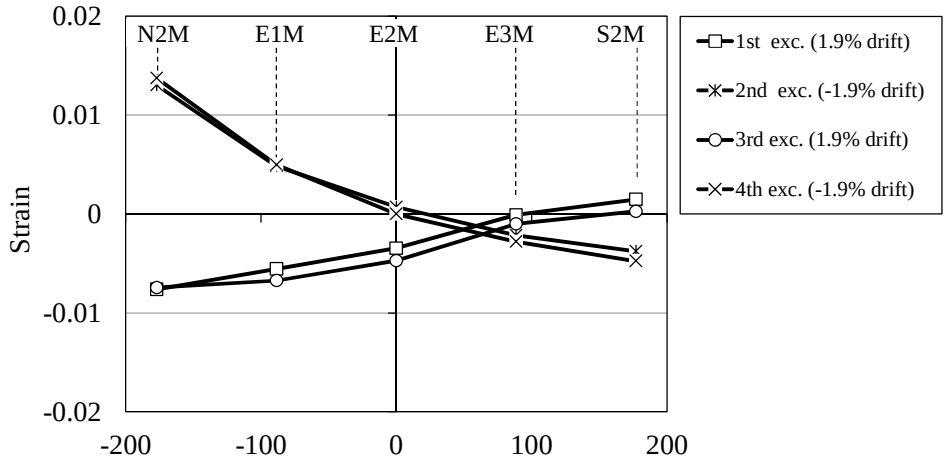

(b) H-19-C1-V

Figure 5.40 Strain distribution along latitudinal direction at 0.5 *D* height from base plate

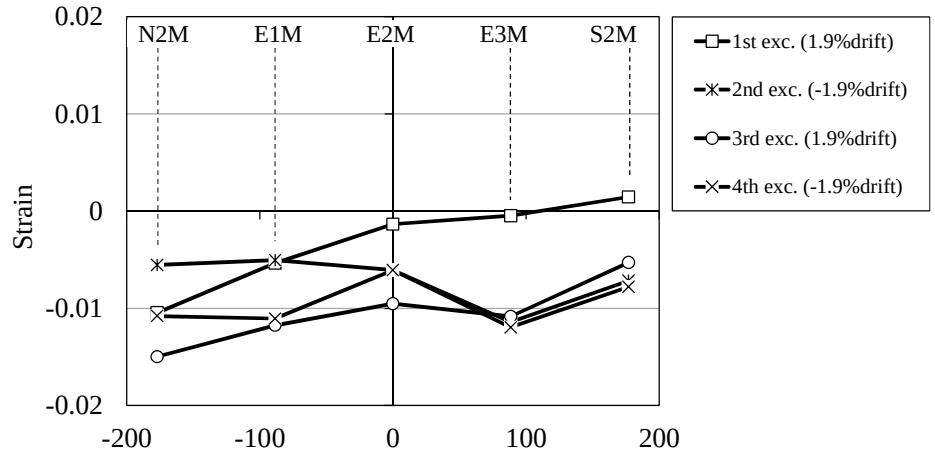

(c) W-6-25-C1-C

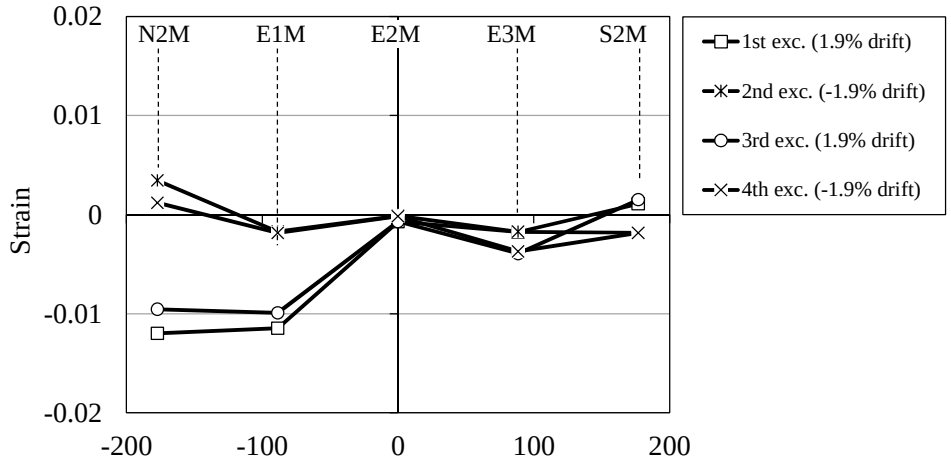

(d) W-6-25-C1-V

Figure 5.40 Strain distribution along latitudinal direction at 0.5*D* height from base plate (continued)

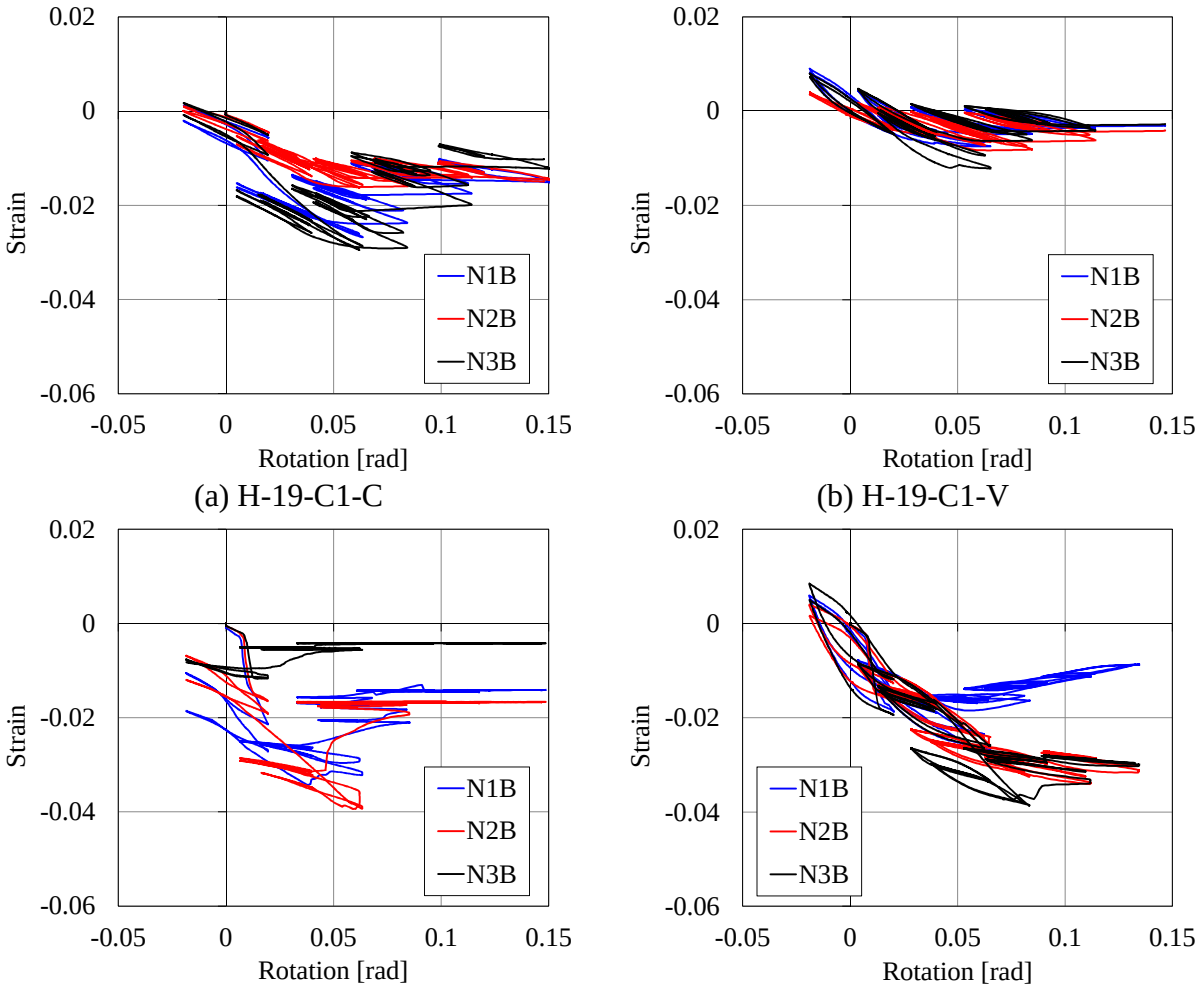

(a) H-19-C1-C (b) H-19-C1-V

(c) W-6-25-C1-C (d) W-6-25-C1-V

Figure 5.41 Strain demand on north flange of specimens at 0.15*D* away from base plate

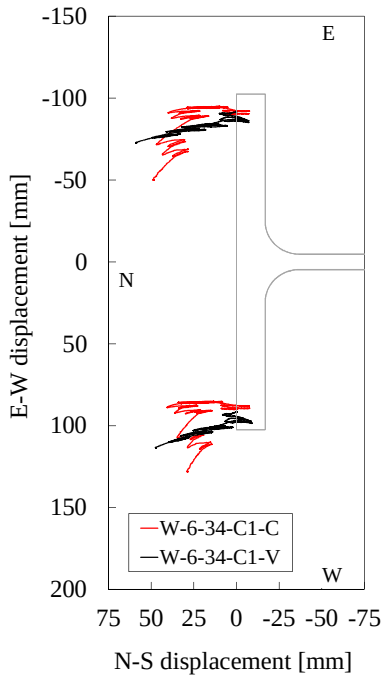

(a) W-6-34-C1-C and W-6-34-C1-V

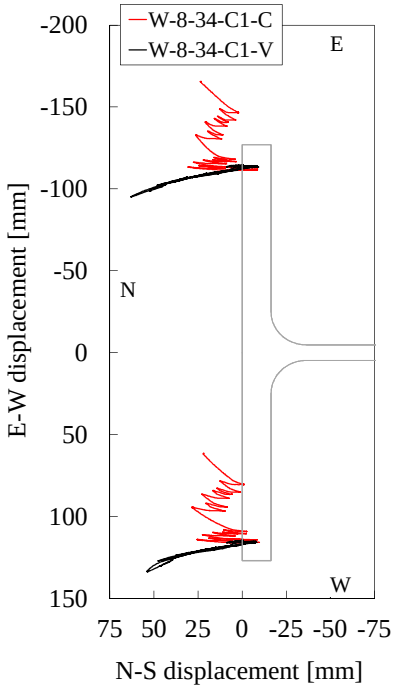

(b) W-8-34-C1-C and W-8-34-C1-V

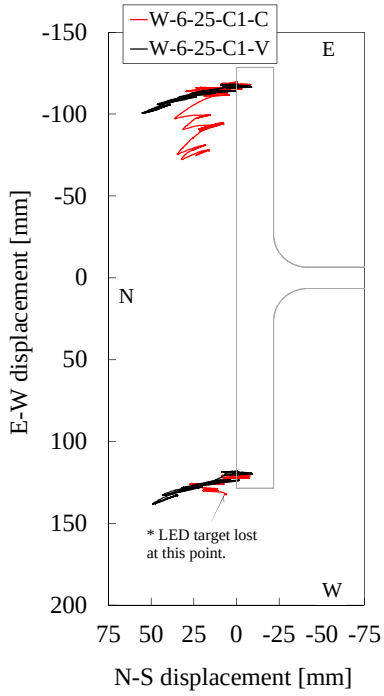

(c) W-6-25-C1-C and W-6-25-C1-V

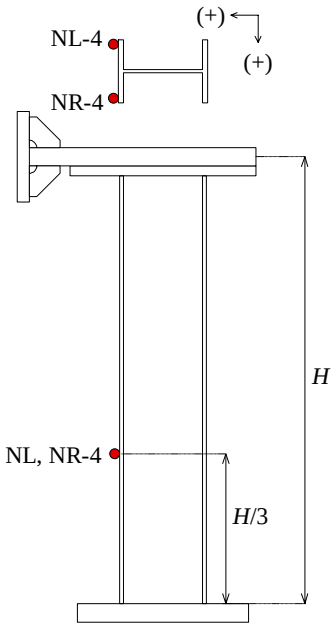

Location of the LED targets

Figure 5.42 Out-of-plane movement of NL4 and NR4 LED targets

REFERENCES

ABAQUS (2014). "ABAQUS/CAE User's Guide version 6.14." Dassault Systèmes Simulia Corp., Providence, RI, USA.

Adam, C., Ibarra, L. F. and Krawinkler, H. (2004). "Evaluation of P-Delta Effects in Non-Deteriorating MDOF Structures from Equivalent SDOF Systems." *13th World Conference on Earthquake Engineering (13WCEE)*, Vancouver, B.C., Canada.

Adam, C. and Jäger, C. (2012). "Seismic Collapse Capacity of Basic Inelastic Structures Vulnerable to the P-delta Effect." *Earthquake Engineering and Structural Dynamics*, 41 (4), 775-793.

Addessi, D., Ciampi, V. (2007). "A regularized force‐based beam element with a damage‐plastic section constitutive law." *International Journal of Numerical Methods in Engineering*, 70 (5), 610-629.

AIJ. (1996). "Japanese Architectural Standard Specification JASS 6 Steel Work." *Architectural Institute of Japan*, Tokyo, Japan. (in Japanese)

AIJ (2007). "Spectral response and performance for long period seismic ground motions." *Architectural Institute of Japan*, Tokyo, Japan. (in Japanese)

AISC (2010a). "Prequalied Connections for Special and Intermediate Steel Moment Frames for Seismic Applications." *ANSI/AISC 358-10*. American Institute for Steel Construction, Chicago, IL, USA.

AISC (2010b). "Seismic Provisions for Structural Steel Buildings." *ANSI/AISC 341-10*. American Institute for Steel Construction, Chicago, IL, USA.

AISC. (2010c). "Specification for structural steel buildings." A*NSI/AISC 360-10*. American Institute for Steel Construction, Chicago, IL, USA.

AISC (2016a). "Prequalied Connections for Special and Intermediate Steel Moment Frames for Seismic Applications." *ANSI/AISC 358-16* American Institute for Steel Construction, Chicago, IL, USA.

AISC (2016b). "Seismic Provisions for Structural Steel Buildings." *ANSI/AISC 341-16*. American Institute for Steel Construction, Chicago, IL, USA.

Akiyama, H., Takahashi, M. (1990). "Influence of Bauschinger Effect on Seismic Resistance of Steel Structures." *Journal of Structural and Construction Engineering*, 418, 49-57. (in Japanese)

Akiyama, H., Kuwamura, H., Yamada, S., Chiu, J., Kikukawa, S. (1992). "Effects of Manufacturing Process on Ultimate Behaviors of Box-Shaped Steel Members." *Journal of Structural Engineering*, Vol. 38B, 399-410. (in Japanese)

Alavi, B., and Krawinkler, H. (2001). "Effects of near-fault ground motions on frame structures." *John A. Blume Earthquake Engineering Center Report*, No. 138, Stanford University.

Alavi, B., and Krawinkler, H. (2004). "Behavior of moment-resisting frame structures subjected to near-fault ground motions." *Earthquake Engineering & Structural Dynamics*, 33(6), 687–706.

Arias, A. (1970). "A measure of earthquake intensity." In: Seismic design for nuclear power plants, edited by Hansen R. J., MIT Press, Cambridge MA, 438-483.

Arita, M., Takeuchi, I., Nikaido, M., Maeda, S., Ito, H. (2015). "Structural Performance of Cold Press Formed Rectangular Hollow Section using 550N/mm^2 Strength Steel (Part 2: Bending Test)." *Summaries of Technical Papers of Annual Meeting Architectural Institute of Japan*, Structure III, 941-942. (in Japanese)

Armstrong, P. J., and Frederick, C. O. (1966). "A mathematical representation of the multiaxial bauschinger effect." *Technical Report*, Berkeley Nuclear Laboratories, Berkeley, California, USA.

ASCE (2005). "Minimum Design Loads For Buildings and Other Structures." A*SCE/SEI 7-05*. American Society of Civil Engineering, Reston, VA, USA.

ASCE (2010). "Minimum Design Loads For Buildings and Other Structures." A*SCE/SEI 7-10*. American Society of Civil Engineering, Reston, VA, USA.

ASCE (2017a). "Minimum Design Loads For Buildings and Other Structures." A*SCE/SEI 7-16*. American Society of Civil Engineers, Reston, VA, USA.

ASCE (2017b). "Seismic Evaluation and Retrofit of Existing Buildings." *ASCE/SEI 41-17*, American Society of Civil Engineers, Reston, VA, USA.

ASTM (2009). "ASTM E8/E8M-09 Standard Test Methods for Tension Testing of Metallic Materials." ASTM International, West Conshohocken, PA, USA.

ASTM (2018). "ASTM A500/A500M-18 Specification for Cold-Formed Welded and Seamless Carbon Steel Structural Tubing in Rounds and Shapes." ASTM International, West Conshohocken, PA, USA.

ATC (1992). "Guidelines for Cyclic Seismic Testing of Components of Steel Structures for Buildings." *Report No. ATC-24*, Applied Technology Council, Redwood City, CA, USA.

AWS (2010). "AWS D1.1/D1.1M:2010 Structural Welding Code- Steel." American Welding Society, Miami, FL, USA.

Bai, Y., Kawano, A., Odawara, K., Matsuo, S. (2012). "Constitutive Models for Hollow Steel Tubes and Concrete Filled Steel Tubes Considering the Strength Deterioration." *Journal of Structural and Constructional Engineering*, 677 (77), 1141-1150.

Bai, Y., and Lin, X. (2015). "Numerical simulation on seismic collapse of thin-walled steel moment frames considering post local buckling behavior." *Thin-Walled Structures*, 94, 424–434.

Bai, Y., Lin, X., Mou, B. (2016). "Numerical Modeling on Post-Local Buckling Behavior of Circular and Square Concrete-Filled Steel Tubular Beam Columns." *International Journal of Steel Structures*, 16 (2), 531-546.

Baker, J. W. (2011). "Conditional Mean Spectrum: Tool for ground motion selection." *Journal of Structural Engineering*, 137(3), 322–331.

Bažant, Z. P. (2000). "Structural stability." *International Journal of Solids and Structures*, 37(1), 55–67.

BCJ (1997). "Structural Provisions for Building Structures (1997 Edition)." Building Center of Japan, Tokyo, Japan (in Japanese)

BCJ (2010). "The Building Standard Law of Japan."Building Center of Japan, Tokyo, Japan (in Japanese)

BCJ (2014). "The Building Standard Law of Japan."Building Center of Japan, Tokyo, Japan (in Japanese)

Black, R. G., Wenger, W. A., Popov. W. A. (1980). "Inelastic Buckling of Steel Struts under Cyclic Load Reversals." Earthquake Engineering Research Center, Berkeley, California, USA.

Boore, D. M. (2005). "On Pads and Filters: Processing Strong-Motion Data." *Bulletin of the Seismological Society of America*, 95(2), 745–750.

Boore, D., and Boomer, J. (2005), "Processinig of strong-motion accelerograms: needs, options and consequences." *Soil Dynamics and Earthquake Engineering*, 25 (2), 93-115.

CESMD (2013). Center for Engineering Strong Motion Data. [online] Available at: <http://www.strongmotioncenter.org/> [Accessed on November 6, 2017].

Chandramohan, R., Baker, J. W., and Deierlein, G. G. (2016). "Quantifying the Influence of Ground Motion Duration on Structural Collapse Capacity Using Spectrally Equivalent Records." *Earthquake Spectra*, 32 (2), 927-950.

Chen, X., Han, X., Cheang, J., Lin, S., Mao, G. (2008). "Dynamic Inelastic Numerical Simulation for a Shaking Table Test of a Full Scale Steel Moment Frame Structure based on OpenSEES." *The 14th World Conference on Earthquake Engineering (14WCEE)*, Beijing, China.

Cheng, X., Chen, Y. and Pan, L. (2013). "Experimental Study on Steel Beam-Columns Composed of Slender H-Sections under Cyclic Bending." *Journal of Constructional Steel Research*, 88, 279-288.

Chiou, B., Darragh, R., Gregor, N., and Silva, W. (2008). "NGA Project Strong-Motion Database." *Earthquake Spectra*, 24(1), 23–44.

Chiu, J. C., Yamada, S., Kuwamura, H., Akiyama, H. (1992). "A Research on the Ability of Cold Forming Box-Shaped Steel Members 1. Stub Column Test." *Summaries of Technical Papers of Annual Meeting Architectural Institute of Japan*, C, Structure II, 1275-1276. (in Japanese)

Christopoulos, C., Pampanin, S., Priestley, M. J. (2003). "Performance-Based Seismic Response of Frame Structures including Residual Deformations. Part I: Single-Degree-of-Freedom Systems." *Journal of Earthquake Engineering*, 7 (1), 97-118.

Chung, Y., Nagae, T., Hitaka, T., and Nakashima, M. (2010) "Seismic resistance capacity of high-rise buildings subjected to long-period ground motions: E-Defense shaking table test." *Journal of Structural Engineering*, 136(6), 637–44.

Clark, P., Frank, K., Krawinkler, H., and Shaw, R. (1997). "Protocol for Fabrication, Inspection, Testing, and Documentation of Beam-Column Connection Tests and Other Experimental Specimens." *SAC Steel Project Background Document*, Report No. SAC/BD-97/02.

Clifton, C., Bruneau, M., MacRae, G., Leon, R. and Fussell, A. (2011). "Steel Structures Damage from the Christchurch Eqrthquake Series of 2010 and 2011." *Bulletin of the New Zealand Society for Earthquake Engineering*, 44 (4), 297-318.

Clough, R. W., Johnston, S. B. (1966). "Effect of stiffness degradation on earthquake ductility requirements." *Proceedings of Second Japan National Conference on Earthquake Engineering*, 227-232.

Coffin, L. F. J. (1954). “A study of the Effects of Cyclic Thermal Stresses on a Ductile Metal.” *Trans. ASME*, 76, 931–950.

Cornell, C. A., Krawinkler, H. (2000). "Progress and Challenges in Seismic Performance Assessment." *PEER Center News*, 3, 1-3.

CSA (2014). "Design of Steel Structures." *CAN/CSA S16-14*, Canadian Standards Association, Mississauga, ON, Canada.

Do, T. N., and Filippou, F. C. (2018). "A damage model for structures with degrading response." *Earthquake Engineering & Structural Dynamics*, 47(2), 311–332.

Dwyer, T. J., Galambos, T. V. (1965). "Plastic Behavior of Tubular Beams Columns." *Journal of the Structural Division*, 91 (4), 153-168.

Elkady, A., Lignos, D. G. (2014). "Modeling of the composite action in fully restrained beam-to-column connections: implications in the seismic design and collapse capacity of steel special moment frames" *Earthquake Engineering and Structural Dynamics*, 43 (4), 1935-1954.

Elkady, A., Lignos, D. G. (2015a). "Analytical investigation of the cyclic behavior and plastic hinge formation in deep wide-flange steel beam-columns." *Bulletin of Earthquake Engineering*, 13 (4), 1097-1118.

Elkady, A., Lignos, D. G. (2015b). "Effect of gravity framing on the overstrength and collapse capacity of steel frame buildings with perimeter special moment frames." *Earthquake Engineering and Structural Dynamics*, 44 (8), 1289-1307.

Elkady, A., Lignos, D. G. (2016). "Dynamic Stability of Deep and Slender Wide-Flange Steel Columns – Full Scale Experiments." *Proceedings of the Annual Stability Conference*, Ontario, Florida, USA.

Elkady, A., Lignos, D. G. (2017). "Full-Scale Cyclic Testing of Deep Slender Wide-Flange Steel Beam-Columns under Unidirectional and Bidirectional Lateral Drift Demands." *16th World Conference on Earthquake Engineering (16WCEE)*, Santiago, Chile.

Elkady, A., Lignos, D. G. (2018a). "Full-Scale Testing of Deep Wide-Flange Steel Columns under Multiaxis Cyclic Loading: Loading Sequence, Boundary Effects, and Lateral Stability Bracing Force Demands." *Journal of Structural Engineering*, 144 (2), 04017189.

Elkady, A., Lignos, D. G. (2018b). "Improved Seismic Design and Nonlinear Modeling Recommendations for Wide-Flange Steel Columns." *Journal of Structural Engineering*, 144 (9), 04018162.

Erochko, J., Christopoulos, C., Tremblay, R., Choi, H. (2011). "Residual Drift Response of SMRFs and BRB Frames in Steel Buildings Designed according to ASCE 7-05." *Journal of Structural Engineering*, 137 (5), 589-599.

Fadden, M., McCormick, J. (2012). "Cyclic Quasi-Static Testing of Hollow Structural Section Beam Members." *Journal of Structural Engineering*, 138 (5), 561-570.

Fadden, M., McCormick, J. (2014). "Finite Element Model of the Cyclic Bending Behavior of Hollow Structural Sections." *Journal of Constructional Steel Research*, 94, 64-75.

Farahi, M., and Erfani, S. (2017). "Developing Representative Dual Loading Protocols for the Columns of Steel Special Moment Frames based on the Seismic Demands on These Members." *Journal of Earthquake Engineering*, 21, 1283-1304.

FEMA (2009). "Quantification of Building Seismic Performance Factors", *FEMA-P695*. Federal Emergency Management Agency, Washington, DC.

FEMA (2012). "Seismic Performance Assessment of Buildings." *FEMA P-58*, prepared by the Applied Technology Council, for the Federal Emergency Management Agency, Washington D. C., USA.

Filippou, F. C., Popov, E. P., Bertero, V. V. (1983). "Effects of Bond Deterioration on Hysteretic Behavior of Reinforced Concrete Joints." *Report EERC 83-19*, Earthquake Engineering Research Center, University of California, Berkeley, USA.

Fogarty, J., El-Tawil, S. (2016). "Collapse Resistance of Steel Columns under Combined Axial and Lateral Loading." *Journal of Structural Engineering*, 142 (1), 04015091.

Fogarty, J., Wu, T. Y., El-Tawil, S. (2017). "Collapse Response and Design of Deep Steel Columns Subjected to Lateral Displacement." *Journal of Structural Engineering*, 143 (9), 04017130.

Foschaar, J. C., Baker, J. W., and Deierlein, G. G. (2011). "Preliminary Assessment of Ground Motion Duration Effects on Structural Collapse." *15th World Conference on Earthquake Engineering (15WCEE)*, Lisbon, Portugal.

Galasso, C., Stillmaker, K., Eltit, C., and Kanvinde, A. (2015). "Probabilistic demand and fragility assessment of welded column splices in steel moment frames." *Earthquake Engineering & Structural Dynamics*, 44(11), 1823–1840.

Gupta, A., Krawinkler, H. (1999). "Prediction of seismic demands for SMRFs with ductile connections and elements." SAC Background Report, SAC/BD-99/06.

Gupta, A., and Krawinkler, H. (2000). "Behavior of ductile SMRFs at various seismic hazard levels." *Journal of Structural Engineering*, 126(1), 98–107.

Hall, J. F., Challa, V. R. M. (1995). "Beam-Column Modeling." *Journal of Engineering Mechanics*, 121 (12), 1284-1291.

Hancock, J. and Bommer, J. J. (2007). "Using spectral matched records to explore the influence of strong-motion duration on inelastic structural response." *Soil Dynamics and Earthquake Engineering*, 27(4), 291–299.

Hartloper, A., and Lignos, D. G. (2017). "Updates to the ASCE-41-13 Provisions for the Nonlinear Modeling of Steel Wide-Flange Columns for Performance-Based Earthquake Engineering." *Eurosteel 2017*, Copenhagen, Denmark.

Hasegawa, T., Takahashi, K., Seki, M., Nagao, T., Mukai, Y., Fukuda, K. (1998). "Comparison between seismic performance of U.S. steel perimeter and Japanese spatial moment resisting frames (Part1-3)." *Summaries of Technical Papers of the Annual Meeting of AIJ*, 903-908. (in Japanese)

Haselton, C. B., Baker, J. W., Stewart, J. P., Whittaker, A. S., Luco, N., Fry, A., Hamburger, R. O., Zimmerman, R. B., Hooper, J. D., Charney, F. A., and Pekelnicky, R. G. (2017). "Response history analysis for the design of new buildings in the NEHRP provisions and ASCE/SEI 7 standard: Part I - overview and specification of ground motions." *Earthquake Spectra*, 33(2), 373–395.

Hwang and Lignos (2017a). "Effect of Modeling Assumptions on the Earthquake-Induced Losses and Collapse Risk of Steel-Frame Buildings with Special Concentrically Braced Frames." *Journal of Structural Engineering*, 143 (9), 04017116.

Hwang and Lignos (2017b). "Earthquake-induced loss assessment of steel frame buildings with special moment frames designed in highly seismic regions." *Earthquake Engineering and Structural Dynamic*s, 46(13), 2141-2162.

Ibarra, L. F., Medina, R. A., and Krawinkler, H. (2002). "Collapse assessment of deteriorating SDOF systems." 12*th European Conference on Earthquake Engineering*, London, UK.

Ibarra, L. F., and Krawinkler, H. (2005). "Global Collapse of Frame Structures Under Seismic Excitations", *John A. Blume Earthquake Engineering Center Report*, No. 152, Stanford University.

Ibarra L. F., Medina R. A., Krawinkler H., (2005). "Hysteretic models that incorporate strength and stiffness deterioration." *Earthquake Engineering and Structural Dynamic*s, 34(12), 1489-1511.

Inamasu, H., Lignos, D. G., Kanvinde, A. (2017). "Effect of Column Base Flexibility on the Hysteretic Response of Wide Flange Steel Columns." *3rd Huixian International Forum on Earthquake Engineering for Young Researchers*, University of Illinois, Urbana-Champaign, USA.

Inoue, K., Higashi, K., Ogawa, K., Tada, M., Hasegawa, T. (1995). "Earthquake response of structural members of rigid frames with RHS columns (Part 1-3)." *Summaries of Technical Papers of the Annual Meeting of AIJ*, 269-274. (in Japanese)

Inoue, K., and Suita, K. (2008). "Additional Bending Moment of Columns due to the P-Δ Effect." *Summaries of Technical Papers of Annual Meeting Architectural Institute of Japan*, Structure III, 759-760. (in Japanese)

Ishida, T., Yamada, S., Shimada, Y. (2012). "Bi-axial Bending Behavior of RHS-columns Including Post-buckling and Deterioration Range." *15th World Conference on Earthquake Engineering (15WCEE)*, Lisbon, Portugal.

Ishida, T., Yamada, S., Shimada, Y. (2013). "Analytical Model of RHS Columns under Random Bi-Directional Horizontal Forces." *Journal of Structural and Constructional Engineering*, 691 (78), 1631-1340. (in Japanese)

Ishida, T., Yamada, S., Shimada, Y. (2014). "Simulation Model of Hysteretic Behavior of RHS Columns under Bi-Directional Horizontal Forces and Vibrate Axial Force." *Journal of Structural and Constructional Engineering*, 699 (79), 641-650. (in Japanese)

Iwan, W. D. (1966). "A distributed-element model for hysteresis and its steady-state dynamic response." *Journal of Applied Mechanics*, 33(42), 893–900.

Ji, H., Kanaya, H., Tabuchi, M. (1985). "A Study on the Behavior of RHS-Column to Beam Connections (Part 3 Effect of Residual Stress of RHS columns)." *Report of AIJ Kinki Branch Meeting*, 473-476. (in Japanese)

Jiao, Y., Kishiki, S., Yamada, S. (2012). "Loading protocols employed in evaluation of seismic behavior of steel beams in weak-beam moment frames." *15th World Conference on Earthquake Engineering (15WCEE)*, Lisbon, Portugal.

JIS (2015). "JIS G 3106 Rolled Steels for Welded Structure." Japanese Industrial Standards Committee, Tokyo, Japan. (in Japanese)

JIS (2016). "JIS G 3466 Carbon Steel Square and Rectangular Tubes for General Structure." Japanese Industrial Standards Committee, Tokyo, Japan.

JISF (2008a). "MDCR0002-2008 Cold Roll-Formed Steel Square Tube for Building Structure." JISF Standard, Tokyo, Japan. (in Japanese)

JISF (2008b). "MDCR0003-2008 Cold Press-Formed Steel Square Tube for Building Structure." JISF Standard , Tokyo, Japan. (in Japanese)

JISF/BRI (2002). "Testing Methods for Evaluation of Structural Performance for Steel Structures." prepared by Japan Iron and Steel Federation (JISF) and Building Center of Japan (BRI). (in Japanese)

Kadono, A., Sasaki, M., Okamoto, K., Akiyama, H., Matsui, C., Inoue, K. (1994). "Experimental study on the effect of yield ratio on the bending strength increasing ration and the ductility of steel structures' members." *Journal of Structural Engineering*, 40B, 673-682. (in Japanese)

Kanno, R. (2016). "Advances in steel materials for innovative and elegant steel structures in Japan – A review." *Structural Engineering International*, 26(3), 242-253.

Kasai, K., Nam. T. T., Maison, B. F. (2016). "Structural collapse correlative analysis using phenomenological fiber hinge elements to simulate two-directional column deteriorations." *Earthquake Engineering and Structural Dynamic*s, 45 (10), 1581-1601.

Katayama, T., Kamura, H., Okamoto, H., Nakamura, N., Inosako, T., Hirano, O. (2002). "Structural Performance of 590N/mm^2 Cold Press-Formed Rectangular Column Part 2. Bending Test." *Summaries of Technical Papers of Annual Meeting Architectural Institute of Japan*, Structure III, 541-542. (in Japanese)

Kato, B., Akiyama, H., Kitazawa, S. (1978). "Deformation Characteristics of Box-Shaped Steel Members Influenced by Local Buckling." *Journal of Structural and Construction Engineering*, 268, 71-76. (in Japanese)

Kato, B., Nishiyama, I. (1980). "Local Buckling Strength and Deformation Capacity of Cold-Formed Steel Rectangular Hollow Section." *Journal of Structural and Construction Engineering*, 294, 45-52. (in Japanese)

Kato, B., Aoki, H., Kurosawa, T. (1988). "Plastic Strain History and Residual Stresses Locked in Cold-Formed Square Steel Tubes." *Journal of Structural and Construction Engineering*, 385, 39-48. (in Japanese)

Kawano, A., Matsui, C., Nakajima, T., Takagi, J. (1996). "Experimental Study on Buckling Behavior and Dissipated Energy of Concrete-Filled Tubular Members under Cyclic Axial Load." *Journal of Structural and Constructional Engineering*, 482, 131-140. (in Japanese)

Kawashima, Y., Nishimura, M. (1973). "Study on buckling strength of steel hollow square sections (Effect of welding and cold forming)." *Summaries of Technical Papers of Annual Meeting, 1007-1008*.

Kido, Y., Yamada, S., Kuwamura, H., Akiyama, H., Kadono, A. (1992). "Stub-Column Test Focused on Material Properties (Part 1. Coupon Test and Box-Shaped Stub-Column Test)." *Summaries of Technical Papers of Annual Meeting Architectural Institute of Japan*, C, Structure II, 1245-1246. (in Japanese)

Korol, R. R., Huboda, J. (1972). "Plastic Behavior of Hollow Structural Sections." *Journal of the Structural Division*, 98 (5), 1007-1023.

Krawinkler, H., Zohrei, M. (1983). "Cumulative damage in steel structures subjected to earthquake ground motions." *Computers & Structures*, 16(1–4), 531–541.

Krawinkler, H., Zohrei, M., Irvani, B. L., Cofie, N., and Tamjed, H. H. (1983). "Recommendation for experimental studies on the seismic behavior of steel components and materials." *John A. Blume Earthquake Engineering Center Report*, No. 61, Stanford University.

Krawinkler, H. (1996). "Cyclic Loading Histories for Seismic Experimentation on Structural Components." *Earthquake Spectra*, 12 (1), 1-12.

Krawinkler, H., Gupta, A., Medina, R., Luco, N. (2000). "Development of loading histories for testing of steel beam-to-column assemblies." *SAC Steel Project Background Document*, Report No. SAC/BD-00/10.

Krawinkler, H., Parisi, F., Ibarra, L., Ayoub, A., and Medina, R. (2001). "Development of a testing protocol for wood frame structures." *CUREE-Caltech Woodframe Project*, No. W-02, Stanford University, CA, USA.

Krawinkler, H. (2009). "Loading Histories for Cyclic Tests in Support of Performance Assessment of Structural Components". *Proceedings of The 3rd International Conference on Advances in Experimental Structural Engineering*. 15-16.

Krishnan, S. (2010). "Modified elastofiber element for steel slender column and brace modeling." *Journal of Structural Engineering*, 136(11), 1350–1366.

Kurata, M., Nakashima, M., Suita, K. (2005a). "Effect of Column Base Behavior on the Seismic Response of Steel Moment Frames." *Journal of Earthquake Engineering*, 9 (2), 415-438.

Kurata, M., Nakashima, M., Suita, K. (2005b). "Test on Large Cyclic Deformation of Steel Tube Columns Having Fixed Column Bases." *Journal of Structural and Construction Engineering*, 598, 149-154. (in Japanese)

Kurata, M., Kanao, I., Liu, D., Nakashima, M. (2007). "Effects of Local Buckling on Deformation Capacity of Steel Box Columns Subjected Cyclic Loading." *Journal of Structural and Construction Engineering*, 613, 155-161. (in Japanese)

Kuwada, R., Koetaka, Y., Suita, K. (2013). "Cyclic Loading Tests of Steel Tube Columns Subjected to Varying Axial Force and Bi-axial Bending Moment." *Summaries of Technical Papers of Annual Meeting Architectural Institute of Japan*, Structure III, 1153-1154. (in Japanese)

Kuwada, R., Koetaka, Y., Suita, K. (2015). "Plastic Deformation Capacity of Cold Press-Formed SHS Columns Determined by Local Buckling and Fracture." *Journal of Structural and Construction Engineering*, Vol. 80, No. 718, 1961-1970. (in Japanese)

Kuwamura, H., Suzuki, T. (1988). "Effect of Stress-Strain Characteristics on the Behavior of Steel Stub-Columns (Part 2. Box Section)." *Summaries of Technical Papers of Annual Meeting Architectural Institute of Japan*, C, Structure II, 1101-1102. (in Japanese)

Kuwamura, H., Akiyama, H., Yamada, S., Chiu, J. C. (1993a). "Experiment on the Mechanical Properties and Their Improvement of Cold Press-Formed Steel Columns." *Journal of Structural and Construction Engineering*, 444, 125-133. (in Japanese)

Kuwamura, H., Chiu, J. C., Akiyama, H. (1993b). "Experiment on the Mechanical Properties and Their Improvement of Cold Roll-Formed Steel Columns." *Journal of Structural and Construction Engineering*, 453, 171-180. (in Japanese)

Kuwamura, H. (1994). "Mechanical Properties of Cold-Formed Steel Square Pipes in Building Structures." *Steel Construction Engineering*, 1 (3), 171-185. (in Japanese)

Lai, S. S., Will, G. T., Otani, S. (1984). "Model for Inelastic Biaxial Bending of Concrete Members." *Journal of Structural and Engineering*, 110 (11), 2563-2584.

Lamarche, C.-P., and Tremblay, R. (2011). "Seismically induced cyclic buckling of steel columns including residual-stress and strain-rate effects." *Journal of Constructional Steel Research*, 67(9), 1401–1410.

LATBSDC. (2017). "An alternative procedure for seismic analysis and design of tall buildings located in the Los Angeles region, 2017 Edition." Los Angeles Tall Building Structural Design Council.

Lignos, D. G. (2008). "Sidesway Collapse of Deteriorating Structural Systems under Seismic Excitations." *Ph.D. dissertation*, Stanford University, CA, USA.

Lignos, D. G., Krawinkler, H. (2010). "A steel Database for Component Deterioration of Tubular Hollow Square Steel Columns under Varying Axial Load for Collapse Assessment of Steel Structures under Earthquakes." *Joint Conference Proceedings of 7th International Conference on Urban Earthquake Engineering (7CUEE) & 5th International Conference on Earthquake Engineering (5ICEE)*, Tokyo, Japan.

Lignos, D. G., Krawinkler, H. (2011). "Deterioration Modeling of Steel Components in Support of Collapse Prediction of Steel Moment Frames under Earthquake Loading." *Journal of Structural Engineering*, 137 (11), 1291-1302.

Lignos, D. G., Krawinkler, H., Whittaker, A., S. (2011). "Prediction and Validation of Sidesway Collapse of Two Scale Models of a 4-Story Steel Moment Frame." *Earthquake Engineering and Structural Dynamics*, 40 (7), 807-825.

Lignos, D. G., Krawinkler, H. (2012). "Sidesway Collapse of Deteriorating Structural Systems under Seismic Excitations." *John A. Blume Earthquake Engineering Center Report*, No. 177, Stanford University.

Lignos, D. G., Krawinkler, H. (2013). "Development and Utilization of Structural Component Databases for Performance-Based Earthquake Engineering." *Journal of Structural Engineering*, 139 (8), 1382-1394.

Lignos, D. G., Hikino, T., Matsuoka, Y., Nakashima, M. (2013). "Collapse Assessment of Steel Moment Frames Based on E-Defense Full-Scale Shake Table Collapse Tests." *Journal of Structural Engineering*, 139 (1), 120-132.

Lignos, D. G., Suzuki, Y. (2013). "Annual report of collapse assessment of steel moment resisting frames designed with high yield ratio steel columns." Technical report at McGill University, McGill University.

Lignos, D. G., Putman, C., and Krawinkler, H. (2015). "Application of Simplified Analysis Procedures for Performance-Based Earthquake Evaluation of Steel Special Moment Frames." *Earthquake Spectra*, 31(4), 1949–1968.

Lignos, D. G., Cravero, J., and Elkady, A. (2016). "Experimental investigation of the hysteretic behavior of wide-flange steel columns under high axial load and lateral drifts demands." *11th Pacific Structural Steel Conference*, Shanghai, China.

Ma, X., Krawinkler, H., Deierlein, G. G. (2011). "Seismic design and behavior of self-centering braced frame with controlled rocking and energy dissipating fuses." *John A. Blume Earthquake Engineering Center Report*, No. 174, Stanford University.

MacRae, G. A., Carr, A. J. and Walpole, W. R. (1990). "The Seismic Response of Steel Frames." *Report No. 90-6*. Department of Civil Engineering, University of Canterbury, Canterbury, New Zealand.

MacRae, G. A., Kawashima, K. (1997). "Post-Earthquake Residual Displacements of Bilinear Oscillators." *Earthquake Engineering and Structural Dynamics*, 26, 701-716.

MacRae, G. A., Kimura, Y., Roader, C. (2004). "Effect of Column Stiffness on Braced Frame Seismic Behavior." *Journal of Structural Engineering*, 130 (3), 381-391.

MacRae, G. A., Urmson, C. R., Walpole, W. R., Hyde, K., Clifton, C. (2009). "Axial Shortening of Steel Columns in Buildings Subjected to Earthquakes." *Bulletin of New Zealand Society for Earthquake Engineering*, 42 (4), 275-287.

Maison, B. F., Popov, E. P. (1980). "Cyclic Response Prediction for Braced Steel Frames." *Journal of the Structural Division*, 106, 1401-1416.

Mahin, S. A., Bertero, V. V. (1976). "Nonlinear Seismic Response of a Coupled Wall System." *Journal of the Structural Division*, 102 (9), 1759-1780.

Maki, M., Furuhara, T., Tsuji, N., Morito, S., Miyamoto, G., Shibata, A. (2014). "Thermomechanical Processing of Steel - Past, Present and Future-." *Tetsu-to-Hagane*, 100 (9), 1062-1075. (in Japanese)

Manson, S. S. (1954). "Behavior of Materials Under Conditions of Thermal Stress." *NACA Technical Report 1170*, Lewis Flight Propulsion Laboratory, Cleveland, OH, USA.

Mavroeidis, G. P., and Papageorgiou, A. S. (2003). "A Mathematical Representation of Near-Fault Ground Motions." *Bulletin of the Seismological Society of America*, 93(3), 1099–1131.

McKenna F. T. (1997). "Object-oriented finite element analysis: Frameworks for analysis, algorithms and parallel computing." PhD dissertation, University of California, Berkeley, CA, USA.

Medina, R. A., Krawinkler, H. (2003). "Seismic Demands for Nondeteriorating Frame Structures and Their Dependence on Ground Motions." *John A. Blume Earthquake Engineering Center Report*, No. 144, Stanford University.

Menegotto, M., Pinto, P. E. (1973). "Method of analysis for cyclically loaded R.C. plane frames including changes in geometry and non-elastic behaviour of elements under combined normal force and bending." *Preliminary Report IABSE*, Vol. 13.

Mergos, P., E., Beyer, K. (2014). "Loading protocols for European regions of low to moderate seismicity." *Bulletin of Earthquake Engineering*, 13 (4), 1097-1118.

Miner, M. A. (1945). "Cumulative damage in fatigue." *Journal of Applied Mechanics*, 12(3), A159–A164.

Mostaghel, N. (1999). "Analytical description of pinching, degrading hysteretic systems." *Journal of Engineering Mechanics*, 125(2), 216–224.

Mukaide, S., Oku, N., Matsuo, K., Tada, M. (2016). "Loading Test in the range of Large Deformation for RHS Columns with Different Manufacturing Process." *Steel Construction Engineering*, 23 (90), 51-64. (in Japanese)

Nakagawa, K., Kamura, H., Hirano, O., Fujisawa, K., Murakami, Y. (2008). "Experimental Study on Deformation Capacity of 550N/mm^2 Class Cold Press Formed Square Steel Pipes." *Summaries of Technical Papers of Annual Meeting Architectural Institute of Japan*, Structure III, 549-550. (in Japanese)

Nakagawa, K., Matsui, K., Oki, K., Omori, A., Kamura, H. (2013). "High-Performance 550N/mm^2 grade Press Formed Square Steel Pipes for Building Structure (Part 2)." *Summaries of Technical Papers of Annual Meeting Architectural Institute of Japan*, Structure III, 1201-1202. (in Japanese)

Nakagawa, H., Sato, Y., Okada, T. (2014). "Structural Performance of Cold-forming Hollow Section using 490N/mm^2 Steel (Part 1: Bending Test)." *Summaries of Technical Papers of Annual Meeting Architectural Institute of Japan*, Structure III, 965-966. (in Japanese)

Nakajima, Y., Fukuda, K., Ichinohe, Y. (2009). "Plastic Deformation of High Strength 590N/mm^2 Cold Press-Formed Rectangular Column." *Summaries of Technical Papers of Annual Meeting Architectural Institute of Japan*, Structure III, 653-654. (in Japanese)

Nakashima, M., Inoue, K., and Tada, M. (1998). "Classification of damage to steel buildings observed in the 1995 Hyogoken-Nanbu earthquake." *Engineering Structures*, 20 (4-6), 271-281.

Nakashima, M., Roeder, C., W., and Maruoka, Y. (2000). "Steel Moment Frames for Earthquakes in United States and Japan." *Journal of Structural Engineering*, 126(8), 861–868.

Nakashima, M., Sawaizumi, S. (2000). "Column-to-Beam Strength Ratio Required for Ensuring Beam-Collapse Mechanisms in Earthquake Reponses of Steel Moment Frames." *12th World Conference on Earthquake Engineering (12WCEE)*, Auckland, New Zealand.

Nakashima, M., Liu, D. (2005). "Instability and Complete Failure of Steel Columns Subjected to Cyclic Loading." *Journal of Engineering Mechanics*, 131 (6), 559-567.

Nakashima, M., Suita, K., Takahashi, M., Nishiyama, M., Katsumata, H., Kajiwara, K., and Koshika, N. (2013). “Quantification of collapse margin of steel high-rise buildings (Part 1).” *Summaries of Technical Papers of Annual Meeting Architectural Institute of Japan*, Structure III, 967-968. (in Japanese)

Neuenhofer, A., Filippou, F. C. (1997). "Evaluation of Nonlinear Frame Finite-Element Models." *Journal of Structural Engineering*, 123 (7), 958-966.

Newell, J. D., Uang, C. M. (2008). "Cyclic Behavior of Steel Wide-Flange Columns Subjected to Large Drift." *Journal of Structural Engineering*, 134 (8), 1334-1342.

Nishioka, K., Ichikawa, K., (2012). "Progress in thermomechanical control of steel plates and their commercialization." *Science and Technology of Advanced Materials*, 13, 1–20.

NIST (2010a). "Evaluation of the FEMA P695 methadology for quantification of building seismic performance factors." NIST GCR 10-917-5, produced by the NEHRP Consultants Joint Venture, a partnership of the Applied Technology Council and the Consortium of Universities for Research in Earthquake Engineering, for the National Institute of Standards and Technology.

NIST (2010b). "Nonlinear structural analysis for seismic design." *NEHRP Seismic Design Technical Brief No. 4*, NIST GCR 10-917-5, produced by the NEHRP Consultants Joint Venture, a partnership of the Applied Technology Council and the Consortium of Universities for Research in Earthquake Engineering, for the National Institute of Standards and Technology.

NIST (2017). "Guidelines for Nonlinear Structural Analysis for Design of Buildings Part I - General." produced by the Applied Technology Council, for the National Institute of Standards and Technology, NIST GCR 17-917-46v1.

Ohashi, M., Yamaguchi, T., Kuwamura, H. (1990). "Development of new steel plates for building use." *Nippon Steel Technical Report*, No. 44. (in Japanese)

Okazaki, T., Lignos, D. G., Midorikawa, M., Ricles, J. M. and Love, J. (2013). "Damage to Steel Buildings Observed after the 2011 Tohoku-Oki Earthquake." *Earthquake Spectra*, 29 (S1), S219-S243.

Ozkula, G., Harris, J., Unang, C. M. (2017). "Observations from Cyclic Tests on Deep, Wide-Flange Beam-Columns." *Engineering Journal*, 1, 45-59.

Pampanin, S., Christopoulos, C., Priestley, M. J. (2003). "Performance-Based Seismic Response of Frame Structures including Residual Deformations. Part II: Multi-Degree-of-Freedom Systems." *Journal of Earthquake Engineering*, 7 (1), 119-147.

PEER (2013). Pacifc Earthquake Engineering Research Center (PEER) NGA Database. [online] Available at: <http://peer.berkeley.edu/nga/> [Accessed on September 2013].

PEER/ATC (2010). "Modeling and Acceptance Criteria for Seismic Design and Analysis of Tall Buildings." *PEER/ATC 72-1*, Prepared for Pacific Earthquake Engineering Research Center (PEER) by Applied Technology Council (ATC), Redwood City, CA, USA.

Ramirez, C. M., Miranda, E. (2012) "Significance of residual drifts in building earthquake loss estimation." *Earthquake Engineering and Structural Dynamics*, 41, 1477-1493.

Ribeiro, F. L. A., Barbosa, A. R., Scott, M. H., Neves, L. C. (2015). "Deterioration Modeling of Steel Moment Resisting Frames Using Finite-Length Plastic Hinge Force-Based Beam-Column Elements." *Journal of Structural Engineering*, 141 (2), 04014112.

Rice, J. R., Tracey, D. M. (1969). "On the ductile enlargement of voids in triaxial stress fields." *Journal of the Mechanics and Physics of Solids*, 17 (3), 201-217.

Richards, P.W., Uang C. M. (2006). "Testing Protocol for Short Links in Eccentrically Braced Frames." *Journal of Structural Engineering*, 132(8), 1183-1191.

Roader, C. W., Schneider, S. P., Carpenter, J. E. (1993). "Seismic Behavior of Moment-Resisting Steel Frames: Analytical Study." *Journal of Structural Engineering*, 119 (6), 1866-1884.

Ruiz-Garcia, J., Miranda, E. (2005). "Performance-Based Assessment of Existing Structures Accounting for Residual Displacements." *John A. Blume Earthquake Engineering Center Report*, No. 153, Stanford University.

Ruiz-Garcia, J., Miranda, E. (2006). "Inelastic displacement ratios for evaluation of structures built on soft soil sites." *Earthquake Engineering and Structural Dynamics*, 35 (6), 679-694.

Sawaizumi, S., Yamaguchi, T., Arita, M., Suzuki, Y., Suzuki, T., Maeda, S. (2012). "Structural Performance of Cold Press Formed Rectangular Column using 550N/mm^2 High Strength Steel (Part 2: Bending Test)." *Summaries of Technical Papers of Annual Meeting Architectural Institute of Japan*, Structure III, 683-684. (in Japanese)

Scott, M. H., Fenves, G. L. (2016). "Plastic Hinge Integration Methods for Force-Based Beam-Column Elements." *Journal of Structural Engineering*, 132 (2), 244-252.

Shafei, B., Zareian, F. (2008). "Development of a Quasi-Static Loading Protocol for Displacement-Sensitive Nonstructural Building Components." *The 14th World Conference on Earthquake Engineering (14WCEE)*, Beijing, China.

Shaw, S. M., Stillmaker, K., Kanvinde, A. M. (2015). "Seismic Response of Partial-Joint-Penetration Welded Column Splices in Moment-Resisting Frames," *Engineering Journal*, Vol. 52, 87-108.

Sivaselvan, M., and Reinhorn, A. M. (2000). "Hysteretic models for deteriorating inelastic structures." *Journal of Engineering Mechanics*, 126(6), 633-640.

Sousa, A. C., Lignos, D. G. (2017). "On the Inverse Problem of Classic Nonlinear Plasticity Models-An application to cyclically loaded structural steels." Report No. 231968, Resilient Steel Structures Laboratory (RESSLab), Ecole polytechnique Fédérale de Lausanne (EPFL).

Spacone, E., Filippou, F. C., Taucer, F. F. (1996). "Fiber Beam-Column Model for Non-linear Analysis of R/C Frames: Part1. Formulation." *Earthquake Engineering and Structural Dynamic*s, 25 (7), 711-725.

Stillmaker, K., Kanvinde, A., and Galasso, C. (2015). "Fracture Mechanics-Based Design of Column Splices with Partial Joint Penetration Welds." *Journal of Structural Engineering*, 142(2), 04015115.

Stoakes, C. D., and Fahnestock, L. A. (2016). "Strong-Axis stability of wide flange steel columns in the presence of weak-axis flexure." *Journal of Structural Engineering*, 142(5), 04016004.

Suita, K., Yamada, S., Tada, M., Kasai, K., Matsuoka, Y. and Shimada, Y. (2008). "Collapse Experiment on 4-Story Steel Moment Frame: Part 2 Detail of Collapse Behavior." *The 14th World Conference on Earthquake Engineering (14WCEE)*, Beijing, China.

Suita, K., Suzuki, Y., Takahashi, M. (2015). "Collapse Behavior of an 18-Story Steel Moment Frame during a Shaking Table Test." *International Journal of High-Rise Buildings*, 4 (3), 171-180.

Suzuki, Y., Kubota, S., Yamaguchi, T., Suzuki, T. (2010). "Structural Performance of Cold Press Formed Rectangular Column using High Yield Strength Steel (Part 2: Bending Test)."

Summaries of Technical Papers of Annual Meeting Architectural Institute of Japan, C-1, Structure III, 917-918. (in Japanese)

Suzuki, Y., Suzuki, T., Kanno, R., Hanya, K., Yamaguchi, T. (2011). "Structural Performance of High Yield Strength Rectangular HSS Columns Subjected to Tensile Axial Force." *Journal of Constructional Steel*, 19, 677-684. (in Japanese)

Suzuki, Y., Lignos, D. G. (2015). "Large scale collapse experiments of wide flange steel beam-columns." *8th International Conference on Behavior of Steel Structures in Seismic Areas (STESSA)*, Shanghai, China.

Suzuki, Y., Lignos, D. G. (2017). "Collapse Behavior of Steel Columns as part of Steel Frame Buildings: Experimental and Numerical Models." *16th World Conference on Earthquake Engineering (16WCEE)*, Santiago, Chile.

Suzuki, Y., Lignos, D. G. (2018a). "Fiber-Based Model for Earthquake-Induced Collapse Simulation of Steel Frame Buildings." *11th U.S. National Conference on Earthquake Engineering (11WCEE)*, Los Angeles, USA.

Suzuki, Y., Lignos, D. G. (2018b). "Improving the Collapse Risk of Steel Structures with High-Performance Steel." *16th European Conference on Earthquake Engineering (16ECEE)*, Thessaloniki, Greece.

Suzuki, T., Sakai, S., Makiya, H., Kimura, K. (1980). "Experimental Study on Elasto-Plastic Behavior of Box-Section Column." *Summaries of Technical Papers of Annual Meeting Architectural Institute of Japan*, Structure, 1153-1154. (in Japanese)

Suzuki, T., Suzuki, Y., Yoshida, Y., Kubota, S., Shimura, Y., Nagata, M. (2008). "Development of structural steel for buildings with high yield ratio and high yield point leading innovative steel structural system." *Nippon Steel Technical Report*, No.97, 64-73. (in Japanese)

Suzuki, Y., Kubota, S., Yamaguchi, T., Suzuki, T. (2010). "Structural Performance of Cold Press Formed Rectangular Column using High Yield Strength Steel (Part 2: Bending Test)." *Summaries of Technical Papers of Annual Meeting Architectural Institute of Japan*, C-1, Structure III, 917-918. (in Japanese)

Tabuchi, M., Kanaya, H., Uemori, H. (1988). "Effect of Mechanical Properties of RHS Formed by Cold Rolling on the Behavior of RHS Members and Connections – Part 1: Mechanical Properties of RHS." *Summaries of Technical Papers of Annual Meeting Architectural Institute of Japan*, Structure II. 969-970. (in Japanese)

Tada, M., Tamai, H., Ohgami, K., Kuwahara, S., Horimoto, A. (2008). "Analytical simulation utilizing collaborative structural analysis system." *The 14th World Conference on Earthquake Engineering (14WCEE)*, Beijing, China.

Takanashi, K., Aburakawa, M., Hamaguchi, H., (2005). "Utilization of High Performance Steels in Urban Structures." *Fourth International Conference on Advances in Steel Structures*, Vol. 2, 1827-1834.

Takeda, T., Sozen, M., Nielsen, N. (1970). "Reinforced concrete response to simulated earthquakes." *Journal of the Structural Division*, 96 (12), 2557-2573.

Tanaka, T., Kanaya, H., Tabuchi, M., Kudo, H. (1993). "Experimental Study on the Mechanical Properties of Cold-Formed Heavy Square Hollow Section." *Report of AIJ Kinki Branch Meeting*, 153-156. (in Japanese)

Tremblay, R., Filiatrault, A., Timler, P., and Bruneau, M. (1995). "Performance of steel structures during the 1994 Northridge earthquake." *Canadian Journal of Civil Engineering*, 22(2), 338-360.

Trifunac, M.D., and Brady, A. G. (1975). "A Study on the Duration of Strong Earthquake Ground Motion", *Bulletin of the Seismological Society of America*, 65(3), 581–626.

Tsai, K. C., Hsiao, C. P., Bruneau. M. (2000). "Overview of Building Damages in 921 Chi-Chi earthquake." *Earthquake Engineering and Engineering Seismology*, 2(1), 93-108.

Tsuda, K., Matsui, C. (1988). "Strength of Square Steel Tubular Beam-Columns under Constant Vertical and Horizontal Loads." *Journal of Structural and Construction Engineering*, 512, 149-156. (in Japanese)

Uang, C. M., Ozkula, G. and Harris, J. (2015). "Observations from Cyclic Tests on Deep, Slender Wide-Flange Structural Steel Beam-Column Members." *Proceedings of The Annual Stability Conference*, Nashville, Tennessee, USA.

UBC (1988). "Uniform Design Code." International Conference of Building Officials, Whittier, CA, USA.

Uchida, Y., Mitani, I., Kadono, A. (1993). "Axial Load Ratio Limitation to Keep a Seismic Safety of Steel Beam Columns." *Journal of Structural and Constructional Engineering*, 454, 139-149. (in Japanese)

Vamvatsikos, D., and Cornell, C. A. (2002). "Incremental dynamic analysis." *Earthquake Engineering & Structural Dynamics*, 31(3), 491–514.

Vian, D., and Bruneau, M. (2003). "Tests to structural collapse of single degree of freedom frames subjected to earthquake excitations." *Journal of Structural Engineering*, 129(12), 1676–1685.

Voce, E. (1955). "A Practical strain hardening function." *Metallurgia*, 51, 219-226.

Wada, A., Connor, J. J., Kawai, H., Iwata, M., Watanabe, A. (1992). "Damage Tolerant Strucure." Fifth U.S.-Japan Workshop on the Improvement of Building Structural Design and Construction Practices, No.5, 1.1-1.13.

Wilkinson, T., Hancock, G. J. (1998). "Tests to Examine the Compact Web Slenderness of Cold-Formed RHS." *Journal of Structural Engineering*, 124 (10), 1166-1174.

Wu, T. Y., El-Tawil, S., McCormick, J. (2018). "Highly Ductile Limits for Deep Steel Columns." *Journal of Structural Engineering*, 144(4).

Yamada, S., Akiyama, H., Kuwamura, H. (1993). "Post-Buckling and Deteriorating Behavior of Box-Section Steel Members." *Journal of Structural and Construction Engineering*, 444, 135-143. (in Japanese)

Yamada, S., Akiyama, H., Kuwamura, H. (1994). "Ultimate Behavior of Box-Section Beam-Columns under Varying Axial Force." *Journal of Structural and Construction Engineering*, 461, 115-122. (in Japanese)

Yamada, S., Kishiki, S. (2004). "Simple Hysteresis Model of Steel for Damper Considering the Bauschinger Effect." *Journal of Structural and Construction Engineering*, 659 (75), 49-57. (in Japanese)

Yamada, S., Ishida, T., Shimada, Y. (2012). "Hysteretic Model of RHS Columns in the Deteriorating Range Governed by Local Buckling." *Journal of Structural and Construction Engineering*, 674 (77), 627-636. (in Japanese)

Yamada, S., Ishida, T., Jiao, Y. (2018). "Hysteretic Behavior of RHS Columns Under Random Cyclic Loading Considering Local Buckling." *International Journal of Steel Structures*, DOI: 10.1007/s13296-018-0087-x.

Yamazaki, S., Minami, S. (1999). "Experimental Study on Inelastic Behavior of Steel Beam-Columns Subject to Varying Axial Force and Cyclic Lateral Load." *Journal of Structural and Construction Engineering*, 519, 95-102. (in Japanese)

Yu, Y. J., Tsai, K. C., Weng, Y. T., Lin, B. Z., Lin, J. L. (2010). "Analytical studies of a full-scale steel building shaken to collapse." *Engineering Structures*, 32, 3418-3430.

Zareian, F., Medina, R. A. (2010). "A Practical Method for Proper Modeling of Structural Damping in Inelastic Plane Structural Systems." Computers & Structures, 88 (1), 45-53.

Zarger, S., Medina, R. A., Miranda, E. (2014). "Cyclic Behavior of Deep Steel Columns Subjected to Large Drifts, Rotations, and Axial Loads." *Tenth U.S. National Conference on Earthquake Engineering*, Anchorage, Alaska, USA.

Zhao, X. L., Hancock, G. J. (1992). "Square and Rectangular Hollow Sections Subject to Combined Actions." *Journal of Structural Engineering*, 118 (3), 648-668.

APPENDIX A: Summary of Steel Column Test Results

In this appendix a detailed description of steel HSS and wide flange column test results discussed in Chapter 5 is presented together with a comprehensive set of figures that show the deformed shape of the member.

A.1 H-27-M-C specimen

Figures A.1 and A.2 show global and local snapshots of H-27-M-C specimen that shows the progression of local buckling during testing, respectively. Figure A.3 shows photos of the post-test observation of the same specimen. The specimen H-27-M-C was tested under monotonic lateral loading protocol and constant axial load ratio P/P_y = -0.3 (i.e., P = -1083kN). The steel column buckled locally at around 1.5% rads of rotation. The same column lost its flexural capacity at about 15% rads. At this drift level the axial shortening of the steel column was about 1.5% of its length. The local buckling takes place on the compression side (i.e., North flange) of the steel column because the lateral loading is a monotonic one. The buckling mode has a half wavelength of 1.0D (D: HSS depth) and the buckling center is located at a height of 0.5D from the top surface of the base plate of the steel column. Once local buckling occurred, axial shortening also began to increase. While the lateral drift increased during the test, the buckling

wave progressed substantially (see Figure A.1e). Note that the south flange did not buckle during the test. Fracture and torsional deflection was not observed in this test, as shown in Figure A.3 that shows more focused images of the location of local buckling as well as the corner locations of the HSS column.

A.2 H-27-S-C specimen

Figures A.3 and A.4 show global and local snapshots of H-27-S-C specimen that shows the progression of local buckling during testing, respectively. Figure A.5 shows photos of the post-test observation of the same specimen. The specimen H-27-S-C was tested under symmetric cyclic lateral loading protocol with a constant axial load ratio of P/P_y=-0.3 (i.e., -1083kN). Local buckling developed in the north and south flange and the moment capped during the second cycle of the 2% drift amplitude. The buckling mode has a half wavelength of 0.8D and the buckling center is located at a height of 0.7D from the top surface of the base plate. Prior to the onset of local buckling, axial shortening was on the order of 0.3% of the column height. The column flexural strength was deteriorated rapidly after the onset of local buckling due to the progression of local buckling wave with the increase of the lateral drift amplitude as well as the presence of axial load on the steel column. Note that this specimen completely lost its flexural strength during the second cycle of the 4% drift amplitude of the symmetric lateral loading protocol. Therefore, the flexural strength became zero and the specimen lost its axial load carrying capacity (i.e., it completely squashed). This can be seen in Figure A.6 that shows the steel column after the completion of the test. Prior to squashing, the axial shortening was 5% of the initial height of the steel column. Once squashing occurred, axial shortening of the steel column rapidly increased and reached to about 10%. Since the specimen became unstable, the

test was completed at this point. Note that fracture due to low cycle fatigue as well as torsional deformations were not observed during this test. This can also be seen from Figure A.6.

A.3 H-27-C1-C specimen

Figures A.7 and A.8 show the progression of local buckling of H-27-C1-C specimen focusing on the local and global view, respectively. Figure A.9 shows photos of the post-test observation of the same specimen. The specimen H-27-C1-C was subjected to a collapse-consistent lateral loading protocol that represented a near-fault ground motion. The axial load ratio applied on the steel column was kept constant and equal to -30% P_y (i.e., -1083kN). The lateral loading protocol was repeated two times prior to the point that the specimen lost its load carrying capacity (i.e., collapse occurred). During the first loading stage (i.e., Phase 1) the maximum drift ratio that this column was subjected to was 5.8% rads. At this loading excursion, the steel column lost about 70% of its flexural strength; however, the axial construction of the steel column was not more than 0.5% of its full height (see Figure A.7b). However, at the end of the first phase of the lateral loading protocol (i.e., target drift was 1.8%), the steel column contracted axially to about 2% of its original length due to the small inelastic cycles that occurred after the large monotonic push. The reason is that in this case local buckling formed on both the north and south flange of the HSS column (see Figures Figure A.7c). During the positive direction of lateral loading (north direction of lateral loading), local buckling at the north flange of the steel column grew; however, the local buckling wave in the south flange of the column did not change. When the column was loaded in the negative loading direction (south direction of loading), the local buckling in the south flange of the steel column grew; in this case, the local buckling wave in the north flange of the steel column did not change. The growth of the buckling wave is

primarily attributed to the location of the neutral axis of the bending moment within the cross section of the steel column as discussed in Section 5.5.6. Since the specimen is subjected to constant axial load, neutral axis shifted close to the south flange of the steel column when the lateral load was positive. When the lateral load changed direction, the neutral axis of the cross section was closer to the north flange of the steel column. Referring to Figure A.7d that illustrates the progression of local buckling as well as the deformed configuration of the steel column at a target drift ratio of about 8% rads, the steel column lost its flexural strength; however, its axial contraction was not more than 3.5% of its full length. During the 11th excursion of Phase 2 protocol (target drift of 5.6%) the specimen fully squashed (see Figure A.7e). From these figures and associated discussion, the buckling mode of the steel column has a half wavelength of 0.8D and the buckling center is located at the height of 0.5D from the top surface of the base plate and prior to squashing. During column squashing, fracture initiated from both corners of the north flange near outside the heat affected zone of the column to the height of the buckling center, as shown in Figures A.9e and A.9f. Since the specimen lost completely its stability, the test was ended at this state. There was no torsional deflection along the height of the specimen during this test. Interestingly, prior to squashing, the axial shortening was 5% of the initial height of the steel column, which is similar to the measured value of the same steel column that was subjected to a symmetric lateral loading protocol (see Section A.3). Once squashing occurred, axial shortening of the steel column rapidly increased and reached to about 10%.

A.4 H-27-C1-V specimen

Figures A.10 and A.11 show global and local snapshots of H-27-C1-V specimen that shows the progression of local buckling during testing, respectively. Figure A.12 shows photos of the post-test observation of the same specimen. The specimen H-27-C1-V was subjected to a collapse-consistent lateral loading protocol representing a near-fault ground motion coupled with varying axial load as if this was an end column of a moment resisting frame. Initially, a -15% P_y (-542kN) was applied to the column representing the applied gravity load prior to an earthquake. This axial load varied from -50% P_y (-1805kN) in compression to 20% P_y (722kN) in tension. The compressive axial load was increasing each time that the steel column was moving laterally to the positive loading direction (north direction of loading). Similarly, the same column was subjected to tensile axial load when it was loaded laterally to the negative loading direction (i.e., south direction of loading). Similarly to the H-27-C1-C specimen, the loading protocol was repeated two times for comparison purposes. Despite the fact that the flexural strength of the steel column deteriorated substantially at about 8% lateral drift ratio, the axial shortening of the same column at this level of lateral deformation was less than 1% of its full length. During the 3rd excursion of Phase 1 lateral loading protocol, the steel column slightly buckled in its north phase. During the 5th excursion of Phase 1 protocol (i.e., target drift is 5.8%), the local buckle of the north flange of the steel column grew as shown in Figures A.10b and A.11b. The buckling mode has a half wavelength of $0.8D$ and the buckling center was located at the height of $0.7D$ from the top surface of the base plate. The center of the local buckling was shifted higher up compared to specimen H-27-C1-C due to the second order moment applied to the column due to the higher compressive axial load compared to the one applied to specimen H-27-C2-C. The specimen was subjected to the remaining inelastic cycles of the loading protocol and Phase 1

loading was completed. During these loading cycles, the applied axial load varied from compression to tension because of the lateral movement of the column from the positive to the negative lateral loading direction and vice versa. The axial load variation stretched the buckling wave on the north flange when the column was subjected to tensile axial load. As the result, the buckling wave did not develop as much as the H-27-C1-C specimen during the same lateral loading cycles; hence, the south flange of the steel column did not buckle at all during Phase 1 loading (see Figure A.11c). This is attributed to the fact that the neutral axis of the column cross section always stayed near its south flange the applied axial load varied as discussed in Section 5.5.6. Thus, the column flexural strength did not deteriorate and kept increasing in the negative loading direction. After the completion of Phase 1 loading protocol, the column axial shortening was up to 0.6% of its length. During the 2nd excursion of the Phase 2 lateral loading protocol, the south flange slightly buckled; however, there the column flexural strength deterioration was negligible in the negative loading direction. During the 5th excursion of Phase 2 lateral loading (i.e., target drift ratio of 8% rad), local buckling at the north flange of the steel column grew (see Figures A.10d and A.11d). Recall that at the end of the 11th excursion of the same loading phase, the H-27-C1-C specimen squashed (see Figures A.7e and A.8e); in the case of H-27-C1-V the local buckling did not develop as much as the H-27-C1-C specimen (see Figures A.10e and A.11e). The maximum axial shortening during the Phase 2 lateral loading protocol was 1% of the column length. The flexural strength of the column deteriorated up to about 30% of its capping moment. Fracture and torsional deflection was not observed during this test. This test was ended after the 11th excursion of Phase 2 protocol due to an accidental load that was applied to the specimen.

A.5 H-27-C2-C specimen

Figures A.13 and A.14 show global and local snapshots of H-27-C2-C specimen that shows the progression of local buckling during testing, respectively. Figure A.15 shows photos of the post-test observation of the same specimen. The specimen H-27-C2-C was subjected to a collapse-consistent lateral loading protocol that represented a long-duration ground motion. This protocol was coupled with a constant axial load ratio of -30% P_y (i.e., P=-1083kN). The loading protocol was repeated two times prior to the sidesway collapse of the specimen. Note that this specimen was tested through the complete loss of its flexural and axial load carrying capacity. Figures A.13 and A.14 show a local and global view of the progression of local buckling of the specimen at a peak drift of the 24th excursion during the Phase 1 protocol associated with a target drift of 5.4% (see Figures A.13b and A.14b); at the 33rd excursion in phase 1 protocol associated with a target drift of -0.6% rads (see Figures A.13c and A.14c); at the last excursion of phase 1 protocol (target drift is 3.3%) and at the 2nd excursion of the Phase 2 protocol associated with a target drift of 4.7% rads (see Figures A.13e and A.14e). At this loading stage the specimen fully squashed. From these figures, the south flange of the steel column buckled during the 3rd excursion of Phase 1 loading at a -2.9% rads drift ratio. The north flange of the same column buckled during the 10th excursion of Phase 1 loading. This occurred while the specimen was displacing laterally from -2.8% to 1.3% drift ratio. The buckling mode had a half wavelength of $0.8D$ and the buckling center was located at the height of $0.7D$ from the top surface of the base plate. Similarly with the H-27-C1-C specimen, the buckling wave kept growing during the inelastic cycles that followed the large monotonic push of 5.4% rads. The long duration collapse loading protocol includes more inelastic cycles than the corresponding one that represents near-fault ground motions; thus, the growth of the local buckling wave was much larger than the

corresponding one from the H-27-C1-C specimen after the completion of Phase 1 lateral loading. This can be clearly seen from Figures A.7c and A.13d. Another interesting observation is the fact that the amount of axial shortening after Phase 1 loading reached to 4.3% of the column length. This is almost twice of the corresponding value of axial shortening of the H-27-C1-C specimen at the same lateral drift and number of inelastic cycles. When the Phase 1 loading was completed, the residual flexural strength of the specimen was nearly zero. However, the steel column was subjected to the Phase 2 loading. Squashing occurred during the 2nd excursion of Phase 2 loading as shown in Figure A.13e and A.14e. The axial shortening increased rapidly from 5% to 10% when squashing. At this point, the test ended because the column was not stable. Fracture as well as torsional deflection was not observed in this test.

A.6 H-27-C2-V specimen

Figures A.16 and A.17 show global and local snapshots of H-27-C2-V specimen that shows the progression of local buckling during testing, respectively. Figure A.18 shows photos of the post-test observation of the same specimen. The specimen H-27-C2-V was subjected to a collapse-consistent lateral loading protocol that represented a long-duration ground motion coupled with varying axial load as if this column was an end column of a steel moment resisting frame. Before the application of lateral loading, the specimen was loaded axially to -0.15P_y (i.e., -542kN). This load represents the axial load applied to the steel column due to gravity. The axial load was then varied from -0.5P_y (i.e., -1805kN) once the column was loaded to the positive loading (i.e., lateral loading to the north direction) to 0.2P_y (i.e., 722kN) in negative loading (i.e., lateral loading to the south direction). The near collapse loading protocol was repeated two times until the specimen lost its flexural strength. The onset of local buckling at the north flange of this

column occurred during the 10th excursion of Phase 1 loading (i.e., target drift of 1.3% rads) and progressed more once the column reached the maximum drift amplitude of Phase 1 loading (i.e., 5.4% rads) as seen from Figures A.16b and A.17b. At this drift ratio, the steel column deteriorated in flexural strength to about 50% of its capping moment. The local buckling mode had a half wavelength of $0.8D$ and the buckling center was located at a height of $0.7D$ from the top surface of the base plate. After this drift amplitude, the column was subjected to the remaining loading cycles of Phase 1 loading. Figures A.16c and A.17c illustrate the progression of local buckling at a target drift amplitude of -0.6%, which was associated with local buckling of the south flange of the steel column. Note that the buckling wave of the north flange of the steel column was stretched during the negative loading excursions (column moving south) because of the tensile axial load that the column experienced during these excursions. Similarly, Figures A.16d and A.17d illustrate the progression of local buckling of the steel column at the last excursion of Phase 1 loading associated with a target drift of 3.3% rads. These inelastic cycles grew the local buckling wave. However, at the end of Phase 1 loading, the maximum column axial shortening was around 0.6% of its length. During Phase 2 loading, the specimen did not fail during the 2nd excursion that the H-27-C2-C specimen had squashed. The flexural strength of the steel column continued to deteriorate due to the cumulative damage of the additional inelastic cycles from Phase 2 loading. Figures A.16e and A.17e illustrate the progression of local buckling of the steel column at the 24th excursion of Phase 2 loading associated with 8.7% rad. From these figures, it is evident that the axial shortening did not change much from Phase 1 loading. This is mostly attributed to the varying axial load ratio that this specimen experienced as opposed to a constant compressive one that an interior column as part of a moment resisting frame would experience. During Phase 2 lateral loading, the flexural

strength of the steel column deteriorated to about 20% of the column capping moment. This occurred at the 24th excursion of Phase 2 loading, which was associated with a 8.7% rads lateral drift ratio. At this point, the measured axial contraction of the steel column was not more than 1.2%. After the 33rd excursion in Phase 2 loading, we confirmed that the flexural strength of the steel column deteriorated substantially; hence the test was ended. Figure A.18 shows a close view of the steel column at the location of local buckling after the end of the test. From this figure, it is evident that fracture due to low cycle fatigue and torsional deflection did not occur.

A.7 H-19-S-C specimen

Figures A.19 and A.20 show global and local snapshots of H-19-S-C specimen that shows the progression of local buckling during testing, respectively. Figure A.21 shows photos of the post-test observation of the same specimen. The specimen H-19-S-C was tested under symmetric cyclic lateral loading protocol coupled with a constant compressive axial load ratio of -0.3 (P = -1949kN). Prior to 2% rads there is no observation of local buckling at any of the flanges of the steel column. During the second cycle of the 2%s rad amplitude of the symmetric cyclic loading protocol, the steel column buckled locally at both the north and south flanges. However, local buckling can be barely seen at this amplitude as shown from Figures A.19a and A.19b that show a local view of the north flange of the steel column at +2% and -2% story drift amplitudes. The same can be seen from Figures A.20a and A.20b that show a global view of the same column at the same drift amplitudes. The buckling mode was clearly visible during the 3% drift amplitudes of the symmetric loading protocol as shown in Figures A.19c and A.19d as well as Figures A.20c and A.20d. The observed buckling mode was the elephant foot mode; hence, all the out-of-plane deflection of the sidewalls of the HSS column progresses outwards. This buckling mode is likely

to happen in cases that the D/t ratio of the HSS column is fairly small (Mukaide et al. 2016). The buckling mode has a half wavelength of $0.6D$ and the buckling center was located at a height of $0.5D$ from the top surface of the base plate. The moment kept deteriorating as the loading protocol progressed and axial shortening increased due to the growth of local buckling. During the 4% drift amplitude of the applied lateral loading protocol, local buckling became much more evident (see Figures A.19e and A.19f). At this stage, column axial shortening was nearly 3% of the column length and its flexural strength was nearly 20% of the capping moment of the column in both loading directions. During the first cycle of the 6% drift amplitude of the employed lateral loading protocol, the buckling wave was completely closed; therefore, the top and bottom edge of the local buckling wave touched each other. This can be seen from Figures A.19g and A.19h. From this point, the steel column moment started increasing again. The same phenomenon was seen in the next excursion during the negative loading direction (i.e., the column was loaded in the south direction). Because local buckling stopped growing, the test ended after the first cycle of 6% drift amplitude. During the 6% drift amplitude, small fracture noises were heard several times; however, fracture was not observed from the post-test specimen observations, as shown in Figure A.21. Note that in this case, the column axial shortening was in the order of 7% of the initial length of the steel column. However, due to the small local slenderness of the cross section (i.e., D/t = 19) compared to the H-27 series tests, column axial shortening is not followed by a rapid loss of axial load carrying capacity of the steel column. Note that torsional deflections were not observed during this test.

A.8 H-19-C1-C specimen

Figures A.22 and A.23 show global and local snapshots of H-19-C1-C specimen that shows the progression of local buckling during testing, respectively. Figure A.24 shows photos of the post-test observation of the same specimen. The specimen H-19-C1-C was subjected to a collapse-consistent lateral loading protocol that represented a near-fault ground motion. The lateral load was coupled with a constant axial load ratio of -0.3 (i.e., P = -1949kN). The loading protocol was repeated four times (each time that the lateral protocol was repeated in noted as "Phase i") until the specimen deteriorated in flexural strength close to zero. Note that after the 6th excursion of Phase 4 loading, we had to reduce the applied compressive axial load on the column from -0.3P_y to -0.25P_y (i.e., -1600kN) because the load capacity of the lateral actuator was about to be exceeded (1000kN). This is due to the lateral load component of the vertical load that we applied on the specimen due to the inclination of the rigid link that connected the plate adapter and the high force MTS (see discussion in Section 5.2.3).

During Phase 1 loading the specimen was able to more or less maintain its flexural strength up to about 6% rads and less than 1% axial shortening. This can be also confirmed from Figures A.22a and A.23a that show the progression of local buckling of the specimen at about 6% drift ratio based on a local and global view, respectively. During the following small inelastic cycles from the large drift amplitude of the employed loading protocol the specimen did not experience major cumulative damage as seen from Figures A.22b and A.23b that show the progression of local buckling of the specimen at the end of Phase 1 loading. Note that the buckling mode was the elephant foot type as observed in H-19-S-C specimen discussed earlier. The buckling mode had a half wavelength of 0.6D and the buckling center was located at the height of 0.5D with respect to

the top surface of the base plate. Due to the asymmetry of the lateral loading protocol the moment in the positive loading direction (column moving north) deteriorated more compared to the moment in the negative loading direction (i.e., column moving south) During Phase 2 loading, local buckling of the north flange of the HSS column progressed as shown in Figures A.22c and A.23c. During this loading excursion, the flexural strength of the column deteriorated to about 70% of its capping moment. Column axial shortening at this drift amplitude was slightly larger than 1% of the column length and in the range of 1.5% by the end of Phase 2 loading. This indicates that for an HSS column with such local slenderness, the progression of local buckling is not large even at fairly large deformation amplitudes associated with near-fault type of ground motions. This can also be seen in Figures A.22d and A.23d that illustrate the progression of local buckling of the specimen at the end of Phase 2 loading.

During Phase 3 loading, the steel column deteriorated in flexural to about 40% of its capping strength at a drift amplitude close to 10% rads. The associated axial shortening of the column was in the range of 2.5% of its length. This can be seen in Figures A.22e and A.23e that show the progression of local buckling at the base of the column at this drift amplitude. Note that after this point, column axial shortening increased fairly fast to about 3% of the column length due to the remaining small inelastic cycles of Phase 3 loading. During Phase 4 loading, once the steel column experienced a 12.2% target drift amplitude (i.e., peak drift of Phase 4 loading) its flexural strength degraded close to zero and the associated axial shortening was in the range of 4% of the steel column length. After this the applied axial load was reduced from 30% to 25% due to equipment limitation and the capping moment after this excursion slightly increased due to the relaxation of the second order moment. Column axial shortening accumulated to about 5.1% of the initial length of the specimen. Figures A.22h and A.23h illustrate the progression of

local buckling at the base location of the column after the end of the test. Fracture and torsional deflection was not observed during this test, as shown in Figure A.24.

A.9 H-19-C1-V specimen

Figures A.25 and A.26 show global and local snapshots of H-19-C1-V specimen that shows the progression of local buckling during testing, respectively. Figure A.27 shows photos of the post-test observation of the same specimen. The specimen H-19-C1-V was subjected to a collapse-consistent lateral loading protocol that represented a near-fault ground motion coupled with varying axial load. The column was first loaded to a compressive axial load of -0.15P_y (-974kN), and it varied from -0.5P_y (-3248kN) when the column was moving laterally to the positive loading direction to 0.2P_y (1299kN) in the negative loading. The loading protocol was repeated 4 times until the specimen because unstable (i.e., complete loss of flexural strength). Referring to Figures A.25a and A.26a, the north flange of the steel column buckled locally in the 5th excursion of phase 1 loading (i.e., 5.9% target drift ratio). The buckling mode was initially developed at a height of 0.7D. A second wave located at a height of 1.1D started growing as it can be seen in Figures A.25c at the peak drift amplitude of Phase 2 loading. Once the second wave buckling started developing, this mode dominated the overall behaviour of the steel column. This can be seen in Figures A.25e to A.26g that show the progression of local buckling at this location during the peak excursion of each loading stage up to 12.2% target drift ratio. Note that in this case, the buckling mode was not similar with the elephant foot mode that was observed in the rest of H-19 series tests. Another interesting issue is the fact that the center of local buckling is further up compared to the cases that were examined with a constant axial load. This is attributed to the fact that during the varying axial load, a high compressive axial load demand

increases the P-delta moment thereby, shifting the location of the maximum moment away from the column base. The steel column was able to maintain its flexural strength up to about 6% rads. Each time that the steel column was loaded into the negative loading direction (i.e., column moving south), the buckling wave was stretched due to axial load variation. In this case, the axial shortening increases linearly with respect to the chord rotation. The maximum axial shortening at the end of the test was about 2% of the column length. The moment in positive loading hit zero during the phase 4 protocol. A ductile tearing was observed at the corner section of the north flange at the center of the buckling wave, as shown in Figure A.27. Torsional deflection was not observed in this test.

A.10 W-6-34-M-C specimen

Figures A.28 and A.29 show global and local snapshots of W-6-34-M-C specimen that shows the progression of local buckling during testing, respectively. Figure A.30 shows photos of the post-test observation of the same specimen. The specimen W-6-34-M-C was tested under monotonic lateral loading protocol with constant axial load of -0.3P_y (-1134kN). In this testing the flexural strength of the column deteriorated at about 4% rads. The north flange and web buckled at 4% drift and the moment capped at this point (see Figures A.28b and A.29b). The buckling mode of the flange had a half wavelength of 1.0D; the buckling center was located at a height of 0.6D from the top surface of the base plate of the specimen. This can be clearly seen from Figures A.28c that shows the progression of local buckling of the column at 6% rad. Once the column was pushed laterally to 10% drift, a second wave buckling began to develop as shown in Figures A.28e. The buckling length of the second wave was equal to 1.0D and the buckling center was at a height of 1.2D from the top surface of the base plate. After this stage, the secondary buckling

was more dominant than the first one and that triggered lateral torsional buckling. This can be seen by a simple comparison between Figures A.28e and A2.8f. From these figures, the primary buckling closer to the base did not develop much between 10% and 16% drift ratios. At 16% drift, the moment deteriorated close to 15% of its capping moment. Axial contraction was 2.4% of the column length at the same drift ratio. South flange did not buckle during the test. Fracture was not observed in this test, as shown in Figure A.30 that illustrates post-test observations after the completion of the test.

When the target drift became 16%, the lateral bracing system deflected a lot and the running beam on the strong floor slipped. However, slip occurred at the very end of the testing; thus, it did not affect the test result. After this test, the lateral supporting system was reinforced as shown in Figure 5.14. Slip occurred due to the fact that the steel column was pushing out of plane due to lateral torsional buckling. The out-of-plane deflection was measured accurately during each test by the Krypton wireless recording system. It was estimated that the out-of-plane force was in the order of 50kN. After the lateral support system was reinforced, there was no observed out of plane movement of the lateral bracing system during the rest testing program of the wide flange steel column specimens.

A.11 W-6-34-S-C specimen

Figures A.31 and A.32 show global and local snapshots of W-6-34-S-C specimen that shows the progression of local buckling during testing, respectively. Figure A.33 shows photos of the post-test observation of the same specimen. The specimen W-6-34-S-C was subjected to a symmetrical cyclic lateral loading protocol coupled with constant axial compressive load of $-0.3P_y$ (-1134kN). In this test the steel column lost completely its flexural strength during the 6%

drift amplitude. At this drift level, the axial shortening was more than 10% of the column length. The north flange and web of the steel column buckled during the 1.5% drift amplitude (see Figures A.31b and A31c), therefore, the moment of the steel column capped at this point. The buckling mode of the column flange had a half wavelength of $0.8D$ and the buckling center was located at a height of $0.4D$ from the top surface of the column base. At the 3% drift amplitude, a second wave buckling formed that had a half wavelength of $0.8D$; the buckling center in this case was located at a height equal to $0.9D$ from the top surface of the column base plate. This can also be seen more evidently from Figures A.31g and A.31h that show the progression of local buckling at the same location for the 5% drift amplitude in the positive and negative loading directions, respectively. Similarly with the same steel column that was tested under monotonic lateral loading, the secondary local buckling triggered lateral torsional buckling. After this stage, torsional deflection grew substantially as shown in Figures A.31. The north flange of the steel column twisted during the positive loading and the south flange twisted out-of-plane of the principal loading to the same amount when the column was moving to the negative loading direction (see discussion in Section 5.5.8). As the result, the centerline of the web was offset by $0.5b$ (b: is the width of column flange) after the end of the test as shown in Figure A.33. In this case, axial shortening of the steel column was substantial (more than 250mm) due to the progression of local and torsional buckling wave that accumulated during both the positive and negative loading. At the first excursion of 6% drift amplitude, the column moment reached zero and the specimen lost its axial load carrying capacity (i.e., unstable). At this point, axial shortening was more than 10% of initial length of the specimen. No indication of fracture was observed during this test, as shown in Figure A.33.

A.12 W-6-34-C1-C specimen

Figures A.34 and A.35 show global and local snapshots of W-6-34-C1-C specimen that shows the progression of local buckling during testing, respectively. Figure A.36 shows photos of the post-test observation of the same specimen. The specimen W-6-34-C1-C was subjected to a collapse-consistent lateral loading protocol that represented a near-fault ground motion coupled with a constant compressive axial load equal to -0.3P_y (-1134kN). In this test the lateral loading protocol was repeated four times prior to the point that the column reached to zero flexural strength. During the 3rd excursion of Phase 1 loading (i.e.,1.9% target drift ratio), the column web buckled. The north flange buckled more during the 5th excursion of Phase 1 loading (i.e., 5.9% target drift) (see Figure A.34a). At this deformation, the column flexural strength reached about 80% of its capping moment. Similarly, to the previous two tests with the same column, the buckling mode of the north flange had a half wavelength of 0.8D and the buckling center was located at a height equal to 0.4D from the top surface of the column base plate. Once the steel column reached the 5th excursion of Phase 2 loading (i.e., associated drift of 7.5% rad), a second wave buckling formed in the north flange of the column (see Figure A.34c). This buckle had a half wavelength of 0.8D and the buckling center was located at a height of 1.0D from the top surface of the column base plate. The second wave buckling triggered torsional deflections to the steel column. Because of the asymmetric loading protocol, the north flange twisted more than the south flange. This can be clearly seen in Figure A.34e. Once the second wave buckling began to develop, most of the deflection progressed in the second wave; the first wave buckling did not grow as much from this loading stage. The axial shortening at the end of the first three loading phases was 2.0% (Phase 1), 3.6% (Phase 2), 4.5% (Phase 3). During Phase 4 loading, the test ended after the steel column was pushed to about 12% rads because its flexural strength

deteriorated close to zero. At this stage, axial shortening was in the range of 5.5%. Despite the fact that the inelastic cumulative damage to the column was substantial, fracture due to low-cycle fatigue was not observed during this test, as shown in Figures A.36a to A.36d that shows the specimen from all sides at the end of the test. Due to lateral torsional buckling, the top end of the north flange of the steel column yielded as shown in Figures A.36e to A.36f.

A.13 W-6-34-C1-V specimen

Figures A.37 and A.38 show global and local snapshots of W-6-34-C1-V specimen that shows the progression of local buckling during testing, respectively. Figure A.39 shows photos of the post-test observation of the same specimen. The specimen W-6-34-C1-V was subjected to the same collapse-consistent lateral loading protocol with the specimen W-6-34-C1-C specimen; the main difference in this case was that the specimen W-6-34-C1-V was tested with a varying axial load. The steel column was first subjected to a compressive axial load equal to -0.15P_y (-567kN) that represented the gravity load applied to this column prior to an earthquake. The axial load varied during the variation of the lateral loading protocol to represent the overturning moment effects on end columns of moment resisting frames. The axial load varied from -0.5P_y (-1890kN) in the positive loading direction (i.e., column moving north) to 0.2P_y (756kN) in the negative loading direction (i.e., column moving south). The specimen had initially twisted due to residual stresses that were applied to column after the completion of the welding procedure at the top and bottom steel plates. Due to this initial imperfection the specimen base plate bolt hole pattern did not fit to the one of the setup. To install the specimen in place, a 19kNm of pre-torque force was applied with two hydraulic jacks. Once the specimen was in place, the lateral loading protocol was repeated 4 times until the specimen's flexural strength substantially deteriorated. In this test

the specimen reached to about 30% of each capping moment at about 12% rad. The associated column axial shortening was minimal even at this drift amplitude due to the variation of the axial load ratio during the test. Referring to Figures A.37 and A.38, the figures on the left show the progression of local buckling at this location at the 5th excursion each one of the three loading phases. This excursion is associated with the largest drift amplitude per loading phase. The figures on the right illustrate the status of the test specimen at the end of each loading phase. During Phase 1 loading, both the first and second wave buckling appeared at the same time (see Figure A.37a). The first buckling wave of the flange had a half wavelength of $0.8D$ and its buckling center was located at a height of $0.4D$ from the top surface of the column base plate. The second buckling wave of the flange had a half wavelength of $0.8D$ and the buckling center was located at a height of $1.0D$ from the top surface of the column base plate. The reason that the second wave buckling occurred early is likely due to the pre-torque installation discussed earlier as well as the fact that at 5.8% rads of Phase 1 loading, the compressive axial load ratio on the steel column became equal to 0.5. The second order moment shifted the location of local buckling further up. Up to the 5th excursion of Phase 3 loading, both the first and second buckling waves grew as shown in Figure A.37c. After the completion of Phase 3 loading, only the second wave continued to grow. Due to the axial load variation, most of the deflection occurred in the north flange in positive and negative loading. Therefore the buckling wave was stretched when the specimen was subjected to negative loading; thus the effect of cumulative damage on the north flange of the steel column with the progression of lateral loading was smaller compared to the same column subjected to a constant axial load ratio. This can be seen in Figures A.39a to A.39d that show a view of the column local buckling from the west and north view. The south flange of the steel column did not seem to buckle through the entire loading

protocol, as shown in Figure A.39c. The stretching of the buckling wave of the north flange is the reason why the column moment did not deteriorate in the negative loading; instead, it kept increasing with the increase of the lateral drift. After the 5th excursion of Phase 4 loading (i.e., 12% drift), the moment degraded to about 30% of the capping moment. The column axial shortening progressed linearly with respect to the column chord rotation. The axial shortening at the end of the first three loading phases was equal to 0.4%, 0.9% and 1.2% of the column length, respectively. Note that fracture due to low cycle fatigue was not observed during this test, as shown from Figures A.39a to A.39d. Due the lateral torsional buckling that occurred during the test, the top end of the north flange of the steel column yielded as it can be seen in Figure A.39e.

A.14 W-6-34-C2-C specimen

Figures A.40 and A.41 show global and local snapshots of W-6-34-C2-C specimen that shows the progression of local buckling during testing, respectively. Figure A.42 shows photos of the post-test observation of the same specimen. The specimen W-6-34-C2-C was tested under a collapse-consistent lateral loading protocol representing a long duration ground motion with constant compressive axial load equal to -0.3P_y (-1134kN). As discussed in Section 3.3, Phase 1 loading protocol represents a maximum considered earthquake (MCE) that the steel column displaces up to 4% drift amplitude. Then the collapse lateral loading protocol is subjected to the specimen during Phase 2 loading. In this test the steel column flexural strength deteriorated to nearly zero and at the same time the axial shortening became equal to about 10% of the column length. The formation and progression of local buckling near the column base is shown in Figures A.40 and A.41 from a local and global view, respectively, at selected drift amplitudes in the negative and positive loading directions. The south flange and web of the steel column

buckled during the 5th excursion of Phase 1 loading (i.e., the associated drift ratio was -2.9% rad). The north flange of the same column buckled during the 10th excursion of Phase 1 loading (i.e., target drift was 1.3%rad). The buckling mode of the steel column included both a first and second wave as shown in Figures A.40 and A.41. The associated buckling lengths were $0.7D$ and $1.0D$, respectively. The centers of each local buckling wave were located to a distance equal to $0.4D$ and $1.0D$ with respect to the top surface of the column base plate. Referring to Figures A.40e and A.40g, the second buckling wave developed more substantially than the first buckling wave. This was the primary reason that lateral torsional buckling was triggered. During Phase 1 loading, the specimen displaced up to about 4% drift amplitude. That made both the north and south flange of the steel column to buckle; thus it was notable the out-of-plane displacement at the location of second buckling wave. After Phase 1 loading, the column flexural strength deteriorated up to 50% of its capping moment mostly due to cyclic deterioration; the column axial shortening at this point was 2.6%. In Phase 2 loading, the specimen kept deteriorating and shortened even more than Phase 1 loading. During Phase 2, the moment became zero and the specimen lost its axial load carrying capacity during the 29th excursion of Phase 2 loading. The test ended due to column squashing. Referring to Figures A.42a and A.42d, the out-of plane distortion of the specimen caused the k-area to stretch a lot and subsequently increased the strain demands in the same region. Due to this distortion, ductile tearing initiated at this location. Figures A.42e and A.42f shows the fractured k-area after the test. The fracture propagated along the longitudinal direction of the web. As shown in Figures A.42g and A.42j, the top end of north and south flange yielded due to the out-of plane deflection.

A.15 W-6-34-C2-V specimen

Figures A.43 and A.44 show global and local snapshots of W-6-34-C2-V specimen that shows the progression of local buckling during testing, respectively. Figure A.45 shows photos of the post-test observation of the same specimen. The specimen W-6-34-C2-V was subjected to a collapse-consistent lateral loading protocol representing a long-duration ground motion coupled with varying axial load. Prior to the application of the loading protocol, the specimen was loaded to a compressive axial load equal to -0.15 P_y (-567kN). This load varied to a maximum compressive load equal to -0.5P_y (-1890kN) when the column was loaded laterally in the positive loading and to a maximum tensile axial load equal to 0.2P_y (756kN) when the column was loaded laterally in the negative loading. In this test the column flexural strength deteriorates to about 40% of its capping moment at a drift amplitude equal to about 10% rads. At this drift ratio, the corresponding column axial contraction was less than 2% of the column initial height indicating that axial shortening in end columns of moment resisting frames can be substantially less than the corresponding one in interior columns of the same story that undergo the same lateral displacements during an earthquake. This can also be seen from Figures A.43 and A.44 that illustrate the progression of local buckling near the base location of the specimen. From these figures, the north flange and web of the steel column buckled locally and the moment capped during the 14th excursion of Phase 1 loading, which is associated with a 2.8% drift ratio. The buckling length was 0.7D and the buckling center was at a distance equal to 0.4D from the top surface of the column base plate. This can be clearly seen from Figure A.43b. During Phase 1 loading, only the north flange of the steel column buckled due to the fact that the neutral axis of the steel column stayed near the south flange with the variation of the axial load from compression to tension when the column laterally moved from the positive to the negative

loading direction (i.e., column moving from north to south). For this reason, the bucking wave near the base of the steel column was stretched during the negative loading. During Phase 2 loading, the south flange of the steel column slightly buckled during 5th excursion of the lateral loading protocol; however, the buckle at this location did not grow much. From this point on, the moment capped in the negative loading; however, the capping moment was always higher than that in the positive loading direction due to the lateral load asymmetry. During Phase 3 loading, the twisting mode became evident in the column; however, the first buckling wave still progressed as shown in Figure A.43f. During the 15th excursion of Phase 3 loading, a fracture noise was heard followed by small fractures at the tip of the bottom end of the north flange as well as the web access hole (see Figures A.45e and A.45f). The column flexural strength did not drop at this point. Instead, a crack on the weld access hole propagated upwards. At the 28th excursion of Phase 3 loading, a fracture at the weld on weld access hole was observed. After completion of Phase 3 loading, it was confirmed that the crack at this location became large and the moment dropped less than 50% of the capping moment. The maximum axial shortening after the completion of Phase 3 loading (maximum drift was 10%) was 1.6%. As shown in Figures A.45g and A.45h, the top end of north flange yielded due to the column out-of plane deflection.

A.16 W-8-34-S-C specimen

Figures A.46 and A.47 show global and local snapshots of W-8-34-S-C specimen that shows the progression of local buckling during testing, respectively. Figure A.48 shows photos of the post-test observation of the same specimen. The specimen W-8-34-S-C was tested under symmetric cyclic loading protocol coupled with a constant compressive axial load equal to -0.3 P_y (-1317kN). In this test both the north and south flange of the steel column buckled during the

1.5% drift amplitude. This became more evident during the 2% drift amplitude as shown in Figures A.46c and A.46d. The buckling mode had a half wavelength of 0.9D and the buckling center was located at 0.8D from the top surface of the column base plate. The buckling wave progressed more during the 3% and 4% drift amplitudes. This can be seen in Figures A.46e to A.46h. A torsional mode became visible at the 3% drift amplitude. Due to local and lateral torsional buckling, the k-area of the south flange near the base of the column was substantially stretched (see Figure A.48b) and a brittle fracture occurred during the 2nd excursion of 4% drift amplitude of this symmetric loading protocol. The flexural strength of the steel column dropped rapidly at this point. The degraded moment of the steel column prior to fracture was equal to 20% of the capping moment. At this drift ratio, the column axial shortening was equal to 3.7% of the column length. The fracture ran along the longitudinal direction as shown in Figures A.48e and A.48f. At this point, the test ended. The top end column flanges did not yield, as shown in Figures A.48g to A.48j.

A.17 W-8-34-C1-C specimen

Figures A.49 and A.50 show global and local snapshots of W-8-34-C1-C specimen that shows the progression of local buckling during testing, respectively. Figure A.51 shows photos of the post-test observation of the same specimen. The specimen W-8-34-C1-C was tested under a collapse-consistent lateral loading protocol that represented a near-fault ground motion coupled with a constant compressive axial load equal to -0.3P_y (-1317kN). This protocol was repeated three times incrementally till the specimen failed. In this test local buckling occurred on both the north and south flange of the steel column during the 2nd and 3rd loading excursion of Phase 1 loading, which represents 1.9% and -1.9% drift ratio, respectively. The buckling mode had a half

wavelength of 1.0D and the buckling center was located at a height equal to 0.5D from the top surface of the column base plate. From Figure A.49, local buckling in both flanges of the steel column kept growing with the progression of lateral loading. After the 5th excursion of Phase 2 loading (i.e., lateral drift of 7.6% rads), the steel column started twisting due to lateral torsional buckling that was triggered by a second wave buckling (see Figure A.49c); however, the torsional deflection was not as large as the one observed in W-8-34-S-C specimen that was tested under a symmetric lateral loading protocol. Because a buckling wave was developed in both the north and south flange of the steel column, axial shortening was accumulated such that it reached 2.5% and 4.3% at the end of Phase 1 and 2 loading, respectively. This can also be seen by Figures A.49b and A.49d. At the end of the 5th excursion of the Phase 3 loading, the flexural strength of the column was almost zero. After this excursion, a brittle fracture occurred at the k-area of the south flange as shown in Figures A.51e and A.51f. At this point, the flexural strength of the steel column dropped rapidly. Fracture initiated due to the substantial out-of-plane distortion of web and flange, as shown in Figures A.51a to A.51d. The column torsional deflection initiated during Phase 2 loading and progressed during Phase 3 loading. At the time of fracture, the column axial shortening was 5.8% of its total length. The top end flanges did not yield, as shown in Figures A.51g to A.51j. The white wash came off from the top north flange of the column due to the energy release from the k-area fracture (Figure A.51h).

A.18 W-8-34-C1-V specimen

Figures A.52 and A.53 show global and local snapshots of W-8-34-C1-V specimen that shows the progression of local buckling during testing, respectively. Figure A.54 shows photos of the post-test observation of the same specimen. The specimen W-8-34-C1-V was subjected to a

collapse-consistent lateral loading protocol representing a near-fault ground motion coupled with a varying axial load ratio. An initial axial compressive load ratio equal to -0.15P_y (-659kN) was initially applied to the column. This load varied to a maximum compressive load equal to -0.5P_y (-2195kN) when the column was moving laterally to the positive direction (i.e., column moving north). When the column was moving laterally to the negative direction (i.e., column moving south), the axial load varied to a maximum tensile load equal to 0.2P_y (878kN). The loading protocol was repeated incrementally four times. Referring to Figures A.52 and A.53, the right side images show the progression of damage at the same location at the end of each loading phase. Local buckling occurred at the north flange of the steel column during the first excursion of the Phase 1 loading, which was associated with a target drift equal to 1.8%. The buckling mode had a half wavelength equal to 0.85D; the buckling center was located at a height equal to 0.5D from the top surface of the column base plate. From Figure A.52, the buckling wave did not progress substantially because of the column stretching when it was moving in the negative loading direction. This was also the main reason that column axial shortening was not much after the end of the test. A torsional deflection was observed from Phase 3 loading; however, the amplitude of this deflection was very small (see sequential deflection in Figures A.52 and A.53). During the 10th excursion of the Phase 2 loading, a fracture noise was heard due to a crack that appeared at the north flange weld access hole, as shown in Figure A.54e (noted as "A"). This did not cause any drop to the column flexural strength. As the loading protocol progressed, the column flexural strength deteriorated cyclically but strength deterioration was not as much as the corresponding one of the steel column subjected to the same lateral loading protocol coupled with constant compressive axial load (W-8-34-C1-C). During Phase 2 and 3 loading, the crack at the weld access hole propagated gradually but it did not have any effect on the column

performance. During the 2nd excursion of the Phase 4 loading, the south flange of the steel column slightly buckled and the negative moment capped. During the 7th excursion of the same loading phase, a fracture noise occurred again, and the other crack was observed as shown in Figure A.54e (noted as “B”). The first crack propagated extensively as well as the second crack appeared, the test was ended. Column axial shortening was approximately linear with respect to the rotation. The top end flanges did not yield, as shown in Figures A.54f and A.51g.

A.19 W-6-25-S-C specimen

Figures A.55 and A.56 show global and local snapshots of W-6-25-S-C specimen that shows the progression of local buckling during testing, respectively. Figure A.57 shows photos of the post-test observation of the same specimen. The specimen W-6-25-S-C was tested under a symmetric cyclic loading protocol coupled with a constant compressive axial load equal to -0.3 P_y (-1741kN). Both the north and south flange slightly buckled during the 1.5% drift amplitude; however, the flexural strength of the column started deteriorating cyclically during the 3% drift amplitude of the symmetric loading protocol. The buckling mode shown in Figure A.55 had a half wavelength equal to 0.9D and the buckling center was located at a height equal to 0.7D from the top surface of the column base. The buckling wave progressed with the increasing amplitude of inelastic cycles of the same protocol and a torsional mode appeared at the 4% drift amplitude. During the 3rd excursion of the 5% drift amplitude, a fracture noise occurred. In the 4th excursion, a tearing at the k-area of the south side was observed, as shown in Figure A.57e. The tearing propagated along the longitudinal direction of the k-area of the same specimen. For this reason, the test ended. The steel column flexural strength degraded about 20% of its capping moment up to this point. At this lateral drift, the corresponding column axial shortening was

more than 7% of the column length. Note that the top end flanges of the column did not yield, as shown in Figure A.57f to A.57i.

A.20 W-6-25-C1-C specimen

Figures A.58 and A.59 show global and local snapshots of W-6-25-C1-C specimen that shows the progression of local buckling during testing, respectively. Figure A.60 shows photos of the post-test observation of the same specimen. The specimen W-6-25-C1-C was subjected to a near collapse lateral loading protocol representing a near fault ground motion coupled with a constant compressive axial load equal to -0.3P_y (-1741kN). The protocol was repeated incrementally four times prior to the end of the test. During Phase 4 loading, the compressive axial load was reduced to -0.2P_y (-1160kN) for the same reason as the H-19-C1-C specimen (limitation of load capacity). This column was able to sustain its flexural strength up to 6% drift with the corresponding axial shortening to be less than 1% of the column length. This can be justified from Figures A.58a and A.58b that show the progression of local buckling near the base location of the steel column at 5.9% rads and 1.4% rads of target drift, respectively, during Phase 1 loading. From these figures, local buckling at this location was minimal during this loading phase. The buckling mode had a half wavelength equal to 0.9D and the buckling center was located at 0.45D from the top surface of the column base plate. During the following loading phases, local buckling in both the north and south flange kept growing (see Figures A.58c to A.58f). After the 5th excursion of Phase 3 loading, a secondary buckling wave was observed. Its length was equal to 0.9D at it formed at a height equal to 1.05D from the top surface of the column base plate. This triggered column twisting as shown in Figure A.58e. In Phase 4 loading, the compressive axial load was reduced to -0.2P_y due to the capacity of the lateral actuator;

therefore, the energy dissipation increased compared to the moment hysteresis during Phase 3 loading; thus, the column axial shortening accumulation decreased during Phase 4 loading. After the completion of this loading phase, the column flexural strength reached to 40% of the capping moment, and the axial shortening was more than 5% of the column length. The test was stopped at this point due to the load capacity of the lateral actuator. Note that the torsional distortion of this column was small as shown in Figures A.60a to A.60d. Fracture did not occur in this case. Furthermore, the top end flanges of the steel column did not yield, as shown in Figures A.60e to A.60h.

A.21 W-6-25-C1-V specimen

Figures A.61 and A.62 show global and local snapshots of W-6-25-C1-V specimen that shows the progression of local buckling during testing, respectively. Figure A.63 shows photos of the post-test observation of the same specimen. The specimen W-8-34-C1-V was subjected to the same collapse-consistent lateral loading protocol with the one that was employed for specimen W-6-25-C1-C. The applied axial load varied together with the lateral loading protocol. The steel column was first loaded axially in compression with an axial load equal to -0.15P_y (-870kN). This load represented the gravity load applied to the column prior to an earthquake. The axial load varied to -0.5P_y (-2901kN) when the column was displacing in the positive loading. Similarly, the axial load varied to 0.2P_y (1160kN) when the column was displacing in the negative loading. The loading protocol was repeated incrementally four times. In this test the steel column was able to maintain its flexural strength to about 6% rads. At this lateral deformation, the corresponding column axial shortening was just 1% of its length. Local buckling first occurred on the north flange of the steel column during the first excursion in phase

1 protocol (target drift was 1.8%). However, it was barely notable. The buckling mode had a half wavelength equal to $0.8D$ and the buckling center was located at a distance equal to $0.45D$ from the top surface of the column base plate. Because of the axial load variation from compression to tension, the buckling wave did not develop; however, local buckling was much more evident after the end of 5th excursion of Phase 2 loading, which was associated with a 7.6% target drift amplitude as seen in Figure A.61c. A small torsional deflection was observed after Phase 3 loading (see Figures A.61e to A.61h and Figures A.63a to A.63d). Column axial shortening varied linearly with respect to the chord rotation of the steel column. The column flexural strength deteriorated cyclically to about 50% of its capping moment at the end of Phase 4 loading. After the completion of Phase 4 loading, a small crack was observed at the weld access hole near the north column bottom flange as shown in Figure A.63e. The top end flanges of the steel column did not yield, as shown in Figures A.63f to A.63i.

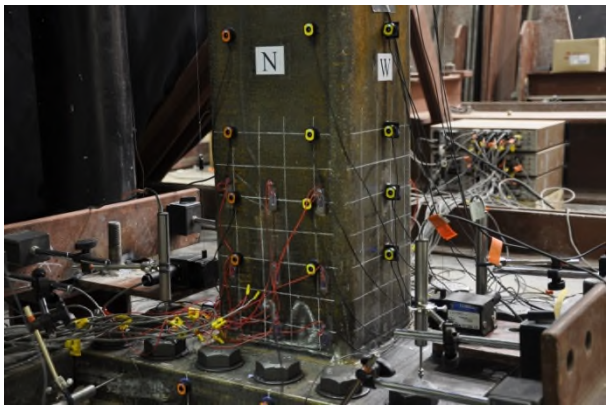

(a) before test

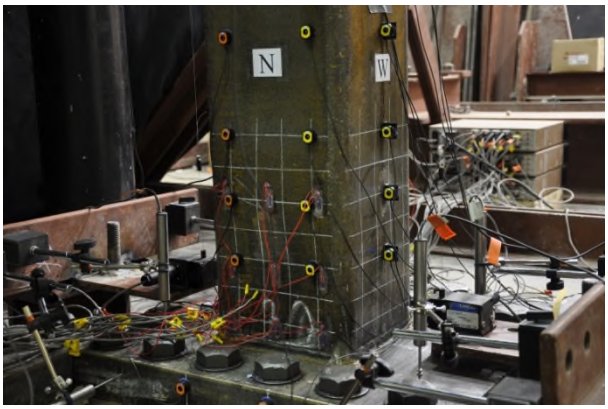

(b) 2% drift

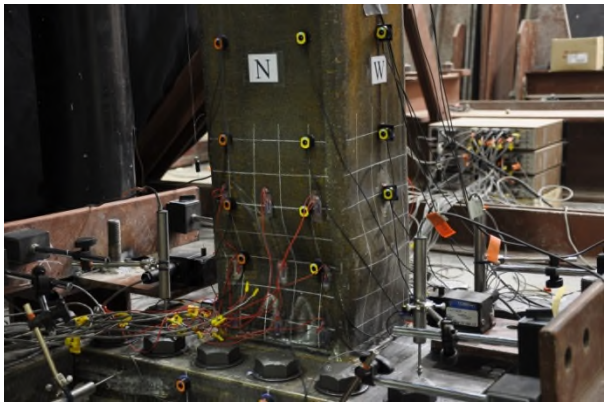

(c) 6% drift

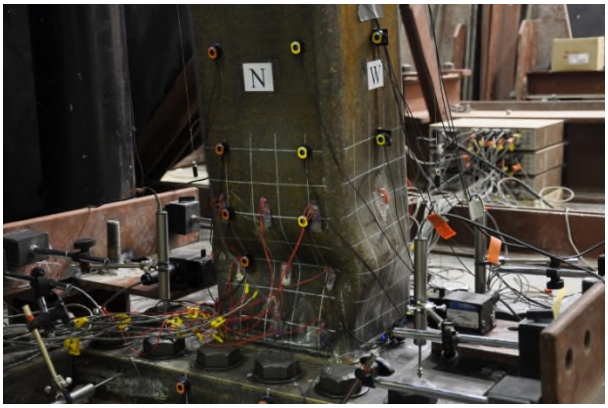

(d) 6% drift

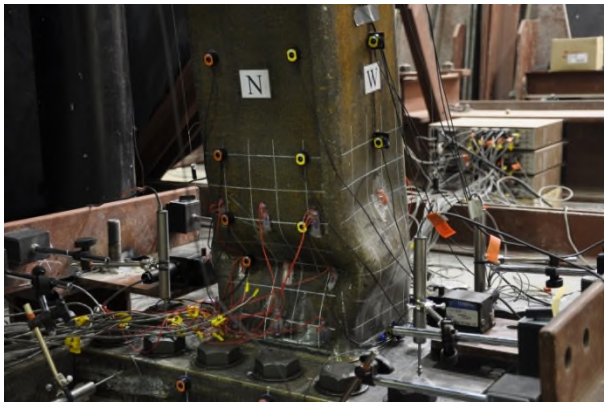

(e) 14% drift

Figure A.1 H-27-M-C: Flange local buckling (North West view)

(a) before test

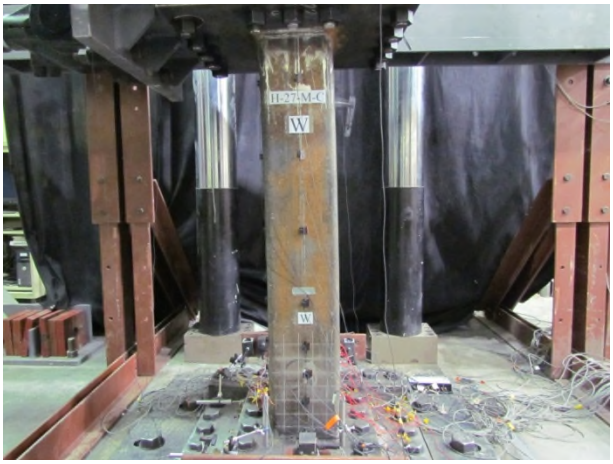

(b) 2% drift

(c) 6% drift

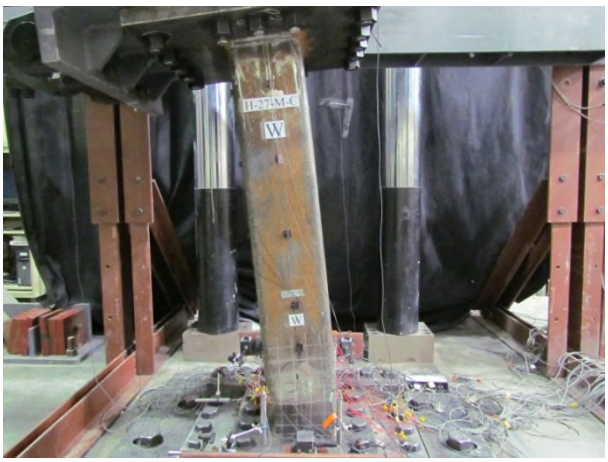

(d) 6% drift

(e) 14% drift

Figure A.2 H-27-M-C: Overall deformed configuration (West view)

(a) North west view

(b) North east view

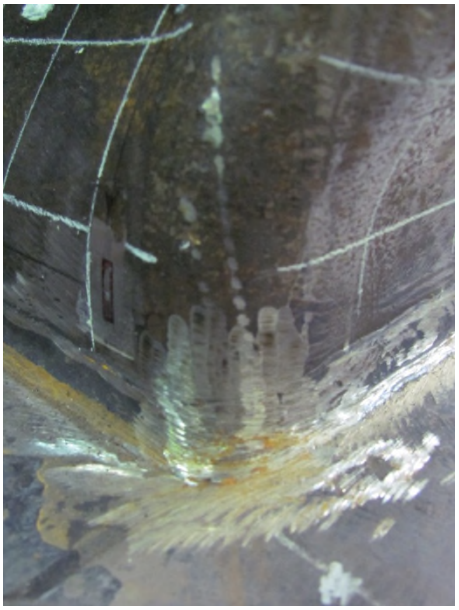

(c) Welding on north west corner

(d) Welding at north east corner

Figure A.3 H-27-M-C: Post-test specimen observation

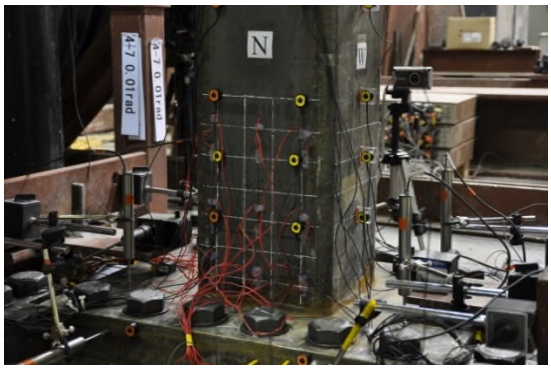

(a) +1% drift

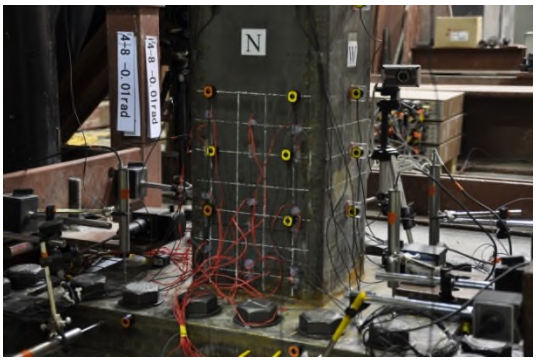

(b) -1% drift

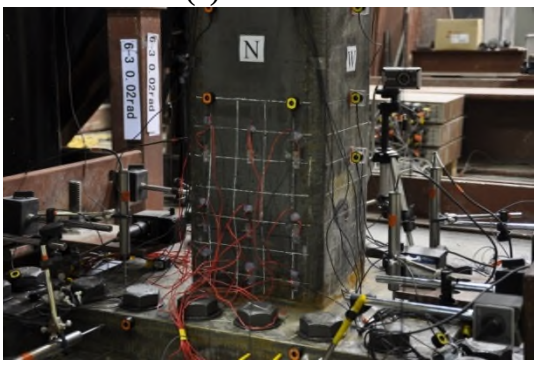

(c) +2% drift

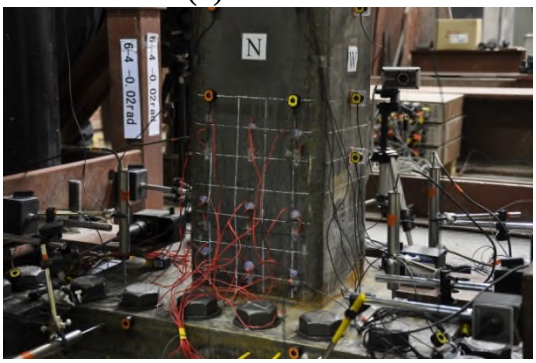

(d) -2% drift

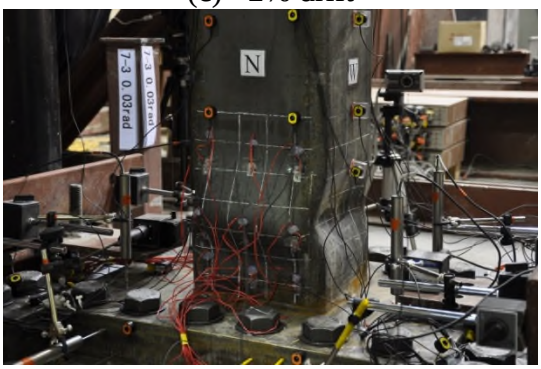

(e) +3% drift

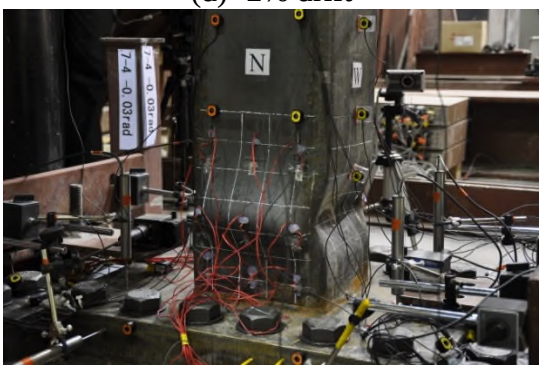

(f) -3% drift

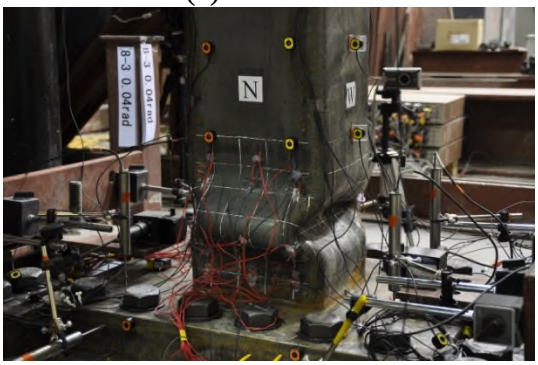

(g) +4% drift

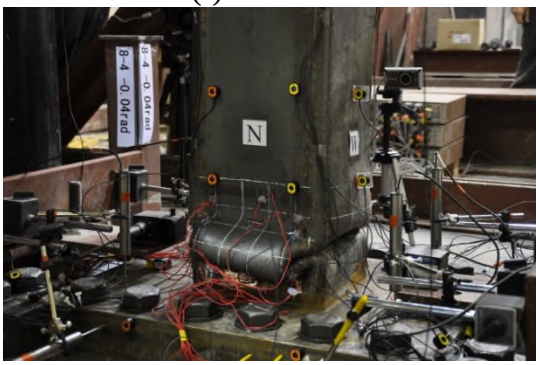

(h) -4% drift (squashed)

Figure A.4 H-27-S-C specimen: Flange local buckling (North West view)

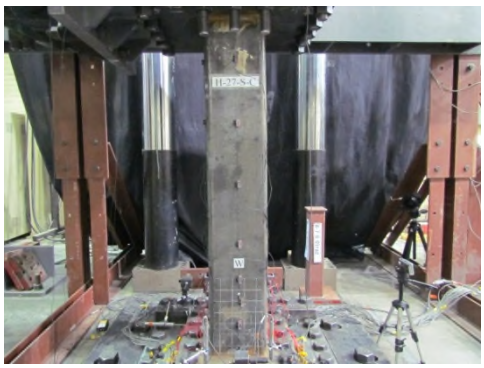

(a) +1% drift

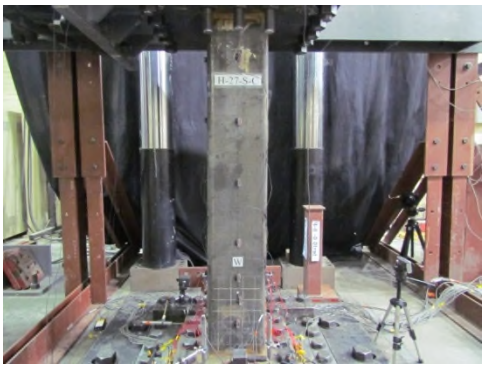

(b) -1% drift

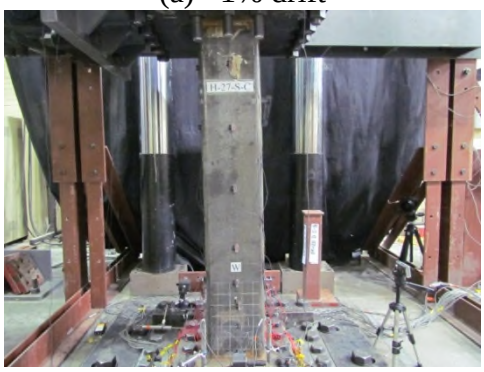

(c) +2% drift

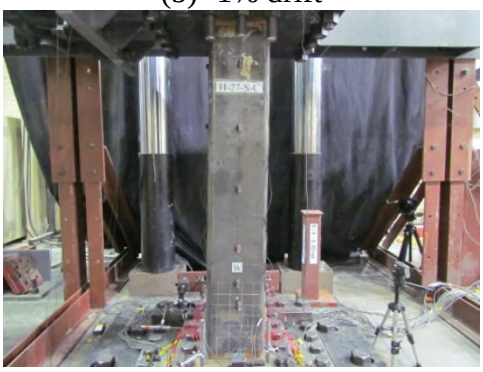

(d) -2% drift

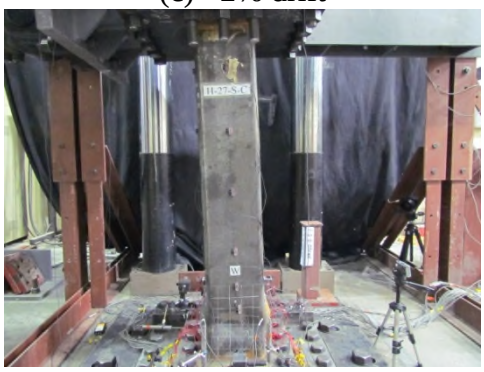

(e) +3% drift

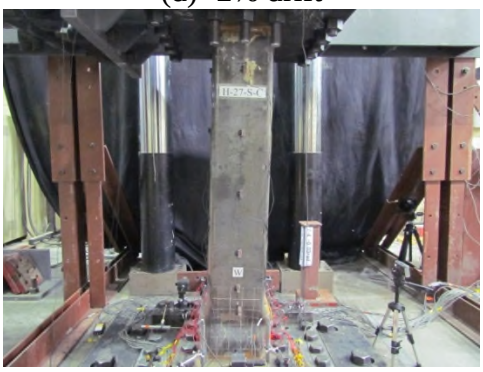

(f) -3% drift

(g) +4% drift

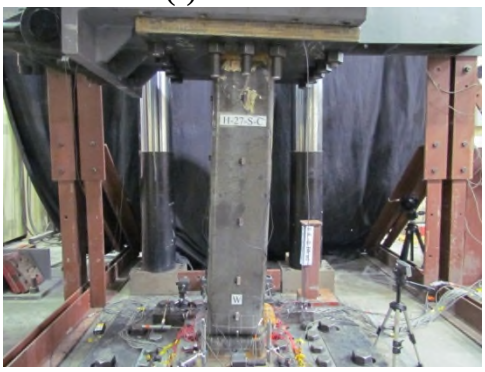

(h) -4% drift (squashed)

Figure A.5 H-27-S-C specimen: Overall deformed configuration (west view)

(a) North view

(b) West view

(c) South view

(d) East view

Figure A.6 H-27-S-C specimen: Post-test specimen observation

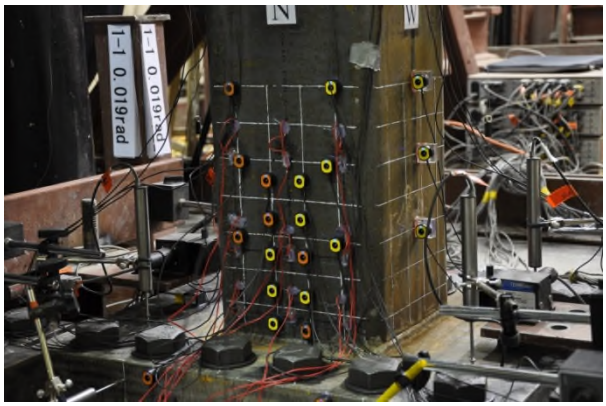

(a) Before test

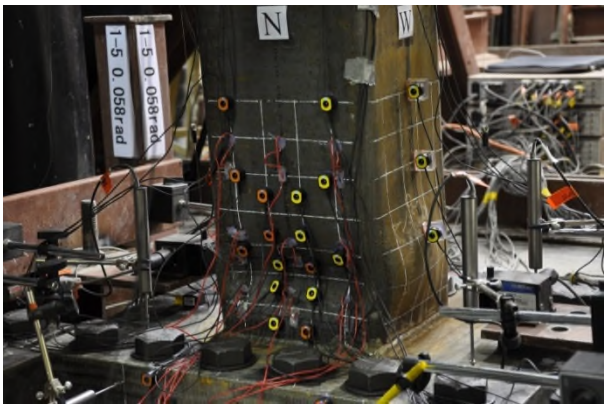

(b) 5th excursion in phase 1 (5.8% drift)

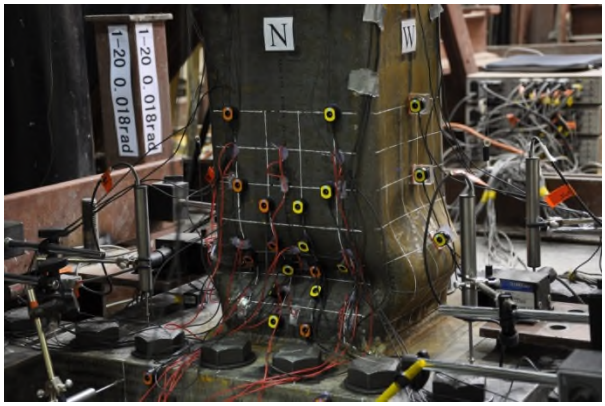

(c) End of phase 1 (1.8% drift)

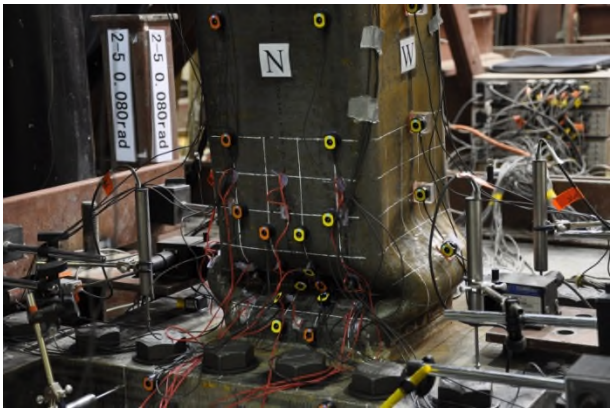

(d) 5th excursion in phase 2 (8% drift)

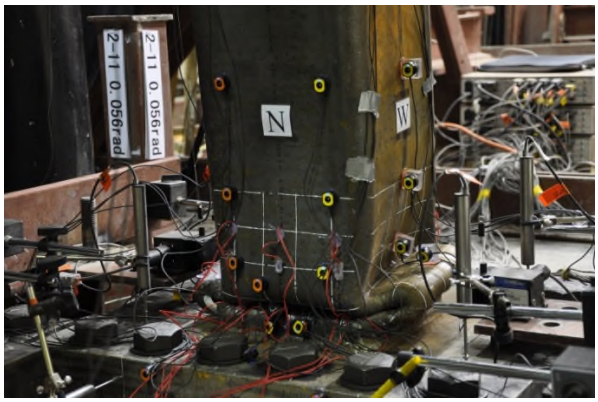

(e) 11th excursion in phase 2 (squashed)

Figure A.7 H-27-C1-C: Flange local buckling (North West view)

(a) Before test

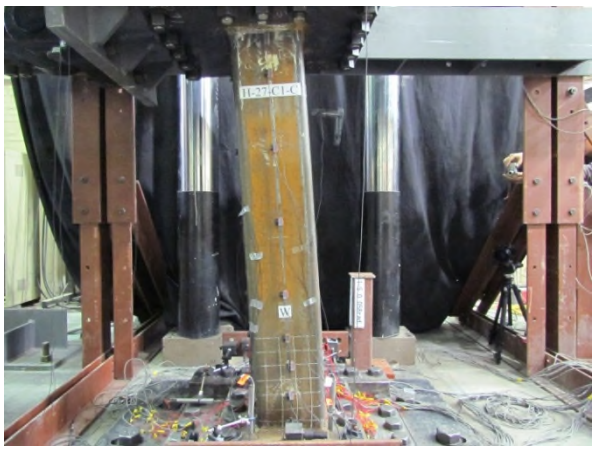

(b) 5th excursion in phase 1 (5.8% drift)

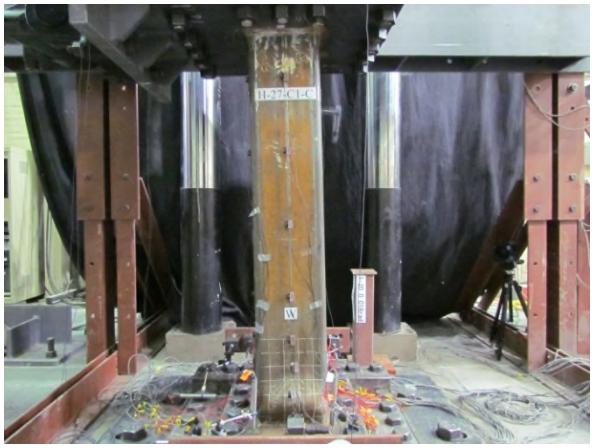

(c) End of phase 1 (1.8% drift)

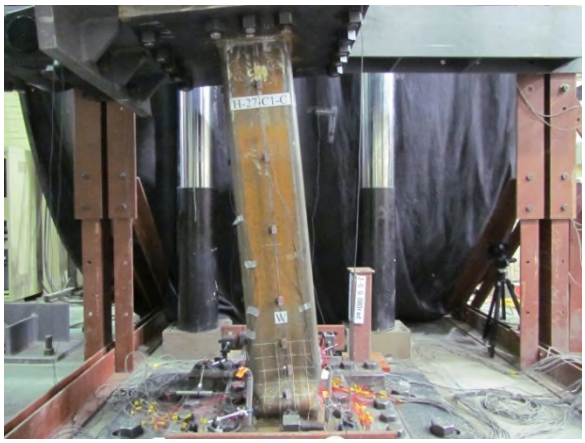

(d) 5th excursion in phase 2 (8% drift)

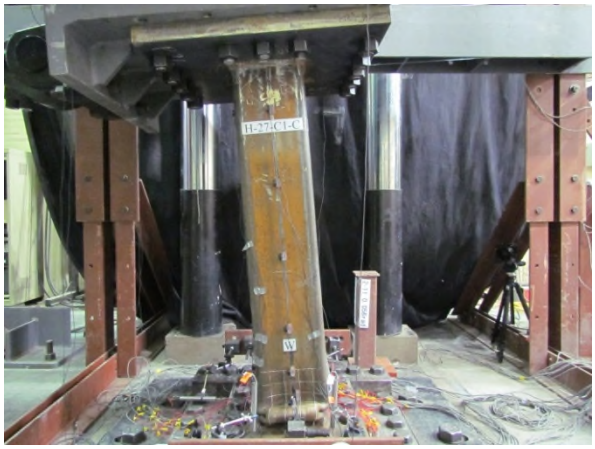

(e) 11th excursion in phase 2 (squashed)

Figure A.8 H-27-C1-C: Overall deformed configuration (West view)

(a) North view

(b) West view

(c) South view

(d) East view

Figure A.9 H-27-C1-C: Post-test specimen observation

(e) North east corner fracture

(f) North west corner fracture

Figure A.9 H-27-C1-C: Post-test specimen observation (continued)

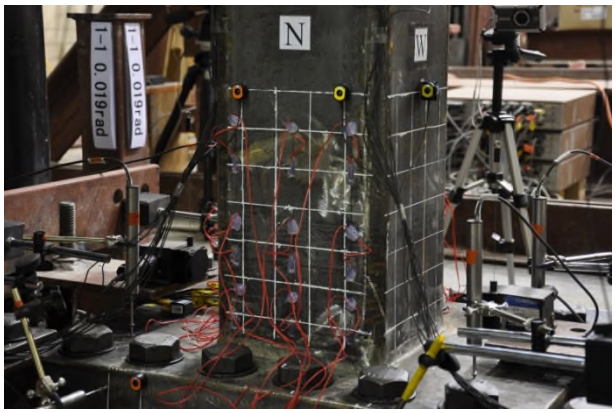

(a) Before test

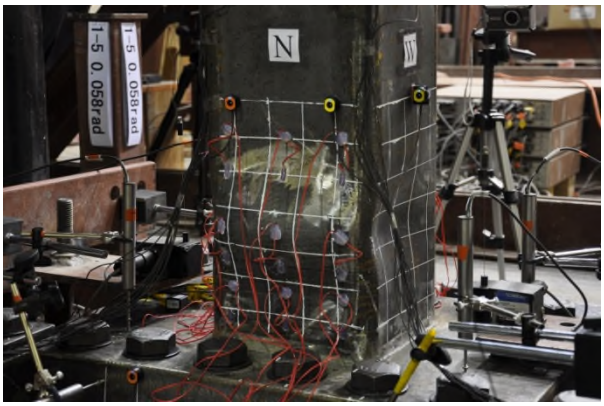

(b) 5th excursion in phase 1 (5.8% drift)

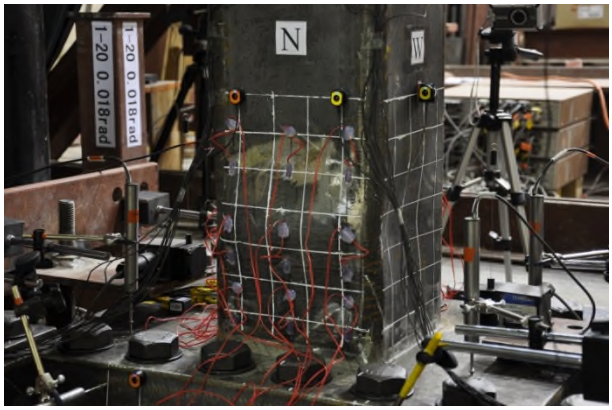

(c) End of phase 1 (1.8% drift)

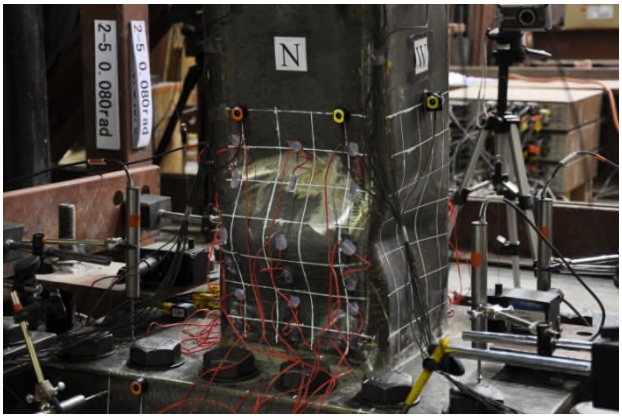

(d) 5th excursion in phase 2 (8% drift)

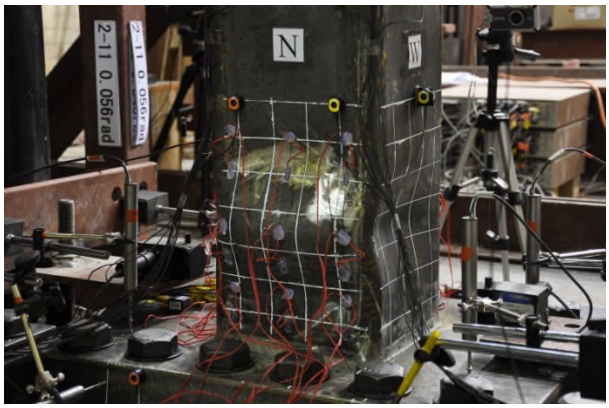

(e) 11th excursion in phase 2 (5.6% drift)

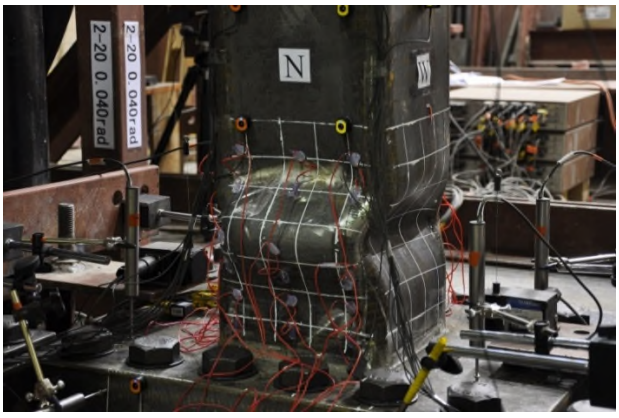

(f) End of phase 2 (4% drift)

Figure A.10 H-27-C1-V: Flange local buckling (North West view)

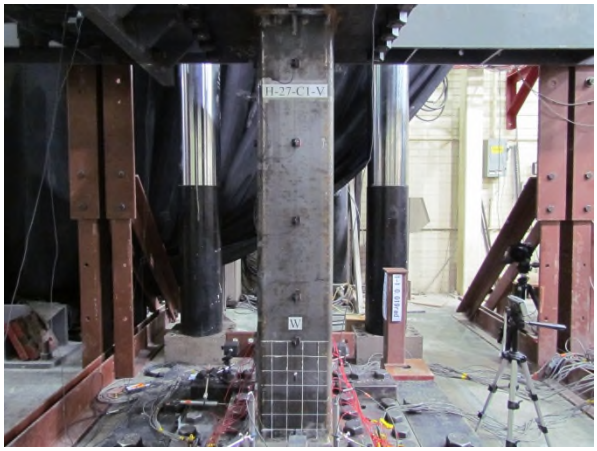

(a) Before test

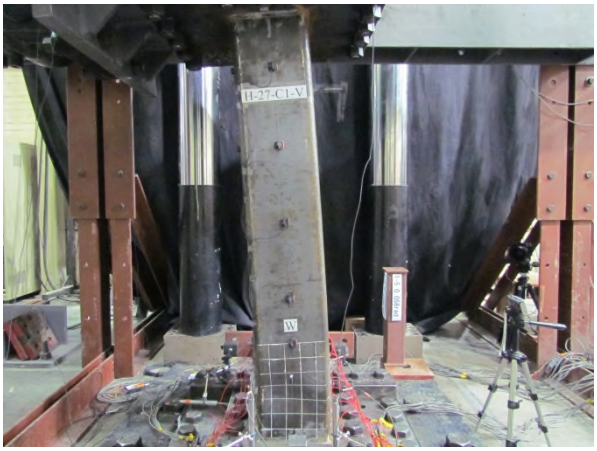

(b) 5th excursion in phase 1 (5.8% drift)

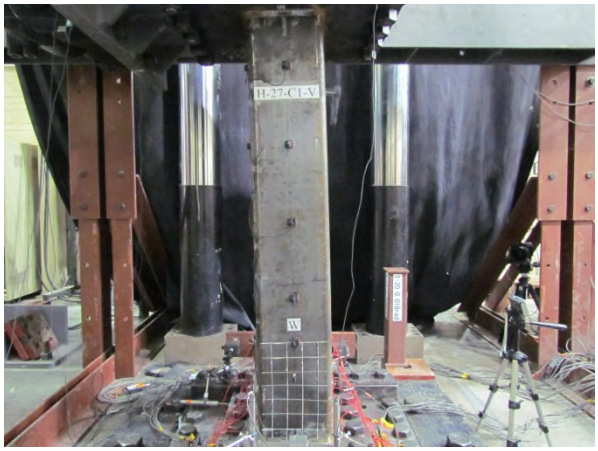

(c) End of phase 1 (1.8% drift)

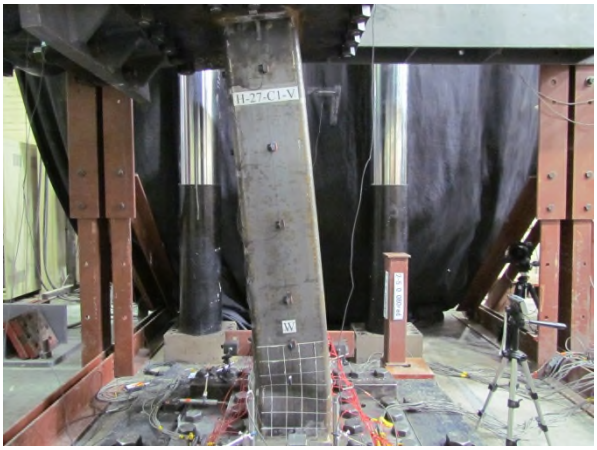

(d) 5th excursion in phase 2 (8% drift)

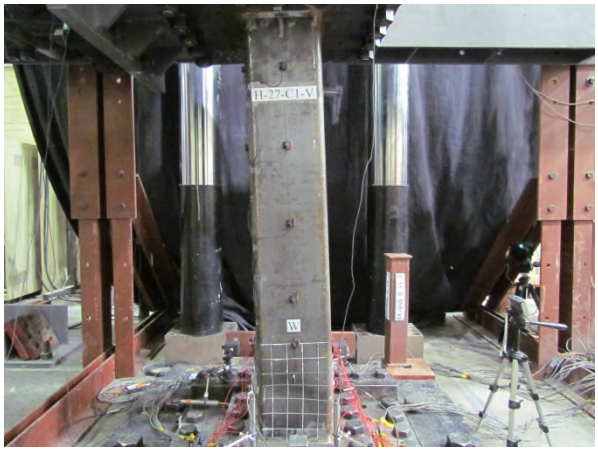

(e) 11th excursion in phase 2 (5.6% drift)

(f) End of phase 2 (4% drift)

Figure A.11 H-27-C1-V: Overall deformed configuration (West view)

(a) North view

(b) West view

(c) South view

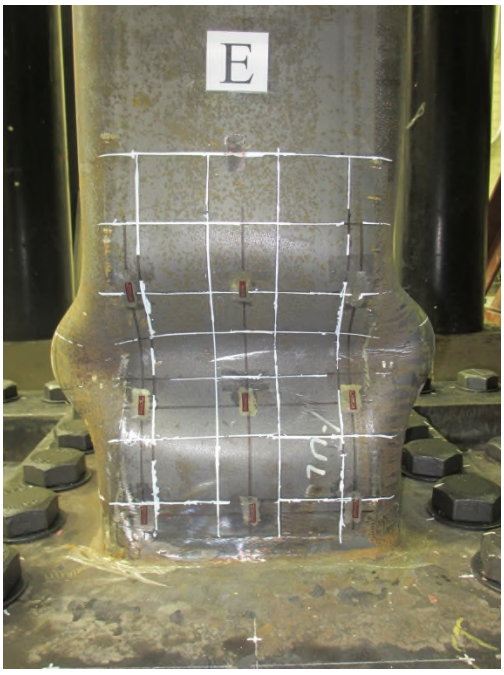

(d) East view

Figure A.12 H-27-C1-V: Post-test specimen observation

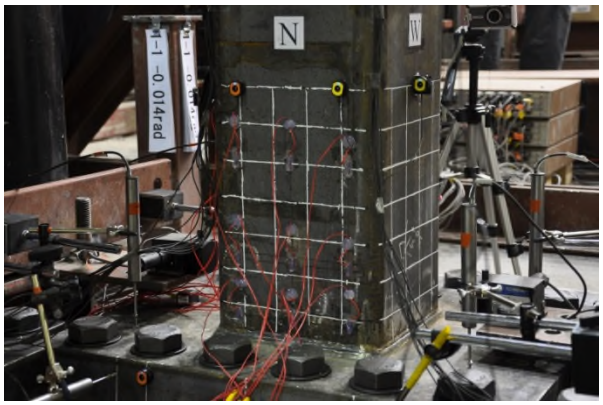

(a) Before test

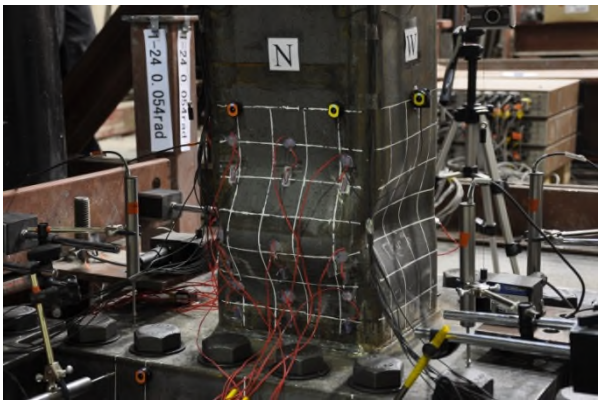

(b) 24th excursion in phase 1 (5.4% drift)

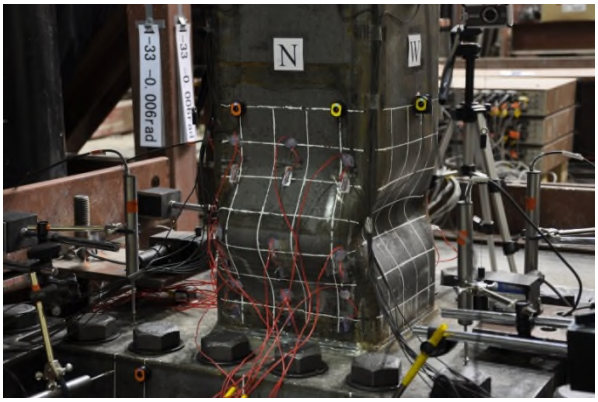

(c) 33rd excursion in phase 1 (-0.6% drift)

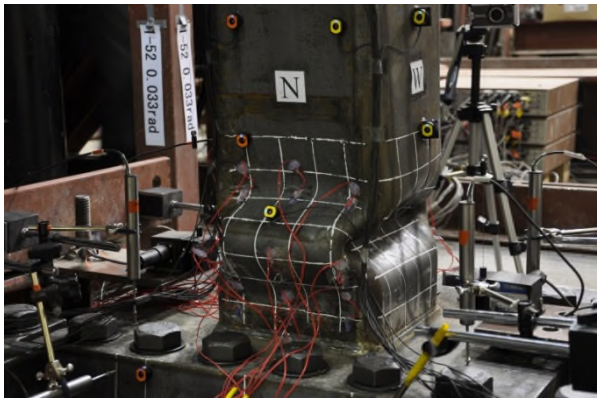

(d) End of phase 1 (3.3% drift)

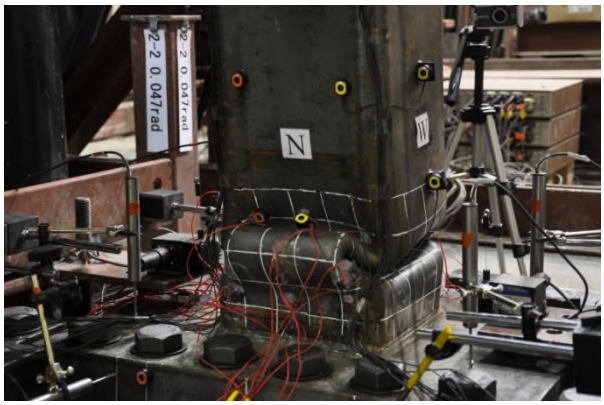

(e) 2nd excursion in phase 2 (squashed)

Figure A.13 H-27-C2-C: Flange local buckling (North West view)

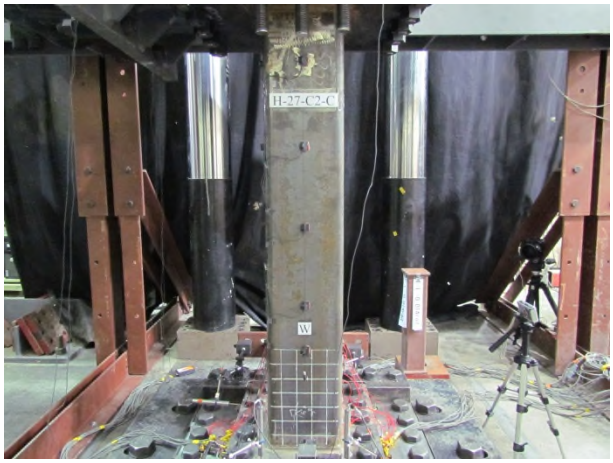

(a) Before test

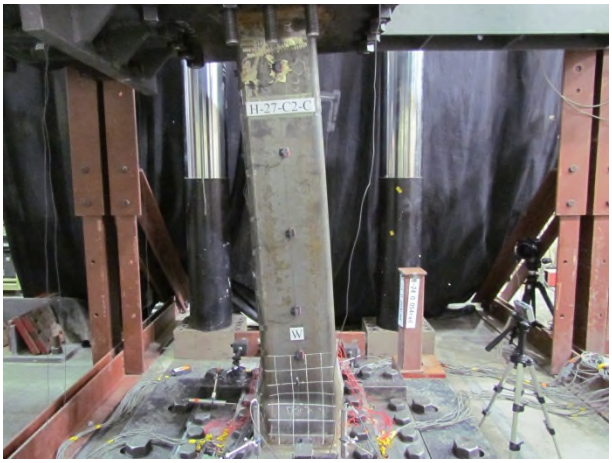

(b) 24th excursion in phase 1 (5.4% drift)

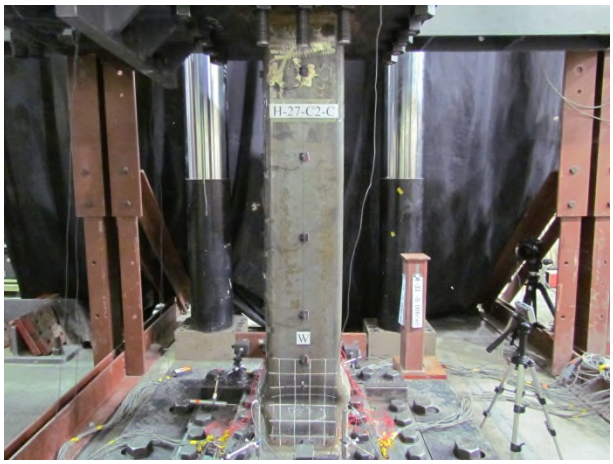

(c) 33rd excursion in phase 1 (-0.6% drift)

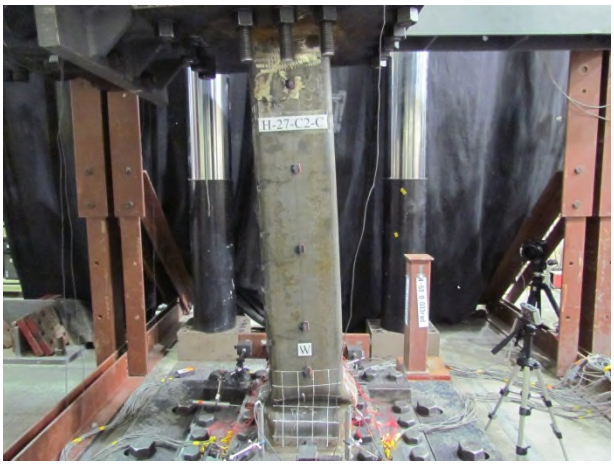

(d) End of phase 1 (3.3% drift)

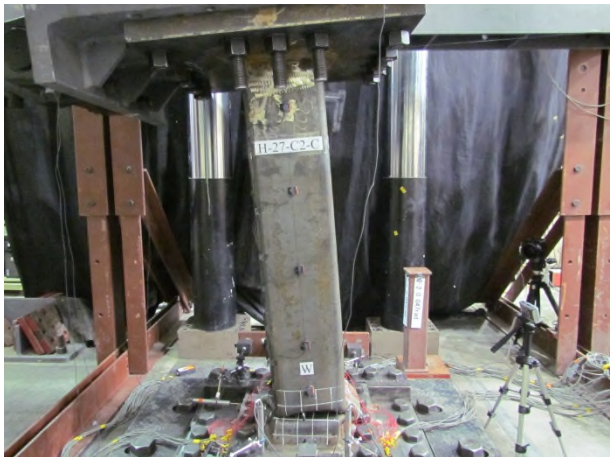

(e) 2nd excursion in phase 2 (squashed)

Figure A.14 H-27-C2-C: Overall deformed configuration (West view)

(a) North view

(b) West view

(c) South view

(d) East view

Figure A.15 H-27-C2-C: Post-test specimen observation

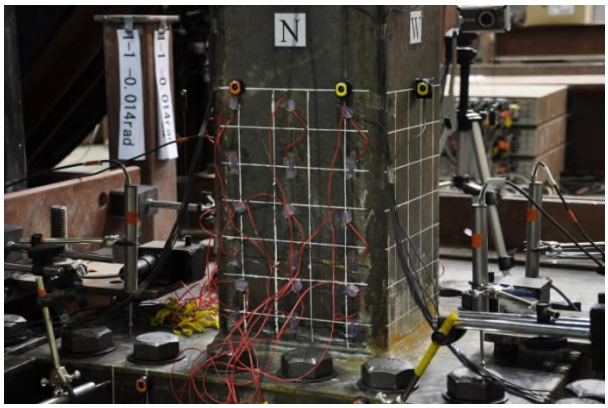

(a) Before test

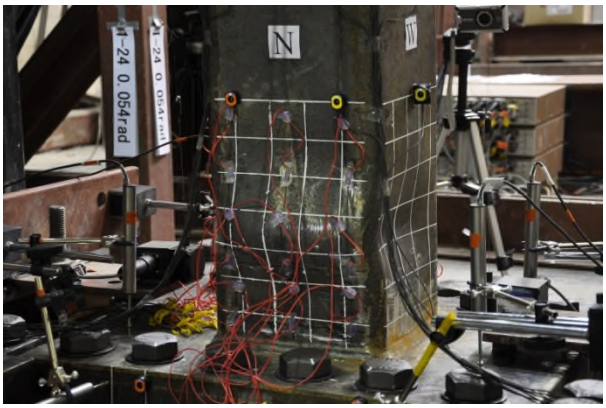

(b) 24th excursion in phase 1 (5.4% drift)

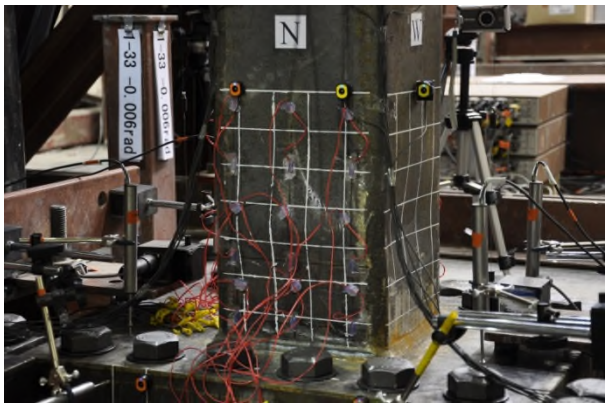

(c) 33rd excursion in phase 1 (-0.6% drift)

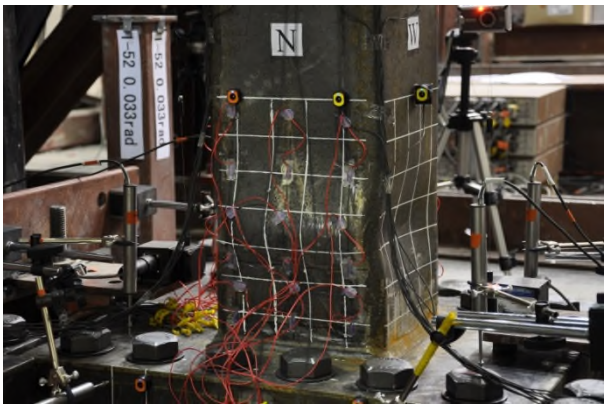

(d) End of phase 1 (3.3% drift)

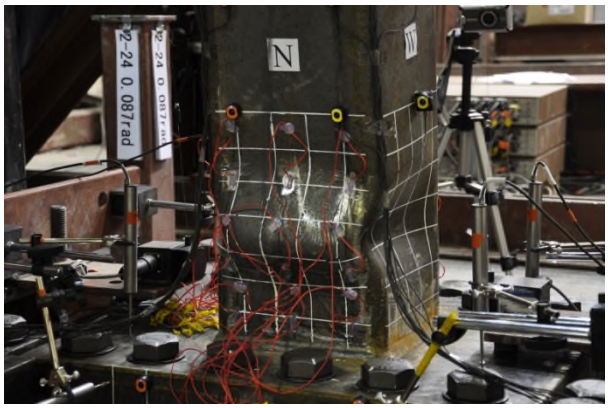

(e) 24th excursion in phase 2 (8.7% drift)

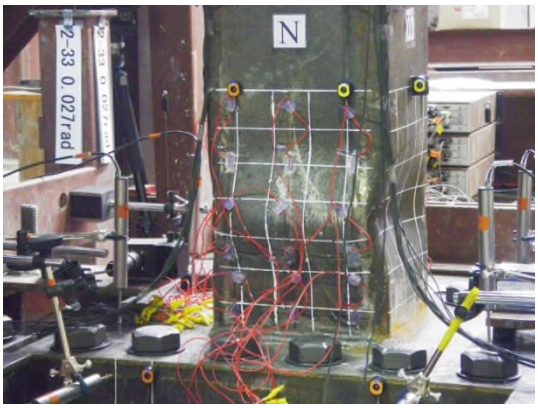

(f) 33rd excursion in phase 2 (2.7% drift)

Figure A.16 H-27-C2-V: Flange local buckling (North West view)

(a) Before test

(b) 24th excursion in phase 1 (5.4% drift)

(c) 33rd excursion in phase 1 (-0.6% drift)

(d) End of phase 1 (3.3% drift)

(e) 24th excursion in phase 2 (8.7% drift)

(f) 33rd excursion in phase 2 (2.7% drift)

Figure A.17 H-27-C2-V: Overall deformed configuration (West view)

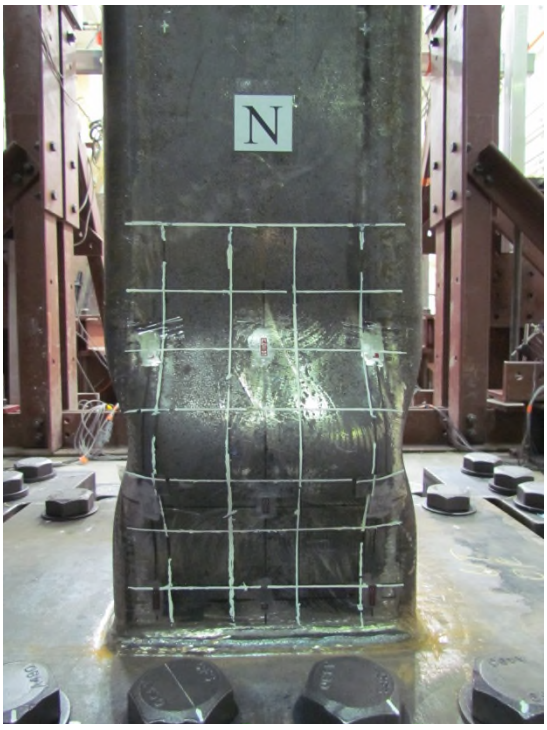

(a) North view

(b) West view

(c) South view

(d) East view

Figure A.18 H-27-C2-V: Post-test specimen observation

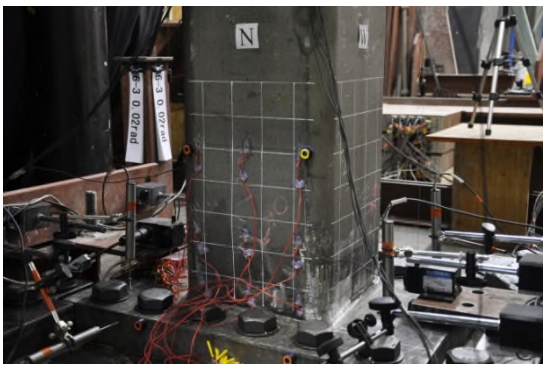

(a) +2% drift

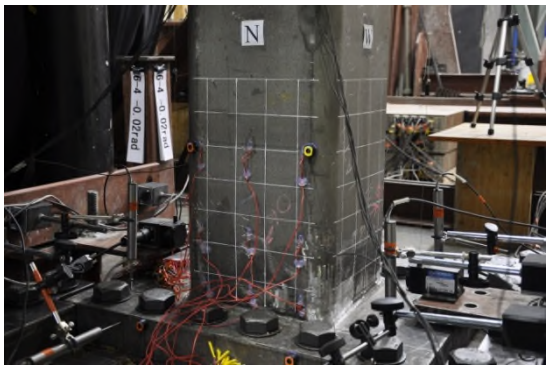

(b) +2% drift

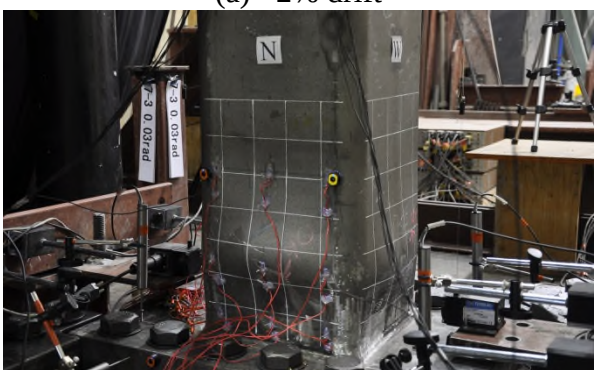

(c) +3% drift

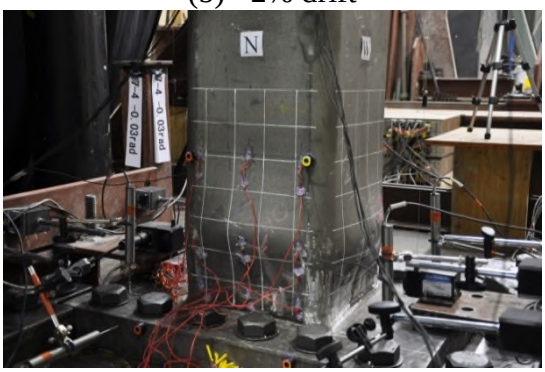

(d) -3% drift

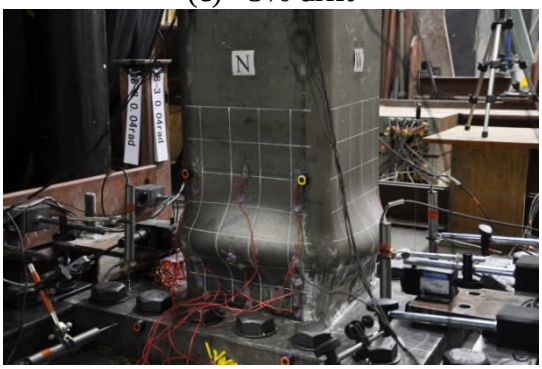

(e) +4% drift

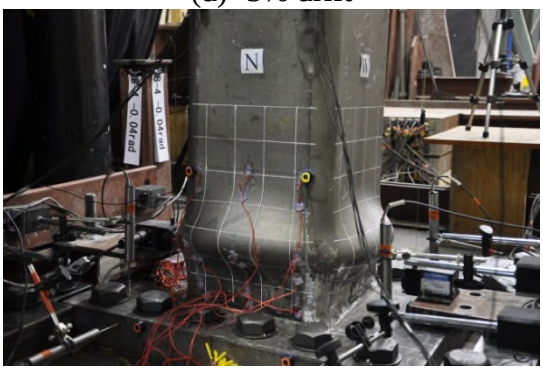

(f) -4% drift

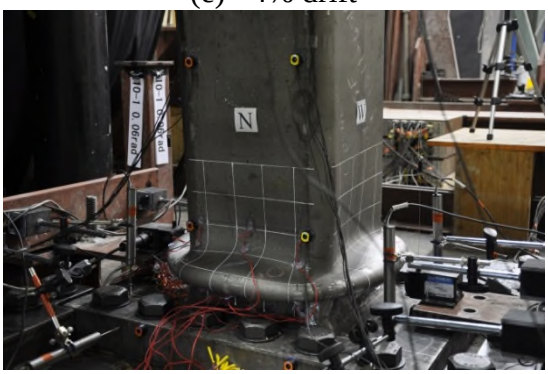

(g) +6% drift

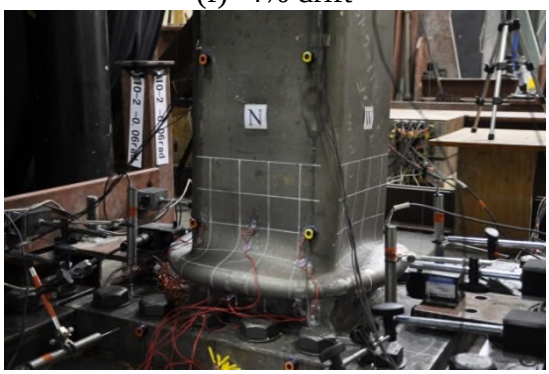

(h) -6% drift

Figure A.19 H-19-S-C: Flange local buckling (North West view)

(a) +2% drift

(b) +2% drift

(c) +3% drift

(d) -3% drift

(e) +4% drift

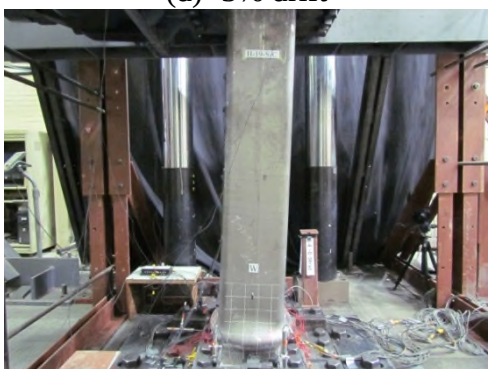

(f) -4% drift

(g) +6% drift

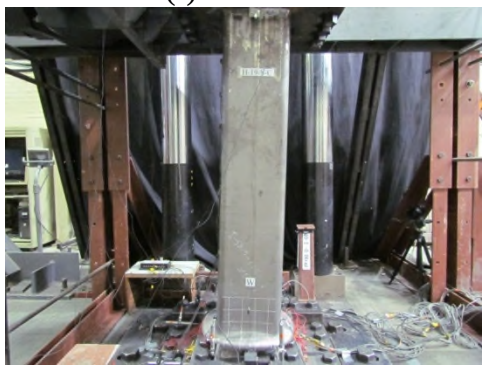

(h) -6% drift

Figure A.20 H-19-S-C: Overall deformed configuration (West view)

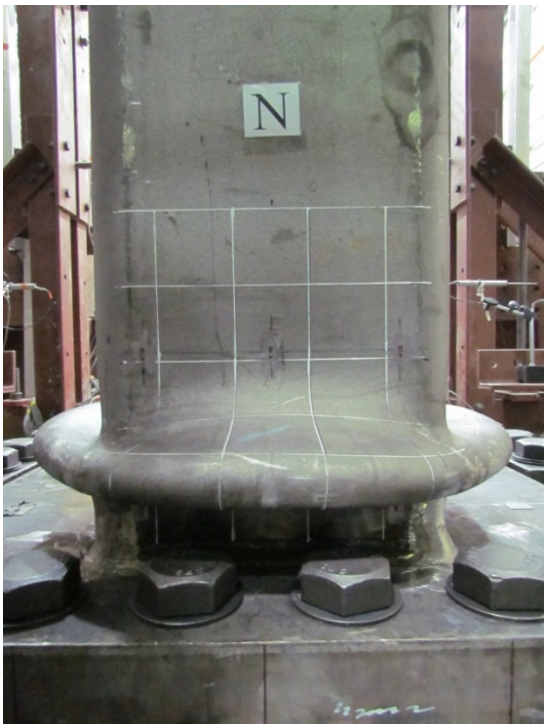

(a) North view

(b) West view

(c) South view

(d) East view

Figure A.21 H-19-S-C: Post-test specimen observation

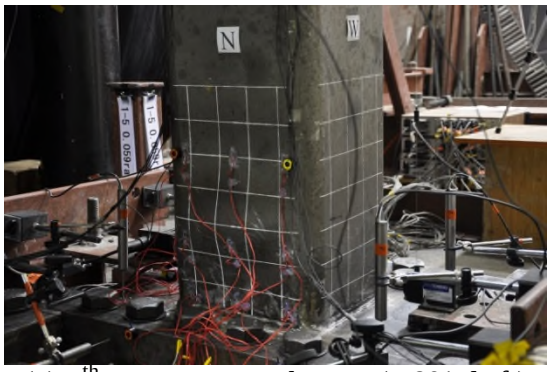

(a) 5th excursion in phase 1 (5.9% drift)

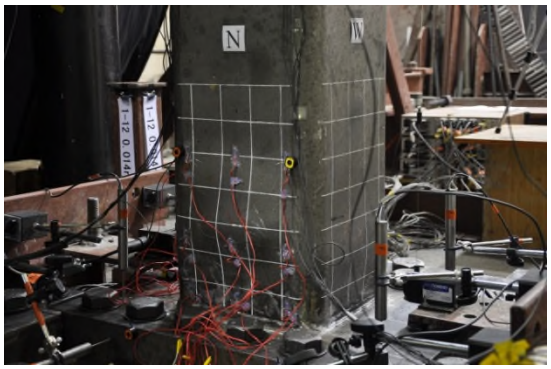

(b) End of phase 1 (1.4% drift)

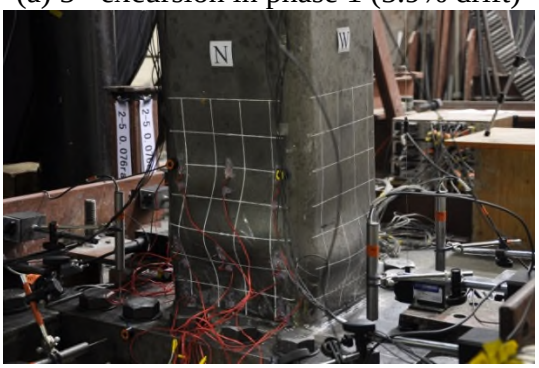

(c) 5th excursion in phase 2 (7.6% drift)

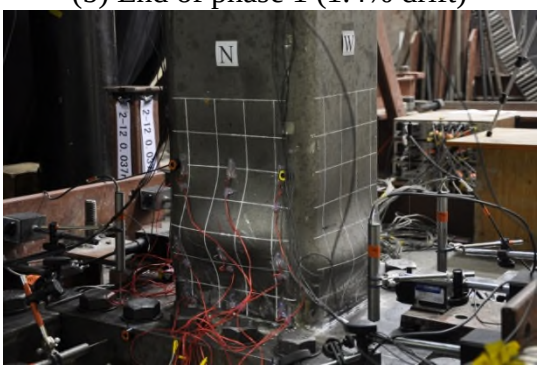

(d) End of phase 2 (3.7% drift)

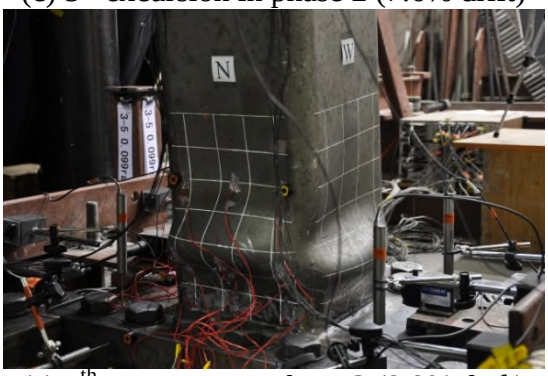

(e) 5th excursion in phase 3 (9.9% drift)

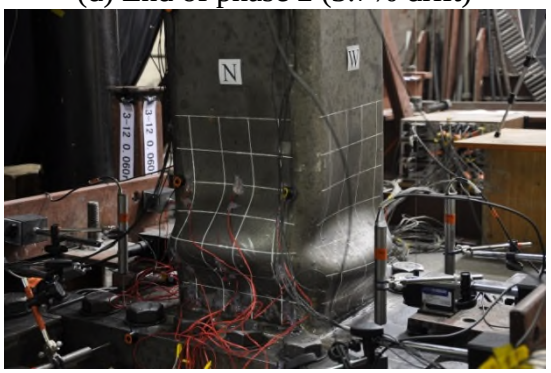

(f) End of phase 3 (6% drift)

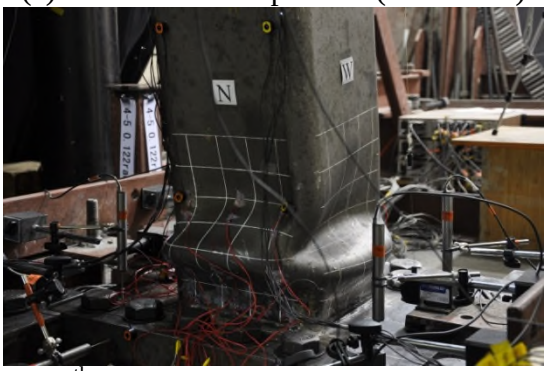

(g) 5th excursion in phase 4 (12.2% drift)

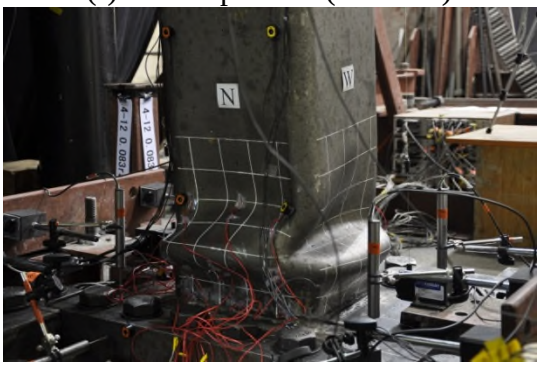

(h) End of phase 4 (8.3% drift)

Figure A.22 H-19-C1-C: Flange local buckling (North West view)

(a) 5th excursion in phase 1 (5.9% drift)

(b) End of phase 1 (1.4% drift)

(c) 5th excursion in phase 2 (7.6% drift)

(d) End of phase 2 (3.7% drift)

(e) 5th excursion in phase 3 (9.9% drift)

(f) End of phase 3 (6% drift)

(g) 5th excursion in phase 4 (12.2% drift)

(h) End of phase 4 (8.3% drift)

Figure A.23 H-19-C1-C: Overall deformed configuration (West view)

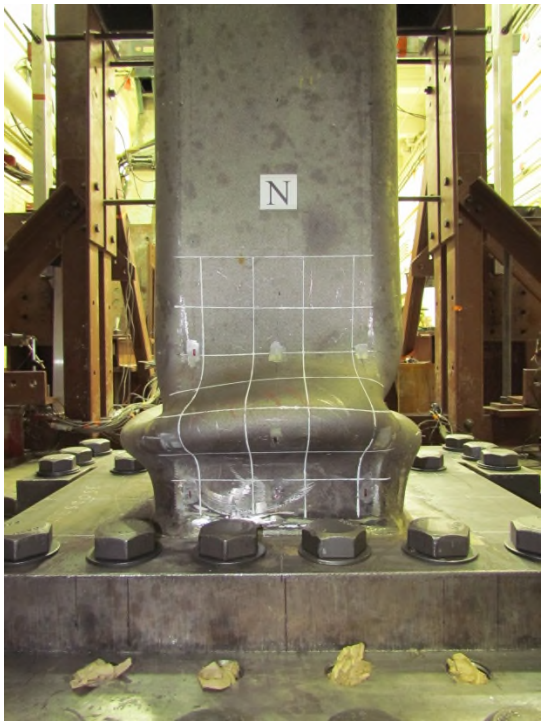

(a) North view

(b) West view

(c) South view

(d) East view

Figure A.24 H-19-C1-C: Post-test specimen observation

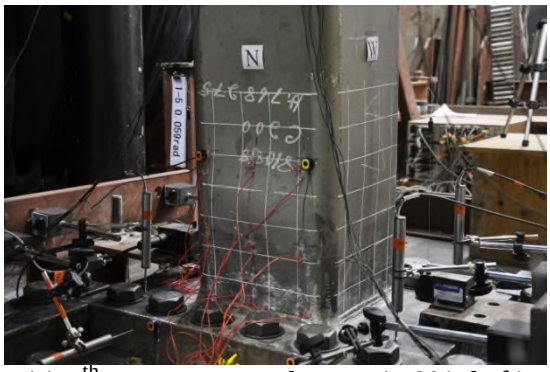

(a) 5th excursion in phase 1 (5.9% drift)

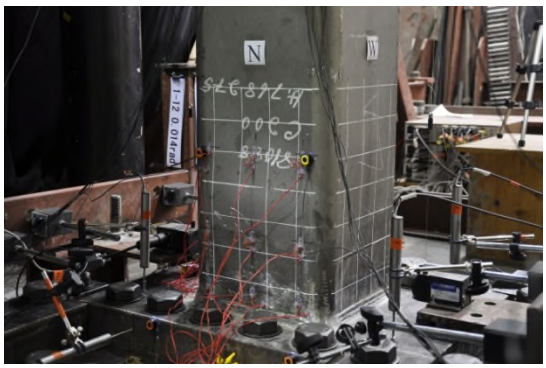

(b) End of phase 1 (1.4% drift)

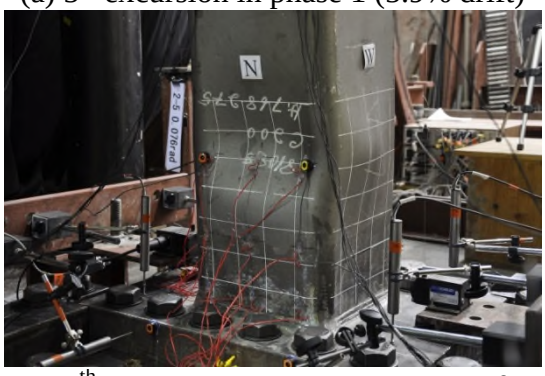

(c) 5th excursion in phase 2 (7.6% drift)

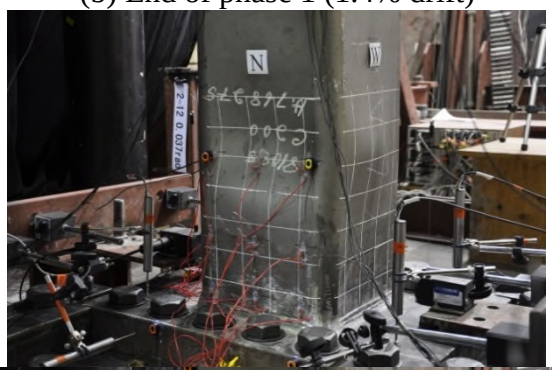

(d) End of phase 2 (3.7% drift)

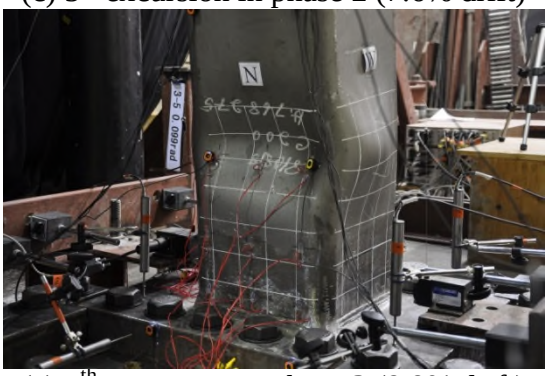

(e) 5th excursion in phase 3 (9.9% drift)

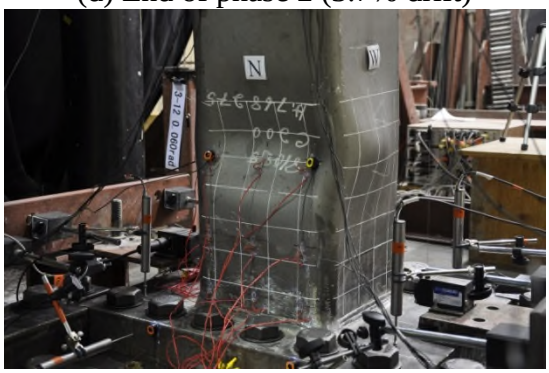

(f) End of phase 3 (6% drift)

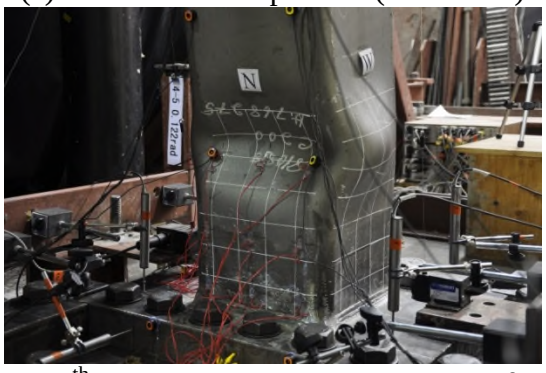

(g) 5th excursion in phase 4 (12.2% drift)

Figure A.25 H-19-C1-V: Flange local buckling (North West view)

(a) 5th excursion in phase 1 (5.9% drift)

(b) End of phase 1 (1.4% drift)

(c) 5th excursion in phase 2 (7.6% drift)

(d) End of phase 2 (3.7% drift)

(e) 5th excursion in phase 3 (9.9% drift)

(f) End of phase 3 (6% drift)

(g) 5th excursion in phase 4 (12.2% drift)

Figure A.26 H-19-C1-V: Overall deformed configuration (West view)

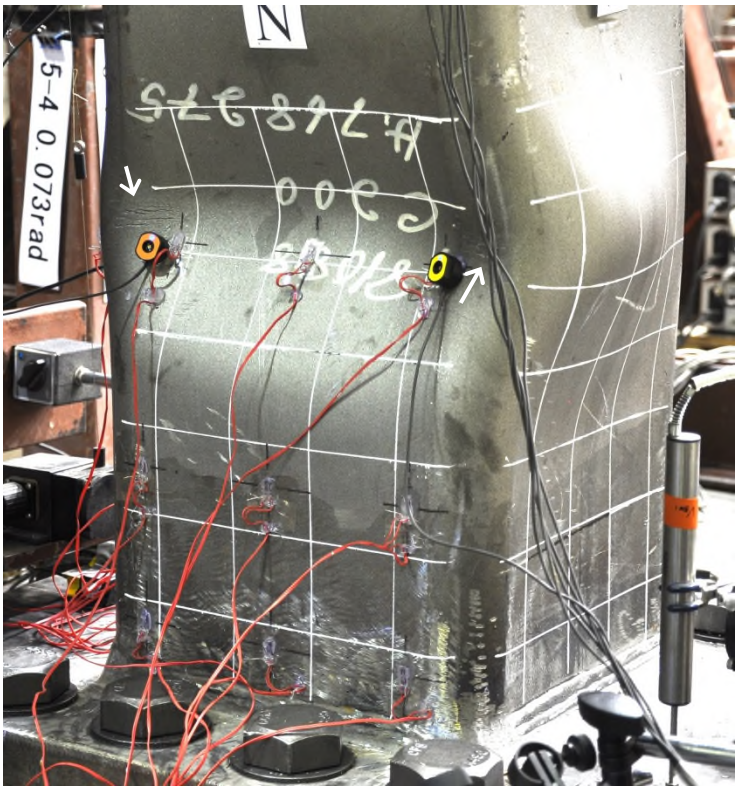

Figure A.27 H-19-C1-V: Post-test specimen observation (North West view)

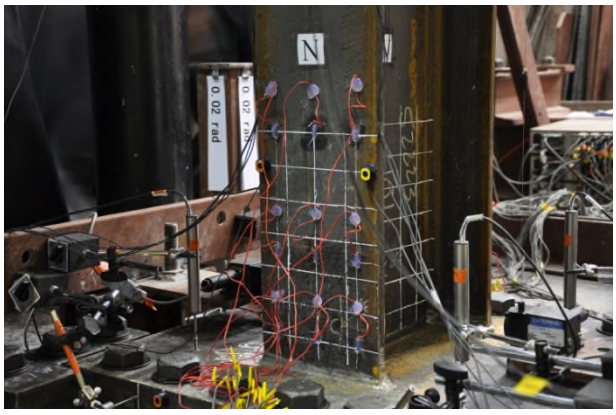

(a) 2% drift

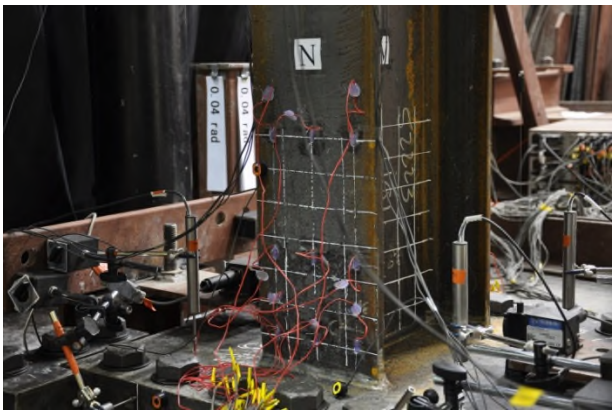

(b) 4% drift

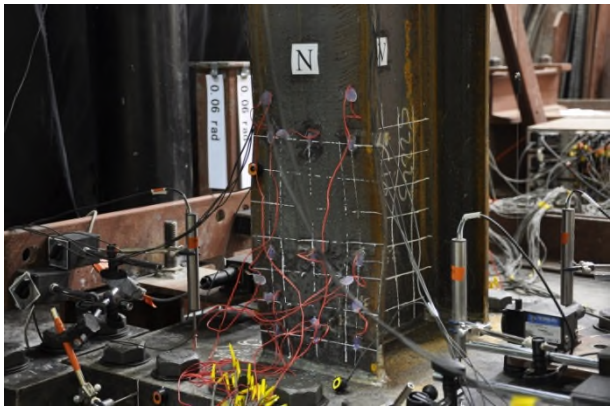

(c) 6% drift

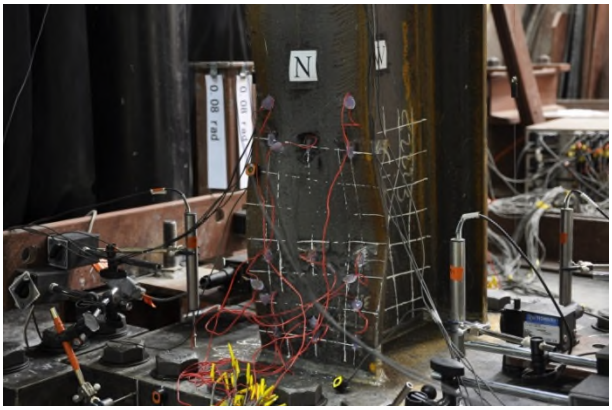

(d) 8% drift

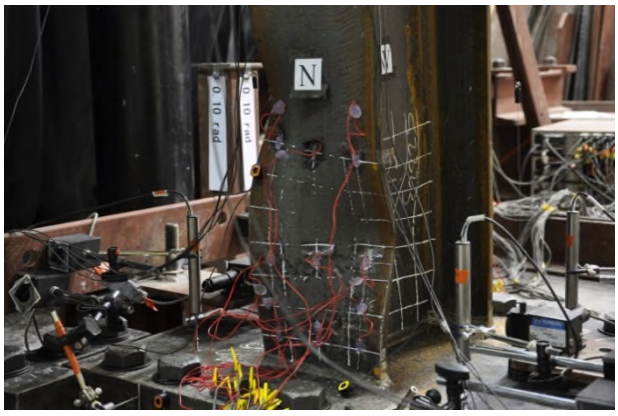

(e) 10% drift

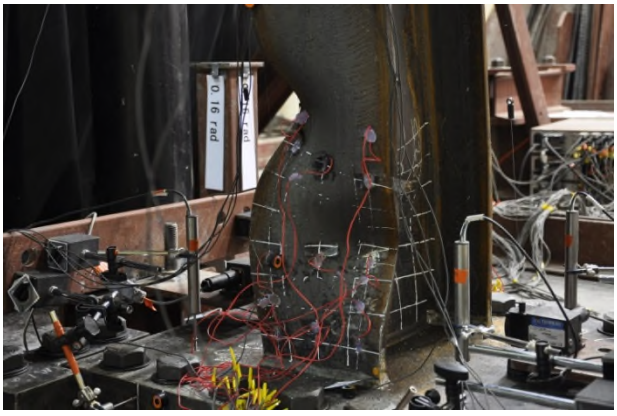

(f) 16% drift

Figure A.28 W-6-34-M-C: Flange local buckling (North West view)

(a) 2% drift

(b) 4% drift

(c) 6% drift

(d) 8% drift

(e) 10% drift

(f) 16% drift

Figure A.29 W-6-34-M-C: Overall deformed configuration (West view)

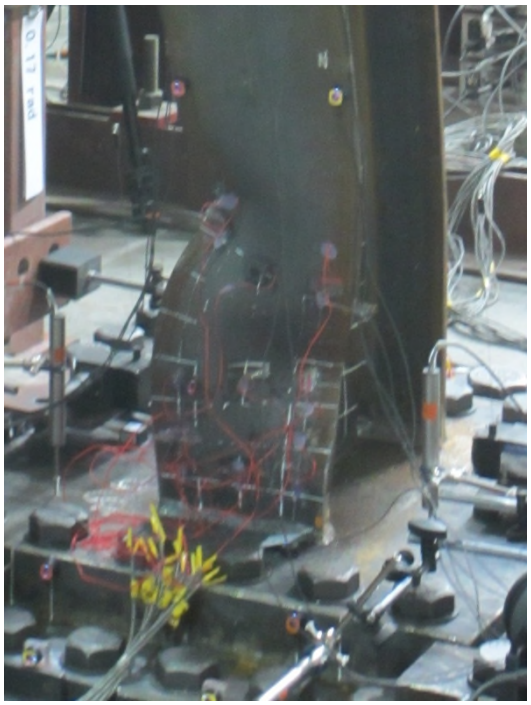

(a) North West view

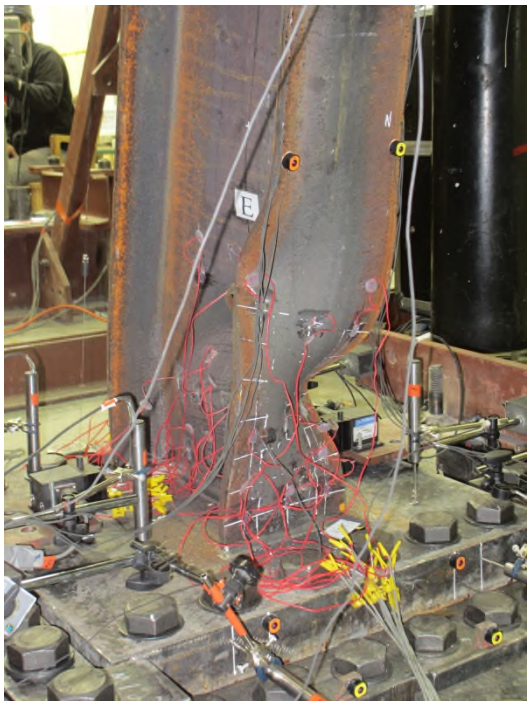

(b) North East view

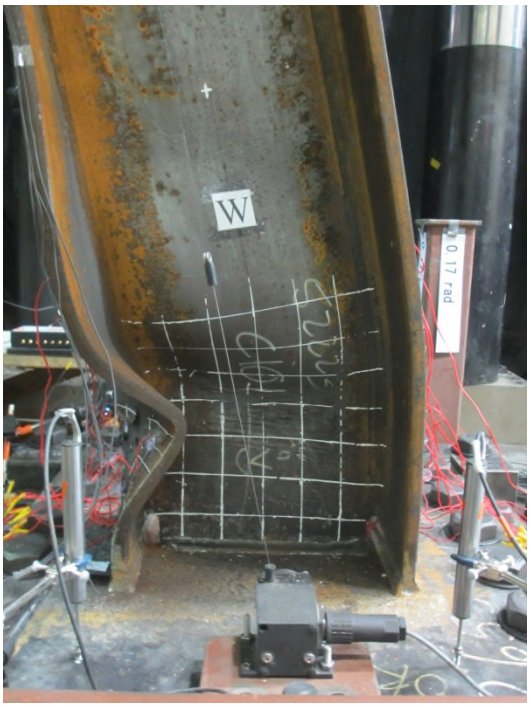

(c) West view

(d) South West view

Figure A.30 W-6-34-M-C: Post-test specimen observation

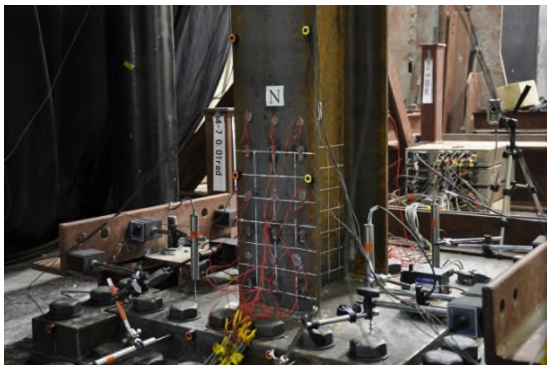

(a) +1% drift

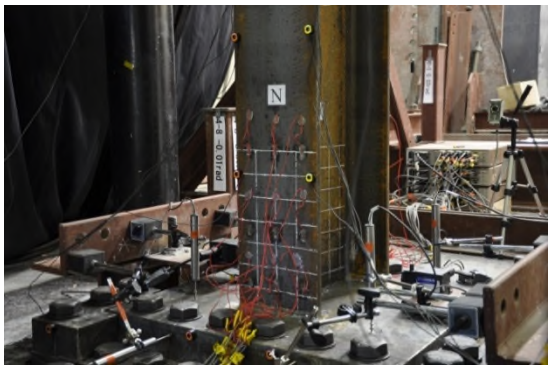

(b) -1% drift

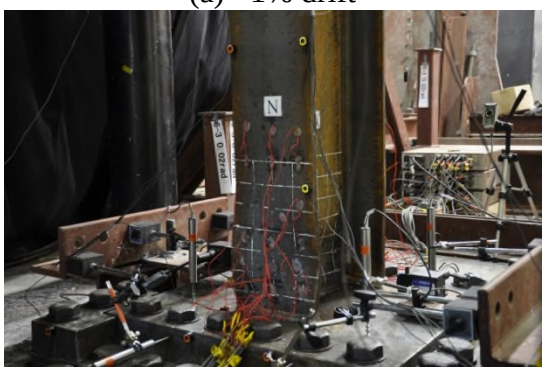

(c) +2% drift

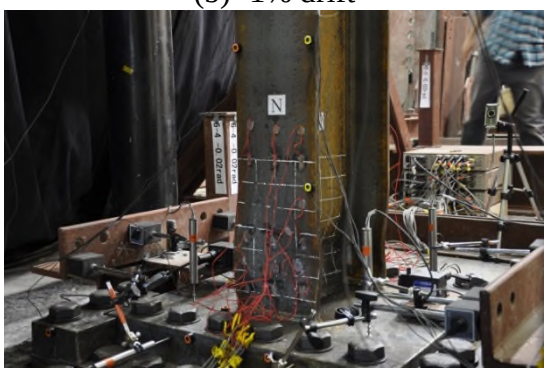

(d) -2% drift

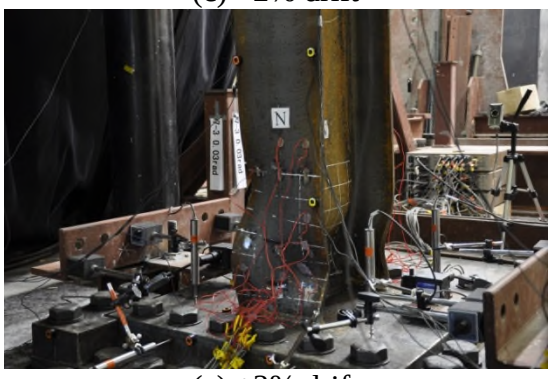

(e) +3% drift

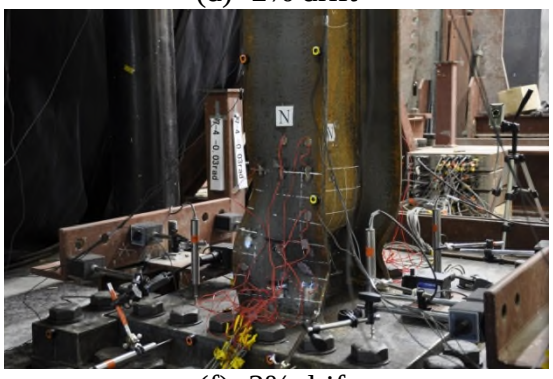

(f) -3% drift

(g) +5% drift

(h) -5% drift

Figure A.31 W-6-34-S-C: Flange local buckling (North West view)

(a) +1% drift

(b) -1% drift

(c) +2% drift

(d) -2% drift

(e) +3% drift

(f) -3% drift

(g) +5% drift

(h) -5% drift

Figure A.32 W-6-34-S-C: Overall deformed configuration (West view)

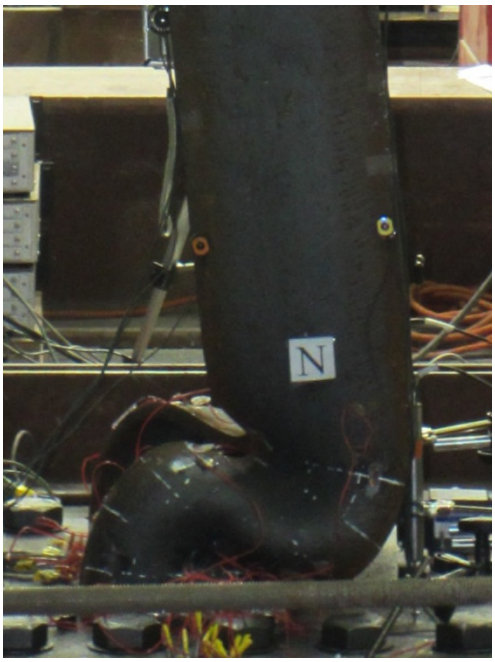

(a) North view

(b) West view

(c) South view

(d) East view

Figure A.33 W-6-34-S-C: Post-test specimen observation

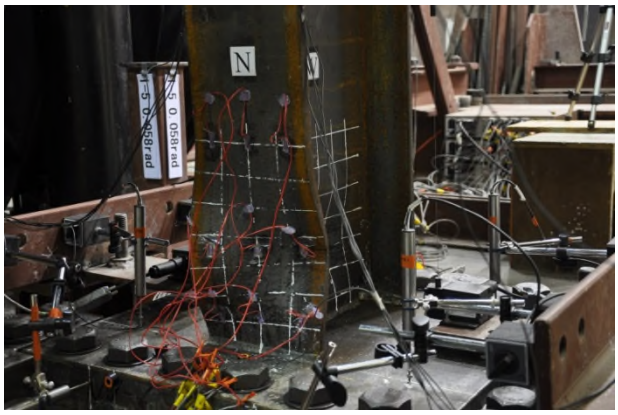

(a) 5th excursion in phase 1 (5.8% drift)

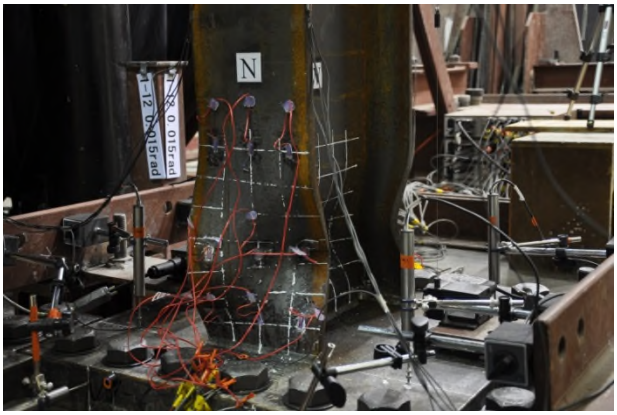

(b) End of phase 1 (1.5% drift)

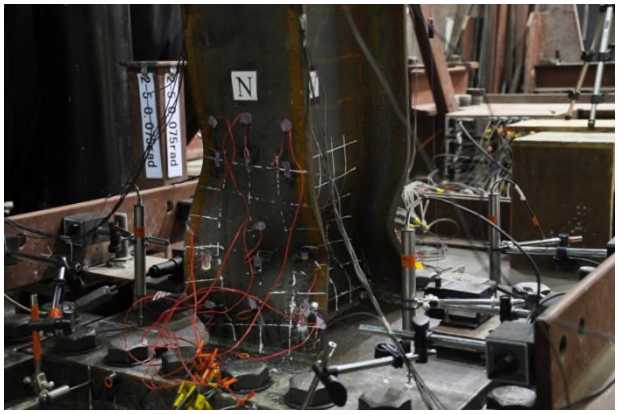

(c) 5th excursion in phase 2 (7.5% drift)

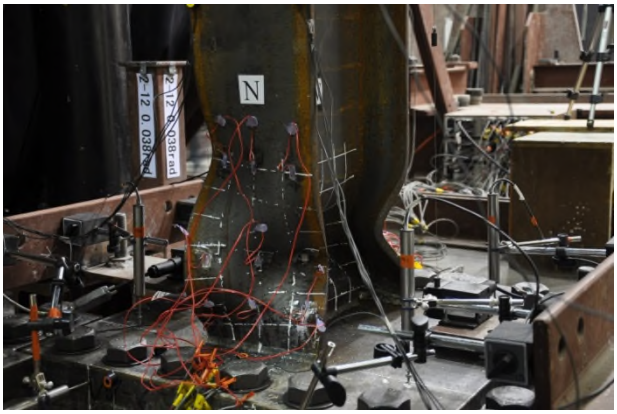

(d) End of phase 2 (3.8% drift)

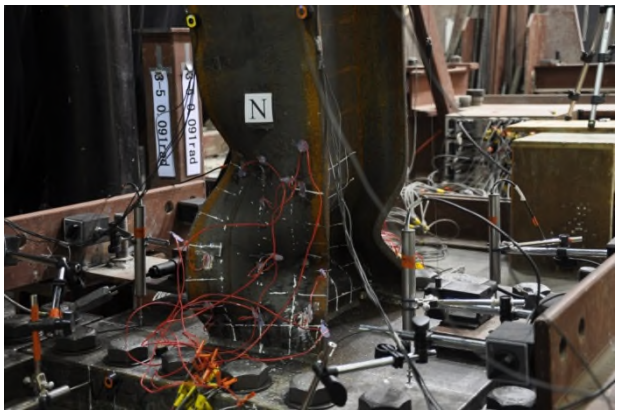

(e) 5th excursion in phase 3 (9.1% drift)

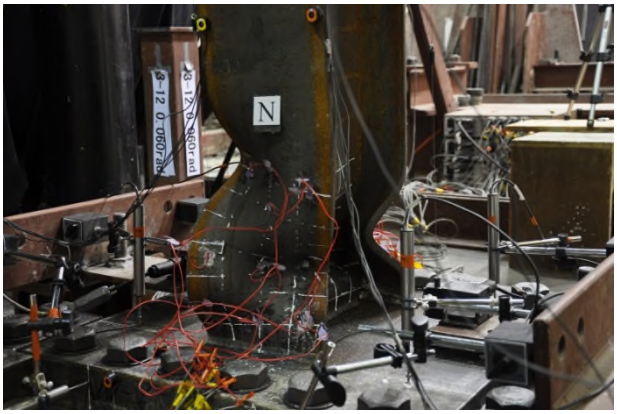

(f) End of phase 3 (6% drift)

Figure A.34 W-6-34-C1-C: Flange local buckling (North West view)

(a) 5th excursion in phase 1 (5.8% drift)

(b) End of phase 1 (1.5% drift)

(c) 5th excursion in phase 2 (7.5% drift)

(d) End of phase 2 (3.8% drift)

(e) 5th excursion in phase 3 (9.1% drift)

(f) End of phase 3 (6% drift)

Figure A.35 W-6-34-C1-C: Overall deformed configuration (West view)

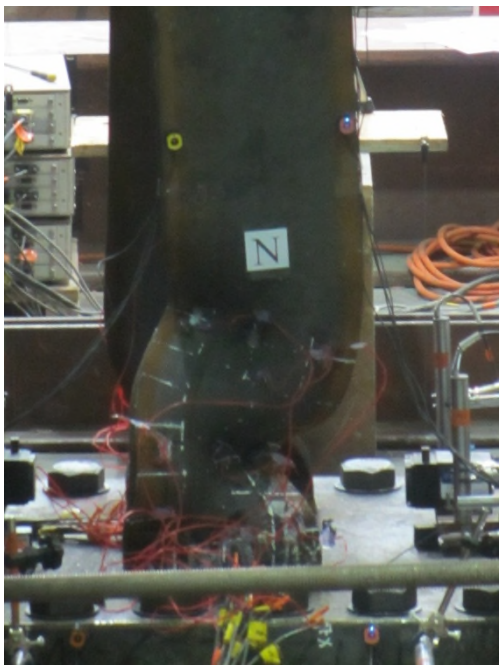

(a) North view

(b) West view

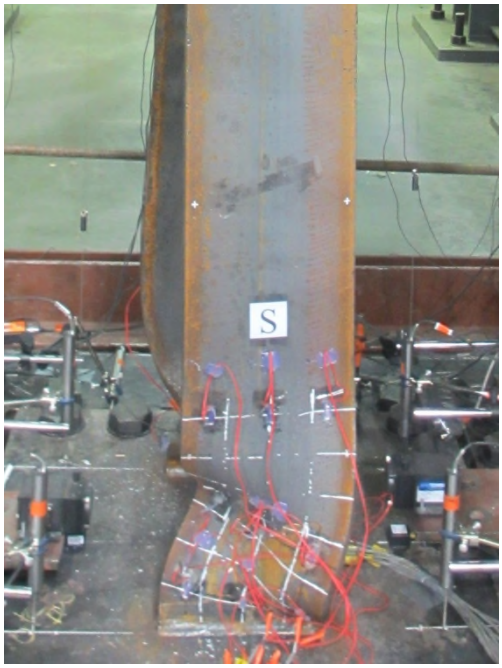

(c) South view

(d) East view

Figure A.36 W-6-34-C1-C: Post-test specimen observation

(e) Top end of north west flange

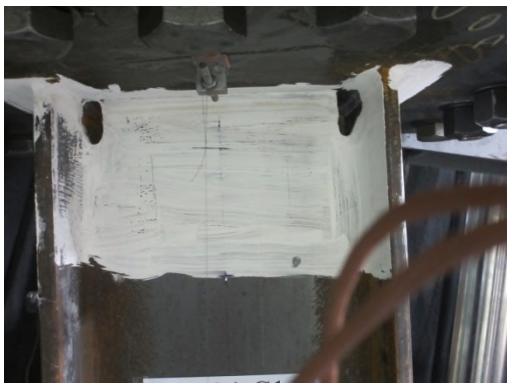

(f) Top end of north west web

Figure A.36 W-6-34-C1-C: Post-test specimen observation (continued)

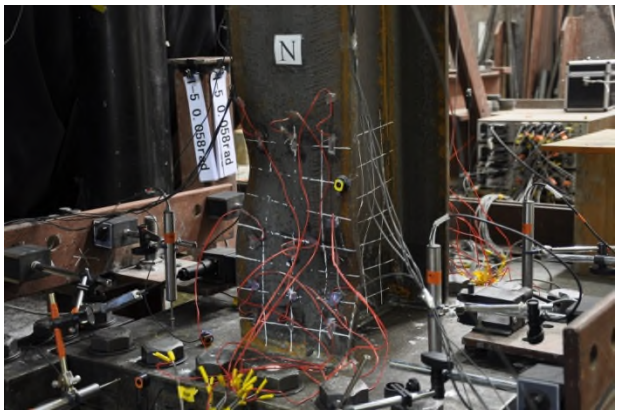

(a) 5th excursion in phase 1 (5.8% drift)

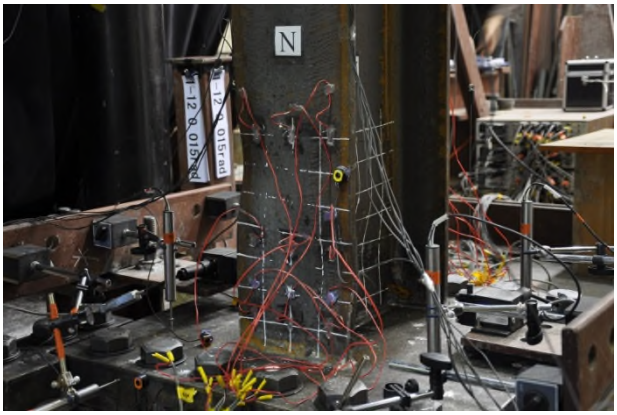

(b) End of phase 1 (1.5% drift)

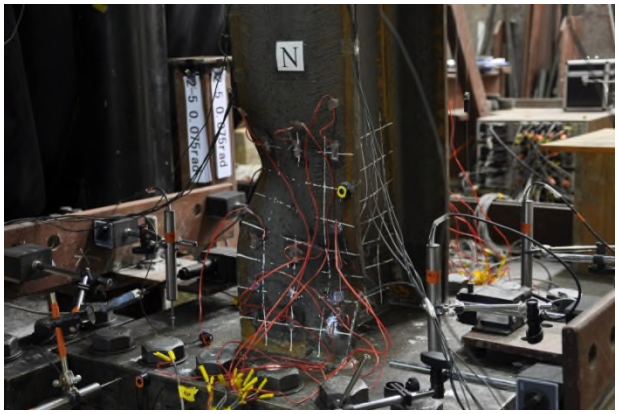

(c) 5th excursion in phase 2 (7.5% drift)

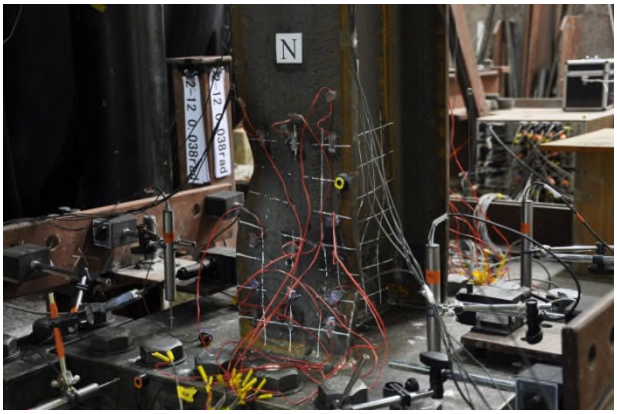

(d) End of phase 2 (3.8% drift)

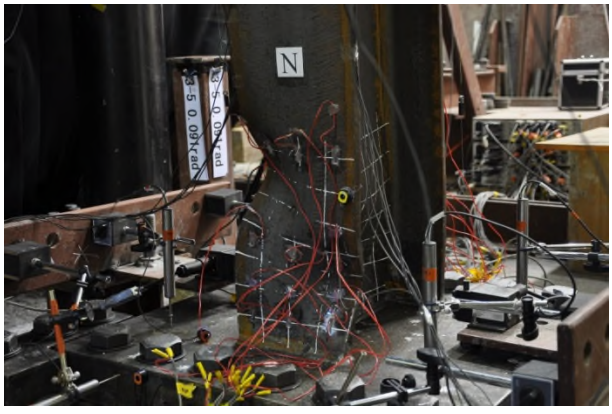

(e) 5th excursion in phase 3 (9.1% drift)

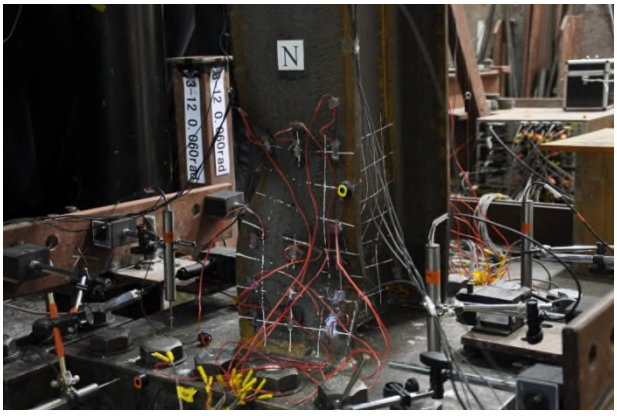

(f) End of phase 3 (6% drift)

Figure A.37 W-6-34-C1-V: Flange local buckling (North West view)

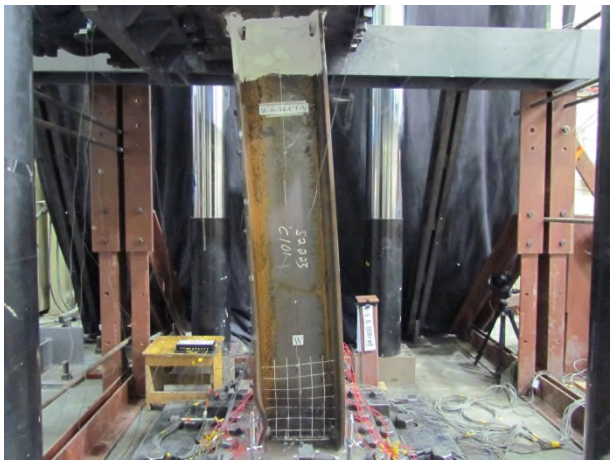

(a) 5th excursion in phase 1 (5.8% drift)

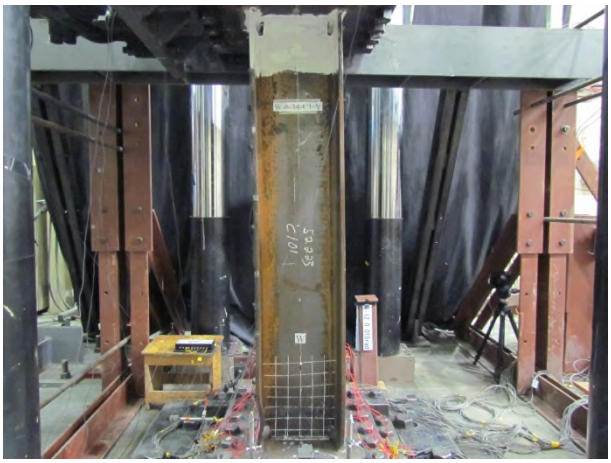

(b) End of phase 1 (1.5% drift)

(c) 5th excursion in phase 2 (7.5% drift)

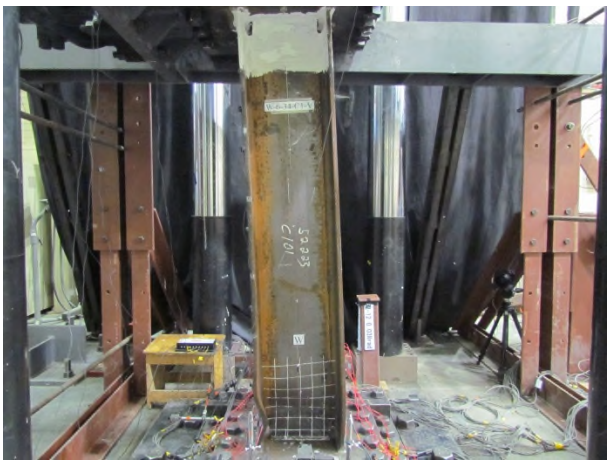

(d) End of phase 2 (3.8% drift)

(e) 5th excursion in phase 3 (9.1% drift)

(f) End of phase 3 (6% drift)

Figure A.38 W-6-34-C1-V: Overall deformed configuration (West view)

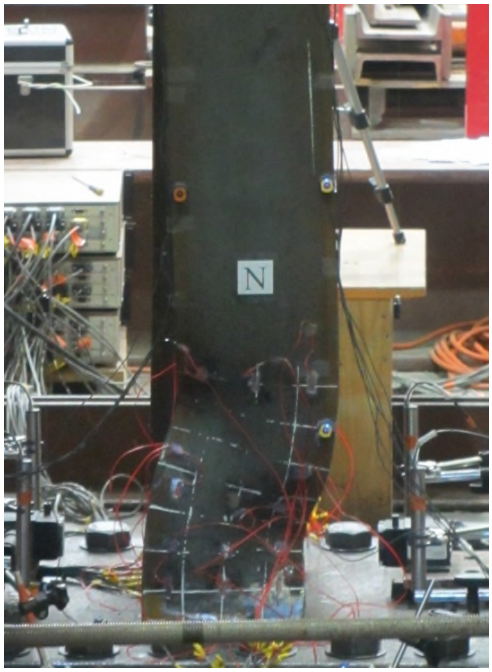

(a) North view

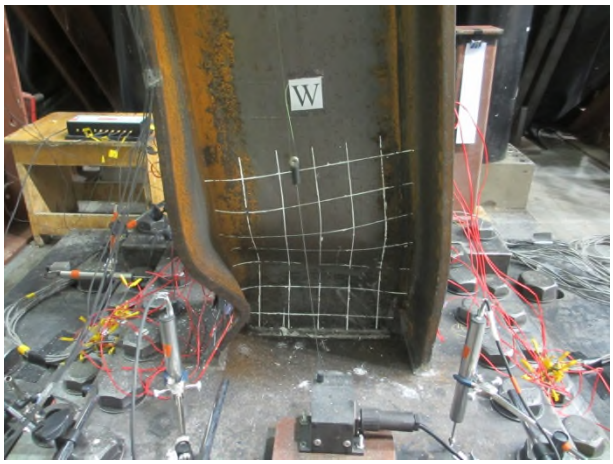

(b) West view

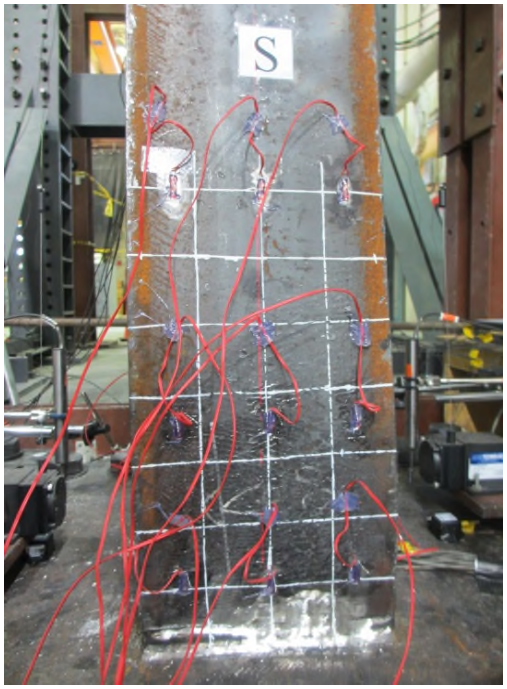

(c) South view

(d) East view

Figure A.39 W-6-34-C1-V: Post-test specimen observation

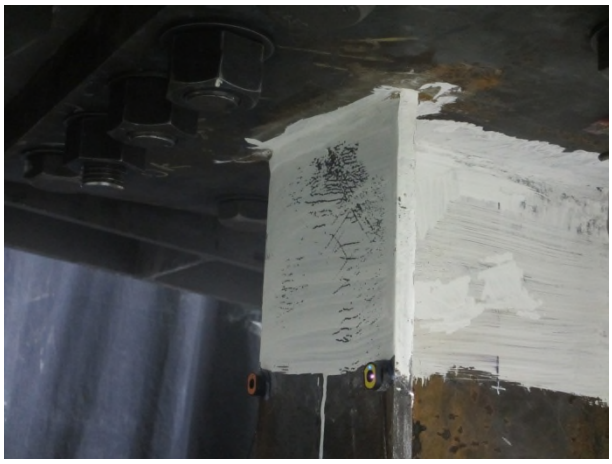

(e) Top end of north west flange

(f) Top end of south flange

(g) Top end of west web

Figure A.39 W-6-34-C1-V: Post-test specimen observation (continued)

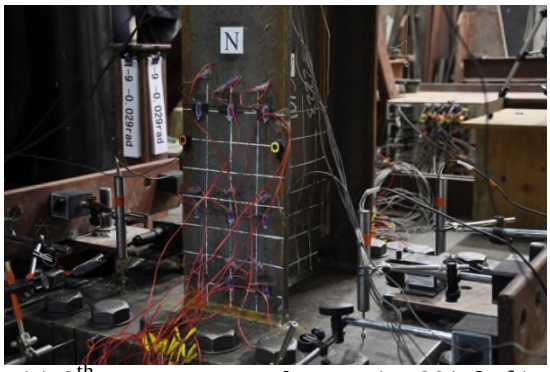

(a) 9th excursion in phase 1 (-2.9% drift)

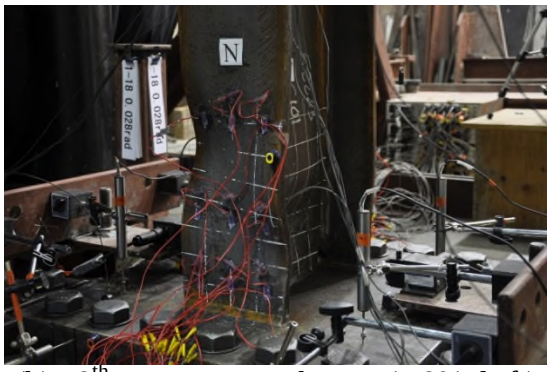

(b) 18th excursion in phase 1 (2.8% drift)

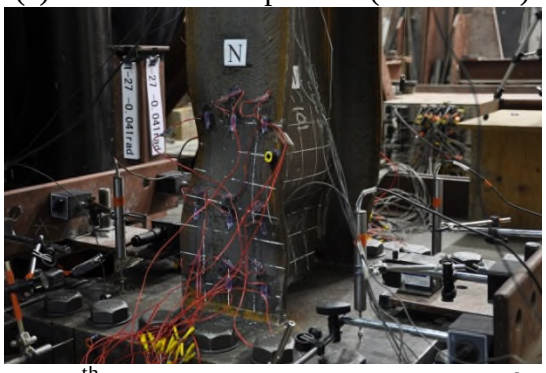

(c) 27th excursion in phase 1 (-4.1% drift)

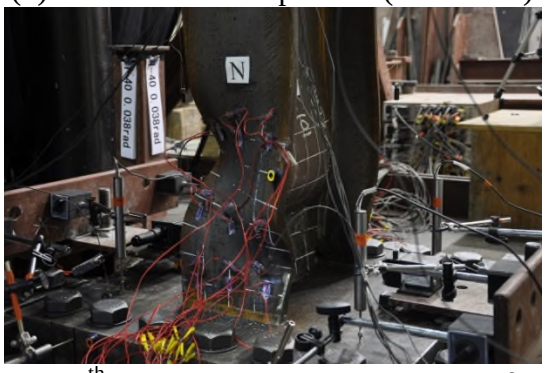

(d) 40th excursion in phase 1 (3.8% drift)

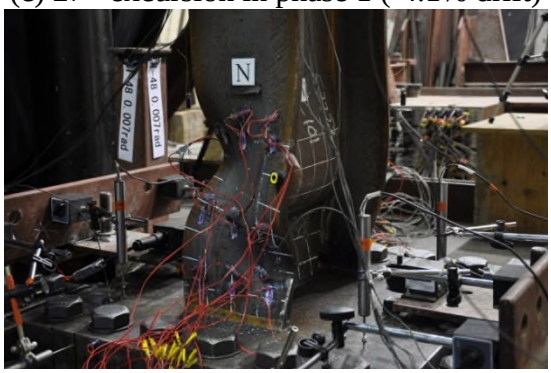

(e) End of phase 1 (0.7% drift)

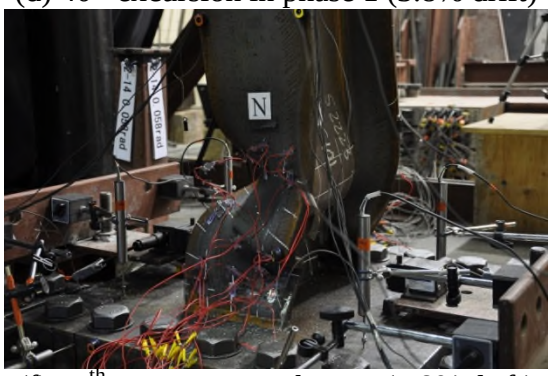

(f) 14th excursion in phase 2 (5.8% drift)

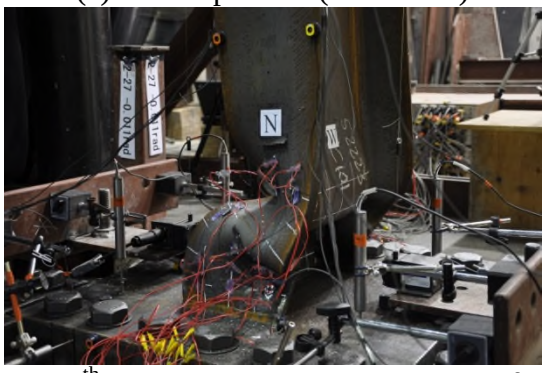

(g) 27th excursion in phase 2 (-1.1% drift)

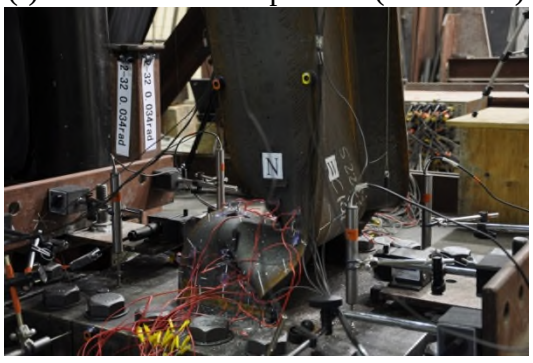

(h) 32th excursion in phase 2 (squashed)

Figure A.40 W-6-34-C2-C: Flange local buckling (North West view)

(a) 9th excursion in phase 1 (-2.9% drift)

(b) 18th excursion in phase 1 (2.8% drift)

(c) 27th excursion in phase 1 (-4.1% drift)

(d) 40th excursion in phase 1 (3.8% drift)

(e) End of phase 1 (0.7% drift)

(f) 14th excursion in phase 2 (5.8% drift)

(g) 27th excursion in phase 2 (-1.1% drift)

(h) 32th excursion in phase 2 (squashed)

Figure A.41 W-6-34-C2-C: Overall deformed configuration (West view)

(a) North view

(b) West view

(c) South view

(d) East view

Figure A.42 W-6-34-C2-C: Post-test specimen observation

(e) North west flange

(f) South west flange

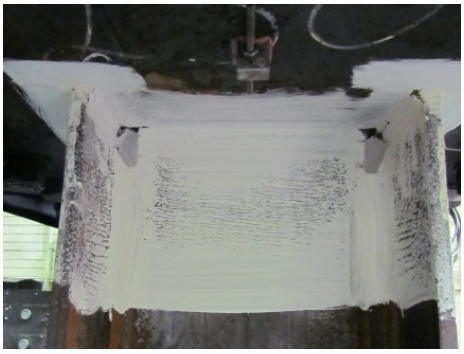

(g) Top end of west web

(h) Top end of north flange

(i) Top end of south flange

(j) Top end of east web

Figure A.42 W-6-34-C2-C: Post-test specimen observation (continued)

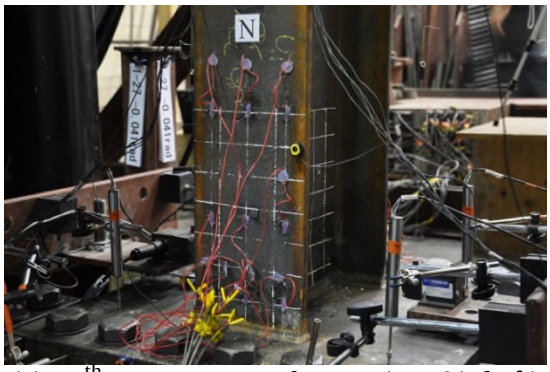

(a) 27th excursion in phase 1 (-4.1% drift)

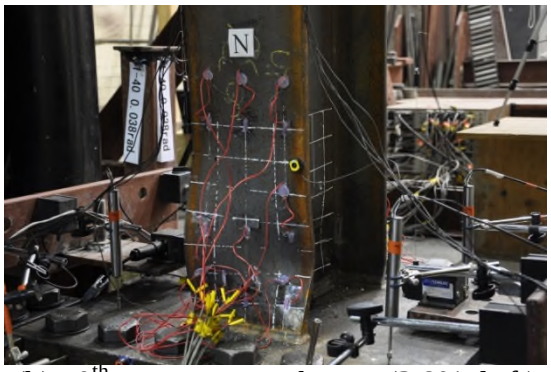

(b) 40th excursion in phase 1 (3.8% drift)

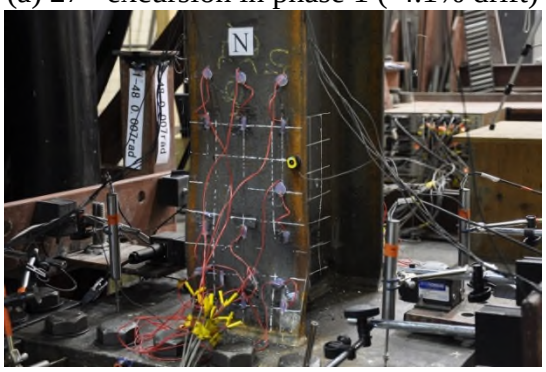

(c) End of phase 1 (0.7% drift)

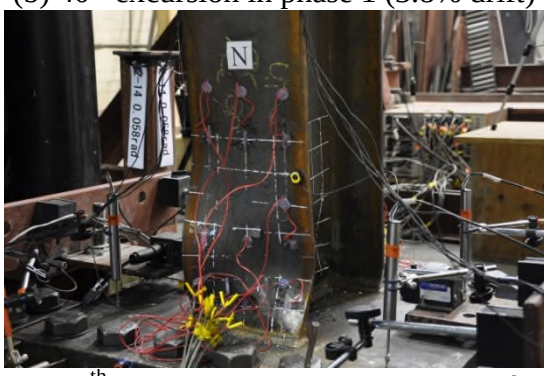

(d) 14th excursion in phase 2 (5.8% drift)

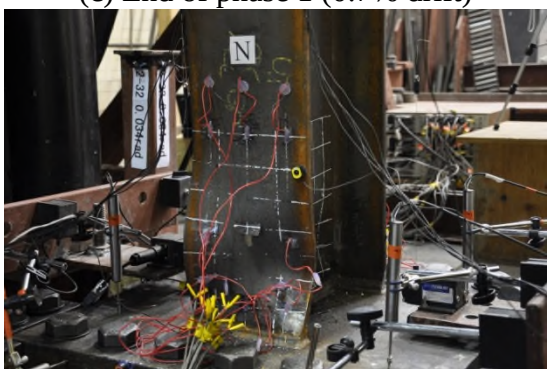

(e) End of phase 2 (3.4% drift)

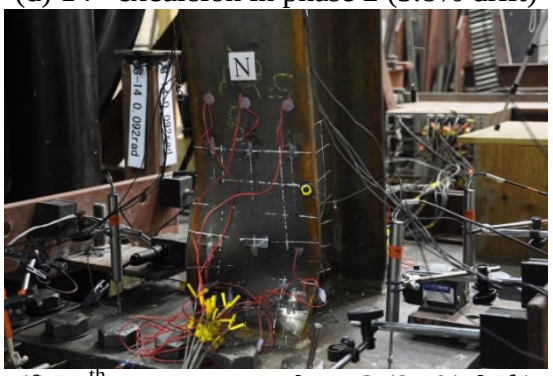

(f) 14th excursion in phase 3 (9.2% drift)

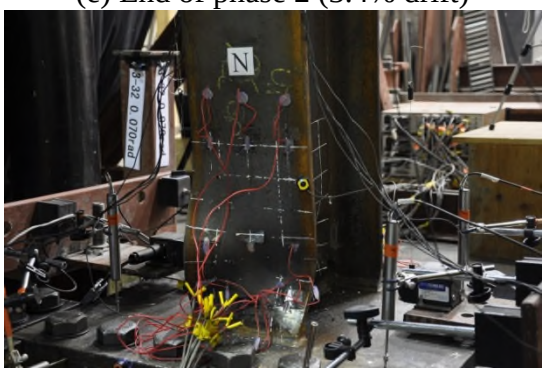

(g) End of phase 2 (7% drift)

Figure A.43 W-6-34-C2-V: Flange local buckling (North West view)

(a) 27th excursion in phase 1 (-4.1% drift)

(b) 40th excursion in phase 1 (3.8% drift)

(c) End of phase 1 (0.7% drift)

(d) 14th excursion in phase 2 (5.8% drift)

(e) End of phase 2 (3.4% drift)

(f) 14th excursion in phase 3 (9.2% drift)

(g) End of phase 2 (7% drift)

Figure A.44 W-6-34-C2-V: Overall deformed configuration (West view)

(a) North view

(b) West view

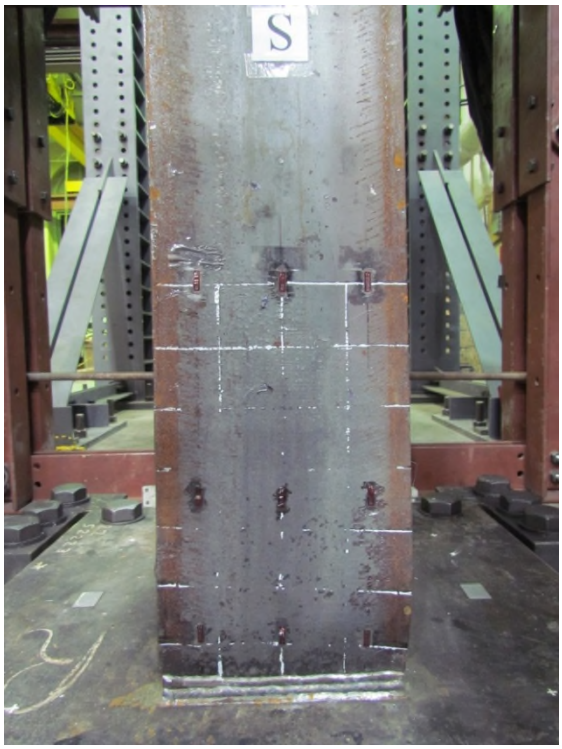

(c) South view

(d) East view

Figure A.45 W-6-34-C2-V: Post-test specimen observation

(e) Tip of north west flange

(f) North west flange and weld access hole

(g) Top end of north east flange

(h) Top end of south west flange

Figure A.45 W-6-34-C2-V: Post-test specimen observation (continued)

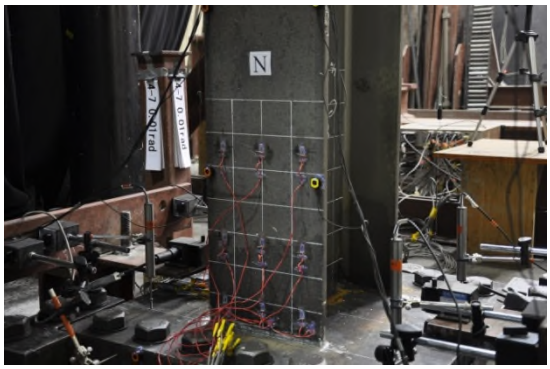

(a) +1%drift

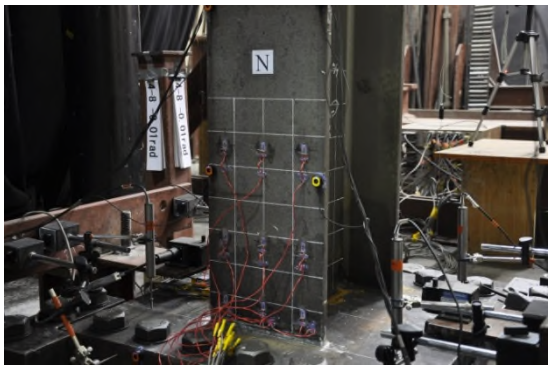

(b) -1% drift

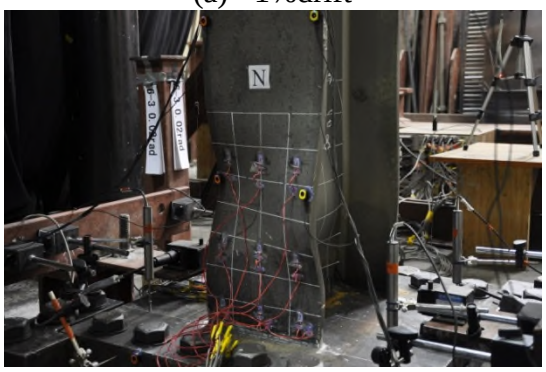

(c) +2% drift

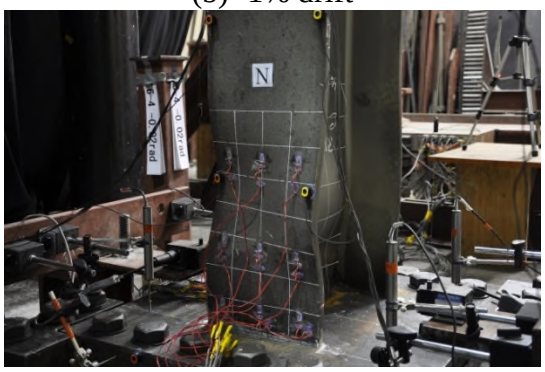

(d) % drift

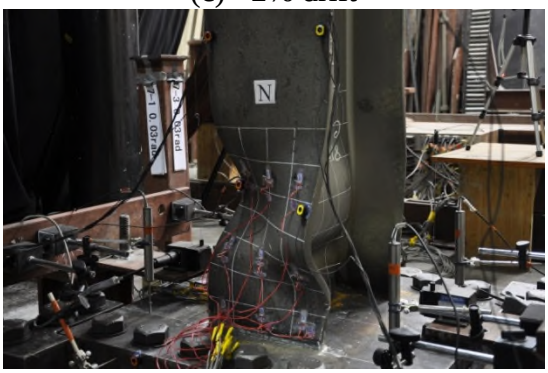

(e) +3% drift

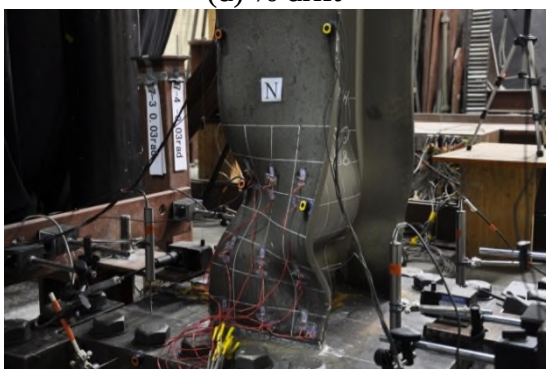

(f) -3% drift

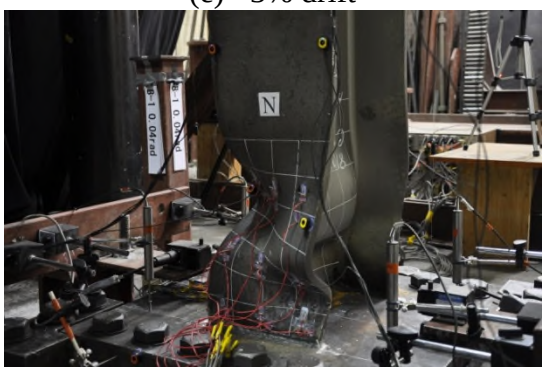

(g) +4% drift

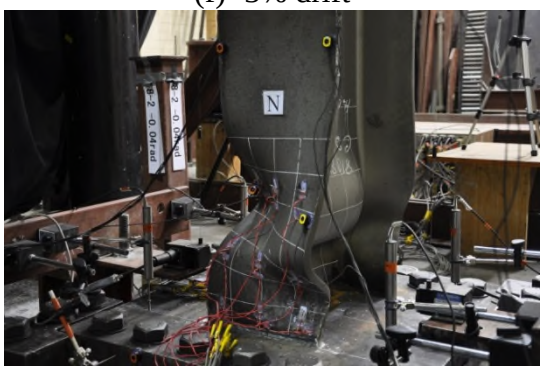

(h) -4% drift

Figure A.46 W-8-34-S-C: Flange local buckling (North West view)

(a) +1%drift

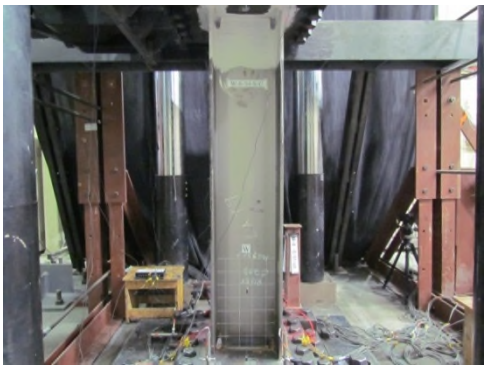

(b) -1% drift

(c) +2% drift

(d) % drift

(e) +3% drift

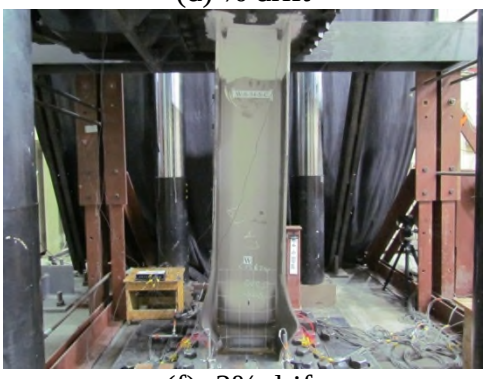

(f) -3% drift

(g) +4% drift

(h) -4% drift

Figure A.47 W-8-34-S-C: Overall deformed configuration (West view)

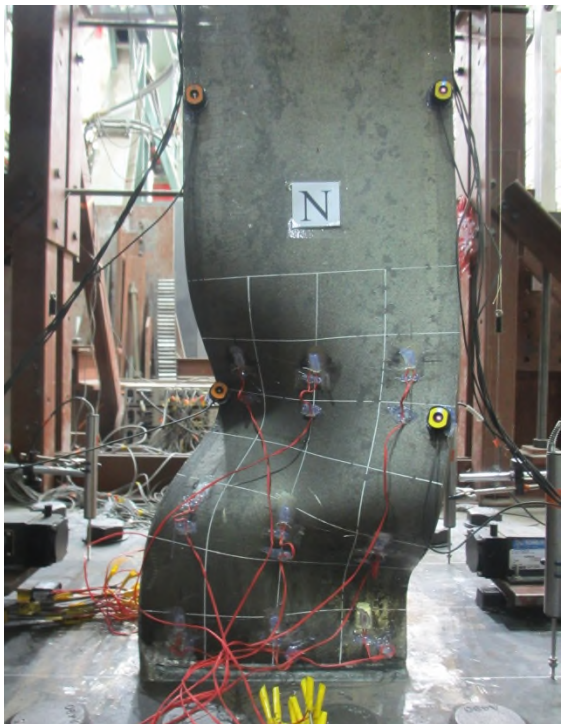

(a) North view

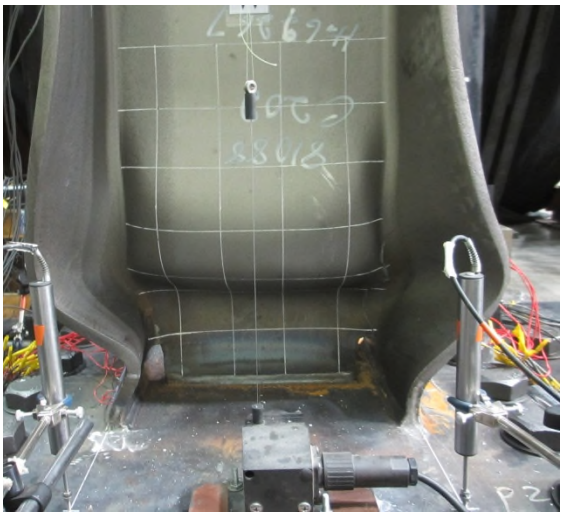

(b) West view

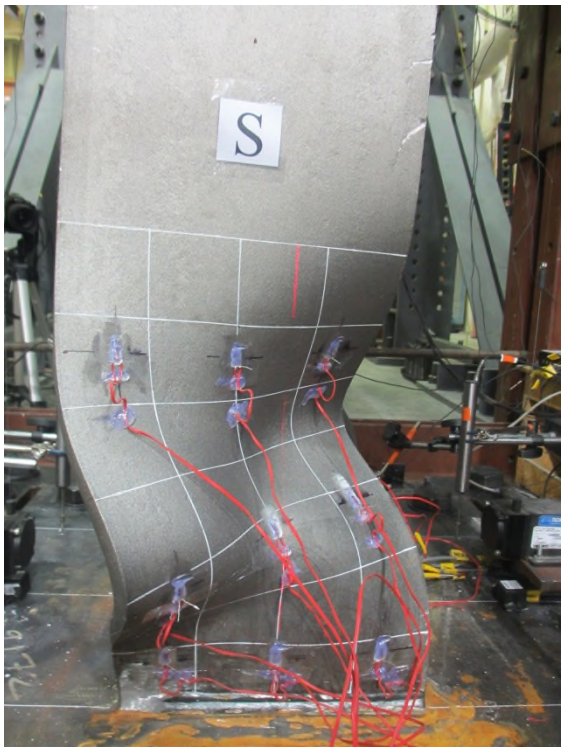

(c) South view

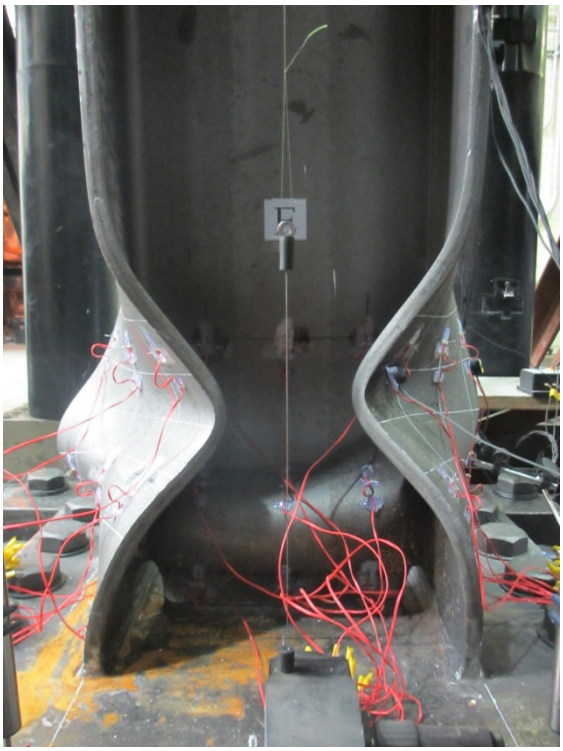

(d) East view

Figure A.48 W-8-34-S-C: Post-test specimen observation

(e) South side K-area (West view)

(f) South side K-area (East view)

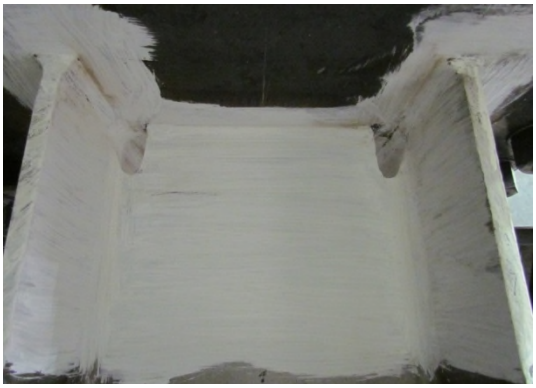

(g) Top end of west web

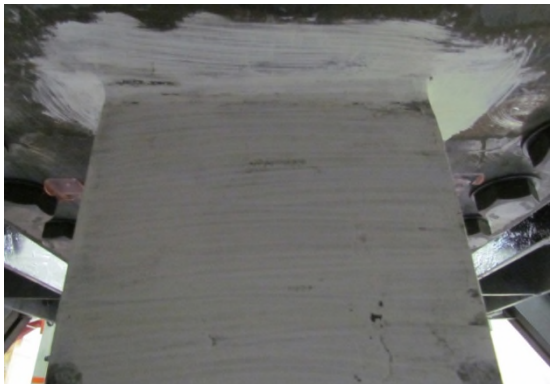

(h) Top end of north flange

(i) Top end of east web

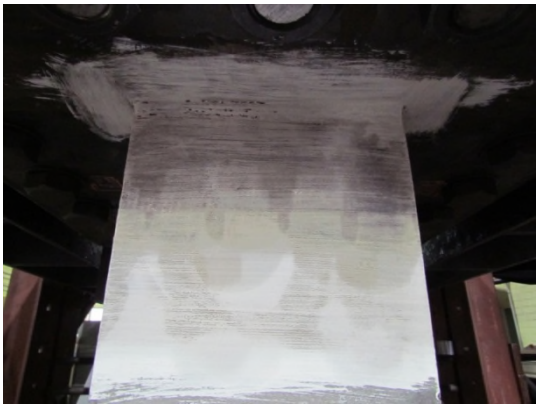

(j) Top end of south flange

Figure A.48 W-8-34-S-C: Post-test specimen observation (continued)

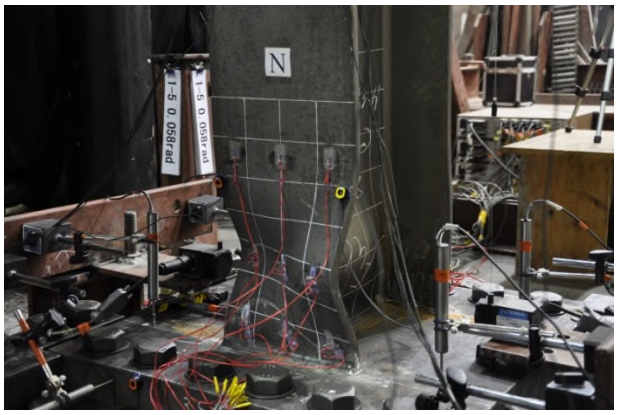

(a) 5th excursion in phase 1 (5.8% drift)

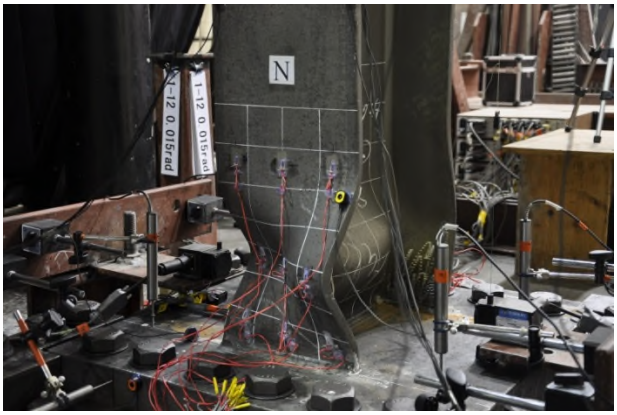

(b) End of phase 1 (1.5% drift)

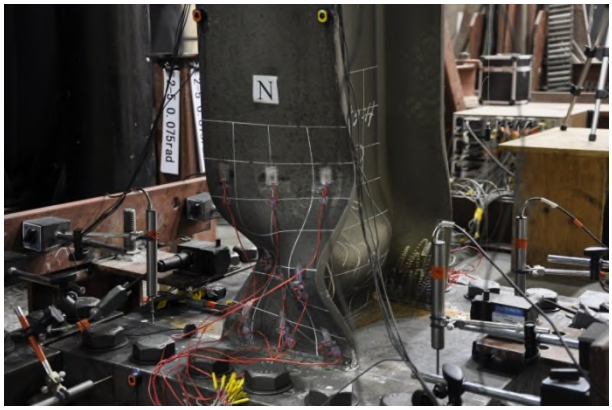

(c) 5th excursion in phase 2 (7.5% drift)

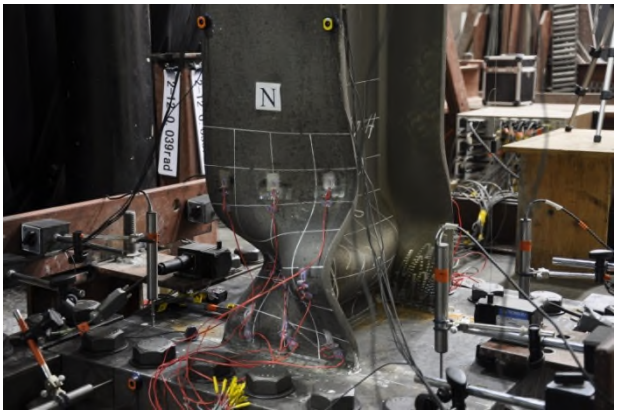

(d) End of phase 2 (3.9% drift)

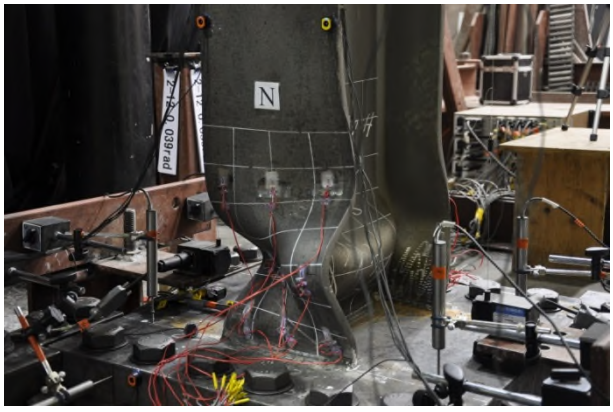

(e) 5th excursion in phase 3 (9.8% drift)

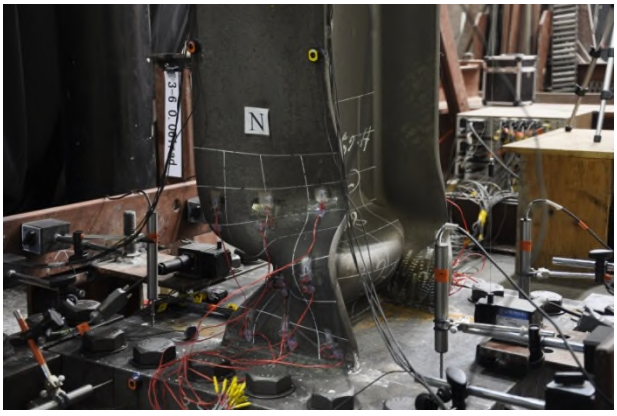

(f) End of test (fractured)

Figure A.49 W-8-34-C1-C: Flange local buckling (North West view)

(a) 5th excursion in phase 1 (5.8% drift)

(b) End of phase 1 (1.5% drift)

(c) 5th excursion in phase 2 (7.5% drift)

(d) End of phase 2 (3.9% drift)

(e) 5th excursion in phase 3 (9.8% drift)

(f) End of test (fractured)

Figure A.50 W-8-34-C1-C: Overall deformed configuration (West view)

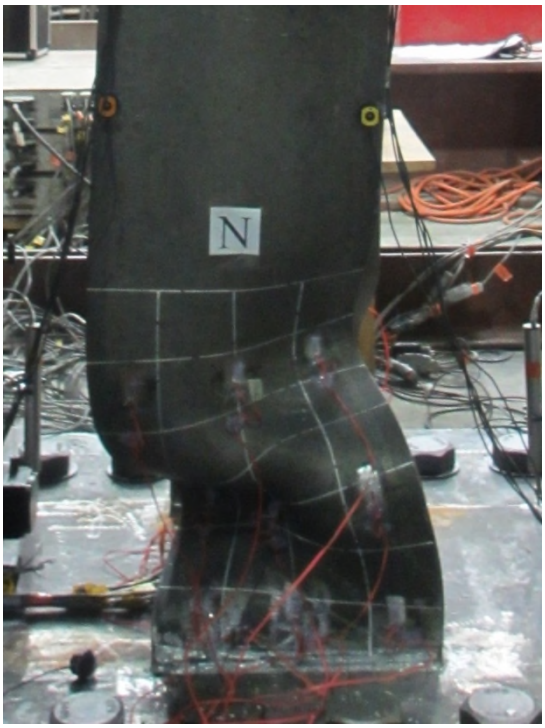

(a) North view

(b) West view

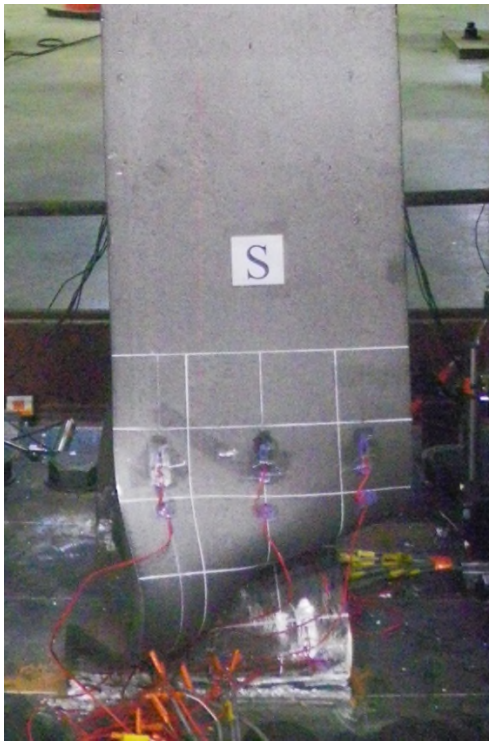

(c) South view

(d) East view

Figure A.51 W-8-34-C1-C: Post-test specimen observation

(e) South side K-area (East view)

(f) South side K-area (West view)

(g) Top end of west web

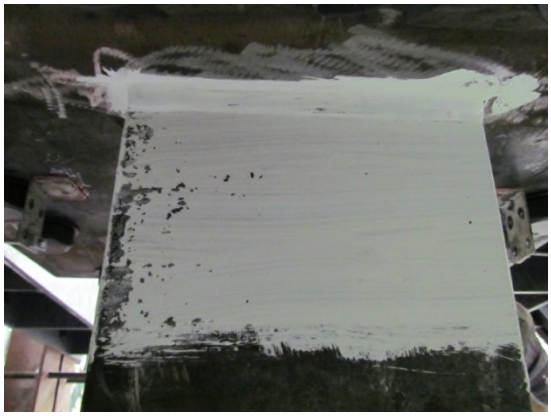

(h) Top end of north flange
(White wash dropped due to the impact of brittle fracture.)

(i) Top end of east web

(j) Top end of south flange

Figure A.51 W-8-34-C1-C: Post-test specimen observation (continued)

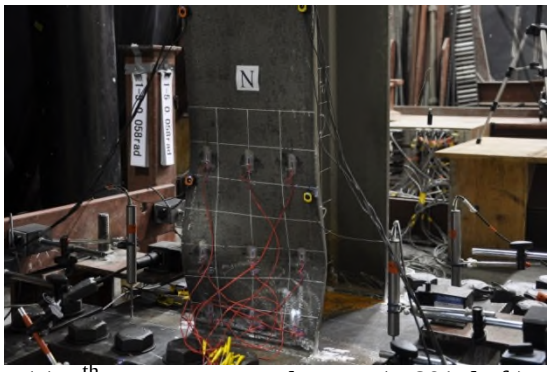

(a) 5th excursion in phase 1 (5.8% drift)

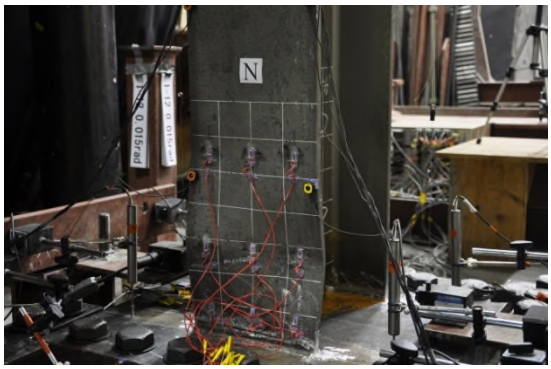

(b) End of phase 1 (1.5% drift)

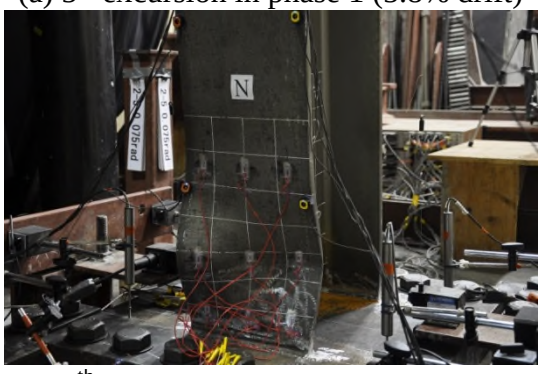

(c) 5th excursion in phase 2 (7.5% drift)

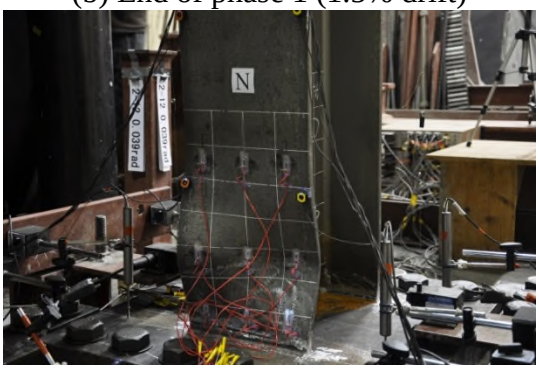

(d) End of phase 2 (3.9% drift)

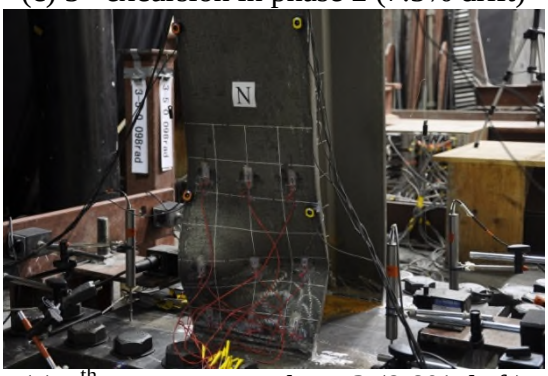

(e) 5th excursion in phase 3 (9.8% drift)

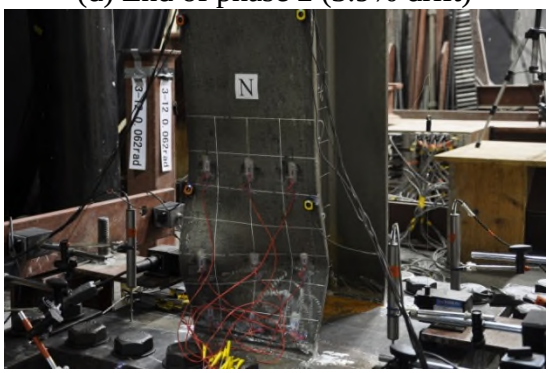

(f) End of phase 3 (6% drift)

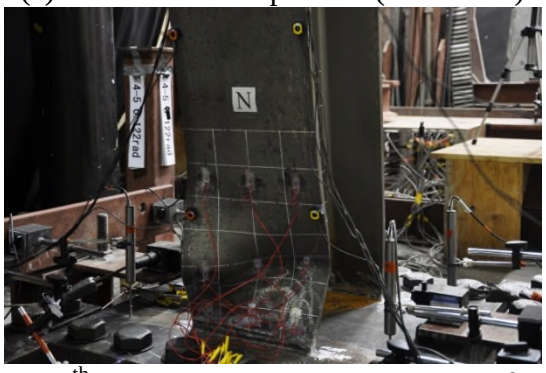

(g) 5th excursion in phase 4 (12.2% drift)

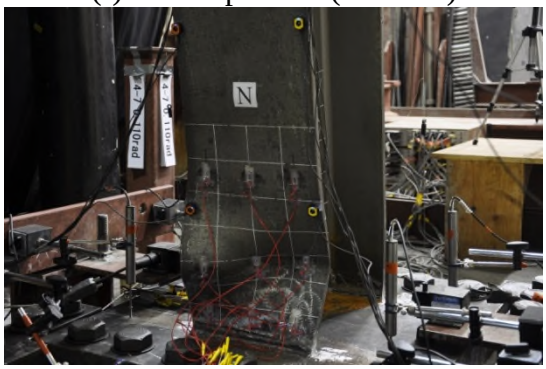

(h) End of test (fractured)

Figure A.52 W-8-34-C1-V: Flange local buckling (North West view)

(a) 5th excursion in phase 1 (5.8% drift)

(b) End of phase 1 (1.5% drift)

(c) 5th excursion in phase 2 (7.5% drift)

(d) End of phase 2 (3.9% drift)

(e) 5th excursion in phase 3 (9.8% drift)

(f) End of phase 3 (6% drift)

(g) 5th excursion in phase 4 (12.2% drift)

(h) End of test (fractured)

Figure A.53 W-8-34-C1-V: Overall deformed configuration (West view)

(a) West view

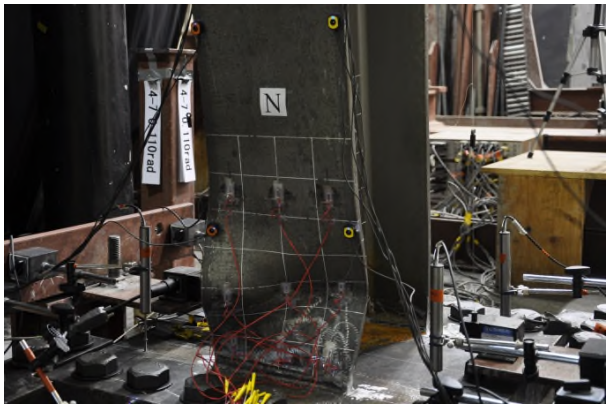

(b) North West view

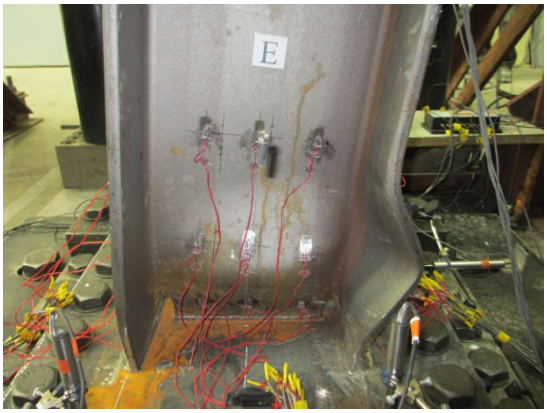

(c) East view

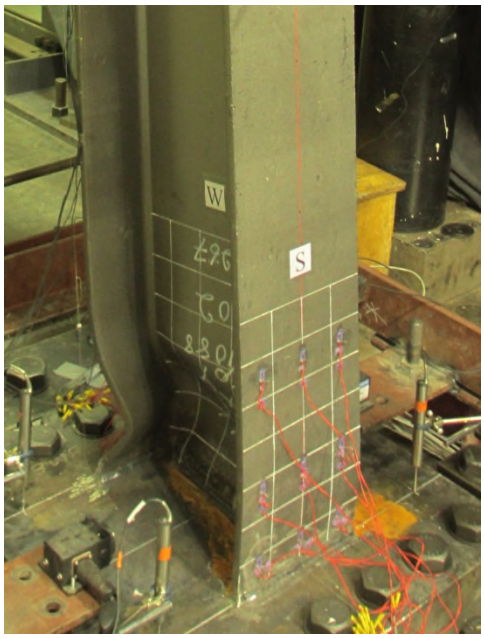

(d) South West view

Figure A.54 W-8-34-C1-V: Post-test specimen observation

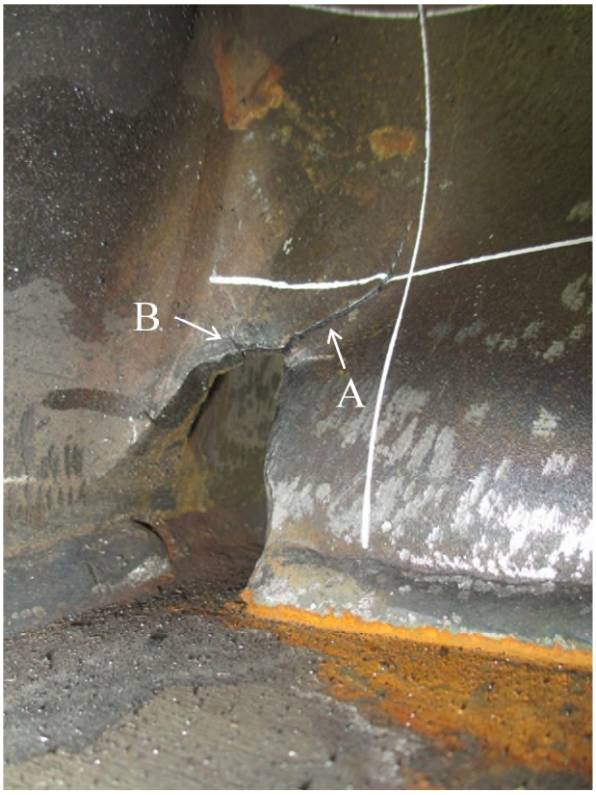

(e) North side weld access hole (West view)

(f) Top end of north east flange

(g) Top end of south east flange

Figure A.54 W-8-34-C1-V: Post-test specimen observation (continued)

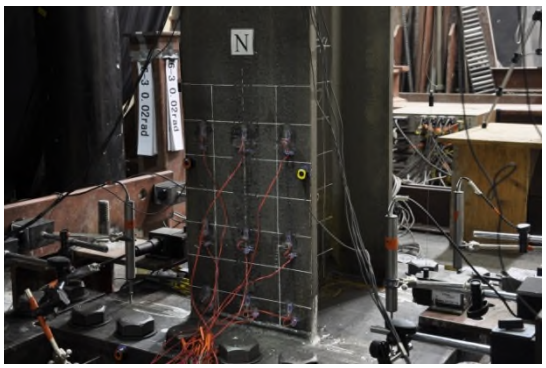

(a) +2% drift

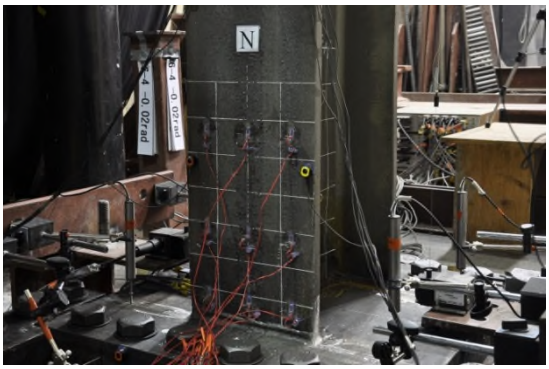

(b) -2% drift

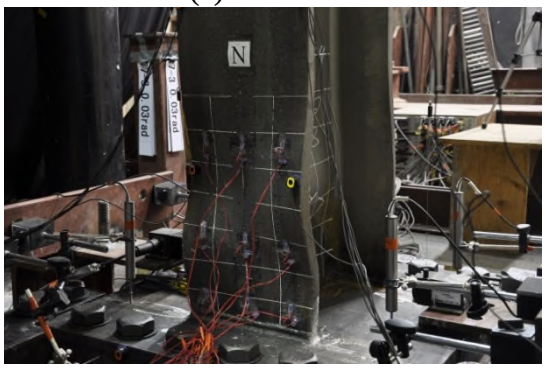

(c) +3% drift

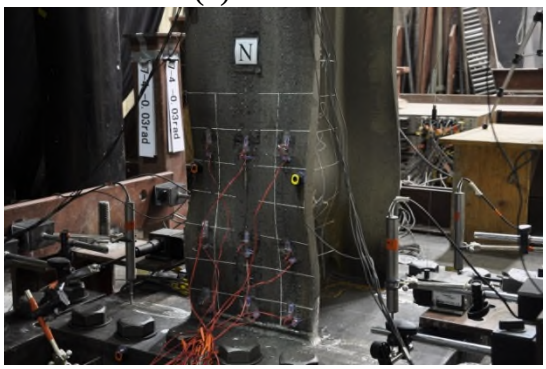

(d) -3% drift

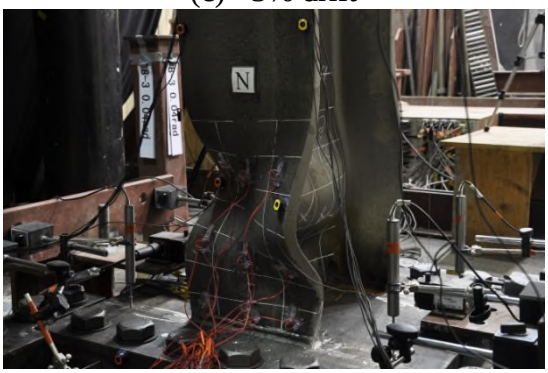

(e) +4% drift

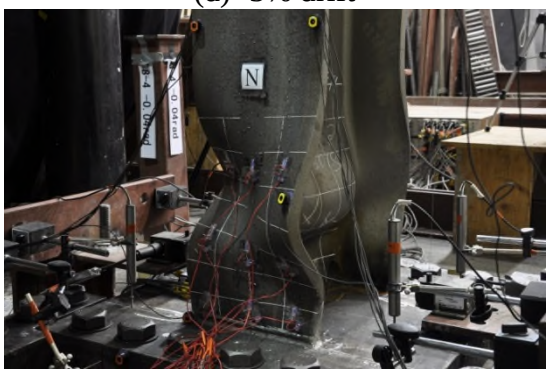

(f) -4% drift

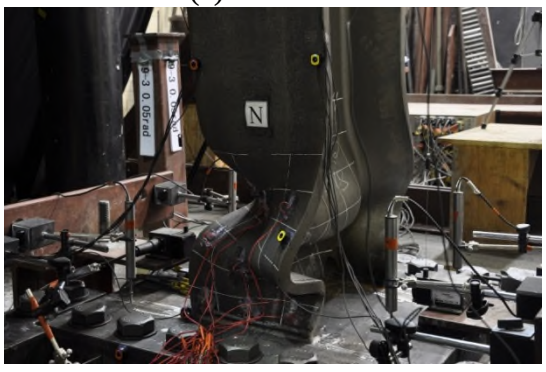

(g) +5% drift

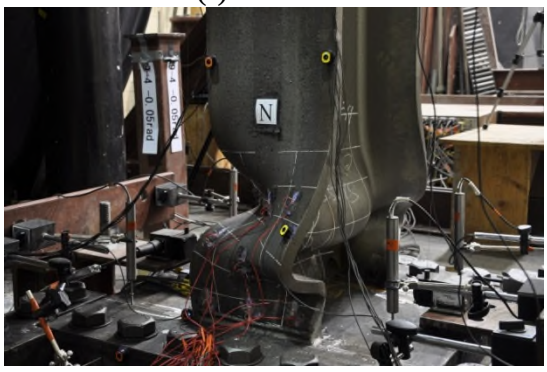

(h) -5% drift

Figure A.55 W-6-25-S-C: Flange local buckling (North West view)

(a) +2% drift

(b) -2% drift

(c) +3% drift

(d) -3% drift

(e) +4% drift

(f) -4% drift

(g) +5% drift

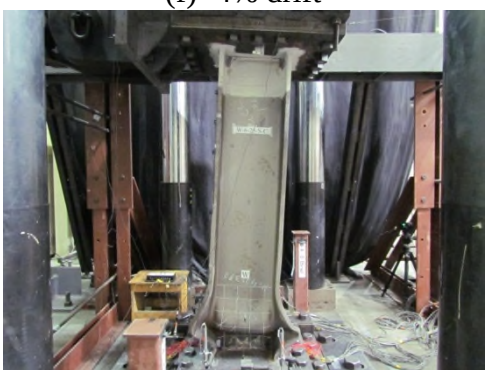

(h) -5% drift

Figure A.56 W-6-25-S-C: Overall deformed configuration (West view)

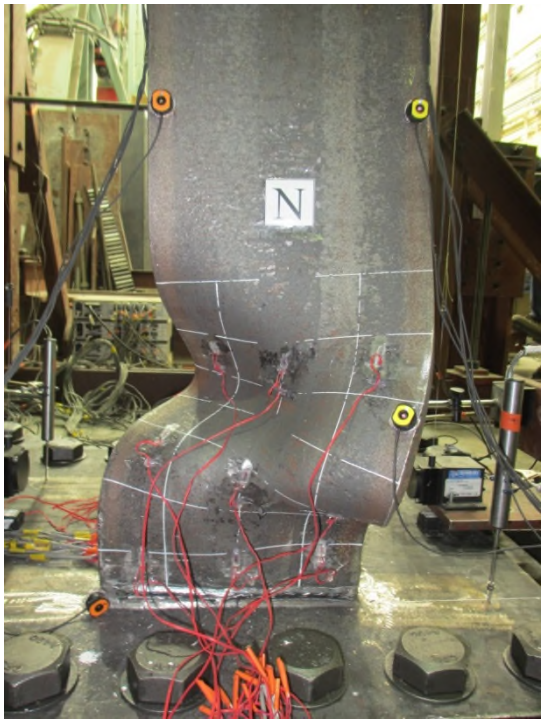

(a) North view

(b) West view

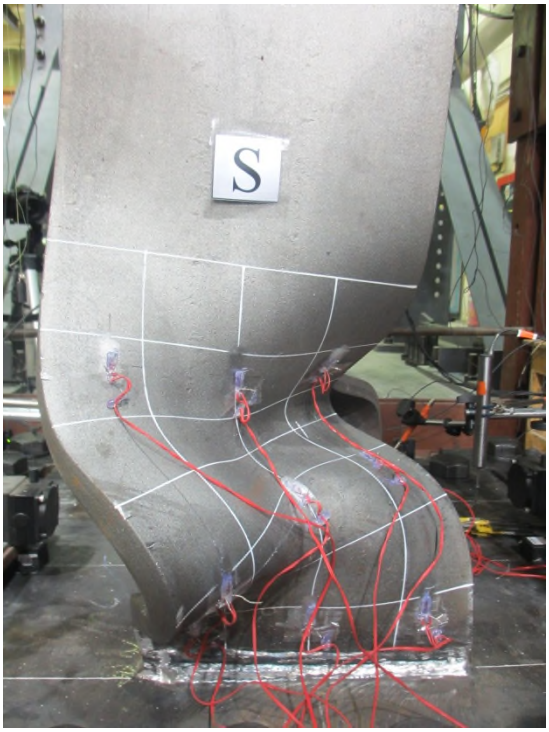

(c) South view

(d) East view

Figure A.57 W-6-25-S-C: Post-test specimen observation

(e) South side K-area (West view)

(f) Top end of west web

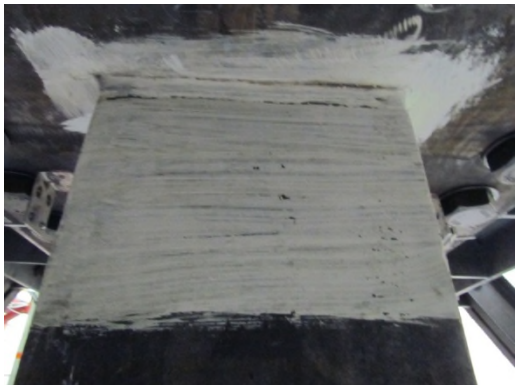

(g) Top end of north flange

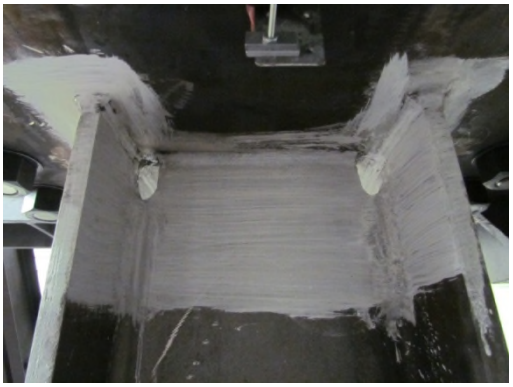

(h) Top end of east web

(i) Top end of south flange

Figure A.57 W-6-25-S-C: Post-test specimen observation (continued)

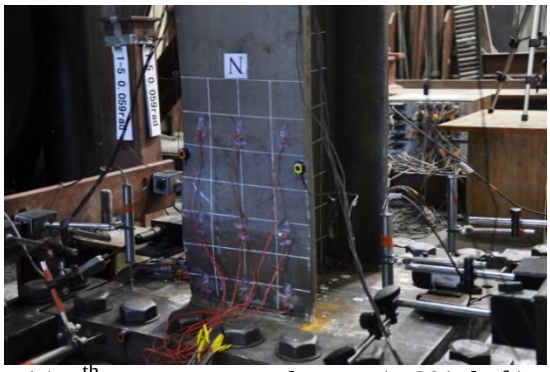

(a) 5th excursion in phase 1 (5.9% drift)

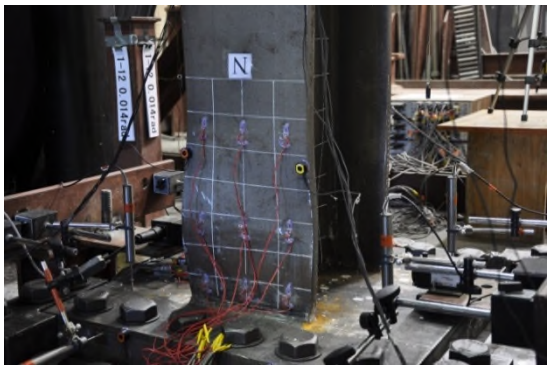

(b) End of phase 1 (1.4% drift)

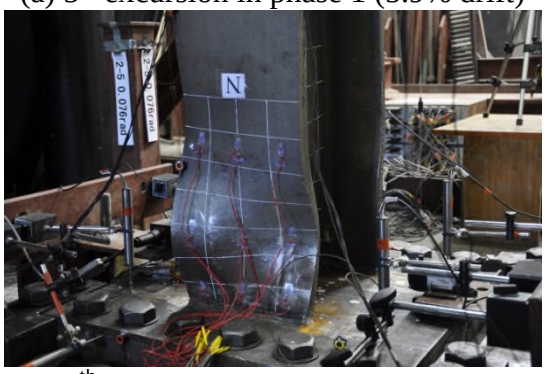

(c) 5th excursion in phase 2 (7.6% drift)

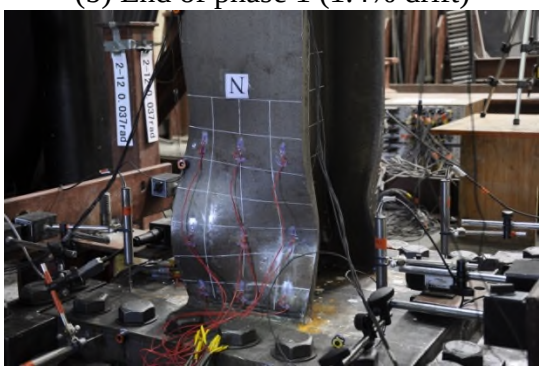

(d) End of phase 2 (3.7% drift)

(e) 5th excursion in phase 3 (9.9% drift)

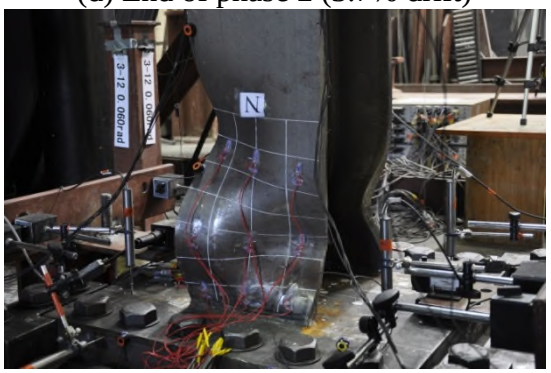

(f) End of phase 3 (6% drift)

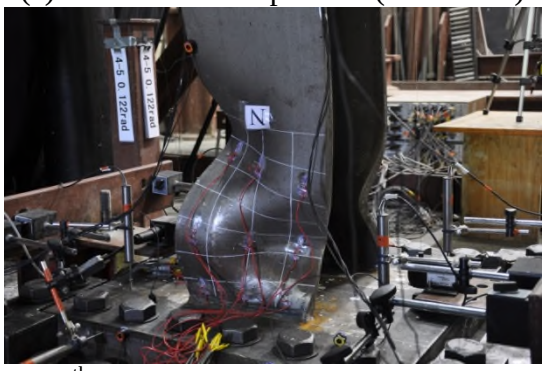

(g) 5th excursion in phase 4 (12.2% drift)

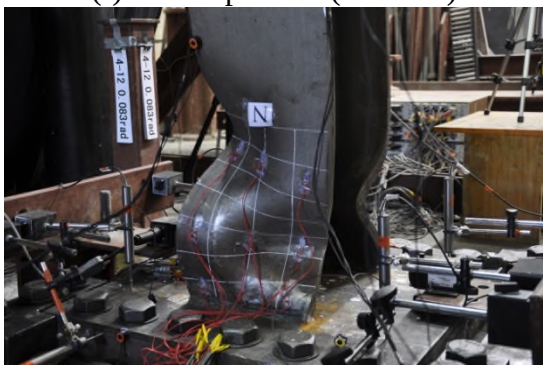

(h) End of phase 4 (8.3% drift)

Figure A.58 W-6-25-C1-C: Flange local buckling (North West view)

(a) 5th excursion in phase 1 (5.9% drift)

(b) End of phase 1 (1.4% drift)

(c) 5th excursion in phase 2 (7.6% drift)

(d) End of phase 2 (3.7% drift)

(e) 5th excursion in phase 3 (9.9% drift)

(f) End of phase 3 (6% drift)

(g) 5th excursion in phase 4 (12.2% drift)

(h) End of phase 4 (8.3% drift)

Figure A.59 W-6-25-C1-C: Overall deformed configuration (West view)

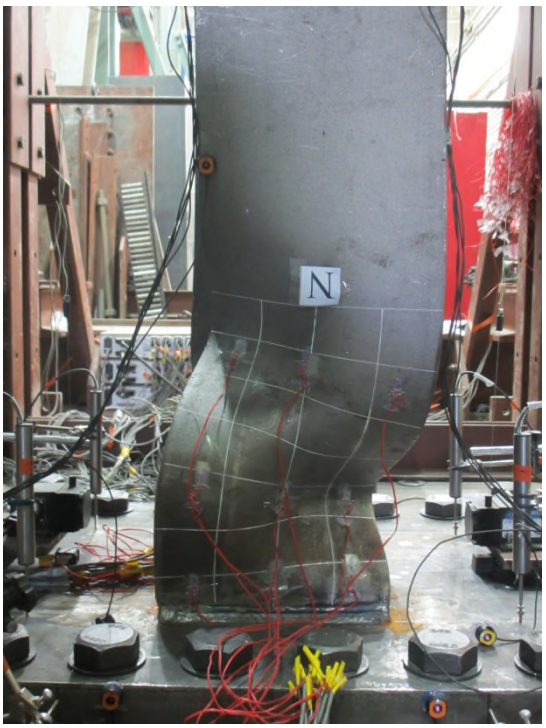

(a) North view

(b) West view

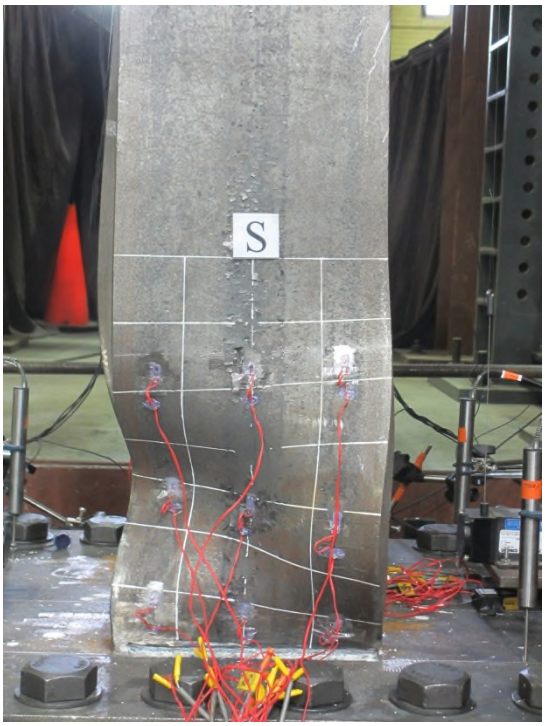

(c) South view

(d) East view

Figure A.60 W-6-25-C1-C: Post-test specimen observation

(e) Top end of west web

(f) Top end of north flange

(g) Top end of east web

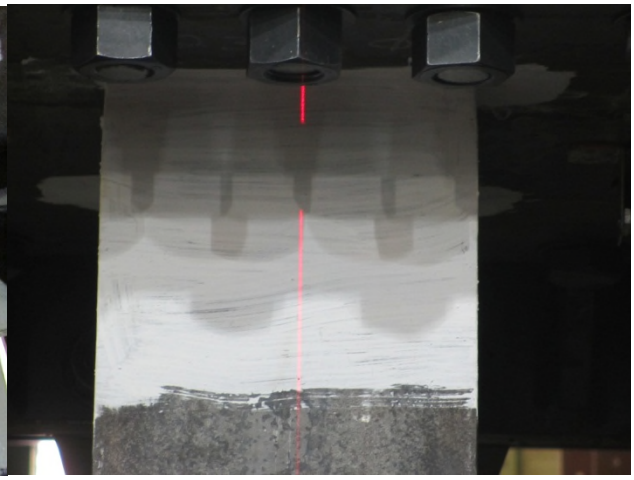

(h) Top end of south flange

Figure A.60 W-6-25-C1-C: Post-test specimen observation (continued)

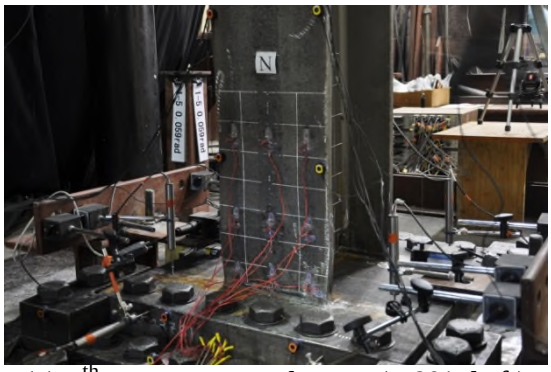

(a) 5th excursion in phase 1 (5.9% drift)

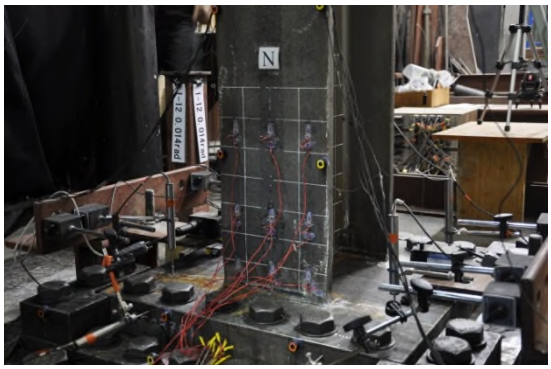

(b) End of phase 1 (1.4% drift)

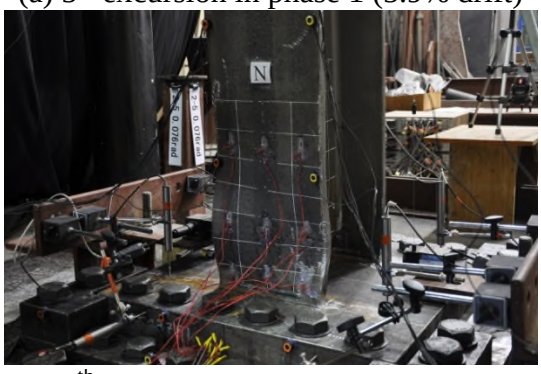

(c) 5th excursion in phase 2 (7.6% drift)

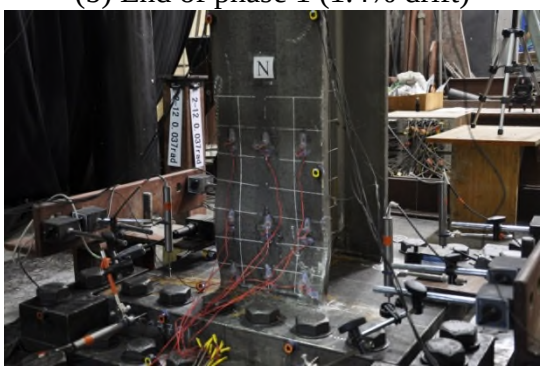

(d) End of phase 2 (3.7% drift)

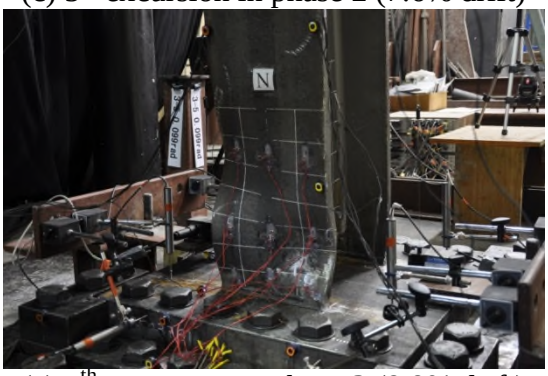

(e) 5th excursion in phase 3 (9.9% drift)

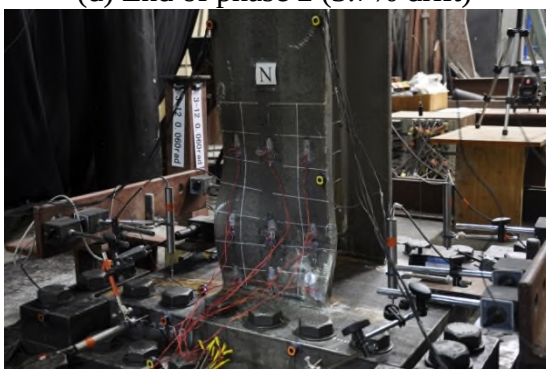

(f) End of phase 3 (6% drift)

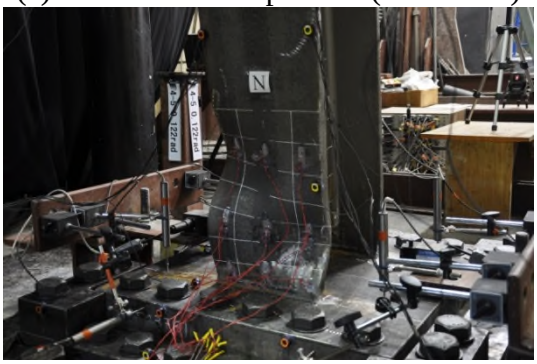

(g) 5th excursion in phase 4 (12.2% drift)

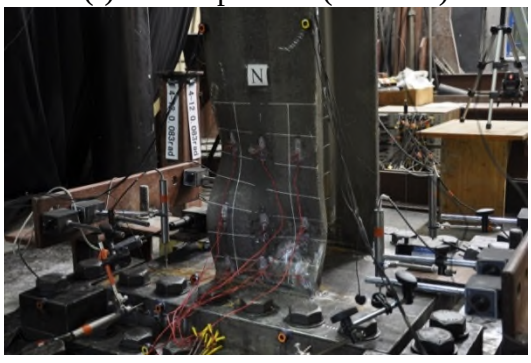

(h) End of phase 4 (8.3% drift)

Figure A.61 W-6-25-C1-V: Flange local buckling (North West view)

(a) 5th excursion in phase 1 (5.9% drift)

(b) End of phase 1 (1.4% drift)

(c) 5th excursion in phase 2 (7.6% drift)

(d) End of phase 2 (3.7% drift)

(e) 5th excursion in phase 3 (9.9% drift)

(f) End of phase 3 (6% drift)

(g) 5th excursion in phase 4 (12.2% drift)

(h) End of phase 4 (8.3% drift)

Figure A.62 W-6-25-C1-V: Overall deformed configuration (West view)

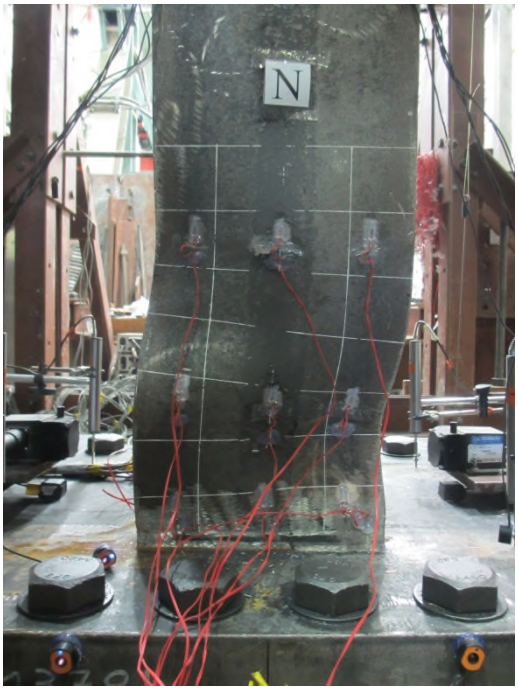

(a) North view

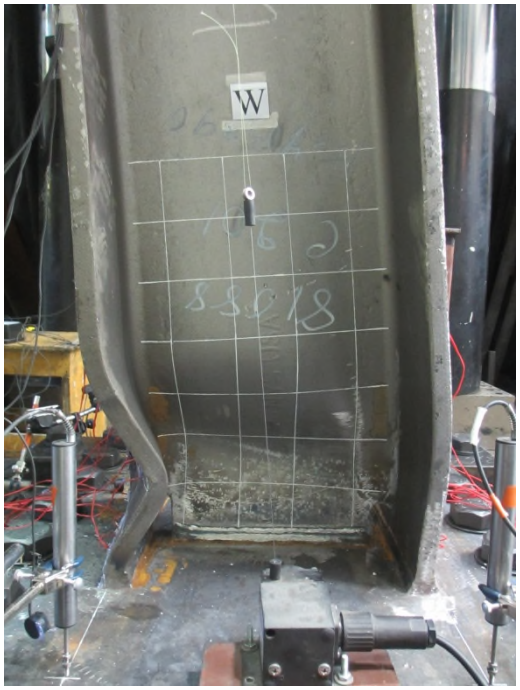

(b) West view

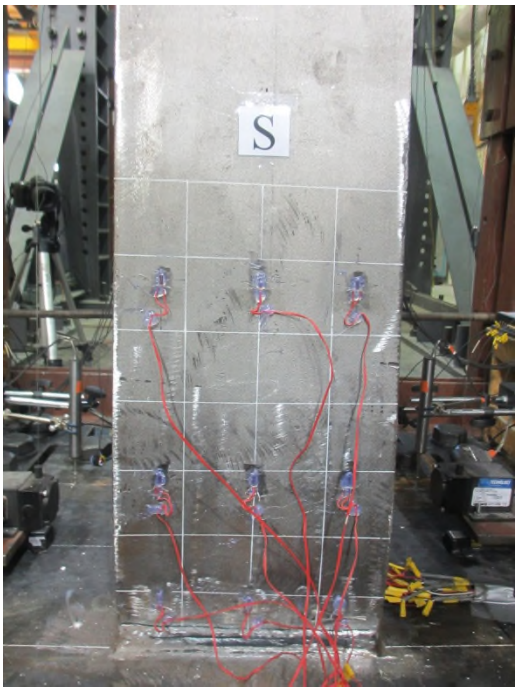

(c) South view

(d) East view

Figure A.63 W-6-25-C1-V: Post-test specimen observation

(e) North side weld access hole (West view)

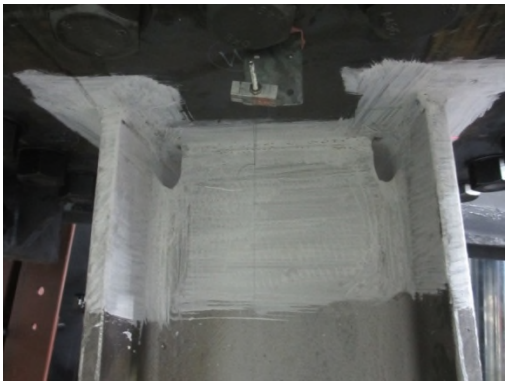

(f) Top end of west web

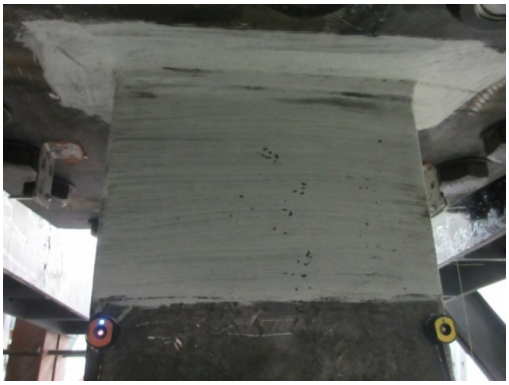

(g) Top end of north flange

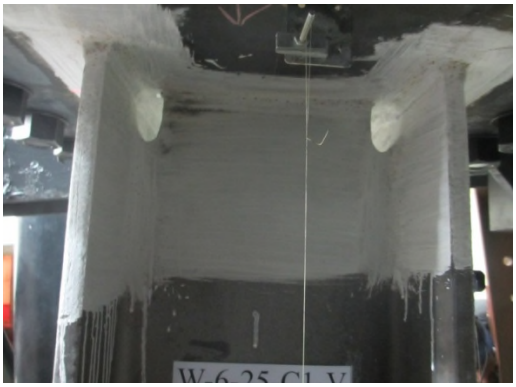

(h) Top end of east web

(i) Top end of south flange

Figure A.63 W-6-25-C1-V: Post-test specimen observation (continued)